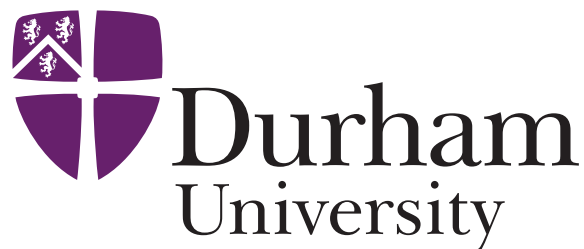


Hidden neutrino physics

Rare processes, new forces, and dark sectors

Matheus Hostert

A Thesis presented for the degree of
Doctor of Philosophy



Institute for Particle Physics Phenomenology
Department of Physics
Durham University
United Kingdom

July 2019

Hidden neutrino physics

Rare processes, new forces, and dark sectors

Matheus Hostert

Submitted for the degree of Doctor of Philosophy

July 2019

Abstract: This is some abstract about this thesis.

Dedicated to

Bárbara, Humberto and Luciana.

Contents

Abstract	2
List of Figures	8
List of Tables	10
1 Introduction	14
1.1 The Standard Model	15
1.1.1 Fields and symmetries	16
1.1.2 Spontaneous symmetry breaking	19
1.1.3 Fermion masses	21
1.2 Evidence for Beyond the Standard Model physics	23
1.3 Extending the Standard Model	26
1.3.1 Portals to hidden sectors	27
2 Neutrinos beyond the Standard Model	30
2.1 The three neutrino paradigm	30
2.2 Oscillations	30
2.2.1 Matter effects	34
2.3 The model space of neutrino physics	37
2.3.1 Mass mechanisms	37
2.3.2 Conventional seesaws	38

2.3.3	Low scale seesaw variants	38
2.3.4	Radiative masses	38
2.3.5	Sources	38
2.4	Scattering	38
3	Neutrino trident scattering	40
3.1	Neutrino-electron scattering	40
3.1.1	Kinematics	41
3.1.2	Measurements	42
3.2	Neutrino trident scattering	42
3.3	Trident Production Cross Section	44
3.3.1	Hadronic Scattering Regimes	48
3.3.2	Breakdown of the EPA	52
3.3.3	Coherent versus incoherent Scattering in Trident Production	58
3.4	Trident Events in LAr Detectors	60
3.4.1	Event Rates	61
3.4.2	Background Estimates for Neutrino Trident in LAr	65
3.5	Conclusions	70
3.6	Individual Backgrounds	73
3.6.1	Pion Production	73
3.6.2	Charm Production	74
3.6.3	CC γ and NC γ	75
4	New fundamental forces at DUNE	76
4.1	Introduction	76
4.2	Leptophilic Z' models	79
4.3	Signatures of leptonic neutral currents	83

4.3.1	Neutrino trident scattering	84
4.3.2	Neutrino-electron scattering	90
4.3.3	Interference effects	91
4.4	DUNE sensitivities	92
4.4.1	Analysis techniques	92
4.4.2	$L_e - L_\mu$	96
4.4.3	$L_\mu - L_\tau$	99
4.5	Conclusions	101
5	A light dark neutrino sector	105
5.1	The Model	107
5.1.1	Portal phenomenology	110
5.2	Dark Matter	113
5.3	Radiative generation of neutrino masses	114
5.4	Model set-up	116
5.5	Neutrino masses	117
5.5.1	Radiative corrections	118
5.6	Searching for the origin of neutrino masses	120
6	Tests of the MiniBooNE anomaly	124
6.1	Dark neutrinos at MiniBooNE	125
6.2	Dark neutrinos in neutrino-electron scattering measurements	127
6.3	MINER ν A and CHARM-II analyses	128
6.4	Results and prospects	130
7	The future of neutrino precision physics	133
8	Conclusions	134

Appendices	135
A Phase space	135
B Form factors	138
C Trident distributions	140
D Trident rates at current facilities	144
D.1 Trident rates in current facilities	144
E Dark neutrino self-energies	148
E.0.1 Self-energy	148

List of Figures

1.1	Artistic rendering of the particles in the Standard Model.	23
2.1	Neutrino oscillations diagram.	31
2.2	Finite temperature corrections to Σ .	36
2.3	The tree-level UV completions of the Weinberg operator.	37
3.1	Neutrino trident production with a contact approximation.	45
3.2	Coherent neutrino trident production total cross sections.	50
3.3	Incoherent neutrino trident production total cross sections.	52
3.4	Comparison of the differential cross section using the EPA and using the full calculation for neutrino trident scattering.	56
3.5	Comparison of the total cross section in the EPA and in the full calculation for neutrino trident scattering.	57
3.6	Ration between coherent and incoherent trident total cross sections.	59
3.7	Kinematical cuts on background samples for dimuon tridents.	70
4.1	Diagrams of the Z' contribution to NC neutrino trident scattering.	85
4.2	BSM enhancement to dimuon neutrino trident production total cross section.	87
4.3	BSM enhancement to dielectron neutrino trident production total cross section.	87
4.4	Dimuon distributions in the presence of a Z' .	88
4.5	Dielectron distributions in the presence of a Z' .	89

4.6	Neutrino-electron scattering distributions in the presence of a Z' .	90
4.7	DUNE sensitivities to a $L_e - L_\mu Z'$.	96
4.8	DUNE sensitivity to a $L_e - L_\mu Z'$ with alternative assumptions.	97
4.9	DUNE sensitivity to a $L_\mu - L_\tau Z'$.	103
4.10	DUNE sensitivity to a $L_\mu - L_\tau Z'$ with alternative assumptions.	104
5.1	Dark neutrino model diagram.	107
5.3	Region of interest for neutrino mass generation in our model.	121
6.1	Dark neutrino signal at MiniBooNE.	126
6.2	Upscattering total cross section.	127
6.3	Diagram of the sidebands in neutrino-electron scattering analyses.	130
6.4	New constraints on dark neutrinos.	131
C.1	Neutrino trident distributions at the DUNE ND.	142
C.2	Additional trident distributions at the DUNE ND.	143

List of Tables

1.1	SM field content.	17
3.1	Neutrino trident production channels and their SM contributions.	46
3.2	Trident rates in LAr detectors.	62
3.3	Rates for particle misID in LAr.	67
3.4	Neutrino trident production background reduction at the DUNE ND. . . .	69
4.1	Neutrino trident and neutrino-electron scattering rates in the SM for different configurations of the LBNF beam.	93
D.1	Descriptions of non-LAr detectors.	145
D.2	Trident rates at non-LAr detectors.	147

Declaration

The work in this thesis is based on research carried out in the Department of Physics at Durham University. No part of this thesis has been submitted elsewhere for any degree or qualification.

Copyright © 2019 Matheus Hostert.

The copyright of this thesis rests with the author. No quotation from it should be published without the author's prior written consent and information derived from it should be acknowledged.

Acknowledgements

I would like to thank my supervisor Silvia Pascoli for her guidance and for her vision as a supervisor. I am lucky to have been your student and to have had the opportunities you gave me. I am also greatly thankful to Peter Ballett, without whom this thesis would have been but a boring collection of pages. Thank you for your patience and for sharing a bit of your crystal clear thinking with me.

Carlos Argüelles, Pedro Machado and Renata Zukanovich Funchal, thank you for the inspiration and support. My collaborators Yuber Perez Gonzalez, Zahra Tabrizi and Yu-Dai Tsai, thank you for all the hard work that made this thesis possible.

Looking further back, I also want to thank Débora Peres Menezes and Marcus Benghi Pinto for introducing me to scientific research so early in my career and understanding the importance of doing so. Nuclear physics and symmetry ideas that at the time seemed so foreign to me have reappeared in my own research several times.

To my family, thank you for supporting my decisions and for being unconditional allies. I would be nothing without the education of my mother and the wisdom of my father. Bê, you are simply the *best*.

Madeline, your support and sense of humour have been truly out of this world. Thank you for being such a great partner and for filling life with laughter.

Chapter 1

Introduction

“It really tied the room together.”

— Jeff Lebowski

These are exciting times in high-energy physics. The Standard Model (SM), our most powerful and well-tested theory of particles and their interactions, triumphs across the experimental landscape and proves to be much more robust than ever anticipated. Yet, as we will see throughout this thesis, once confronted with some of the simplest questions about the Universe, it provides unsatisfactory answers and, most surprisingly, little theoretical guidance on what may lie beyond. While there is no guarantee that the questions we ask are indeed “good” ones, to many, the limitations of the SM attest to the need of a new paradigm in particle physics. Whatever it may be, it makes the series of negative results in particle physics all the more thrilling. Uncertain moments like the one we live are frequent in the history of physics. For many times we saw established theoretical expectations and increasingly fine-tuned models making way for elegant theories like Special Relativity, for new particles such as the neutrino and for new ideas like spontaneous symmetry breaking (SSB).

In practice, of course, such grandiose endeavors are reduced to much less noble but no less important efforts. The frequency of negative results and the need to over-constrain our models make the search for new physics a true exercise in patience. Nevertheless, it is in a persistent and curious spirit that this thesis stands. The common theme of the work developed here is that of *hidden neutrino physics*, both in the sense of rare

neutrino processes and of hidden sectors beyond the SM. Hidden, dark or secret are all terms associated with new particles that hide not at high energies with $\mathcal{O}(1)$ couplings, but rather at lower scales with couplings to the SM that are much smaller than one. With the exciting theoretical and experimental prospects in neutrino and dark matter physics, we believe that it is all the more timely to think harder about what neutrinos, hidden particles of their own, may teach us about this type of hidden physics.

We start this thesis by reminding ourselves of the main features and limitations of the SM in this chapter, and delving into unique aspects of neutrino physics in the next. This way, we hope to set the scene and motivate the direction we pursue in the following chapters. Indeed, the processes of neutrino trident production and neutrino-electron scattering we discuss in Chapter 3 are a testimony of the unique properties of neutrinos and the bright prospects in experimental neutrino physics. As a concrete example, we will see in Chapter 4 how such signatures probe new gauge interactions much weaker than those in the SM ($g \lesssim 10^{-3}$). The fact that neutrinos are the only neutral fermions in the SM also has interesting consequences for mass generation and naturally connects them to neutral hidden sectors. We explore this connection with a specific model at hand in Chapter 5, scrutinizing its phenomenology at short-baselines in Chapter 6. Finally, in Chapter 7 we look towards the far future and highlight the impact of a near-future entry-level neutrino factory in neutrino physics.

1.1 The Standard Model

The Standard Model (SM) of particle physics is a Yang-Mills theory [1] of strong, weak and electromagnetic (EM) particle interactions based on an $SU(3) \times SU(2) \times U(1)$ local gauge symmetry. The first remarkable aspect of the theory is in the fact that it relies on the same idea that explains Maxwell's equations, the principle of gauge invariance. In this way, it is hard to pin down the official conception of the SM, although it is widely associated with the appearance of a model first developed by Sheldon L. Glashow [2], Steven Weinberg [3] and Abdus Salam [4]. Unconcerned with quarks and the strong force, this spontaneously broken $SU(2) \times U(1)$ local gauge symmetry already reflected most of what we know about the electroweak (EW) interactions of leptons nowadays. In fact, the spontaneous broken symmetry that was used already predicted the existence of a charged

massive vector boson, the W^\pm , a neutral massive vector boson, the Z , and of a massless generator of the unbroken $U(1)_{\text{EM}}$ group, the photon γ . Beyond unifying the weak and EM forces, the breaking through the Higgs mechanism [5, 6] implied that an additional scalar particle, the higgs boson H , had to exist. This last prediction was experimentally validated after the discovery of a neutral scalar boson at the LHC in 2012 [7, 8], the last SM particle to be experimentally observed.

The strong force had a much richer and more turbulent history. The quark model, developed by Murray Gell-Mann and George Zweig [9, 10] in 1964, had great success in explaining the growing number of hadronic resonances found by experiments. However, it was not until asymptotic freedom was discovered in non-Abelian gauge theories [11, 12] that quantum chromodynamics (QCD) was really born. QCD is an $SU(3)$ local gauge theory describing the interaction of quarks and gluons, and is vastly different from any other theory we will encounter in this thesis. Its uniqueness is best exemplified through color confinement, the property that colored particles must always be present in bound colorless states, called hadrons. For QCD, confinement is guaranteed below the scale $\Lambda_{\text{QCD}} \approx 250$ MeV, below which strong processes are non-perturbative. This is to be contrasted with asymptotic freedom, where the strong interactions between quarks and gluons become asymptotically weaker at higher energies. The presence of new degrees of freedom other than quarks and gluons at low energies, namely the hadrons, is a clear evidence of a phase transition and makes QCD a unique topic within the SM. At times we will refer to known results in this theory, but it usually has little bearings on electroweak physics.

1.1.1 Fields and symmetries

We now set out for a more precise definition of the SM field content, discussing some details of local gauge invariance. All fermion fields in the SM are Weyl fields of either definite left-handed (LH) or right-handed (RH) chirality. An equivalent statement is that SM fields are eigenvectors of γ_5 : $\gamma_5\psi_R = \psi_R$ for RH, and $\gamma_5\psi_L = -\psi_L$ for LH fields. This is an important feature that allows us to work with 2 component Weyl spinors and makes explicitly manifest the chiral nature of weak interactions. The LH field content and their representation under the different gauge groups is shown in Table 1.1. Note that only LH particles transform non-trivially under $SU(2)_L$. Also shown is the Higgs field H , a complex

	Q_L^α	L^α	\bar{u}_R^α	\bar{d}_R^α	\bar{e}_R^α	H	G	W	B
$SU(3)_c$	3	1	3̄	3̄	1	1	8	1	1
$SU(2)_L$	2	2	1	1	1	2	1	3	1
$U(1)_Y$	1/3	-1	-4/3	2/3	2	1	0	0	1

Tab. 1.1. The representation of the SM left-handed Weyl fields, complex scalar and gauge bosons under each gauge group of the SM. For $U(1)_Y$, the charge is shown instead. All fermions carry a flavour index $\alpha = e, \mu$ or τ .

scalar field, doublet under $SU(2)$. As we will see in the next section, H is responsible for the breaking of $SU(2)_L \times U(1)_Y \rightarrow U(1)_{\text{EM}}$. From the observed EM charges Q_{EM} , the $SU(2)_L$ isospin T_3 , and by virtue of the Gell-Mann-Nishijima formula [13, 14]

$$Q_{\text{EM}} = T_3 + \frac{Y}{2}, \quad (1.1.1)$$

the hypercharge Y of each SM field is fixed. The *local* gauge transformation of the matter fields are given by

$$\psi \rightarrow \exp\{ig\theta^a(x)T^a\}\psi, \quad (1.1.2)$$

where g is the gauge coupling constant, a counts the number of generators T^a , and $\theta^a(x)$ are arbitrary parameters that depend on space-time coordinates x^μ . To achieve local gauge invariance, we require the following gauge fields associated with each group:

$$SU(3)_C : \{G_1(x), \dots, G_8(x)\}, \quad SU(2)_L : \{W_1(x), W_2(x), W_3(x)\}, \quad U(1)_Y : B(x), \quad (1.1.3)$$

corresponding to the eight gluons, the $SU(2)$ gauge fields and the hypercharge field. Note that the number of gauge fields matches the number of generators in each group, *e.g.* for $SU(N)$ there are $N^2 - 1$ generators. For the original $SU(2) \times U(1)$ theory, this implied that in addition to the charged gauge fields, which explained Fermi's theory for beta decays, and the observed massless photon, there must have been an additional neutral gauge field corresponding to some linear combination of W^3 of $SU(2)_L$ and B of $U(1)_Y$. This striking prediction was in fact first confirmed by Gargamelle, a bubble chamber experiment, through the observation of accelerator neutrinos scattering into final states with no charged leptons [15].

The SM is a non-Abelian theory, since its symmetry group contains direct products of two $SU(N)$, $N > 1$, groups. The generators of a given group equipped with commutators form

a Lie Algebra, obeying $[T^a, T^b] = if^{abc}T_c$, with f^{abc} being the group structure constant. In the special case $f^{abc} = 0$, the generators commute and the group is said to be Abelian, like in the case of $U(1)_Y$. Otherwise, the group is non-Abelian and the theory displays a much richer underlying dynamics. Take an a -dimensional Yang-Mills theory and define $\theta = T^a\theta^a$ and $U = e^{ig\theta}$. We can now perform gauge transformations on the relevant matter fields ψ , gauge fields $\mathbf{A}_\mu = T_a A_\mu(x)^a$ and derivatives of matter fields as follows

$$\psi \rightarrow U\psi, \quad \mathbf{A}_\mu \rightarrow U\mathbf{A}_\mu U^{-1} - \frac{i}{g}(\partial_\mu U)U^{-1}, \quad \partial_\mu \psi \rightarrow U\partial_\mu \psi + \psi(\partial_\mu U). \quad (1.1.4)$$

As we can see, the last term is not invariant due to the local character of the gauge transformations. To preserve gauge invariance, a covariant derivative, transforming as $D_\mu \rightarrow UD_\mu U^{-1}$, now replaces the ordinary derivative. It is defined as

$$D_\mu = \partial_\mu + ig\mathbf{A}, \quad \text{such that} \quad D_\mu \psi \rightarrow UD_\mu \psi, \implies \bar{\psi}i\cancel{D}\psi \rightarrow \bar{\psi}i\cancel{D}\psi. \quad (1.1.5)$$

The invariant term above is the fermion kinetic term. Beyond fermion propagation, it is the main way to describe fermion-gauge interactions in the SM. In particular, the full covariant derivative in the SM is given by

$$D_\mu = \partial_\mu + ig W_\mu^a \tau_a + i\frac{Y}{2}g' B_\mu + i\frac{g_s}{2} G_\mu^b \lambda_b, \quad (1.1.6)$$

where $\tau_a = \sigma_a/2$ are the generators built from Pauli matrices acting on the doublets of $SU(2)_L$, and λ_b the generators built from the Gell-Mann matrices acting on the triplet representations of $SU(3)_c$. The factors of 1/2 come from the canonical This also fixes the different gauge couplings of the SM. Finally, the gauge invariant kinetic terms for the gauge bosons are

$$\mathcal{L}_{\text{Gauge}} = -\frac{1}{4}G_{\mu\nu}^a G_a^{\mu\nu} - \frac{1}{4}W_{\mu\nu}^a W_a^{\mu\nu} - \frac{1}{4}B_{\mu\nu} B^{\mu\nu}, \quad (1.1.7)$$

where $F_{\mu\nu}^a = \partial_\mu F_\nu^a - \partial_\nu F_\mu^a - g_F f^{abc} F_{b\mu} F_{c\nu}$ with g_F the relevant gauge coupling. The kinetic term in Abelian theories concern only the propagation of gauge bosons, however, for non-Abelian groups the term proportional to g_F in $F_{\mu\nu}^a$ introduces interactions among the gauge bosons proportional to g and g^2 . Therefore, a non-Abelian theory is already an interacting theory without the addition of any matter fields.

1.1.2 Spontaneous symmetry breaking

So far we have only discussed the gauge and fermionic content of the SM. The scalar sector is, in fact, quite special. The only scalar particle, the higgs boson, is responsible for spontaneously breaking $SU(2)_L \times U(1)_Y$ to $U(1)_{\text{EM}}$ after it acquires a non-zero vacuum expectation value (vev). This introduces a mass scale in the theory which, apart from dimensionless couplings, sets the scale of EW physics. Note that because it is a scalar particle, a non-zero vev does not violate the symmetries of space-time, namely Lorentz invariance. The higgs is a complex scalar field and a doublet under $SU(2)_L$, and so we can write

$$H = \frac{1}{\sqrt{2}} \begin{pmatrix} G_1^+ + iG_2^+ \\ h^0 + iG_3^0 \end{pmatrix} = \frac{e^{iG_a \tau^a}}{\sqrt{2}} \begin{pmatrix} 0 \\ h \end{pmatrix}. \quad (1.1.8)$$

The relevant Lagrangian in the SM reads

$$\mathcal{L}_{\text{higgs}} \supset (D^\mu H)^\dagger (D_\mu H) - V(H), \quad V(H) = \mu^2 H^\dagger H + \lambda (H^\dagger H)^2. \quad (1.1.9)$$

where μ^2 has mass dimension 2, being the only dimensionful parameter in the SM. If $\mu^2 < 0$, minimizing the potential $V(H)$ requires $\langle 0 | H | 0 \rangle = (0, v/\sqrt{2})^T$, where $v^2 = -\mu^2/\lambda$ is the vev chosen to lie in the real and neutral direction. We now can then expand around the true vacuum of the theory by redefining the fields $G_a \rightarrow G_a/v$ and $h \rightarrow h + v$. At this point, a rewriting of the potential reveals the mass and interactions of every component of the scalar doublet. Note, however, that it contains no mass terms for G_1 , G_2 and G_3 . These are the Goldstone bosons of the theory, and although they are massless, they do possess interactions with the scalar and gauge boson fields. One way to understand their role is to perform an $SU(2)_L \times U(1)_Y$ gauge transformation in our Lagrangian such that the resulting higgs doublet reads

$$H \rightarrow e^{-iG_a \tau^a/v} H = \frac{1}{\sqrt{2}} \begin{pmatrix} 0 \\ h + v \end{pmatrix}. \quad (1.1.10)$$

This transformation must also be applied to the gauge fields, fixing the gauge. This particular choice is rather convenient and is known as the unitary gauge. We then find

$$\begin{aligned} \mathcal{L}_{\text{higgs}} \supset & -\frac{1}{2} m_h^2 h^2 - \lambda v h^3 - \frac{\lambda}{4} h^4 \\ & + M_W^2 W_\mu^\dagger W^\mu \left[1 + \frac{2h}{v} + \frac{h^2}{v^2} \right] + \frac{M_Z^2}{2} Z_\mu Z^\mu \left[1 + \frac{2h}{v} + \frac{h^2}{v^2} \right], \end{aligned} \quad (1.1.11)$$

where $m_h = \sqrt{2\lambda}v = 125.18 \pm 0.16$ GeV [16]. Most importantly, after SSB, the higgs kinetic term has given us three massive and one massless vector bosons, defined as

$$W_\mu^\pm = \frac{1}{\sqrt{2}} (W_\mu^1 \mp i W_\mu^2), \quad Z_\mu = c_w W_\mu^3 - s_w B_\mu, \quad A_\mu = c_w B_\mu - s_w W_\mu^3. \quad (1.1.12)$$

where s_w (c_w) is the sine (cosine) of the weak angle, defined by $c_w = g/\sqrt{g^2 + g'^2}$. These fields correspond to the mediators of the weak charged-current interactions ($M_W = gv/2 = 80.387 \pm 0.016$ GeV [16]), weak neutral-current ($M_Z = M_W/c_w = 91.1876 \pm 0.0021$ GeV [17]) neutral boson and the massless photon A_μ , mediator of the unbroken EM interactions. They interact with the higgs boson via the triple and quadruple vertex terms above. The interactions with matter are obtained from the fermion kinetic terms, where the charged, neutral and electromagnetic currents are defined and written as

$$\begin{aligned} \mathcal{L}_{NC} &= e J_\mu^\gamma A^\mu + \frac{g}{c_w} J_\mu^Z Z^\mu, \quad J_\mu^\gamma = \bar{\psi} Q_{EM} \gamma_\mu \psi, \quad J_\mu^Z = \bar{\psi} \gamma_\mu \left[\left(\frac{T_3}{2} - Q_{EM} s_w^2 \right) - \frac{T_3}{2} \gamma^5 \right] \psi, \\ \mathcal{L}_{CC} &= \frac{g}{\sqrt{2}} (J_\mu^+ W^{\mu+} + J_\mu^- W^{\mu-}), \quad J_\mu^+ = \frac{1}{2} \bar{\psi}_u \gamma_\mu (1 - \gamma^5) \psi_d + \text{h.c.}, \end{aligned} \quad (1.1.13)$$

where $\psi \in \{\nu_L, e_L, u_L, d_L, e_R, u_R, d_R\}$, and $\psi_{u,d}$ denoting fermions with $T_3 = \pm 1/2$. From the weak currents we note two important aspects: *i*) weak interactions indeed violate parity and possess a $V - A$ structure, *ii*) charged-current interactions are purely LH as they should be since no RH fields are charged under $SU(2)_L$. After SSB, only the EM current is conserved $\partial^\mu J_\mu^\gamma = 0$.

In the discussion above, we fixed the gauge of the SM to simplify the EW Lagrangian. This is not necessary and, in fact, another possibility is to keep all terms involving the Goldstone fields G_a and eliminate off-diagonal kinetic terms of the type $Z_\mu \partial^\mu G_3$ by introducing the following gauge breaking Lagrangian to the SM

$$\mathcal{L}_{R_\xi} = -\frac{(\partial_\mu A^\mu)^2}{2\xi_\gamma} - \frac{(\partial_\mu Z^\mu + \xi_Z M_Z G_3^0)^2}{2\xi_Z} - \frac{|\partial_\mu W^{\mu-} + i\xi_W M_W G^-|^2}{2\xi_W}. \quad (1.1.14)$$

This is known as the R_ξ gauge, where the explicit dependence on the gauge breaking parameters ξ serves as a useful diagnostic of gauge invariance in physical observables. The Lorentz gauge is recovered for $\xi = 0$ and the Feynman-'t Hooft gauge with $\xi = 1$. The additional advantage of using this method is that it allows us to trace the Goldstone degrees of freedom. The pseudoscalar fields G^\pm and G_3 end up behaving very similarly to the W^\pm and Z gauge bosons. In fact, at high-energies it can be shown that the Goldstone

bosons are equivalent to the longitudinal polarization states of their respective gauge bosons [18, 19]. This is known as the Goldstone boson equivalence theorem, and it turns out to be very important to understand processes like $W_L W_L$ and $Z_L Z_L$ scattering. At very high-energies and without the Higgs boson, such processes grow indefinitely ($\sigma \propto s$), spoiling the unitarity of the S -matrix. The fact that this problem was solved by including contributions from h exchange provided a no-lose theorem for the LHC: either the higgs boson would be discovered, or new physics must appear to unitarize these processes.

1.1.3 Fermion masses

The EW sector is also responsible for the generation of fermion masses in the SM. As noted before, all LH fermions in the SM are $SU(2)_L$ doublets, just like the higgs. This allows us to construct the so-called Yukawa terms,

$$\mathcal{L}_{\text{Yukawa}} = y_e (\bar{L}_\alpha H) e_R + y_u (\bar{Q}_L \tilde{H}) u_R + y_d (\bar{Q}_L H) d_R + \text{h.c.}, \quad (1.1.15)$$

where we defined the charge-parity (CP) conjugated higgs field $\tilde{H} = i\sigma_2 H^* = (h + v + iG_3, G_1 - iG_2)^T$. After SSB, these interaction terms endow charged-leptons and quarks with a dirac mass term of the form

$$m_\psi \bar{\psi} \psi = m_\psi (\bar{\psi}_L \psi_R + \bar{\psi}_R \psi_L), \quad \text{with} \quad m_\psi = \frac{y_\psi v}{2}, \quad (1.1.16)$$

where $\psi_{L,R} = P_{L,R} \psi = (1 \mp \gamma_5) \psi / 2$ are the chiral projections of the fermion field ψ . To include all three families of fermions we promote $y_\psi \rightarrow \mathbf{y}_\psi$, a 3×3 matrix.

In the quark sector, the Yukawa matrix is off-diagonal and the different generations mix. The physical quark masses are found after rotating the up and down quarks, left and right, as $u_{L,R}^\alpha = (V_{L,R}^{u*})_{\alpha i} u_{L,R}^i$ and $d_{L,R}^\alpha = (V_{L,R}^{d*})_{\alpha i} d_{L,R}^i$. The diagonal mass matrix is then $\mathbf{m}^{u,d} = \mathbf{V}_L^{u,d} \mathbf{y}_{u,d} \mathbf{V}_R^{u,d\dagger} v / \sqrt{2}$. Note that after this procedure we cannot help but introduce mixing in the charged current. This defines the Cabibbo-Kobayashi-Maskawa (CKM) matrix [20, 21], $\mathbf{V}_{\text{CKM}} = \mathbf{V}_L^u \mathbf{V}_L^{d\dagger}$. The CKM matrix is nearly diagonal, so the mixing between quark flavour and mass eigenstates is small. From the unitarity of the rotation matrices, neutral currents remain invariant

$$\sum_{\alpha,\beta} \bar{\psi}_L^\alpha \Gamma^\mu \psi_L^\beta = \sum_{i,j} \bar{\psi}_L^i \left(\sum_{\alpha,\beta} (V_L)_{\alpha i} (V_L^*)_{\beta j} \right) \Gamma^\mu \psi_L^j = \sum_{i,j} \bar{\psi}_L^i \Gamma^\mu \psi_L^j, \quad (1.1.17)$$

where Γ^μ are the neutral-current couplings and gamma matrices. Crucially, the latter have no flavour dependence and so the SM forbids flavour changing neutral currents (FCNC). This mechanism was first proposed by Glashow, Illiopoulos and Maiani to explain why decays of the type $K^0 \rightarrow \mu\mu$ were unobserved. Famously referred to as the GIM mechanism, this relies on the flavour universal nature of SM neutral currents and on the unitarity of the CKM. As we will see, this mechanism also plays an important role in the neutrino sector and in many extensions of the SM.

Summarizing, we saw how a single parameter with massive dimensions in the scalar potential of the SM leads to SSB. This is then “propagated” to the rest of the SM through the higgs kinetic terms and Yukawa couplings. At this point it is possible to appreciate two problems with the SM mass generation mechanism. Firstly, it implies that all Yukawa couplings are just parameters to be inferred from the measured masses of particles. That is, the SM makes no statements and provides no explanations as to why the Yukawas that we observe in nature are what they are. This is known as the flavour puzzle: what explains the different observed values of the fermion masses? This problem is aggravated when we consider the lepton sector, where neutrino masses and mixing are drastically different from the quark sector. The second problem concerns the neutrino sector, and is perhaps the biggest motivation behing studying neutrino physics. The SM predicts exactly massless neutrinos in the absence of ν_R fields. Although

Before moving on to more speculative topics, a few comments are in order. EW SSB seems to be, as far as we know, a real phenomenon. It explains why the symmetries of the SM were so well hidden the first place: true symmetries of Nature seem to not be shared by the vacuum. While the evidence for EW SSB comes mainly from studying fundamental particles, its consequences do not concern only particle physics. EW physics helps us understand the past and future of our own Universe. In the early Universe, at hight temperatures, it is expected that the EW symmetry is restored [22–24]. If this is the case, the EW phase transition provides a unique test of the higgs mechanism and points to a completely different Universe from our own, where finite temperature effects and non-perturbative physics play a major role. In addition, we have no reason to expect the vacuum structure of the Universe to be as simple as in the discussion above. After all, the stability of our own vacuum is not even guaranteed within the SM [25, 26]. Radiative

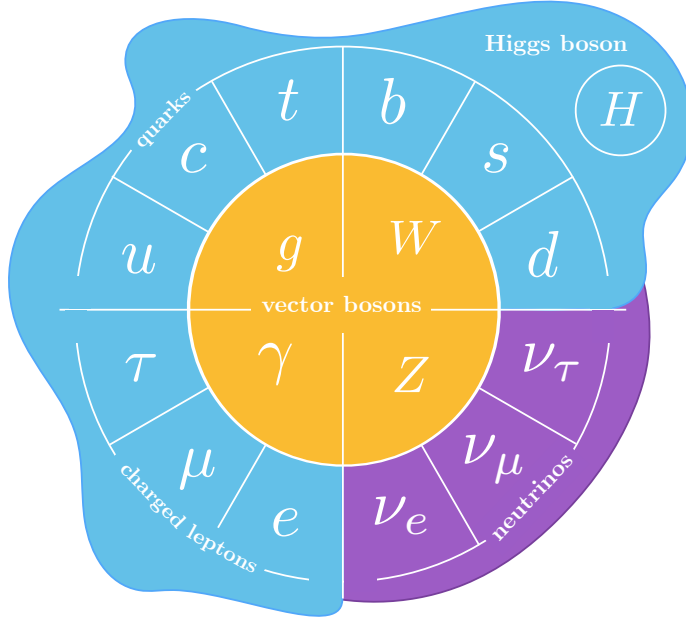


Fig. 1.1. Artistic rendering of the particles in the Standard Model.

corrections to the higgs self-coupling λ alter the shape of the scalar potential and imply we may live in a local, rather than global, minimum of the potential. For these reasons, studying the higgs sector, confirming that it generates all fermion masses in the SM and why it seemingly fails to do so in the case of the neutrino are all important questions worth pursuing.

1.2 Evidence for Beyond the Standard Model physics

The most important building aspects and building blocks of the SM have been laid out above. Now, a different question will concern us: is this theory sufficient to explain fundamental particles and their interactions? We have already stumbled upon a few problems of the SM, but even before that one must already suspect that the SM is not a final theory. It does not explain gravity. This tells us that the SM should be treated as an effective theory valid up until the Planck mass $M_{\text{Pl}} = (\hbar c / 2G_{\text{Newton}})^{1/2} \approx 10^{19}$ GeV, where the effects of gravity are expected to be large¹. This very own fact already brings us to one of the most controversial evidences for beyond the Standard Model (BSM) physics.

¹This is a naive expectation based on the observation that the Schwarzschild radius $\ell_s = 2G_{\text{Newton}}m/c^2$ and the Compton wavelength $\ell_c = h/mc$ of a particle become comparable at $m \approx M_{\text{Pl}}$.

The hierarchy problem The lack of evidence for new physics at the LHC can be argued to be more than just unfortunate. If no new physics is indeed present between the EW and the Planck scale, then the cut-off of the SM, beyond which the effective field theory is no longer valid, is $\Lambda = M_{\text{Pl}}$. This implies that unless symmetries are at play, terms of dimensions d are suppressed or are of the order of Λ^{4-d} . However, in the SM $m_h^2 \ll \Lambda$, suggesting a fine-tuning of many orders of magnitude. Quantum corrections to the higgs mass, $m_h^2 = m_{\text{bare}}^2 + \delta m_h^2$, are dominated by the top quark and go as $\delta m_h^2 = y_t^2 \Lambda^2 / 8\pi^2$. This quadratically divergent result implies that to obtain the observed light higgs mass, whatever new physics that may appear at the scale Λ (possibly even below M_{Pl}) must cancel the fermion loops to order m_h^2/Λ^2 . In other words, the matching condition for the renormalization of m_h^2 parameter becomes fine-tuned to order m_h^2/Λ^2 in the presence of such cut-off. Supersymmetric theories are notorious candidates that solve this problem, but so far we are yet to find any evidence for them. One may argue that indeed there exists a “desert” between the EW and the Planck scale, and that some miraculous mechanism is at play in quantum gravity that may solve the fine-tuning problem. In that case, a solution to all following items in this list must be found there, or somewhere outside the realm of particle physics.

The strong-CP problem The QCD Lagrangian admits the following field-strength contraction term

$$\mathcal{L} \supset \frac{\theta \alpha_s^2}{8\pi} G_{\mu\nu}^a \tilde{G}_a^{\mu\nu}, \quad \text{where} \quad \tilde{G}_{\mu\nu}^a = \frac{\epsilon_{\mu\nu\rho\sigma}}{2} G^{a\rho\sigma}. \quad (1.2.1)$$

This can be shown to be a surface term (a total divergence in the action) and can be neglected in perturbative calculations. Nevertheless, this term induces CP violation in the strong sector via non-perturbative effects, leading to a large electric dipole moment for free neutrons [27], which is orders of magnitude above the experimental upper limits [28]. The most popular scenario to explain the smallness of θ is the Peccei-Quinn symmetry [29], a global chiral $U(1)$. The breaking of this symmetry leads to the prediction of a Goldstone boson, the axion.

Matter-antimatter asymmetry The observed baryon asymmetry of the Universe contradicts the standard Cosmology, which predicts that matter and anti-matter were created

in equal amounts in the Big Bang. The SM does not provide enough source of CP violation to explain this phenomenon. Popular scenarios to explain this are EW baryogenesis and Leptogenesis, where the latter relies on the CP violation from a heavy neutrino sector and its translation into a baryon asymmetry through Spharelon processes.

Dark matter Measurements of the redshift of galaxy clusters in the 1930's [30] and galaxy rotation curves in the 70's [31], are among the pioneering work that showed that the gravitational potential in such astrophysical scales is much deeper than the one extrapolated from luminous matter. Already at the time, astronomers would refer to the source of this additional gravitational influence as Dark Matter (DM). As Astrophysics and Cosmology evolved, concrete evidence for DM continued to build up. Evidence for DM is now present at a variety of scales, from the precise measurements of the cosmic microwave background (CMB) [32], the matter distribution in galaxy cluster mergers [33], and the observed large scale structure of the Universe [34]. In fact, from CMB power spectrum we can infer the DM density today as [32]

$$\Omega_{\text{DM}} h^2 = 0.1200 \pm 0.0012 \quad (1.2.2)$$

with $\Omega_{\text{DM}} = \rho_{\text{DM}}/\rho_c$ the energy density of DM in units of the critical density $\rho_c \approx 10^{-26} \text{ kg/m}^3$, and $h = H_0/(100 \text{ km s}^{-1}/\text{Mpc}^{-1}) = 0.674 \pm 0.005$ the scaled Hubble expansion rate. This is roughly five times larger than the density of baryons, understood as all other non-relativistic matter. The latter is also measured through the relative abundances of light elements during Big Bang Nucleosynthesis (BBN) [35], where DM plays no role and providing further evidence for non-baryonic DM.

The nature of DM is not yet understood and many possibilities are under discussion. Modified gravity models explain local astrophysical observations, but struggle to explain all CMB datasets and X-ray observations of mergers of galaxy clusters [36]. Primordial black holes [37] have also been put forward as DM candidates and have triggered great interest due to their connection to the detection of gravitational waves. However, the most popular hypothesis at this point remains that DM is made of new particles. This new state better be neutral, to have evaded our detection, and sufficiently long-lived, so that it may linger until today after its production in the early Universe. The fluid of such particles would have to display negligible pressure and viscosity, and to have been created cold so as to help form clumpy structures in the Universe with its gravitational influence. This points

us to a particle that is massive, collisionless and, yet, very abundant today. Most notably, DM models have often focused on the possibility of a weakly-interacting massive particle (WIMP). In this paradigm, DM particles, say χ , are produced in the early Universe through its weak interactions with the SM plasma. At later times, approximately at temperatures of the order of the DM mass m_χ , DM production stops and annihilation into SM particles dominates. As the Universe cools and expands, the DM gas is diluted and annihilation is no longer effective, *freezing-out* the DM population at around $T \approx m_\chi/20$. In particular, the relic density obtained in this mechanism is of the order $\Omega_\chi H_0^2 \approx 0.1 \text{ pb}/\sigma$, where σ stands for the thermally averaged cross section of χ annihilation into SM particles. The fact that $\sigma \approx 1 \text{ pb}$ allows to reproduce the current DM density and is of the order of typical weak cross sections (as in mediated by weak bosons) is known as the WIMP-miracle. WIMP DM is a collisionless and thermal candidate, although DM candidates that are non-thermal, or collisionless, or both exist.

Neutrino masses One of the most important evidences for BSM physics is the fact that neutrinos have mass. This comes from the plethora of experimental evidence for neutrino oscillations, which we explore in the next chapter. Put simply, neutrino oscillation data requires at least 2 non-zero and non-degenerate massive neutrinos. Although one might argue that this is solved by the mere addition of at least 2 RH neutrino states to the SM which are complete singlets of the symmetry, this simple extension still requires further study and experimental confirmation. In addition, such states would be the only SM particle to admit a Majorana mass term of the type $M \bar{\nu}^c R \nu_R$, and unless new symmetries are introduced, there is no reason to expect that M is exactly zero. Therefore, it is customary to think that neutrino masses are the first indications of physics beyond the SM observed in controlled laboratory conditions.

1.3 Extending the Standard Model

In extending the SM one may take several approaches. We can be guided by experimental results and tensions, by increased symmetries and elegance in our theories, or by complete agnosticism. While we lack a single compelling evidence for the direct detection of a new particle, we can interpret many of the problems outlined above as evidence for new states.

The existence of DM and neutrino masses, in particular, suggests (but does not require) that these new states may be a new sector of electromagnetically neutral particles. Here, the SM provides no guidance for their masses or symmetries, and so a mixture of all three approaches outlined before is common in the literature. This thesis is no exception.

Dark sectors are a typical prediction of theories with

Our BSM extensions all involve light and hidden new states, which have evaded detection to the smallness of their couplings to the SM. This point of view is compelling from a DM and neutrino perspective.

only neutral particle in the SM , in the spotlight

In this sense, our job is to search “under the lightpost”, using current and future experiments to look for new physics in a opportunistic way. Not only is this a cheap and viable exercise, it would offers an explanation as to why the SM performs so well as a theory and against most experimental tests. A modular view of the Universe, with the visible SM sector and potential dark sectors barely influencing each other wou

Given the hints that dark sectors beyond the SM may exist, we would like to investigate all the possible ways the particles in this sector may interact with the SM. One way to tackle this question is to build effective field theories, where one studies all operators which are allowed by the content and symmetries of the SM. The idea is to construct a series of $d > 4$ operators in $1/\Lambda^{d-4}$, where Λ is the scale of the new physics. This approach thrives on its generality, but can become complicated very quickly with growing d . Most importantly, the scale Λ is assumed to be large, so that all new degrees of freedom have been integrated out of the theory. This is suitable for extensions involving particles which are very heavy, but the series is no longer well defined for new physics that is light and kinematically accessible at our experiments. In this case, the kinematics of the new particles play a role, forcing us to write down the field content and symmetry group of the new physics. This is the approach we will follow in this thesis.

1.3.1 Portals to hidden sectors

We would like our SM extensions to follow specific guiding principles and organize them in a meaningful way. One way to do so is to study all the low dimension neutral operators

that the SM has to offer. In contrast to effective field theories, we want renormalizable operators with $d < 4$ which are also gauge invariant. As it turns out, only a few such operators exist, which we usually refer to as *portals*. We dedicate this section to presenting these.

Neutrino portal Arguably the most motivated portal, this $d = 5/2$ operator can be written as

$$\left(\bar{L}_a^\alpha \cdot \tilde{H} \right), \quad (1.3.1)$$

where we made the spinor index a explicit. Any fermion field which couples to this operator acquires couplings to SM neutrinos. This typically induces off-diagonal mass terms in the Lagrangian, leading to mixing between the new species and all massive neutrinos in the broken phase of the SM. The new particle is then commonly referred to as *heavy neutral lepton* or right-handed neutrino, though its chirality is a matter of convention.

Vector portal Any new vector particle X^μ may couple to the $d = 2$ field strength of the SM hypercharge

$$B_{\mu\nu}, \quad (1.3.2)$$

through its own field strength tensor $X^{\mu\nu}$. The resulting term, $B_{\mu\nu}X^{\mu\nu}$, is an off-diagonal kinetic term for the massive bosons. To work in a basis of physical states with diagonal mass terms, where the propagators are in their standard form, one usually performs a field redefinition. For this reason, this term is usually referred to as kinetic mixing. If much lighter than the EW scale, the new vector particle is usually called a dark photon, otherwise it may also go by the name of a dark Z . Models with the term

$$Z_\mu X^\mu \quad (1.3.3)$$

also come up in the literature, known as mass-mixing between the new vector particle and the SM Z . This term is not gauge invariant, but may arise in the broken phase of BSM theories with additional doublet scalars, like in two-higgs-doublet models (2HDM). However, several charged degrees of freedom typically appear and experimental constraints are more severe.

Higgs portal New scalar particles can mix with the SM higgs boson via

$$H^\dagger H. \quad (1.3.4)$$

In this case there are more possibilities depending on the nature of the new scalar field. Analogously to the SM, one could write $H^\dagger H S^\dagger S$ for a charged, or $H^\dagger H S$ for a singlet complex scalar. The latter term is the only super-renormalizable operator connecting the SM fields to new physics which is allowed. The phenomenology can be quite different depending on the charges of the new scalar, but in general The second operator has been discussed in detail in Ref. [38] and arises naturally in relaxion models ...).

A very simple BSM model with such portal arises in scalar singlet S extensions, where one generates the term $H^\dagger H S^\dagger S$ [39]. Remarkably, this extension can also have consequences to the "little hierarchy" problem, as the new scalar also contributes to the Higgs self-energy [40].

Fermionic currents A whole set of neutral operators in the SM come from the fermionic currents

$$J^\mu \equiv \bar{\Psi} \gamma^\mu \Psi, \quad (1.3.5)$$

where $\Psi \in \{Q_L, L, u_R, d_R, \ell_R\}$. This provides SM currents which can be associated with new conserved charges. The first condition is that it be locally conserved $\partial_\mu J^\mu = 0$.

Pseudo-scalar Axions [41].

Chapter 2

Neutrinos beyond the Standard Model

“”

— Madeline Line

2.1 The three neutrino paradigm

Neutrinos provide the most compelling evidence for physics beyond the SM. In this chapter we explore why and discuss some of the most important properties of neutrinos for their experimental study.

Neutrinos are purely weakly interacting fields

Neutrinos – Pauli + Madame Wu + Freinberg numus + Lederman

2.2 Oscillations

Neutrino oscillations can arise when a superposition of neutrino mass eigenstates is produced, propagates macroscopic distances and scatters inside a detector. Given sufficiently long baselines, neutrino flavour transitions may always occur due to mixing, but for a sinusoidal dependence on baseline coherence must be preserved throughout the process. We will now derive the standard formula for the oscillation probability in vacuum, $P(\nu_\alpha \rightarrow \nu_\beta)$ (matter effects are discussed in Section 2.2.1). This exercise can be done in multiple ways

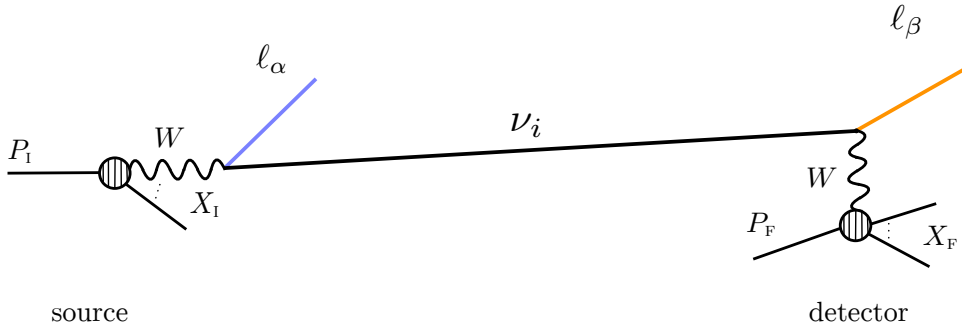


Fig. 2.1. The usual set-up of an oscillation experiment. We show the source, where a process $P_i \rightarrow \nu_\alpha X_i$ happens (note that $P_i = \ell_\alpha$ is allowed and that P_i may be a scattering process), and the detector, where $\nu_\beta P_i \rightarrow \ell_\beta X_f$.

and most often derivations will rely on the neutrino states to be plane-wave solutions. This approach leads to correct expressions for $P(\nu_\alpha \rightarrow \nu_\beta)$ in virtually all cases of interest, but it is a rather poor conceptual description of oscillations and a very limited framework. Instead we will derive the oscillation formula starting from a quantum mechanical wave-packet approach, and encounter a few conditions for oscillations to happen. More sophisticated treatments in Quantum Field Theory (QFT) have been known for some time [42–44], and their results have been shown to be directly mapped onto the wave-packet approach [45]. Nonetheless, neutrino oscillations are notorious for being conceptually confusing and the correct method to compute such processes is still debated in the literature [46]. One may seek consolation in the fact that a few aspects are common to all approaches, for instance the ultra-relativistic nature of the mass states through expansions of $\sqrt{m^2 + p^2}$ and the need for momentum uncertainties in the initial and final neutrino processes.

Our setup is the same as most neutrino oscillations experiments and is represented in Fig. 2.1. We will first discuss the production and detection processes, and then study the oscillations per se. Initially, a neutrino flavour state ν_β is produced by a CC reaction at the source, $P_i \rightarrow \nu_\beta X_i$. More precisely, a state $|f\rangle$ is produced,

$$|f\rangle = \hat{S} |P_i\rangle, \quad \hat{S} \approx \hat{1} - i \int d^4x H_{\text{int}}^{\text{CC}}(x), \quad (2.2.1)$$

where \hat{S} is the S-matrix operator approximated to first order in weak coupling and

$$H_{\text{int}}^{\text{CC}}(x) = \sqrt{2}G_F \sum_\alpha \bar{\nu}_\alpha(x) \gamma^\mu P_L \ell_\alpha(x) J_\mu(x) + \text{h.c.}, \quad (2.2.2)$$

is the interaction Hamiltonian between the neutrino current and the current $J_\mu(x)$ that

describes the transition $P_I \rightarrow X_I$. After ℓ_α and the final particles interact with the medium, $\langle f |$ is reduced to $\langle \ell_\alpha, X_I | f \rangle$, which ought to ensure that only neutrino flavour states ν_α are produced, according to our flavour basis definition. Unfortunately, flavour states are not well-defined and do not span a Fock space. We want to work instead with the eigenstates of the free Hamiltonian, which are the ones we can easily evolve in time. With this in mind, we define the following amplitude

$$A_{\alpha k}(\vec{p}, h)^P \equiv \langle \nu_k(\vec{p}, h), \ell_\beta, X_I | \hat{S} | P_I \rangle, \quad \text{with} \quad A_{\alpha k}(\vec{p}, h) = U_{\alpha k}^* M_{\alpha k}(\vec{p}, h), \quad (2.2.3)$$

where we factored out a mixing angle in the definition of $M_{\alpha k}$ and made the helicity index h explicit. By virtue of the completeness relation with massive neutrino eigenstates, we can insert the identity in $\langle \ell_\alpha, X_I | f \rangle$ and define a *normalized* neutrino flavour state as

$$|\nu_\alpha\rangle^P = N_P \sum_{k,h} \int d^3 p A_{\alpha k}^P(\vec{p}, h) |\nu_k(\vec{p}, h)\rangle, \quad N_P^{-2} = \sum_{k,h} \int d^3 p |A_{\alpha k}^P(\vec{p}, h)|^2. \quad (2.2.4)$$

An analogous discussion holds for the detection process $\nu_\beta P_F \rightarrow \ell_\beta X_F$, where a detection flavour state $|\nu_\alpha\rangle^D$ with an amplitude for detection $A_{\alpha k}(\vec{p}, h)^D$ can be defined. Before we move on to a discussion about oscillations, we want to emphasize two points. First, the normalization of the flavour state is a clear sign that we are working in a quantum mechanical description. To compute probabilities, we rely on normalized states. In a QFT description, however, the normalization is not necessary, but so is the concept of $P_I \rightarrow X_I$ in the first place. There, the full process in Fig. 2.1 can be computed directly through the use of long-distance propagators, and if the production, propagation and detection parts of the amplitude squared factorize, an object equivalent to the oscillation probability can be extracted. This factorization is implicitly assumed in our calculation. Secondly, the decay rate of the P_I particle can be computed as

$$|A^P|^2 = \left| \langle \nu_\alpha(\vec{p}, h), \ell_\beta, X_I | \hat{S} | P_I \rangle \right|^2 = \sum_{k,h} |U_{\alpha k}|^2 \int d^3 p |M_{\alpha k}^P(\vec{p}, h)|^2, \quad (2.2.5)$$

and it becomes evident that the decay rate is given by the *incoherent* sum of the decay rate into different massive neutrinos. No interference is present as the states $|\nu_k\rangle$ are assumed to be orthonormal to each other. This remains true in the QFT description [44].

Now, one is left to compute the functions $M_{\alpha k}$. This is a rather involved process, but one can show that the form of these functions resemble simple wavepackets [45]. In doing so,

many approximations are necessary, in particular, that of ultra-relativistic neutrinos. More precisely, the most relevant assumptions are *i*) flipped-helicity terms ($h = +$ for neutrinos), suppressed by m_k^2/E_k^2 , are ignored, *ii*) all neutrinos travel in the same direction, $\vec{p} \rightarrow p$, and *iii*) the production and detection processes are not sensitive to the neutrino mass differences, amounting to replacing $M_{\alpha k} \approx M_\alpha$. Under these assumptions, we are justified to take normalized gaussian wavepackets for production and detection flavour states as an *ansatz*,

$$|\nu_\alpha\rangle^i = \sum_k U_{\alpha k}^* \int dp \psi_k^i(p) |\nu_k(p)\rangle, \quad \psi_k^i(p) = (2\pi \sigma_p^{i2})^{-1/4} \exp\left[-\frac{(p-p_k)^2}{4\sigma_p^{i2}}\right], \quad (2.2.6)$$

with σ_p^i being the spread around the central momenta p_k and $i = P, D$.

Now that the flavour states are written in terms of the eigenstates of the free Hamiltonian, we know how to evolve them and how to write the flavour transition amplitude after a time t and distance L

$$\begin{aligned} A(\nu_\alpha \rightarrow \nu_\beta) &= \langle \nu_\beta^D | e^{-i\hat{E}t+i\hat{P}L} | \nu_\alpha^P \rangle \\ &= N \sum_k U_{\alpha k}^* U_{\beta k} \int dp \exp\left[-iE_k(p)t + ipL - (p-p_k)^2/4\sigma_p^2\right], \end{aligned} \quad (2.2.7)$$

where $E_k(p) = \sqrt{p^2 + m_k^2}$ and N is a normalization factor coming from the normalization of the wavepackets and a single integral over p . We have also defined the global energy uncertainty on momentum $\sigma_p^{-2} = (\sigma_p^P)^{-2} + (\sigma_p^D)^{-2}$. This may also be related to the global uncertainty on production and detection positions through $\sigma_x \sigma_p \approx 1/2$. Finally, to integrate over the remaining p integral, we can taylor expand around the central wavepacket momentum

$$E_k(p) \approx E_k + v_k(p-p_k), \quad \text{with} \quad v_k = \frac{\partial E_k(p)}{\partial p} \Big|_{p=p_k} = \frac{p_k}{E_k}, \quad E_k = \sqrt{p_k^2 + m_k^2}. \quad (2.2.8)$$

Performing the final integral over p , integrating over t (an unmeasured quantity) and squaring the amplitude, one obtains a formula for the oscillation probability

$$P(\nu_\alpha \rightarrow \nu_\beta) = \sum_{k,j} U_{\alpha k}^* U_{\alpha j} U_{\beta k} U_{\beta j}^* e^{-2\pi i L/L_{kj}^{\text{osc}}} P_{kj}^{\text{coh}} P_{kj}^{\text{loc}}, \quad (2.2.9)$$

where we defined

$$P_{kj}^{\text{loc}} = \exp\left(-2\pi^2 \xi^2 \left(\frac{\sigma_x}{L_{kj}^{\text{osc}}}\right)^2\right), \quad P_{kj}^{\text{coh}} = \exp\left(\frac{L |\Delta m_{kj}^2|^2}{16 E^2 \sigma_x}\right), \quad (2.2.10)$$

and the important scales of the problem can be identified as

$$L_{kj}^{\text{osc}} = \frac{4\pi E}{\Delta m_{kj}^2}, \quad p_k \approx E - (1 - \xi) \frac{m_k^2}{2E}, \quad E_k \approx E + \xi \frac{m_k^2}{2E}, \quad (2.2.11)$$

with ξ measuring the deviation from ultra-relativistic behaviour.

For most application, $P_{kj}^{\text{coh}} = P_{kj}^{\text{loc}} = 1$, and one recovers the standard oscillation formulae.

A more useful way of writing it is

$$\begin{aligned} P(\nu_\alpha \rightarrow \nu_\beta) = & \delta_{\alpha\beta} - 2 \sum_{k>j} \text{Re} \left\{ U_{\alpha k}^* U_{\alpha j} U_{\beta k} U_{\beta j}^* \right\} \left[1 - \cos \left(\frac{\Delta m_{kj}^2 L}{2E} \right) \right] \\ & - 2 \sum_{k>j} \text{Im} \left\{ U_{\alpha k}^* U_{\alpha j} U_{\beta k} U_{\beta j}^* \right\} \sin \left(\frac{\Delta m_{kj}^2 L}{2E} \right) \end{aligned} \quad (2.2.12)$$

2.2.1 Matter effects

Neutrinos are neutral particles and their rare interactions allow them to propagate through matter without losing energy in collisions with the medium particles. Nevertheless, in a similar fashion to photons, neutrinos undergo coherent forward scattering, acquiring an effective refractive index in the presence of a medium. In contrast to photons, which undergo Compton scattering, neutrinos are only charged under the weak force and can only undergo CC or NC interactions. The weakness of these interactions at low energies implies that matter effects arise only when neutrinos have transversed sufficiently large distances or are in a sufficiently dense environment. In principle, for large matter effects all that is necessary is a net weak charge for the medium, provided by the neutrons in the case of the Earth. However, for such effects to be observable in neutrino oscillation experiments, an additional condition exists: different flavour states must exhibit different interaction potential with the medium. In the SM, this is possible due to the CC interactions that are exclusively between electron-neutrino states and electrons in the medium.

The time evolution of the flavour states is again given by the Schröedinger equation in the presence of an interaction potential

$$i \frac{d}{dx} |\nu_\alpha\rangle = \left[U \frac{\hat{m}^2}{2E} U^\dagger + \hat{V}(x) \right] |\nu_\alpha\rangle, \quad (2.2.13)$$

where we have already used the ultra-relativistic approximations from before, applying $H_0 |\nu_\alpha\rangle \approx U [p\hat{1} + \hat{m}^2/2p] U^\dagger |\nu_\alpha\rangle$ and $t \approx x$. Solving this equation is a much more complicated task than in the vacuum case. Full analytical solutions are only known in

specific cases, such as when the column density of matter particles is constant [1]. In general, this may be solved numerically for a given choice of \hat{V} , although several perturbative expansions exist [2].

Various calculations of the neutrino matter potential exist, but often these rely on averages over the particle background and are difficult to generalize to non-standard cases. Here, we sketch the approach of Refs. [47, 48], where the neutrino potential arises from finite temperature and finite density corrections to the neutrino dispersion relation. In particular, the dispersion relations arises from

$$\det\{\not{k} - \Sigma\} = 0, \quad (2.2.14)$$

guaranteeing non-trivial solutions to the Dirac equation $(\not{k} - \Sigma)\nu_L = 0$, with k^μ the neutrino four-momentum and Σ its self-energy. For LH neutrino states ν_L , we can write the neutrino self-energy in the most general form and make explicit the background dependent contribution as [49]

$$\Sigma = m - (a_L \not{k} + b_L \not{u} + c_L [\not{k}, \not{u}]) P_L. \quad (2.2.15)$$

where u is the 4-velocity of the medium, a_L , b_L and c_L are scalar functions of Lorentz invariants $w = k \cdot u$ and $\kappa = (w^2 - k^2)^{1/2}$, and m is the vacuum neutrino mass. The presence of the medium introduces a preferential frame, namely the rest frame of the medium with $u = (1, 0, 0, 0)$. Also note that in vacuum, only terms proportional to \not{k} exist, and the pole of the neutrino propagator is unchanged. To lowest order, g^2/m_W^2 , only b_L contributes and it is proportional to the medium particle-antiparticle asymmetry, both statements not holding for higher order terms of the form g^2/m_W^4 [50]. The neutrino self-energy is in fact a gauge-dependent quantity, so the physical observables of interest are the dispersion relations, $(1 - a_L)(w - \kappa) - b_L = 0$ for neutrinos and $(1 - a_L)(w + \kappa) - b_L = 0$ for antineutrinos. To lowest order, however, the dispersion relations are much simpler,

$$w \approx \kappa + \frac{m^2}{2\kappa} + V_{\text{eff}}, \quad V_{\text{eff}} = -b_L, \quad (2.2.16)$$

where we defined the effective potential, which for ultra-relativistic neutrinos arises precisely from the difference between the total and kinetic energy $V_{\text{eff}} = w - \kappa$. This also shows us how to calculate the neutrino refractive index $n = |\vec{k}|/k^0$.

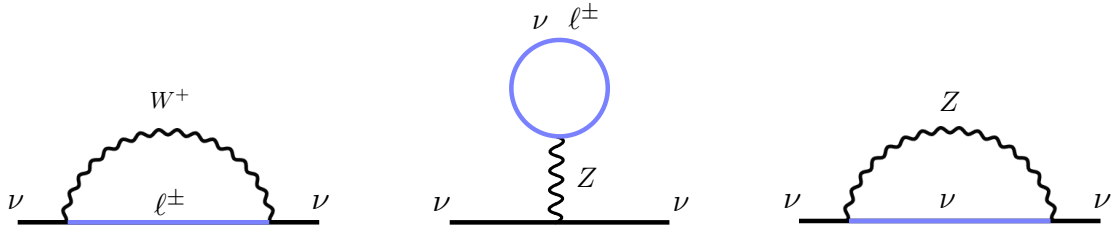


Fig. 2.2. Finite temperature and density corrections to the neutrino self-energy. These can be used to infer the effective matter potential for neutrinos.

Now the problem reduces to computing Σ in finite temperature field theory. For most applications of thermal mass calculations, replacing vacuum propagators by the thermal propagators from the real-time formalism is sufficient. In particular, the fermion thermal propagator of interest is

$$S(P) = (\not{P} + m) \left[\frac{1}{P^2 - m^2 + i\epsilon} + i2\pi\delta(P^2 - m^2)f(P) \right], \quad (2.2.17)$$

with $f(P) = \{\exp[(|P \cdot u| - \text{sgn}(P \cdot u)\mu_f)/T] + 1\}^{-1}$ is the occupational number of the fermions in the thermal bath of temperature T and chemical potential μ_f . Similar expressions exist for bosonic propagators. Finally, as an example, explicit computation of the self-energy in Fig. 2.2 yields

$$\Sigma = -i \frac{g^2}{16c_W^2} \int \frac{d^4 P}{(2\pi)^4} \gamma^\mu P_L iS(P+K) \gamma^\nu P_L iD_{\mu\nu}(P), \quad D_{\mu\nu} = \frac{-g_{\mu\nu} + \frac{P_\mu P_\nu}{M_Z^2}}{P^2 - M_Z^2 + i\epsilon}. \quad (2.2.18)$$

Putting it all together, the potential for neutrinos of flavour α on a background of protons, neutrons and electrons is

$$\begin{aligned} V_\alpha^e &= -\frac{G_F}{\sqrt{2}} \left(2\delta_{\alpha e} 1 - 4s_W^2 \right) (N_e - N_{\bar{e}}), \\ V_\alpha^p &= \frac{G_F}{\sqrt{2}} \left(1 - 4s_W^2 \right) (N_p - N_{\bar{p}}), \\ V_\alpha^n &= -\frac{G_F}{\sqrt{2}} (N_n - N_{\bar{n}}). \end{aligned} \quad (2.2.19)$$

For antineutrino an overall minus sign is introduced. Note the ν_e potential is the only one where CC interactions contribute, and so it is the sole responsible for non-trivial flavour evolution in Eq. (2.2.13). One may wonder about radiative corrections to these potentials in the SM and whether additional flavour non-universality can be achieved through the difference in charged-lepton masses. These effects, however, are known to be extremely

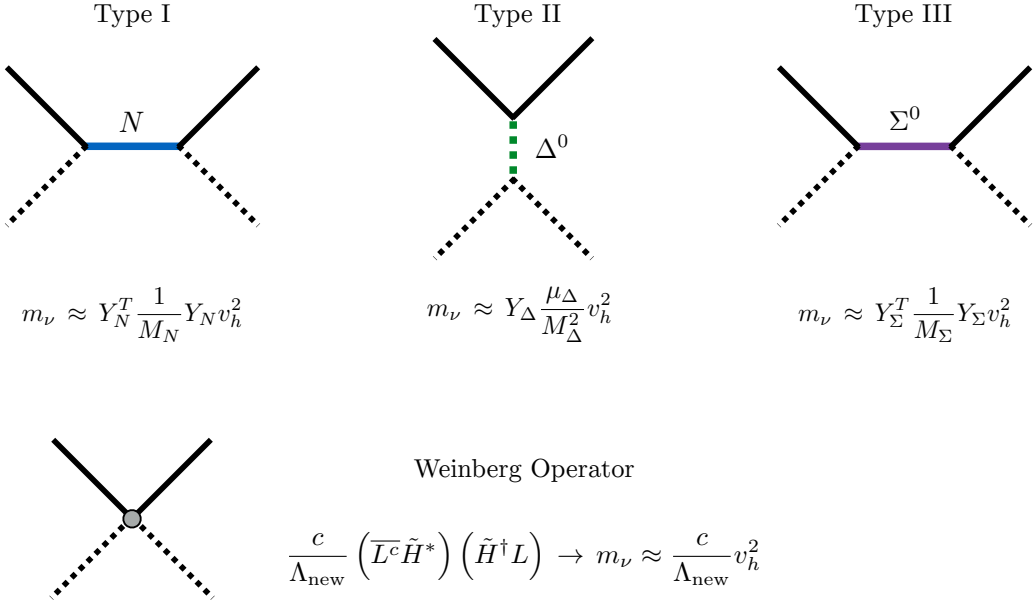


Fig. 2.3. The only three UV completions of the $d = 5$ Weinberg operator with their respective contributions to light neutrino masses.

small in the SM [51], where $(V_\tau - V_\mu)/V_e \approx 5 \times 10^{-5}$ for a neutral unpolarized medium like the Earth.

2.3 The model space of neutrino physics

A more ambitious task than measuring the low-energy properties of neutrinos is to understand the theoretical origins of neutrino mass and mixing. Here, the possibilities are manifold. The high-scale dynamics, typical of many neutrino mass models, is incredibly hard to test, so it is fair to say we have more neutrino mass models than ways to test them. Nevertheless, many of these models possess similar features. They may rely on the seesaw mechanism, on radiative neutrino mass generation or in extended scalar sectors. On top of that, new symmetries and fundamental forces may also be at play. We will explore a small fraction of this model space.

2.3.1 Mass mechanisms

In Fig. 2.3, we show these unique tree-level completions of the Weinberg operator.

For a review on low-scale models see [52].

2.3.2 Conventional seesaws

2.3.3 Low scale seesaw variants

2.3.4 Radiative masses

The most straightforward extension of the SM which can generate neutrino masses at loop level is perhaps the so-called Zee-Babu model.

2.3.5 Sources

To find a source of neutrinos, all we have to do is to look for environments where the Weak force is prominently manifested. A natural candidate, as we have seen in the discovery of the neutrino, are nuclear reactors. Fortunately, the list does not stop there. Abundant neutrino sources include the Sun, the atmosphere, the Big-Bang, particle accelerators and astrophysical environments processes such as supernovae, active galactic nuclei and others.

2.4 Scattering

Neutrino cross sections are an invaluable observable to understand the weak force and to search be able to study oscillation physics. Due to the purely weakly interacting nature of neutrinos, they also serve as a strong test of *stronger than weak* interactions with matter, that is, new interactions with $G_X > G_F$. In fact, if sufficiently clean, neutrino scattering processes provide the strongest limits on light new mediators of masses from a few MeV to a few GeV []. In this section, we present the standard scattering channels used in oscillation experiments, as well as other curious processes that are relatively poorly studied.

Accelerator experiments typically produce neutrinos of a few GeV energies to achieve $\mathcal{O}(1)$ oscillation phases $\Delta m_{\text{atm}}^2 L/E$ within thousands of km. Drastically different energy regimes are impractical either due to diluted fluxes at longer baselines ($\Phi \propto 1/L^2$), or due to thresholds to produce muons in CC interactions ($E_\nu > m_\ell + m_\ell^2/2m_H$ in reactions of the type $\nu_\ell H \rightarrow \ell^\pm H'$). Also important is the fact that such experiments rely on the neutrino flux produced in proton-on-target collisions, where charged mesons are subject to magnetic fields for focusing (see Section 2.3.5). This produces neutrinos with a wide spectrum, typically referred to as wide-band-beam spectrum, and are hard to model due

to hadroproduction and focusing uncertainties []. In this way, the expected neutrino event rate in neutrino detectors inherits two sources of uncertainties which are difficult to disentangle: the un-oscillated flux spectra and the neutrino-nucleus cross sections. The latter observable is subject to large nuclear effects, which require either precision data or accurate descriptions of the nuclear environment.

Take the MiniBooNE experiment, for instance, where the average neutrino energy is $\langle E_\nu \rangle \approx 800$ MeV. The nucleons struck by the neutrinos in the processes of interest are inside Carbon nuclei, and so their interactions with the nuclear medium are important. Even in the crudest approximation for a nucleus, that of a $T = 0$ Fermi gas of free protons and neutrons, nucleons may have quite large momenta in the rest frame of the nucleus, $|p| \lesssim 250$ MeV, being comparable to the incoming neutrino energies. In addition to fermi motion, the Pauli exclusion principle suppresses possible final state configurations in the nucleus. Pauli blocking, possibly exchanging EM charges, knocking-out additional particles or being absorbed in the nuclear medium. The importance of nuclear effects is perhaps most famously illustrated by the CCQE measurement at MiniBooNE [53], where a disagreement of 20% was observed between the MC prediction and the data, unless the axial mass M_A was set to be ≈ 1.32 GeV, much larger than the world-average of $M_A = 1.03 \pm 0.02$ GeV. This was later understood as a missing contribution from two-particle two-hole meson exchange currents (where the neutrino interacts with a nucleon pair, rather than with an individual nucleon), shown to be as large as 30% of the CCQE cross section used by the experiment [54].

Currently several neutrino event generators exists, the most popular being GENIE [55], GiBUU [56], NEUT [57] and NuWro [58].

Chapter 3

Neutrino trident scattering

This chapter is dedicated to the study of rare neutrino scattering processes. Before we can explore the possibilities to constrain new physics, it is very important we understand our theoretical predictions in the SM. In this thesis we will see that leptonic and semi-leptonic neutrino scattering is a crucial tool to understand and go beyond the SM. This chapter is dedicated to a refresher on neutrino-electron scattering and to original work developed on the calculation and phenomenology of neutrino trident scattering. These two processes were the object of study of experiments back in the 80's and 90's, but the high beam luminosity achieved at current neutrino experiments and expected at future facilities (typically beyond 10^{21} protons on target), the relatively large fiducial masses of high- Z materials (typically 100 ton) of modern detectors, and improved particle identification (PID) capabilities allows to return to this topic at lower energies ($E_\nu = \text{few GeV}$) with a refreshed approach.

3.1 Neutrino-electron scattering

Neutrino-electron scattering has long been a valuable probe of both the SM and potential new physics [59–62]. It is important to note that in the presence of novel leptophilic currents, experiments searching for e^+e^- tridents would also observe anomalous $\nu - e$ event rates. In fact, given the larger statistics present in the $\nu - e$ scattering sample, this channel is expected to provide the leading constraints in our scenarios with tree-level couplings to electrons.

In order to compute the $\nu - e$ cross section in the presence of the new leptophilic interactions we need to consider an analogous modification of the NC scattering amplitude

$$\begin{aligned} \mathcal{M}_{\nu_\alpha - e} = & -\frac{G_F}{\sqrt{2}} [\bar{u}(k_2) \gamma^\mu (1 - \gamma_5) u(k_1)] \\ & \times [\bar{u}(p_2) \gamma_\mu (C_\alpha^V - C_\alpha^A \gamma_5) u(p_1)], \end{aligned} \quad (3.1.1)$$

where the vector (C_V) and axial (C_A) effective couplings include both the SM and BSM contributions

$$C_\alpha^V = -\frac{1}{2} + 2s_W^2 + \delta_{\alpha e} + \frac{Q_e^V Q_\alpha^L}{2\sqrt{2}G_F} \frac{(g')^2}{M_{Z'}^2 + 2m_e T_e}, \quad (3.1.2a)$$

$$C_\alpha^A = -\frac{1}{2} + \delta_{\alpha e} + \frac{Q_e^A Q_\alpha^L}{2\sqrt{2}G_F} \frac{(g')^2}{M_{Z'}^2 + 2m_e T_e}, \quad (3.1.2b)$$

with, as usual, $s_W \equiv \sin \theta_W$, being θ_W the weak angle and T_e is the kinetic energy of the recoil electron. The loop-induced kinetic mixing in the $L_\mu - L_\tau$ model also induces a $\nu - e$ coupling

$$C_\alpha^V = -\frac{1}{2} + 2s_W^2 + \delta_{\alpha e} + \frac{1}{\sqrt{2}G_F} \frac{g' e \varepsilon(q^2)}{M_{Z'}^2 + 2m_e T_e}. \quad (3.1.3)$$

The differential cross section is then given by

$$\begin{aligned} \frac{d\sigma_{\nu_\alpha - e}}{dT_e} = & \frac{2m_e G_F^2}{\pi} \left[\left(C_\alpha^L \right)^2 + \left(C_\alpha^R \right)^2 \left(1 - \frac{T_e}{E_\nu} \right)^2 \right. \\ & \left. - C_\alpha^L C_\alpha^R m_e \frac{T_e}{E_\nu^2} \right]. \end{aligned} \quad (3.1.4)$$

where the left and right handed constants are given by

$$C_\alpha^L \equiv \frac{1}{2} (C_\alpha^V + C_\alpha^A) \quad \text{and} \quad C_\alpha^R \equiv \frac{1}{2} (C_\alpha^V - C_\alpha^A).$$

For antineutrino scattering one obtains the cross section by exchanging $C_\alpha^L \leftrightarrow C_\alpha^R$.

3.1.1 Kinematics

The kinetic energy of the outgoing electron is bounded by kinematics and the energy resolution of the detector, which effectively sets a threshold energy T_{th} such that

$$T_{\text{th}} \leq T_e \leq T_{\text{max}}, \quad (3.1.5)$$

with $T_{\max} = 2E_\nu^2/m_e + 2E_\nu$, the maximum kinetic energy attainable. We define the effective total cross section for an initial neutrino energy E_ν as

$$\sigma_{\text{eff}}(E_\nu, T_{\text{th}}) = \int_{T_{\text{th}}}^{T_{\max}} \frac{d\sigma}{dT_e} dT_e. \quad (3.1.6)$$

This definition also ensures that the enhancement due to very light mediators becomes constant at around $\sqrt{2m_e T_{\text{th}}}$, as discussed in Ref. [62]. This is a consequence of the detector threshold and of the 2-body kinematics of the process. Finally, electroweak radiative corrections have been computed in the SM [63, 64], but will not be included here. Since they correspond to a change of a few percent we do not expect them to affect very much our results.

3.1.2 Measurements

MINERvA

CHARM-II, CHARM,

TEXONO, GEMMA, DAYA BAY?

Solar neutrinos - BOREXINO, SNO, Super-K

3.2 Neutrino trident scattering

Trident events are processes predicted by the SM as the result of (anti)neutrino-nucleus scattering with the production of a charged lepton pair [65–69], $\overset{(-)}{\nu}_\alpha + \mathcal{H} \rightarrow \overset{(-)}{\nu}_{\alpha \text{ or } \kappa(\beta)} + \ell_\beta^- + \ell_\kappa^+ + \mathcal{H}$, $\{\alpha, \beta, \kappa\} \in \{e, \mu, \tau\}$ ¹ where \mathcal{H} denotes a hadronic target. Depending on the (anti)neutrino and charged lepton flavours in the final-state, the process will be mediated by the Z^0 boson, W boson or both. Coherent interactions between (anti)neutrinos and the atomic nuclei are expected to dominate these processes as long as the momentum transferred Q is significantly smaller than the inverse of the nuclear size [65]. For larger momentum transfers incoherent elastic and deep-inelastic scattering become increasingly relevant [70]. Although this process exists for all combinations of same-flavour or mixed flavour charged-lepton final-states, to this day only the ν_μ -induced dimuon mode, $\overset{(-)}{\nu}_\mu + \mathcal{H} \rightarrow \overset{(-)}{\nu}_\mu + \mu^+ + \mu^- + \mathcal{H}$, has been observed. The first measurement of this trident signal performed

¹Throughout the manuscript we will consider α, β, κ as flavour indexes.

by CHARM II [71] is also the one with the largest statistics: 55 signal events in a beam of neutrinos and antineutrinos with $\langle E_\nu \rangle \approx 20$ GeV. Other measurements by CCFR [72] and NuTeV [73] at larger energies soon followed.

As the measurement of trident events may provide a sensitive test of the weak sector [74] as well as placing constraints on physics beyond the SM [72, 75–80] it is relevant to investigate how to probe it further at current and future neutrino experiments. Atmospheric neutrinos, for instance, may provide a feasible measurement of the dimuon channel, as pointed out in Ref. [78]². Other trident modes were also recognized to be relevant by the authors of Ref. [70] who calculated the cross sections for trident production in all possible flavour combinations and estimated the number of events expected for the DUNE and SHiP experiments. They used the Equivalent Photon Approximation (EPA) [81] to compute the cross section in the coherent and incoherent regimes of the scattering. The EPA, however, is known to breakdown for final state electrons [65, 82, 83] leading, as we will demonstrate here, to an overestimation of the cross section that in some cases is by more than 200%.

In this work, we present a unified treatment of the coherent and incoherent trident calculation beyond the EPA for all modes. We then compute the number and distribution of events expected in each mode at various near detectors, devoting particular attention to the case of liquid argon (LAr) detectors, as they are expected to lead the field of precision neutrino scattering measurements over the next few decades thanks to their excellent tracking and calorimetry capabilities. Finally, we address the likely backgrounds that may hinder these experimental searches — a question that we believe to be of utmost importance given the rarity of the process, and one that has been omitted in earlier sensitivity studies [70, 76].

This paper is organized as follows. In Sec. 3.3, we explain how to correctly calculate the trident SM cross sections, comparing our results to the EPA and explicitly showing the breakdown of this approximation. In Sec. 3.4, we discuss the trident event rates and kinematic distributions at the near detectors of several present and future neutrino oscillation experiments based on LAr technology: the three detectors of the Short-Baseline Neutrino (SBN) Program at Fermilab [84] and the near detector for the long-baseline Deep Underground Neutrino Experiment (DUNE) [85, 86], also located at Fermilab. We also consider the potential gains from an optimistic future facility: a 100 t LAr detector

²The authors of Ref. [78] have performed the full calculation of the trident process and made their code publicly available.

subject to the novel low-systematics neutrino beam of the Neutrinos from STORed Muons (ν STORM) project [87,88]. We discuss the sources of background events at these facilities, providing a GENIE-level analysis [89] of how to reduce these backgrounds and assessing the impact they are expected to have on the trident measurement. In Sec. ??, we discuss other near detectors that use more conventional technologies: the Interactive Neutrino GRID (INGRID) [90–93], the on-axis iron near detector for T2K at J-PARC, as well as three detectors at the Neutrino at the Main Injector (NuMI) beamline at Fermilab, the one for the Main INjector ExpeRiment ν -A (MINER ν A) [94,95] and the near detectors for the Main Injector Oscillation Search (MINOS) [96,97] and the Numi Off-axis ν_e Appearance (NO ν A) experiment [98,99].

3.3 Trident Production Cross Section

In this section we consider neutrino trident production in the SM, defined as the process where a (anti)neutrino scattering off a hadronic system \mathcal{H} produces a pair of same-flavour or mixed flavour charged leptons

$$\stackrel{(-)}{\nu}_\alpha(k_1) + \mathcal{H}(P) \rightarrow \stackrel{(-)}{\nu}_{\alpha'}(k_2) + \ell_\beta^-(p_-) + \ell_\kappa^+(p_+) + \mathcal{H}(P'), \quad (3.3.1)$$

where $\beta(\kappa)$ corresponds to the flavour index of the negative (positive) charged lepton in both neutrino and antineutrino cases. Neutrino trident scattering can be divided into three regimes depending on the nature of the hadronic target: coherent, incoherent elastic and deep inelastic, when the neutrino scatters off the nuclei, nucleons and quarks, respectively. At the energies relevant for neutrino oscillation experiments, the deep inelastic scattering contribution amounts at most to 1% of the total trident production cross section [70] and we will not consider it further.

The cross section for trident production has been calculated before in the literature, both in the context of the $V - A$ theory [65–67] and in the SM [74], while the EPA treatment was developed in Refs. [81–83]. Most calculations have focused on the coherent channels [65–67,74,81] but the incoherent process has been considered in [65,66]. More recently, calculations using the EPA have been performed for coherent scattering with a dimuon final-state [76], and for all combinations of hadronic targets and flavours of final-states in [70]. While the EPA is expected to agree reasonably well with the full calculation

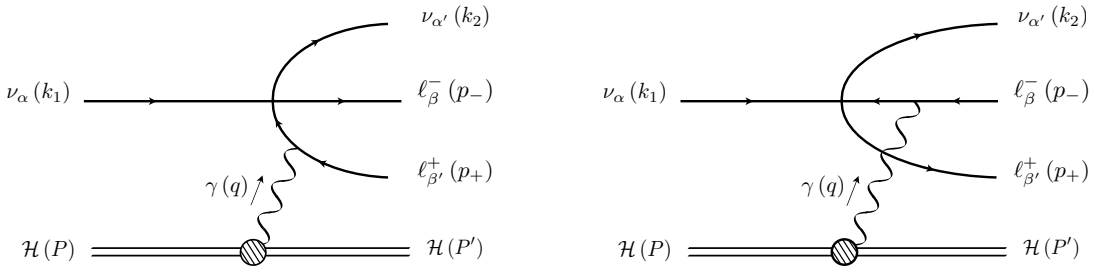


Fig. 3.1. Diagrams contributing to the neutrino trident process in the four-point interaction limit of the Standard Model.

for coherent channels with dimuon final-states, the assumptions of this approximation are invalid for the coherent process with electrons in the final-state [65, 82, 83]. For this reason, we perform the full $2 \rightarrow 4$ calculation without the EPA in a manner applicable to any hadronic target, following a similar approach to Refs. [65, 66]. Our treatment of the cross section allows us to quantitatively assess the breakdown of the EPA in both coherent and incoherent channels for all final-state flavours, an issue we come back to in Sec. 3.3.2.

We write the total cross section for neutrino trident production off a nucleus \mathcal{N} with Z protons and $(A - Z)$ neutrons as the sum

$$\sigma_{\nu\mathcal{N}} = \sigma_{\nu c} + \sigma_{\nu d}, \quad (3.3.2)$$

where $\sigma_{\nu c}$ ($\sigma_{\nu d}$) is the coherent (incoherent) part of the cross section. The relevant diagrams for these processes in the coherent or incoherent regimes involve the boson Z^0 , W or both mediators, depending on the particular mode. In the four-point interaction limit, depicted in Fig. 5.1, these reduce to only two contributions³, one where the photon couples to the negatively and one to the positively charged lepton. In Table 3.1, we present the processes we will consider in this thesis as well as the SM contributions present in each. Although our formalism applies also to processes with final-state τ leptons, the increased threshold and their suppressed cross section makes them irrelevant for the experiments of interest in this study and we do not consider them further. The trident amplitude for a coherent ($X = c$) or incoherent ($X = d$) scattering regime can be written as

$$i\mathcal{M} = L^\mu(\{p_i\}, q) \frac{-ig_{\mu\nu}}{q^2} H_X^\nu(P, P'), \quad (3.3.3)$$

³An additional diagram involving a $WW\gamma$ vertex has also been neglected, since it is of order $1/M_W^4$.

Trident channel	SM Contributions	V	A
$\nu_\mu \mathcal{H} \rightarrow \nu_\mu \mu^- \mu^+ \mathcal{H}$	CC + NC	$1/2 + 2 s_W^2$	$1/2$
$\nu_\mu \mathcal{H} \rightarrow \nu_\mu e^- e^+ \mathcal{H}$	NC	$-1/2 + 2 s_W^2$	$-1/2$
$\nu_\mu \mathcal{H} \rightarrow \nu_e e^+ \mu^- \mathcal{H}$	CC	1	1
$\nu_e \mathcal{H} \rightarrow \nu_e e^- e^+ \mathcal{H}$	CC + NC	$1/2 + 2 s_W^2$	$1/2$
$\nu_e \mathcal{H} \rightarrow \nu_e \mu^- \mu^+ \mathcal{H}$	NC	$-1/2 + 2 s_W^2$	$-1/2$
$\nu_e \mathcal{H} \rightarrow \nu_\mu \mu^+ e^- \mathcal{H}$	CC	1	1

Tab. 3.1. Neutrino trident processes considered in this thesis. Antineutrino induced channels are analogous.

where $\{p_i\} = \{k_2, p_-, p_+\}$ is the set of outgoing leptonic momenta. $L^\mu(\{p_i\}, q)$ is the total leptonic amplitude

$$L^\mu \equiv -\frac{ieG_F}{\sqrt{2}} [\bar{u}(k_2)\gamma^\tau(1-\gamma_5)u(k_1)] \times \bar{u}(p_-) \left[\gamma_\tau(V - A\gamma_5) \frac{1}{(\not{q} - \not{p}_+ - m_+)} \gamma^\mu \right. \\ \left. + \gamma^\mu \frac{1}{(\not{p}_- - \not{q} - m_-)} \gamma_\tau(V - A\gamma_5) \right] v(p_+), \quad (3.3.4)$$

and $H_X^\nu(P, P')$ is the total hadronic amplitude

$$H_X^\nu \equiv \langle \mathcal{H}(P) | J_{\text{E.M.}}^\nu(q^2) | \mathcal{H}(P') \rangle, \quad (3.3.5)$$

with $q \equiv P - P'$ denoting the transferred momentum, m_+ (m_-) the positively (negatively) charged lepton mass and $J_{\text{E.M.}}^\nu(q^2)$ the electromagnetic current for the hadronic system \mathcal{H} (a nucleus or a nucleon). The flavour indices have been omitted from the vector V and axial A couplings, determined by $V \equiv g_V^{\alpha'} \delta_{\alpha\alpha'} \delta_{\beta\beta'} + \delta_{\alpha'\beta'} \delta_{\alpha\beta}$ and $A \equiv g_A^{\alpha'} \delta_{\alpha\alpha'} \delta_{\beta\beta'} + \delta_{\alpha'\beta'} \delta_{\alpha\beta}$ in accordance to Eq. (3.3.1) and shown in Table 3.1.

We can write the differential cross section as

$$\frac{d^2\sigma_{\nu X}}{dQ^2 d\hat{s}} = \frac{1}{32\pi^2(s - M_{\mathcal{H}}^2)^2} \frac{H_X^{\mu\nu} L_{\mu\nu}}{Q^4}, \quad (3.3.6)$$

where $s = (k_1 + P)^2$, $\hat{s} \equiv 2(k_1 \cdot q)$, $Q^2 = -q^2$ and $M_{\mathcal{H}}$ is the mass of the hadronic target.

We have also introduced the hadronic tensor $H_X^{\mu\nu}$

$$H_X^{\mu\nu} \equiv \overline{\sum_{\text{spins}}} (H_X^\mu)^* H_X^\nu. \quad (3.3.7)$$

The two scattering regimes in which the hadronic tensor is computed will be discussed in more detail in Sec. 3.3.1. The leptonic tensor, $L^{\mu\nu}$, integrated over the phase space of the three final-state leptons, $d^3\Pi(k_1 + q; \{p_i\})$, and merely summed over final and initial spins

is given by

$$L^{\mu\nu}(k_1, q) \equiv \int d^3\Pi(k_1 + q; \{p_i\}) \left(\sum_{\text{spins}} (L^\mu)^* L^\nu \right). \quad (3.3.8)$$

We can use $L^{\mu\nu}$ to define two scalar functions, one related to the longitudinal (L_L) and the other to the transverse (L_T) polarization of the exchanged photon

$$L_T = -\frac{1}{2} \left(g^{\mu\nu} - \frac{4Q^2}{\hat{s}^2} k_1^\mu k_1^\nu \right) L_{\mu\nu}, \quad \text{and} \quad L_L = \frac{4Q^2}{\hat{s}^2} k_1^\mu k_1^\nu L_{\mu\nu}. \quad (3.3.9)$$

This allows us to write the differential cross section as a sum of a longitudinal and a transverse contribution [100] as follows

$$\frac{d^2\sigma_{\nu X}}{dQ^2 d\hat{s}} = \frac{1}{32\pi^2} \frac{1}{\hat{s} Q^2} \left[h_X^T(Q^2, \hat{s}) \sigma_{\nu\gamma}^T(Q^2, \hat{s}) + h_X^L(Q^2, \hat{s}) \sigma_{\nu\gamma}^L(Q^2, \hat{s}) \right], \quad (3.3.10)$$

where we have defined two functions for the flux of longitudinal and transverse virtual photons

$$h_X^T(Q^2, \hat{s}) \equiv \frac{2}{(E_\nu M_H)^2} \left[k_{1\mu} k_{1\nu} - \frac{\hat{s}^2}{4Q^2} g_{\mu\nu} \right] H_X^{\mu\nu}, \quad \text{and} \quad (3.3.11a)$$

$$h_X^L(Q^2, \hat{s}) \equiv \frac{1}{(E_\nu M_H)^2} k_{1\mu} k_{1\nu} H_X^{\mu\nu}, \quad (3.3.11b)$$

and two leptonic neutrino-photon cross sections associated with them⁴

$$\sigma_{\nu\gamma}^T(Q^2, \hat{s}) = \frac{L_T}{2\hat{s}}, \quad \text{and} \quad \sigma_{\nu\gamma}^L(Q^2, \hat{s}) = \frac{L_L}{\hat{s}}. \quad (3.3.12)$$

The kinematically allowed region in the (Q^2, \hat{s}) plane can be obtained by considering the full four-body phase space, as in [65–67]. The limits for such physical region are given by

$$Q_{\min}^2 = \frac{M_H \hat{s}^2}{2E_\nu(2E_\nu M_H - \hat{s})}, \quad Q_{\max}^2 = \hat{s} - m_L^2, \quad (3.3.13a)$$

$$\hat{s}_{\min} = \frac{E_\nu}{2E_\nu + M_H} [m_L^2 + 2E_\nu M_H - \Delta] \quad \hat{s}_{\max} = \frac{E_\nu}{2E_\nu + M_H} [m_L^2 + 2E_\nu M_H + \Delta], \quad (3.3.13b)$$

with $m_L \equiv m_+ + m_-$, and

$$\Delta \equiv \sqrt{(2E_\nu M_H - m_L^2)^2 - 4M_H^2 m_L^2}.$$

Let us emphasize that Eq. (3.3.10) is an exact decomposition, and does not rely on any approximation of the process. In the following section, we will show how to calculate the

⁴Note that we include a factor of $1/2$ in $\sigma_{\nu\gamma}^T$ to match the polarization averaging of the on-shell cross section: $\sigma_{\nu\gamma}^{\text{on-shell}} = \frac{1}{2\hat{s}} \left(\overline{\sum_r} (\epsilon_r^\mu)^* \epsilon_r^\nu L_{\mu\nu} \right) \Big|_{Q^2=0} = \frac{1}{4\hat{s}} (-g^{\mu\nu} L_{\mu\nu}) \Big|_{Q^2=0} = \frac{L_T}{2\hat{s}} \Big|_{Q^2=0} = \sigma_{\nu\gamma}^T(0, \hat{s}).$

flux functions h_X^T and h_X^L from Eq. 3.3.11 in different scattering regimes. The total cross section for the process can then be computed by finding $\sigma_{\nu\gamma}^L$ and $\sigma_{\nu\gamma}^T$ from Eqs. (3.3.4), (3.3.8) and (3.3.9) and integrating over all allowed values of Q^2 and \hat{s} . Note that $\sigma_{\nu\gamma}^L$ and $\sigma_{\nu\gamma}^T$ are universal functions for a given leptonic process and need only to be computed once.

3.3.1 Hadronic Scattering Regimes

Depending on the magnitude of the virtuality of the photon, $Q = \sqrt{-q^2}$, the hadronic current can contribute in different ways to the trident process. Thus, given the decomposition in Eq. (3.3.10), the change in the hadronic treatment translates to computing the flux factors h_X^T and h_X^L for each scattering regime. From those flux factors, $\sigma_{\nu c}$ and $\sigma_{\nu d}$ can be calculated.

Coherent Regime ($H_c^{\mu\nu}$)

In the coherent scattering regime the incoming neutrino interacts with the whole nucleus without resolving its substructure. For this to occur frequently, we need small values of Q . Despite the relatively large neutrino energies in contemporary neutrino beams, this is still allowed for trident.

In this regime, the hadronic tensor $H_c^{\mu\nu}$ for a ground state spin-zero nucleus of charge Ze can be written in terms of the nuclear electromagnetic form factor $F(Q^2)$, discussed in more detail in Appendix ??, as

$$H_c^{\mu\nu} = 4Z^2 e^2 \left| F(Q^2) \right|^2 \left(P^\mu - \frac{q^\mu}{2} \right) \left(P^\nu - \frac{q^\nu}{2} \right). \quad (3.3.14)$$

From Eq. 3.3.11, we find that the transverse and longitudinal flux functions for the coherent regime are

$$h_c^T(Q^2, \hat{s}) = 8Z^2 e^2 \left(1 - \frac{\hat{s}}{2E_\nu M} - \frac{\hat{s}^2}{4E_\nu^2 Q^2} \right) |F(Q^2)|^2, \quad (3.3.15a)$$

$$h_c^L(Q^2, \hat{s}) = 4Z^2 e^2 \left(1 - \frac{\hat{s}}{4E_\nu M} \right)^2 |F(Q^2)|^2, \quad (3.3.15b)$$

where E_ν is the energy of the incoming neutrino and M is the nuclear mass. For a fixed value of \hat{s} in the physical region, the h_c^T flux function becomes zero at Q_{\min} while the

longitudinal component does not. This different behaviour can be seen explicitly in their definitions, Eqs. (3.3.15), as the terms in the parenthesis in h_c^T cancel each other at Q_{\min} . This does not occur for h_c^L since the physical values of \hat{s} are always smaller than $E_\nu M$ in this hadronic regime. Due to this fact, Q_{\min} , which according to Eq. (3.3.13a) depends on both the neutrino energy and target material, can be approximated to

$$Q_{\min} \approx \frac{\hat{s}}{2E_\nu},$$

which only depends on the incoming neutrino energy. On the other hand, as Q becomes large, the flux functions $h^{T,L}$ become quite similar, $h_c^T \approx 2h_c^L$, and favour small values of \hat{s} . After some critical value of the virtuality Q , $h_c^{T,L}$ become negligible due to the nuclear form factor. The Q value at which this happens depends on the target material, but not on the incoming neutrino energy. For instance, in the case of an Ar target the flux functions basically vanish for $Q \gtrsim 250$ MeV.

The final cross sections for coherent neutrino trident production on Argon can be seen in Fig. 3.2. Despite thresholds being important for the behaviour of these cross sections for GeV neutrino energies, we can see that mixed channels quickly become the most important due to their CC nature. At large energies one can then rank the cross sections from largest to smallest as CC, CC+NC, and NC only channels. Nevertheless, one must be aware of the fact that the cross sections are dominated by low Q^2 even at large energies, leading to large effects due to the final-state lepton masses as discussed in [70].

Incoherent Regime ($H_d^{\mu\nu}$)

At larger Q^2 , the neutrino interacts with the individual nucleons of the nucleus. In this incoherent regime $H_d^{\mu\nu}$ is given by the sum of the contributions of the two types of nucleons: protons ($N = p$) and neutrons ($N = n$), so

$$H_d^{\mu\nu}(P, P') = Z H_p^{\mu\nu}(P, P') + (A - Z) H_n^{\mu\nu}(P, P'), \quad (3.3.16)$$

where each $H_N^{\mu\nu}$ is the square of the matrix element of the nucleon electromagnetic current summed over final and averaged over initial spins. Neglecting second class currents, the matrix elements take the form

$$\langle N(P') | J_{E.M.}^\mu(Q^2) | N(P) \rangle = e \bar{u}_N(P') \left[\gamma^\mu F_1^N(Q^2) - i \frac{\sigma^{\mu\nu} q_\nu}{2M_N} F_2^N(Q^2) \right] u_N(P), \quad (3.3.17)$$

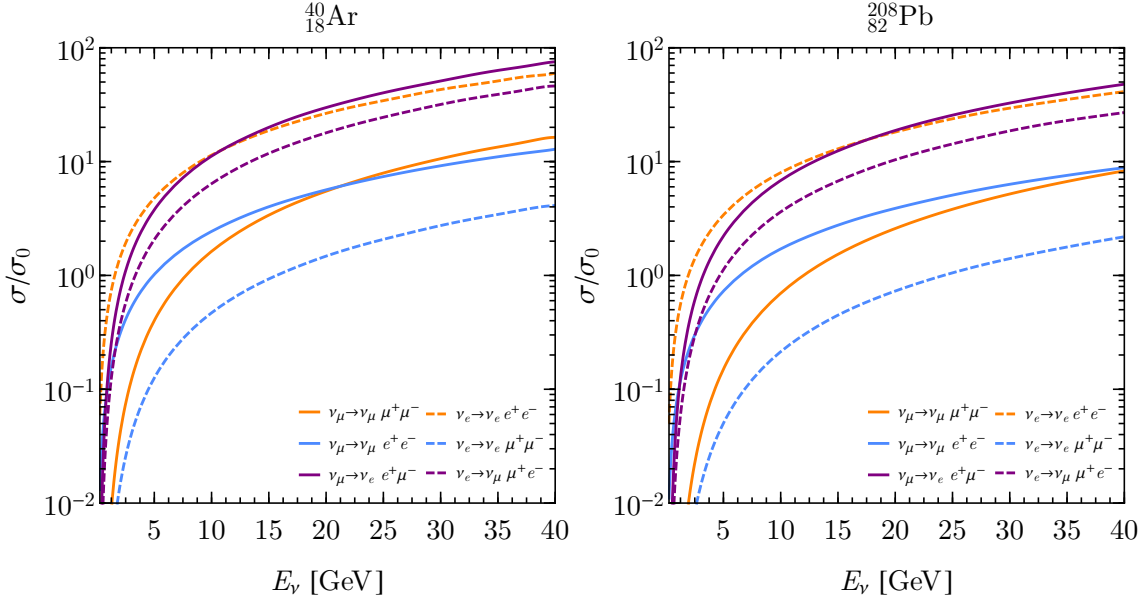


Fig. 3.2. Cross sections for coherent neutrino trident production on ^{40}Ar (left) and ^{208}Pb (right) normalized to $\sigma_0 = Z^2 10^{-44} \text{ cm}^2$. The full (dashed) lines correspond to the scattering of an incoming ν_μ (ν_e) produced by the NC (light-blue), CC (purple), and CC+NC (orange) SM interactions.

with $F_{1,2}^N(Q^2)$ the Dirac and Pauli form factors, respectively. The hadronic tensors are then given by [101]

$$H_N^{\mu\nu} = e^2 \left[4 H_1^N(Q^2) \left(P^\mu - \frac{q^\mu}{2} \right) \left(P^\nu - \frac{q^\nu}{2} \right) - H_2^N(Q^2) \left(Q^2 g^{\mu\nu} + q^\mu q^\nu \right) \right], \quad (3.3.18)$$

where the $H_1^N(Q^2)$ and $H_2^N(Q^2)$ form factors, functions of $F_{1,2}^N(Q^2)$, are given in Appendix ???. The flux functions in the incoherent regime can then be calculated as

$$h_N^T(Q^2, \hat{s}) = 8 e^2 \left[\left(1 - \frac{\hat{s}}{2E_\nu M_N} - \frac{\hat{s}^2}{4E_\nu^2 Q^2} \right) H_1^N(Q^2) + \frac{\hat{s}^2}{8E_\nu^2 M_N^2} H_2^N(Q^2) \right], \quad (3.3.19a)$$

$$h_N^L(Q^2, \hat{s}) = 4 e^2 \left[\left(1 - \frac{\hat{s}}{4E_\nu M_N} \right)^2 H_1^N(Q^2) - \frac{\hat{s}^2}{16E_\nu^2 M_N^2} H_2^N(Q^2) \right]. \quad (3.3.19b)$$

In the case of the proton, the flux functions $h_p^{\text{T,L}}$ have some unique features given the presence of both electric and magnetic contributions. Specifically, the transverse function is non-zero at $Q = Q_{\min}$ for a fixed \hat{s} , due to the additional term proportional to H_2^p . Indeed, for large values of \hat{s} , the H_2^p term dominates the transverse function. An opposite behaviour occurs for the longitudinal component. There, the H_1^p term dominates over the second term for all physical values of \hat{s} , Q , and for any incoming neutrino energy. On the other hand, the flux functions of the neutron, which have only the magnetic moment contribution, have somewhat different characteristics. While h_n^T behaves similarly to h_p^T ,

that is, it is dominated by the second term for large values of \hat{s} , h_n^L is zero at Q_{\min} due to the exact cancellation between the $H_{1,2}^n$ terms. This cancellation is not evident from Eq. (3.3.19b); however, simplifying the longitudinal component for the neutron case, one finds

$$h_n^L(Q^2, \hat{s}) = 4e^2 \left(1 + \frac{Q^2}{4M_n^2}\right) \frac{Q^2}{4M_N^2} \left(1 - \frac{\hat{s}}{2E_\nu M_N} - \frac{\hat{s}^2}{4E_\nu^2 Q^2}\right) |F_2^n(Q^2)|^2,$$

which is zero for $Q = Q_{\min}$. Also, this shows why h_p^L does not vanish at Q_{\min} since there we have the additional contribution of the electric component.

When the neutrino interacts with an individual nucleon inside the nucleus, one must be aware of the nuclear effects at play. One such effect is Pauli blocking, a suppression of neutrino-nucleon interactions due to the Pauli exclusion principle. Modelling the nucleus as an ideal Fermi gas of protons and neutrons, one can take Pauli blocking effects into account by requiring that the hit nucleon cannot be in a state which is already occupied [68]. This requirement is implemented in our calculations by a simple replacement of the differential incoherent cross section

$$\frac{d^2\sigma_{\nu d}}{dQ^2 d\hat{s}} \rightarrow f(|\vec{q}|) \frac{d^2\sigma_{\nu d}}{dQ^2 d\hat{s}},$$

where $|\vec{q}|$ is the magnitude of the transferred three-momentum in the lab frame. In particular, following [68], assuming an equal density of neutrons and protons, we have

$$f(|\vec{q}|) = \begin{cases} \frac{3}{2} \frac{|\vec{q}|}{2k_F} - \frac{1}{2} \left(\frac{|\vec{q}|}{2k_F}\right)^3, & \text{if } |\vec{q}| < 2k_F, \\ 1, & \text{if } |\vec{q}| \geq 2k_F, \end{cases} \quad (3.3.20)$$

where k_F is the Fermi momentum of the gas, taken to be 235 MeV. This is a rather low value of k_F and the assumption of equal density of neutrons and protons must be taken with care for heavy nuclei. We refrain from trying to model any additional nuclear effects as we believe that this is the dominant effect on the total incoherent rate, particularly when requiring no hadronic activity in the event. The net result is a reduction of the incoherent cross section by about 50% for protons and 20% for neutrons. Unless clearly stated otherwise, we always include Pauli blocking in our calculations.

Our final cross sections for this regime can be seen in Fig. 3.3. One can clearly see that the neutron contribution is subdominant, and that, up to factors of Z^2 , the proton one is comparable to the coherent cross section. Note that now the typical values of Q^2 are

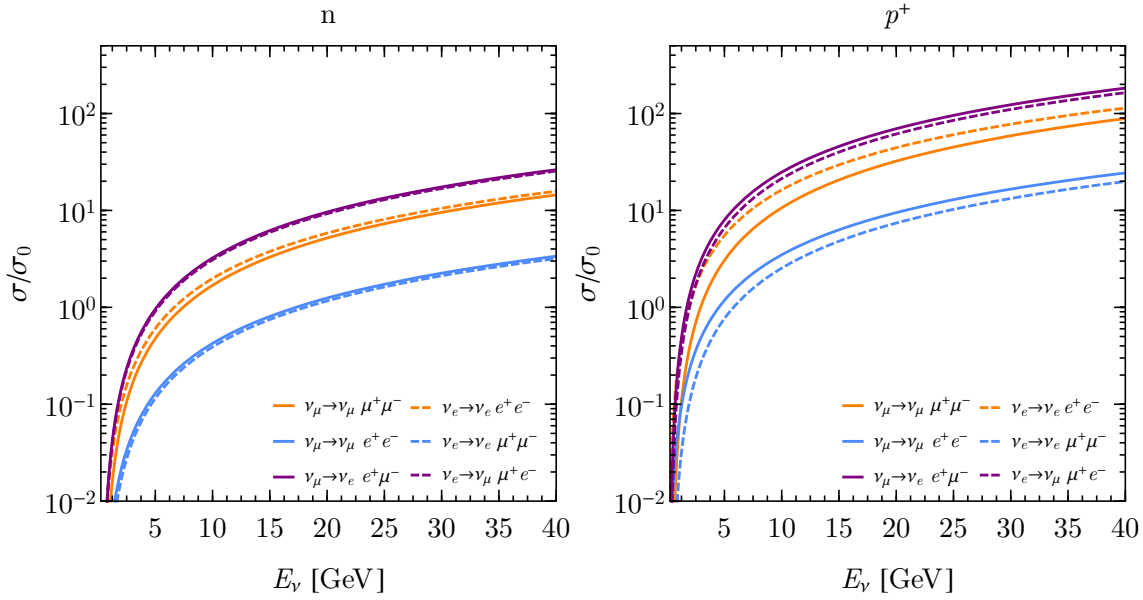


Fig. 3.3. Cross sections for incoherent neutrino trident production on neutrons (left) and protons (right), including Pauli blocking effects as described in the text, normalized to $\sigma_0 = 10^{-44} \text{ cm}^2$. The full (dashed) lines correspond to the scattering of an incoming ν_μ (ν_e) produced by the NC (light-blue), CC (purple), and CC+NC (orange) SM interactions.

much larger than in the coherent regime and the impact of the final-state lepton masses is much smaller.

3.3.2 Breakdown of the EPA

In order to understand the breakdown of the EPA in the neutrino trident case, let us first remind briefly the reader about the Weizsäcker–Williams method of equivalent photons in Quantum Electrodynamics (QED) [102, 103], and the main reason for its validity in that theory. The EPA, first introduced by E. Fermi [104], is based on a simple principle: when an ultra-relativistic particle P_i approaches a charged system C_s , like a nucleus, it will perceive the electromagnetic fields as nearly transverse, similar to the fields of a pulse of radiation, *i.e.*, as an on-shell photon. Therefore, it is possible to obtain an approximate total cross section for the inelastic scattering process producing a set of final particles P_f , $\sigma_t(P_i + C_s \rightarrow P_f + C_s)$, by computing the scattering of the incoming particle with a real photon integrated over the energy spectrum of the off-shell photons,

$$\sigma_t(P_i + C_s \rightarrow P_f + C_s) \approx \int dP(Q^2, \hat{s}) \sigma_\gamma(P_i + \gamma \rightarrow P_f; \hat{s}, Q^2 = 0), \quad (3.3.21)$$

where the photo-production cross section for the process $P_i + \gamma \rightarrow P_f$, $\sigma_\gamma(P_i + \gamma \rightarrow P_f; \hat{s}, Q^2 = 0)$, depends on the center-of-mass energy of the P_i -photon system, $\sqrt{\hat{s}}$. Here $dP(Q^2, \hat{s})$ corresponds to the energy spectrum of the virtual photons, that is, the probability of emission of a virtual photon with transferred four-momentum Q^2 resulting in an center-of-mass energy $\sqrt{\hat{s}}$. For trident scattering off a nuclear target, this probability can be approximated by [76, 81]

$$dP(Q^2, \hat{s}) = \frac{Z^2 e^2}{4\pi^2} |F(Q^2)|^2 \frac{d\hat{s}}{\hat{s}} \frac{dQ^2}{Q^2}. \quad (3.3.22)$$

A crucial fact in QED is that the cross section $\sigma_\gamma^{\text{QED}}(P_i + \gamma \rightarrow P_f; \hat{s}, 0)$ is inversely proportional to \hat{s} ,

$$\sigma_\gamma^{\text{QED}}(P_i + \gamma \rightarrow P_f; \hat{s}, 0) \propto \frac{1}{\hat{s}}.$$

We see clearly that small values of \hat{s} and consequently of the transferred four-momentum Q^2 dominate the cross section. Hence, the on-shell contribution is much more significant than the off-shell one, so the EPA will be valid and give the correct cross section estimate for any QED process.

Now, let us consider the case of neutrino trident production. In this case, the equivalent-photon cross section in the four-point interaction limit has a completely opposite dependence on the center-of-mass energy; it is *proportional* to \hat{s} ,

$$\sigma_\gamma^{\text{FL}}(P_i + \gamma \rightarrow P_f; \hat{s}, 0) \propto G_F^2 \hat{s}.$$

This dependence is a manifestation of the unitarity violation in the Fermi theory. Therefore, we can see that for weak processes larger values of \hat{s} , and, consequently, larger values of Q^2 are more significant [82, 83]. The EPA is then generally not valid for the neutrino trident production, as the virtual photon contribution dominates over the real one. Nevertheless, one may wonder if there is a situation in which the EPA can give a reasonable estimate for a neutrino trident process. As noticed in the early literature [82, 83], the presence of the nuclear form factor introduces a cut in the transferred momentum which, in turn, makes the EPA applicable for the specific case of the dimuon channel in the coherent regime. Let us discuss this in more detail.

Recalling our exact decomposition, Eq. (3.3.10), it is necessary to consider two assumptions

for implementing the EPA [82]:

1. The longitudinal polarization contribution to the cross section can be neglected, i.e.,

$$\sigma_{\nu\gamma}^L(Q^2, \hat{s}) \approx 0;$$

2. The transverse polarization contribution to the cross section can be taken to be on-shell, i.e., $\sigma_{\nu\gamma}^T(Q^2, \hat{s}) \approx \sigma_{\nu\gamma}^T(0, \hat{s})$.

Assuming for now that these approximations hold, we can find a simplified expression for the coherent neutrino-target process, described by Eqs. (3.3.10) and (3.3.15), in terms of the photon-neutrino cross section⁵:

$$\sigma_{\text{EPA}} = \frac{Z^2 e^2}{4\pi^2} \int_{m_L^2}^{\hat{s}_{\max}} \frac{d\hat{s}}{\hat{s}} \sigma_{\nu\gamma}^T(0, \hat{s}) \int_{(\hat{s}/2E_\nu)^2}^{Q_{\max}^2} \frac{|F(Q^2)|^2}{Q^4} [Q^2(1-y) - M_H^2 y^2] dQ^2, \quad (3.3.23)$$

where we introduced the fractional change of the nucleus energy y , defined as $\hat{s} = (s - M_H^2)y$, and the integration limits can be obtained from (3.3.13) after considering that $m_L^2 \ll E_\nu M_H$. Keeping only the leading terms in the small parameter y [81], we recover the EPA applied to the neutrino trident case

$$\sigma_{\text{EPA}} = \int \sigma_{\nu\gamma}^T(0, \hat{s}) dP(Q^2, \hat{s}), \quad (3.3.24)$$

where $dP(Q^2, \hat{s})$ is given in Eq. (3.3.22). The EPA in the form of Eq. (3.3.24) has been used in trident calculations for the coherent dimuon channel [76] as well as for coherent mixed- and electron-flavour trident modes and incoherent trident modes [70]. Using our decomposition, we can explicitly compute both $\sigma_{\nu\gamma}^L$ and $\sigma_{\nu\gamma}^T$ and verify if the EPA conditions are satisfied for any channel and, if they are not, quantify the error introduced by making this approximation. For that purpose, we will compare the results of the full calculation, Eq. (3.3.10), with the EPA results, Eq. (3.3.24), by computing the following ratios in the physical region of the (Q, \hat{s}) plane,

$$\frac{\sigma^L(Q^2, \hat{s}) h_c^L(Q^2, \hat{s})}{\sigma^T(Q^2, \hat{s}) h_c^T(Q^2, \hat{s})}, \quad \frac{\sigma_{\nu\gamma}^T(Q^2, \hat{s})}{\sigma_{\nu\gamma}^T(0, \hat{s})}. \quad (3.3.25)$$

The first ratio in Eq. (3.3.25) will indicate where the longitudinal contribution can be neglected compared to the transverse one; while, the second ratio will show where the transverse contribution behaves as an on-shell photon.

⁵An analogous expression can be obtained for the incoherent regime from Eq. (3.3.19).

As an illustration of the general behaviour, we show in Fig. 3.4 those ratios of cross sections for an incoming ν_μ of fixed energy $E_\nu = 3$ GeV colliding coherently with an ^{40}Ar target, for the dielectron (left panels), mixed (middle panels) and dimuon (right panels) channels. On the top panels of Fig. 3.4 we see that the longitudinal component can be neglected for $Q \lesssim m_\alpha$, for the dielectron and dimuon channels, $\alpha = e, \mu$, while in the mixed case there is a much less pronounced hierarchy between the transverse and longitudinal components. On the bottom panels we have the comparison between on-shell and off-shell transverse photo-production cross sections. Again, we find that the EPA is only valid for $Q \lesssim m_\alpha$ for the dielectron and dimuon channels. For the mixed case, there is only a very small region in $Q < 10^{-2}$ GeV for which the off-shell transverse cross section is comparable to the on-shell one. This relative suppression of the off-shell cross section can be understood by noticing that Q enters the lepton propagators, suppressing the process for $Q \gtrsim m_\alpha$. For mixed channels it is then the smallest mass scale (m_e) that dictates the fall-off of the matrix element in Q , whilst the heaviest mass (m_μ) defines the phase space boundaries, rendering most of this phase space incompatible with the EPA assumptions.

These results explicitly show that the EPA is, in principle, not suitable for any neutrino trident process as it can overestimate the cross section quite substantially by treating the photo-production cross section at large Q^2 as on-shell. However, as previously mentioned, in the coherent regime the nuclear form factor introduces a strong suppression for large values of Q^2 . In general, this dominates the behaviour of the cross sections for values of Q^2 smaller than the purely kinematic limit, Q_{\max}^2 , and of the order of $\Lambda_{\text{QCD}}/A^{1/3} \approx 0.06$ GeV for coherent scattering on ^{40}Ar . In the dimuon case, the latter scale happens to be smaller than the charged lepton masses, implying that the region where the EPA breaks down is heavily suppressed due to the nuclear form factor. The same cannot be said about coherent trident channels involving electrons, as the nuclear form factor suppression happens for much larger values of Q than the EPA breakdown. Furthermore, for incoherent scattering the nucleon form factors suppress the cross sections only for much larger Q values, $Q \approx 0.8$ GeV. The effective range of integration then includes a significant region where the EPA assumptions are invalid, leading to an overestimation of the incoherent cross section for every process regardless of the flavours of their final-state charged leptons.

In some calculations, artificial cuts have been imposed on the range of Q^2 , affecting the

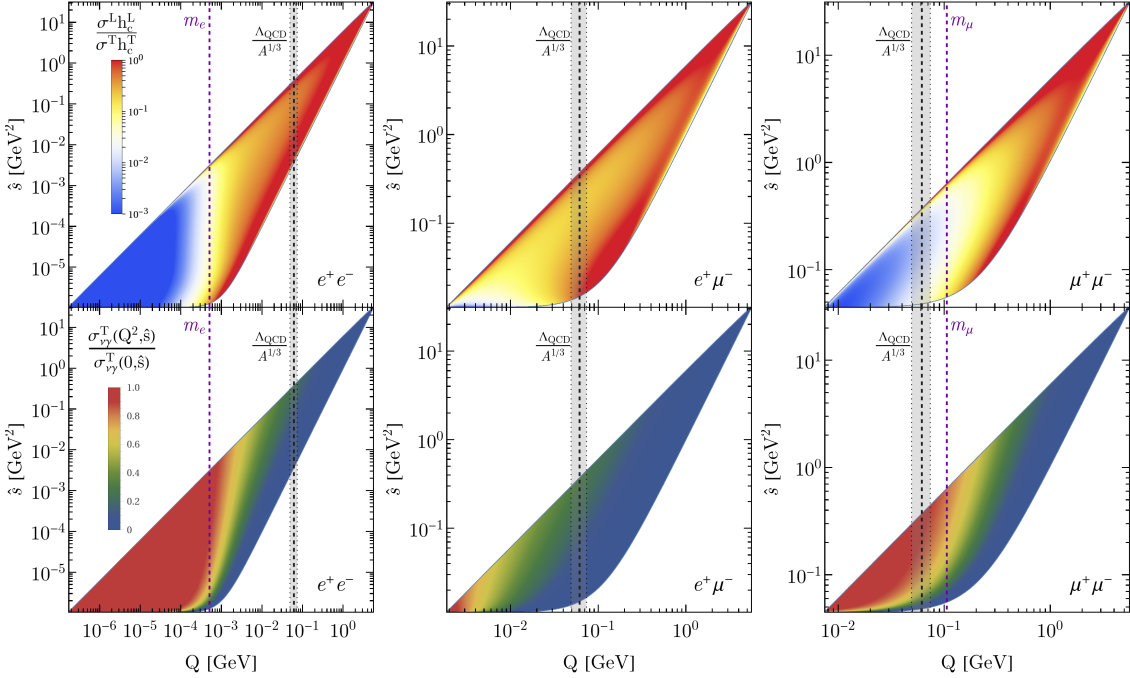


Fig. 3.4. Comparison between the full calculation of the trident production coherent cross section and the EPA in the kinematically allowed region of the (Q, \hat{s}) plane for an incoming ν_μ with fixed energy $E_\nu = 3$ GeV colliding with an ${}^{40}\text{Ar}$ target. The left, middle and right panels correspond to the dielectron, mixed and dimuon final-states, respectively. The top panels correspond to the comparison between the longitudinal and transverse contributions while the bottom ones show the ratio between the transverse cross sections computed for a specific value of Q with the cross section for an on-shell photon. The thick black dashed lines correspond to the cut in the Q^2 integration at $\Lambda_{\text{QCD}}^2/A^{2/3}$, and the shadowed region around these lines account for a variation of 20% in the value of this cut. The purple dashed lines are for $Q = m_\alpha$, $\alpha = e, \mu$ for the unmixed cases.

validity of the EPA. In Ref. [70], it is claimed that to avoid double counting between different regimes, an artificial cut must be imposed, lowering the upper limit of integration in Q^2 . Ref. [70] chooses a value of $Q_{\max}^{\text{cut}} = \Lambda_{\text{QCD}}/A^{1/3}$ in the coherent regime (black thick dashed lines in Fig. 3.4), and $Q_{\min}^{\text{cut}} = \max(\Lambda_{\text{QCD}}/A^{1/3}, \hat{s}/2E_\nu)$ and $Q_{\max}^{\text{cut}} = 1.0$ GeV in the incoherent regime. We believe that no such cut is required on physical grounds⁶, and their presence will impact the EPA cross section quite dramatically. Let us first consider the dimuon case in the coherent regime, where the EPA assumptions hold reasonably well in the relevant parts of phase space. By introducing a value for Q_{\max}^{cut} we would be decreasing the total relevant phase space for the process, reducing the total cross section. Therefore, despite the EPA tendency to overestimate the cross section in this channel, an artificial cut in Q^2 can actually lead to an underestimation of the cross section. In the

⁶It should be noted that the coherent and incoherent regimes have different phase space boundaries and that the form factors should guarantee their independence.

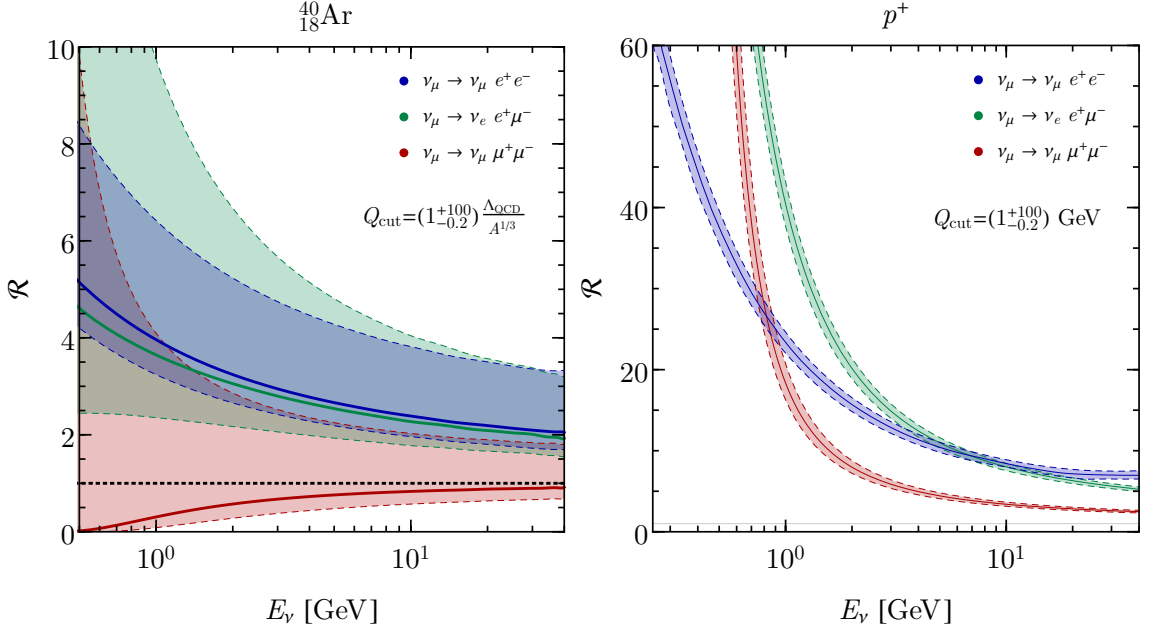


Fig. 3.5. Ratio \mathcal{R} of the trident cross section calculated using the EPA to the full four-body calculation. Left panel: Ratio in the coherent regime on ^{40}Ar . The full curves correspond to the central value of Q_{cut} , and the upper (lower) boundary corresponds to a choice 100 times larger (20% smaller). Right panel: Ratio in the incoherent regime for scattering on protons, where the full curves corresponds to the central value of 1.0 GeV, and the upper (lower) boundary corresponds to a choice 100 times larger (20% smaller); we have taken the lower limit in the integration on Q to match the choice of the coherent regime and we do not include Pauli blocking in these curves. A guide to the eye at $\mathcal{R} = 1$ is also shown.

electron channels, where the EPA breakdown is much more dramatic, we can expect that the overestimation of the cross section by the EPA is reduced by the cut $Q_{\text{max}}^{\text{cut}}$. In fact, one way to improve the EPA for the dielectron channel is to artificially cut on the Q^2 integral around the region where the approximation breaks down [105]. This cut does then improve the coherent EPA calculation by decreasing the overestimation of the cross section. However, an energy independent cut cannot provide a good estimate of the cross section over all values of E_ν . To illustrate our point and to quantify the errors induced by the EPA, we show on the left panel of Fig. 3.5 the ratio \mathcal{R} of the trident cross section calculated using the EPA with an artificial cut at Q_{cut}^2 , as performed in [70], to the full calculation used in this work as a function of the incoming neutrino energy:

$$\mathcal{R} = \frac{\sigma_{\text{EPA}}(E_\nu)|_{Q_{\text{cut}}}}{\sigma_{\text{4PS}}(E_\nu)}. \quad (3.3.26)$$

In this plot we vary the artificial cut on Q^2 around the choice of [70] (shown as the central dashed line) in two ways. First we reduce it by 20%, and then increase it by a large factor,

recovering the case with no Q^2 cut. From this, our conclusions about the validity of the approximation are confirmed, and it becomes evident that the trident coherent cross section is very sensitive to the choice of Q_{cut}^2 . In particular, the EPA with all the assumptions that lead to Eq. (3.3.24) and the absence of a Q^2 cut can lead to an overestimation of all trident channels, including the dimuon one. Once the cut is implemented, however, the approximation becomes better for the dimuon channel, but still unacceptable for the electron ones. It is also clear that an energy independent cut cannot give the correct cross section at all energies. This is particularly troublesome for detectors subjected to a neutrino flux covering a wide energy range such as the near detectors for DUNE and MINOS or MINER ν A. Moreover, Eq. (3.3.24) fails at low energies, and generally, overestimates the coherent cross sections by at least 200%. At these energies, one must be wary of the additional approximations in Eq. (3.3.24) regarding the integration limits and the small y limit.

On the right panel of Fig. 3.5 we illustrate what happens in the incoherent regime, where the nucleon form factors impact the cross section at much larger values of Q^2 and have a slower fall-off. We see that the incoherent cross section is dramatically overestimated over the full range of E_ν considered and for any trident mode. The discrepancy is particularly important for $E_\nu \lesssim 5$ GeV and larger than in the coherent regime by at least an order of magnitude⁷. We also see that the cuts on Q^2 impact the EPA calculation much less dramatically, and that its use is unlikely to yield the correct result.

Given these problems with both coherent and incoherent cross section calculations due to the breakdown of the EPA for trident production, in what follows we will use the complete four-body calculation.

3.3.3 Coherent versus incoherent Scattering in Trident Production

Let us now comment on the significance of the coherent and incoherent contributions to the total cross for the different trident channels. In Fig. 3.6 we present the ratio of the coherent and the incoherent scattering cross sections to the total cross section for an ${}^{40}\text{Ar}$

⁷There are some differences in the treatment of the hadronic system between the EPA calculation in [70] and the one presented here. However, these differences are of the order 10% to 20%. Note also that we do not implement any Pauli blocking when calculating \mathcal{R} to avoid ambiguities over the choice of the range of Q^2 .

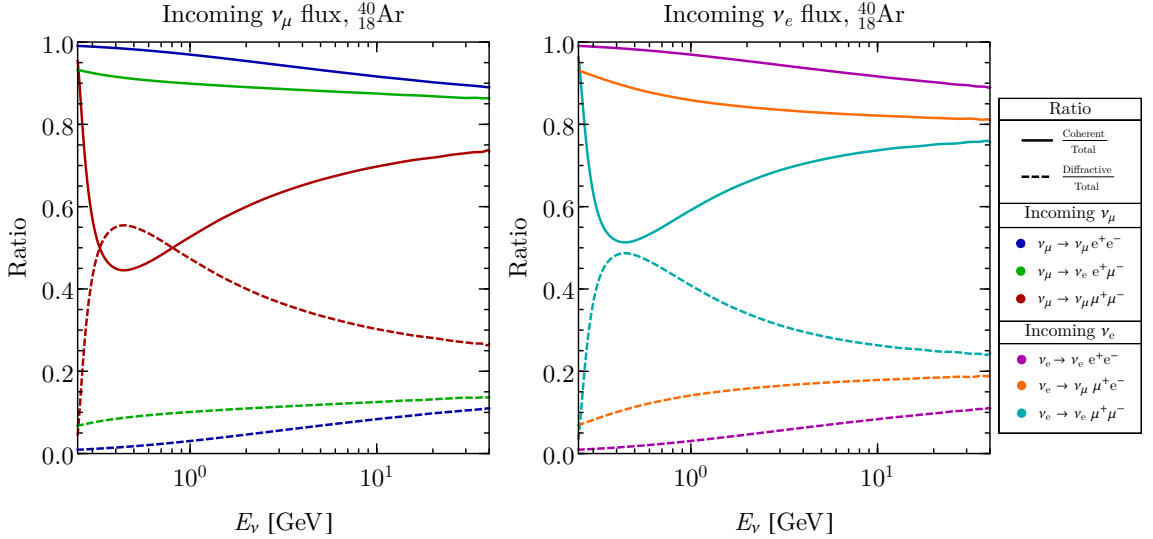


Fig. 3.6. On the left (right) panel we show the ratio of the coherent (full lines) and the incoherent (dashed lines) contributions to the total trident cross section for an incoming flux of $\nu_\mu(\nu_e)$ as a function of E_ν for an ${}^{40}\text{Ar}$ target.

target for an incoming ν_μ (left) and ν_e (right) neutrino. We can see that the coherent regime dominates at all neutrino energies when there is an electron in the final-state, especially in the dielectron case. This can be explained by noting that the Q^2 necessary to create an electron pair is smaller than the one needed to create a muon; thus, coherent scattering is more likely to occur for this mode. Conversely, as one needs larger momentum transferred to produce a muon (either accompanied by an electron or another muon) the incoherent regime becomes more likely in these modes, as we can explicitly see in Fig. 3.6. Because of this effect the incoherent contribution is $\lesssim 10\%$, except for the dimuon channel where it can be between 30 and 40% in most of the energy region. Furthermore, when we compare the two incoming types of neutrinos, we see that for an incoming ν_μ the incoherent contribution is larger than the coherent one in the range $0.3 \text{ GeV} \lesssim E_\nu \lesssim 0.8 \text{ GeV}$, while for an incoming ν_e this never happens. This difference can be explained by the fact that CC and NC contributions are simultaneously present for the scattering of an initial ν_μ creating a muon pair, whereas for an initial ν_e creating a muon pair, we will only have the NC contribution, see Table 3.1.

An important difference between the coherent and incoherent regimes will be in their hadronic signatures in the detector. Neutrino trident production is usually associated with zero hadronic energy at the vertex, a feature that proved very useful in reducing backgrounds in previous measurements. Whilst this is a natural assumption for the

coherent regime, it need not be the case in the incoherent one. In fact, in the latter it is likely that the struck nucleon is ejected from the nucleus in a significant fraction of events with Q exceeding the nuclear binding energy⁸. Since the dominant incoherent contribution comes from scattering on protons, these could then be visible in the detector if their energies are above threshold. On the other hand, the struck nucleon is subject to many nuclear effects which may significantly affect the hadronic signature, such as interactions of the struck nucleon in the nuclear medium as well as reabsorption. Our calculation of Pauli blocking, for example, shows large suppressions ($\sim 50\%$) precisely in the low Q^2 region, usually associated with no hadronic activity. This then raises the question of how well one can predict the hadronic signatures of incoherent events given the difficulty in modelling the nuclear environment. We therefore do not commit to an estimate of the number of incoherent events that would have a coherent-like hadronic signature, but merely point out that this might introduce additional uncertainties in the calculation, especially in the $\mu^+\mu^-$ channel where the incoherent contribution is comparable to the coherent one. Finally, from now on we will refer to the number of trident events with no hadronic activity as coherent-like, where this number can range from coherent only to coherent plus all incoherent events.

3.4 Trident Events in LAr Detectors

In this section we calculate the total number of expected trident events for some present and future LAr detectors with different fiducial masses, total exposures and beamlines. In Table ?? we specify the values used for each set-up and in Fig. ?? we show the total production cross section for each neutrino trident mode of Table 3.1 as well as the neutrino fluxes as a function of E_ν at the position of each experiment.

⁸The peak of our incoherent Q^2 distributions happens at around $Q \approx 300$ MeV, much beyond the typical binding energy for Ar (see Appendix ??). Without Pauli suppression, however, we expect this value to drop.

3.4.1 Event Rates

The total number of trident events, N_X^Ψ , expected for a given trident mode at any detector is written as

$$N_X^\Psi = \text{Norm} \times \int dE_\nu \sigma_{\nu X}(E_\nu) \frac{d\phi_\nu(E_\nu)}{dE_\nu} \epsilon(E_\nu), \quad (3.4.1)$$

where $\sigma_{\nu X}$ can be the trident total ($X = \mathcal{N}$), coherent ($X = c$) or incoherent ($X = d$) cross sections for a given mode, ϕ_ν is the flux of the incoming neutrino and $\epsilon(E_\nu)$ is the efficiency of detection of the charged leptons. In the calculations of this section, we assume an efficiency of 100%⁹. The normalization is calculated as

$$\text{Norm} = \text{Exposure [POT]} \times \frac{\text{Fiducial Detector Mass} \times N_A}{m_T} [\text{target particles}],$$

where m_T is the molar mass of the target particle and N_A is Avogadro's number. Two features of the cross sections are important for the event rate calculation: threshold effects, especially for channels involving muons in the final-state, and cross section's growth with energy. In particular, we expect higher trident event rates for experiments with higher energy neutrino beams.

We start our study with the three detectors of the SBN program, one of which, μ BooNE, is already installed and taking data at Fermilab. These three LAr time projection chamber detectors are located along the Booster Neutrino Beam line which is by now a well-understood source, having the focus of active research for over 15 years. Although the number of trident events expected in these detectors is rather low, they may offer one of the first opportunities to study trident events in LAr, as well as to better understand their backgrounds in this medium and to devise improved analysis techniques. After that we study the proposed near detector for DUNE. This turns out to be the most important LAr detector for trident production since it will provide the highest number of events in both neutrino and antineutrino modes. Finally, having in mind the novel flavour composition of neutrino beams from muon facilities, we investigate trident rates at a 100 t LAr detector for the ν STORM project. This last facility could offer a very well understood neutrino beam with as many electron neutrinos as muon antineutrinos from muon decays, creating new possibilities for trident scattering measurements.

⁹See Section C for a discussion on the detection efficiencies for trident events and backgrounds.

Channel	SBND	μ BooNE	ICARUS	DUNE ND	ν STORM ND
$\nu_\mu \rightarrow \nu_e e^+ \mu^-$	10	0.7	1	2844 (235)	159
	1	0.08	0.1	369 (33)	18
$\bar{\nu}_\mu \rightarrow \bar{\nu}_e e^- \mu^+$	0.4	0.02	0.04	122 (2051)	23
	0.04	0.003	0.004	16 (262)	3
$\nu_e \rightarrow \nu_\mu e^- \mu^+$	0.05	0.003	0.004	22 (7)	9
	0.008	0.0005	0.0008	5 (1)	2
$\bar{\nu}_e \rightarrow \bar{\nu}_\mu e^+ \mu^-$	0.005	0.0003	0.0005	5 (14)	—
	0.001	0.0001	0.0001	1 (3)	—
Total $e^\pm \mu^\mp$	10	0.7	1	2993 (2307)	191
	1	0.1	0.1	391 (299)	23
$\nu_\mu \rightarrow \nu_\mu e^+ e^-$	6	0.4	0.7	913 (58)	73
	0.2	0.04	0.02	57 (5)	3
$\bar{\nu}_\mu \rightarrow \bar{\nu}_\mu e^- e^+$	0.2	0.01	0.02	34 (695)	9
	0.01	0.001	0.002	2 (41)	0.5
$\nu_e \rightarrow \nu_e e^- e^+$	0.2	0.01	0.02	50 (13)	32
	0.01	0.001	0.002	4 (1)	2
$\bar{\nu}_e \rightarrow \bar{\nu}_e e^+ e^-$	0.02	0.001	0.002	10 (34)	—
	0.0009	0.0001	0.0002	1 (2)	—
Total $e^+ e^-$	6	0.4	0.7	1007 (800)	114
	0.2	0.0	0.02	64 (49)	6
$\nu_\mu \rightarrow \nu_\mu \mu^+ \mu^-$	0.4	0.03	0.04	271 (32)	9
	0.3	0.03	0.04	135 (14)	5
$\bar{\nu}_\mu \rightarrow \bar{\nu}_\mu \mu^- \mu^+$	0.01	0.001	0.001	14 (177)	2
	0.01	0.0009	0.001	7 (93)	1
$\nu_e \rightarrow \nu_e \mu^+ \mu^-$	0.002	0.0001	0.0001	1 (0.5)	0.4
	0.001	0.0001	0.0001	0.5 (0.2)	0.2
$\bar{\nu}_e \rightarrow \bar{\nu}_e \mu^+ \mu^-$	0.0002	0.0000	0.0000	0.3 (0.9)	—
	0.0001	0.0000	0.0000	0.1 (0.3)	—
Total $\mu^+ \mu^-$	0.4	0.0	0.0	286 (210)	11
	0.3	0.0	0.0	143 (108)	6

Tab. 3.2. Total number of **coherent** (top row) and **incoherent** (bottom row) trident events expected at different LAr experiments for a given channel. The numbers in parentheses are for the antineutrino running mode, when present. These calculations considered a detector efficiency of 100%.

The SBN Program The SBN Program at Fermilab is a joint endeavour by three collaborations ICARUS, μ BooNE and SBND to perform searches for eV-sterile neutrinos and study neutrino-Ar cross sections [84]. As can be seen in Tab. ??, SBND has the shortest baseline (110 m) and therefore the largest neutrino fluxes (shown in Fig. ?? and taken from Fig. 3 of [84]). The largest detector, ICARUS, is also the one with the longest baseline (600 m) and consequently subject to the lowest neutrino fluxes. The ratio between the fluxes at the different detectors are $\phi_{\mu\text{BooNE}}/\phi_{\text{SBND}} = 5\%$ and $\phi_{\text{ICARUS}}/\phi_{\text{SBND}} = 3\%$. The neutrino beam composition is about 93% of ν_μ , 6% of $\bar{\nu}_\mu$ and 1% of $\nu_e + \bar{\nu}_e$.

Considering the difference in fluxes and the total number of targets in each of these

detectors, one can estimate the following ratios of trident events: $N_{\mu\text{BooNE}}^{\Psi}/N_{\text{SBND}}^{\Psi} \sim 8\%$ and $N_{\text{ICARUS}}^{\Psi}/N_{\text{SBND}}^{\Psi} \sim 10\%$. Unfortunately, since the fluxes are peaked at a rather low energy ($E_{\nu} \lesssim 1 \text{ GeV}$), where the trident cross sections are still quite small ($\lesssim 10^{-42} \text{ cm}^2$) we expect very few trident events produced. The exact number of trident events for those detectors according to our calculations is presented in Tab. 3.2. For each trident channel the first (second) row shows the number of coherent (incoherent) events. As expected, less than a total of 20 events across all channels can be detected by SBND, and a negligible rate of events is expected at μBooNE and ICARUS.

DUNE Near Detector The DUNE experiment will operate with neutrino as well as antineutrino LBNF beams produced by directing a 1.2 MW beam of protons onto a fixed target [85, 86]. The design of the near detector is not finalised, but the current designs favour a mixed technology detector combining a LAr TPC with a larger tracker module. In this work, we will assume that DUNE ND is a LAr detector located at 574 m from the target with a fiducial mass of 50 t [106]. As the trident event rate scales with the density of the target, any tracker module will not significantly influence the total event rate, and does not feature in our estimates; although, its presence is assumed to improve reconstruction of final-state muons. Our estimates can be easily scaled for the final design by using Eq. (3.4.1).

For the first 6 years of data taking (3 years in the neutrino plus 3 years in the antineutrino mode) the collaboration expects $1.83 \times 10^{21} \text{ POT/year}$ with a plan to upgrade the beam after the 6th year for 2 extra years in each beam mode with double exposure, making a total of $1.83 \times (3 + 2 \times 2) \times 10^{21} \text{ POT}$ for each mode [107]. We will assume the total 10-year exposure in our calculations. . as the relevant fluxes at the DUNE ND location (see Fig. ??). The beam composition of the neutrino (antineutrino) beam is about 96% ν_{μ} ($\bar{\nu}_{\mu}$), 4% $\bar{\nu}_{\mu}$ (ν_{μ}) and 1% $\nu_e + \bar{\nu}_e$.

The number of trident events for DUNE ND can be found in Tab. 3.2. The numbers in parentheses correspond to antineutrino beam mode. Note that although the trident cross sections are the same for neutrinos and antineutrinos, the fluxes are a bit lower for the antineutrino beam, as a consequence we predict a lower event rate for this beam¹⁰. Due

¹⁰A similar difference will apply to the processes constituting the background to the trident process, although there is an additional suppression in many channels due to the lower antineutrino cross sections.

to the much higher energy and wider energy range of the neutrino fluxes at DUNE ND, as compared to the SBN detectors, DUNE can observe a considerable number of trident events, about 300 times the number of trident events expected for SBND just in the neutrino mode. Moreover, the subdominant component of each beam mode will also contribute to the signal. For example, we expect to observe 2051 trident events in the $\bar{\nu}_\mu \rightarrow \bar{\nu}_e e^- \mu^+$ channel in the antineutrino mode. However, we also expect 235 events in the $\nu_\mu \rightarrow \nu_e e^+ \mu^-$ channel produced by the subdominant component of ν_μ in the antineutrino beam. We have considered 100% detection efficiency here, however, we will see in Sec. 3.4.2 that after implementing hadronic vetos, detector thresholds and kinematical cuts to substantially reduce the background we expect an efficiency of about 47%-65% on coherent tridents, depending on the channel (see Tab. 3.4).

The mixed flavour trident channel is the one with the highest statistics (more than 6000 events adding neutrino and antineutrino beam modes), 11% of which are produced by incoherent scattering. The dielectron channel comes next with a total of a bit more than 1900 events, 5% of which are produced by incoherent scattering. Although the dimuon channel is the less copious one, with only about 750 events produced, almost 34% of these events are produced by a incoherent process. This can be understood by recalling our discussions in Sec. 3.3.3.

Finally, we note that a dedicated high-energy run at DUNE has been mooted, to be undertaken after the full period of data collecting for the oscillation analysis. Thanks to the higher energies of the beam, this has the potential to see a significant number of neutrino tridents, provided it can collect enough POTs.

ν STORM In this section we study the trident rates for a possible LAr detector for the proposed ν STORM experiment [87, 88]. The ν STORM facility is based on a neutrino factory-like design and has the goal to search for sterile neutrinos and study neutrino nucleus cross sections [108]. Although this proposal is in its early days, ν STORM has the potential to make cross section measurements with unprecedented precision. In its current design, 120-GeV protons are used to produce pions from a fixed target with the pions subsequently decaying into muons and neutrinos. The muons are captured in a storage ring and during repeated passes around the ring they decay to produce neutrinos. Consequently, the storage ring is an intense source of three types of neutrino flavours:

ν_μ from π^+ and K^+ decays, which will be more than 99% of the total flux, ν_e and $\bar{\nu}_\mu$ from recirculated muon decays which will comprise less than 1% of the total flux. An important point, however, is that the neutrinos coming from the pion and kaon decays can be separated by event timing from the ones produced by the stored muons. This distinction allows the ν_μ flux to be studied almost independently from the $\bar{\nu}_\mu$ and ν_e flux. In addition, it implies after the initial flash of meson-derived events, that the flux consists of as many electron neutrinos as muon antineutrinos. We will assume a LAr detector for ν STORM at a baseline of 50 m with 100 t of fiducial mass with an exposure of 10^{21} POT. The neutrino fluxes, assuming a central μ^+ momentum of 3.8 GeV/c in the storage ring, are taken from Ref. [88] and are shown in Fig. ??.

In Tab. 3.2, we show the results of our calculations for ν STORM. More than 97% of the events from the incoming ν_μ are from pion decays and only less than 3% from kaon decays. Since we only consider the decay of mesons with positive charges and we expect neutral and wrong charge contamination to be small, we do not have trident events from incoming $\bar{\nu}_e$. The total number of mixed flavour, dielectron and dimuon channel events is, respectively, 214, 120 and 17, much less than what can be achieved at the larger neutrino energies available at the DUNE ND. The novel flavour structure of the beam does enhance the contribution of ν_e induced tridents with respect to the $(\bar{\nu}_\mu)$ ones, but this contribution only becomes dominant for the e^+e^- tridents in the muon decay events. Finally, we emphasize that the experimental design parameters for ν STORM are far from definite. Increasing the energy of stored muons and the size of the detector are both viable options which could significantly enhance the rates we present.

3.4.2 Background Estimates for Neutrino Trident in LAr

The study of any rare process is a struggle against both systematic uncertainties in the event rates and unavoidable background processes. True dilepton signatures are naturally rare in neutrino scattering experiments, but with modest rates of particle misidentification a non-trivial background arises. In this section we estimate the background to trident processes in LAr and its impact on the trident measurement. We perform our analysis only for DUNE ND, in neutrino and antineutrino mode, but our results are expected to be broadly applicable to other LAr detectors. We have generated a sample of 1.1×10^6

background events using GENIE [89] for incident electron and muon flavour neutrinos and antineutrinos. It is worth noting, however, that this event sample will in fact be smaller than the total number of neutrino interactions expected in the DUNE ND. Our goal, therefore, will be to demonstrate that with modest analysis cuts background levels can be suppressed significantly such that they become comparable to or smaller than the signals we are looking for. In the absence of events that satisfy our background definition, we argue that the frequency of that type of event is less than one in 1.1×10^6 interactions of the corresponding initial neutrino.

To account for misreconstruction in the detector, we implement resolutions as a gaussian smear around the true MC energies and angles. We assume relative energy resolutions as $\sigma/E = 15\%/\sqrt{E}$ for e/γ showers and protons, and $6\%/\sqrt{E}$ for charged pions and muons. Angular resolutions are assumed to be 1° for all particles (proton angles are never smeared in our analysis). The detection thresholds are a crucial part of the analysis, since for many channels one ends up with very soft electrons. We take thresholds to be 30 MeV for muons and e/γ showers kinetic energy, 21 MeV for protons and 100 MeV for π^\pm [86].

Background Candidates

We focus on three final-state charged lepton combinations: $\mu^+\mu^-$, $\mu^\pm e^\mp$ and e^+e^- . Genuine production of these states is possible in background processes, but usually rare, deriving from meson resonances or other prompt decays. The majority of the background is expected to be from particle misidentification (misID). We assume that protons can always be identified above threshold and that neutrons leave no detectable signature in the detector. In addition, we require no charge ID capabilities from the detector and assume that the interaction vertex can always be reconstructed. Under these assumptions, we have incorporated three misidentifications which will affect our analysis, and give our naive estimates for their rates in Tab. 3.3. Any other particle pairs are assumed to be distinguishable from each other when needed.

The requirement of no hadronic activity helps constrain the possible background processes, but one is still left with significant events with invisible hadronic activity and other coherent neutrino-nucleus scatterings. These are then reduced by choosing appropriate cuts on physical observables, exploring the discrepancies between our signal and the background.

misID	Rate
γ as e^\pm	0.05
γ as e^+e^-	0.1 (w/ vertex) 1 (no vertex + overlapping)
π^\pm as μ^\pm	0.1

Tab. 3.3. Assumed misID rates for various particles in a LAr detector. We take these values to be constant in energy.

In our GENIE analysis, we include all events that have final-states identical to trident, or that could be interpreted as a trident final-state considering our proposed misID scenarios. Our dominant sources of background for $\mu^+\mu^-$ tridents are ν_μ -initiated charged-current events with an additional charged pion in the final-state ($\nu_\mu CC1\pi^\pm$). For e^+e^- tridents, the most important processes are neutral current scattering with a π^0 (NC π^0), while for mixed $e^\pm\mu^\mp$ tridents, the ν_μ -initiated charged-current events with a final-state π^0 (CC π^0) dominate the backgrounds. In each case, the pion is misidentified to mimic the true trident final-state. Other relevant topologies include charm production, CC γ and $\nu_e CC\pi^\pm$. For a detailed discussion of these backgrounds processes we refer the reader to Appendix 3.6.

Estimates for the DUNE ND

In this section we provide estimates for the total background for each trident final-state for the DUNE ND. The number of total inclusive CC interactions in the 50 t detector due to neutrinos of all flavours is calculated to be 5.18×10^8 . We scale our background event numbers to match this, and argue that one has to reach suppressions of order $10^{-6} - 10^{-5}$ to have a chance to observe trident events. Whenever our cuts remove all background events from our sample, we assume the true background rate is one event per 1.1×10^6 ν interactions and scale it to the appropriate number of events in the ND, applying the misID rate whenever relevant. Within our framework, this provides a conservative estimate as the true background is expected to be smaller.

Our estimates are shown in Table 3.4. We start with the total number of background candidates N_B^{misID} , using only the naive misID rates shown in Table 3.3. These are much larger than the trident rates we expect, by at least 2 orders of magnitude. Next, we veto any hadronic activity at the interaction vertex, obtaining N_B^{had} . We emphasize that this veto also affects the incoherent tridents in a non-trivial way, and therefore we remain

agnostic about the hadronic signature of these. Finally, one can look at the kinematical distributions of coherent trident in Section C and try to estimate optimal one dimensional cuts for the DUNE ND based on the kinematics of the final-state charged leptons. This is a simple way to explore the striking differences between the peaked nature of our signal and the smoother background. In a real experimental setting it is desirable to have optimization methods for isolating signal from background, preferably with a multivariate analyses. However, even in our simple analysis, cutting on the small angles to the beamline and the low invariant masses of our trident signal can achieve the desired background suppressions. For the $\mu^+\mu^-$ tridents we show the effect of our cuts in Fig. 3.7. The cuts are defined to be $m_{\mu^+\mu^-}^2 < 0.2 \text{ GeV}^2$, $\Delta\theta < 20^\circ$, $\theta_\pm < 15^\circ$. The kinematics is very similar in the other trident channels, with slightly less forward distributions for electrons. For the e^+e^- channel we take $m_{e^+e^-}^2 < 0.1 \text{ GeV}^2$, $\Delta\theta < 40^\circ$ and $\theta_\pm < 20^\circ$. The asymmetry between the positive and negative charged leptons is visible in the distributions, where the latter tends to be more energetic. This feature was not explored in our cuts, as it is not significant enough to further improve background discrimination. In the mixed flavour tridents, however, one sees a much more pronounced asymmetry. The muon tends to carry most of the energy and be more forward than the electron, which can make the search for this channel more challenging due to the softness of the electron in the high energy event. Nevertheless, the low invariant masses and forward profiles can still serve as powerful tool for background discrimination, provided the event can be well reconstructed. We assume that is the case here and use the following cuts on the background: $m_{e^\pm\mu^\mp}^2 < 0.1 \text{ GeV}^2$, $\Delta\theta < 20^\circ$, $\theta_e < 40^\circ$ and $\theta_\mu < 20^\circ$. When performing kinematical cuts, we also include the effects of detection thresholds after smearing. For a discussion on the impact of these thresholds on the trident signal see Section C.

The resulting signal efficiencies due to our cuts and thresholds are shown in the last two columns of Table 3.4. One can see that these are all $\approx 50\%$ or greater for our coherent samples, whilst all background numbers remain much below the trident signal. The incoherent samples are also somewhat more affected by our cuts than the coherent ones. If one is worried about the contamination of coherent events by incoherent ones, then the kinematics of the charged leptons alone can help reduce this, independently of the hadronic energy deposition of the events. For instance, in the case where all $\mu^+\mu^-$ incoherent events appear with no hadronic signature, then after our cuts the incoherent

Channel	$N_B^{\text{misID}}/N_{\text{CC}}$	$N_B^{\text{had}}/N_{\text{CC}}$	$N_B^{\text{kin}}/N_{\text{CC}}$	$\epsilon_{\text{sig}}^{\text{coh}}$	$\epsilon_{\text{sig}}^{\text{dif}}$ ¹¹
$e^\pm \mu^\mp$	$1.67 (1.62) \times 10^{-4}$	$2.68 (4.31) \times 10^{-5}$	$4.40 (3.17) \times 10^{-7}$	0.61 (0.61)	0.39 (0.39)
$e^+ e^-$	$2.83 (4.19) \times 10^{-4}$	$1.30 (2.41) \times 10^{-4}$	$6.54 (14.1) \times 10^{-6}$	0.48 (0.47)	0.21 (0.21)
$\mu^+ \mu^-$	$2.66 (2.73) \times 10^{-3}$	$10.4 (9.75) \times 10^{-4}$	$3.36 (3.10) \times 10^{-8}$	0.66 (0.67)	0.17 (0.16)

Tab. 3.4. Reduction of backgrounds at the DUNE ND in neutrino (antineutrino) mode and its impact on the signal for each distinguishable trident final-state. N_B^{misID} stands for total backgrounds to trident after only applying misID rates, N_B^{had} are the backgrounds after the hadronic veto, and N_B^{kin} reduce the latter with detection thresholds and kinematical cuts (see text for the cuts chosen). These quantities are normalized to the total number of CC interactions in the ND N_{CC} (flavour inclusive). We also show the impact of our detection thresholds and kinematical cuts on the trident signal via efficiencies for coherent only ($\epsilon_{\text{sig}}^{\text{coh}}$) and incoherent only samples ($\epsilon_{\text{sig}}^{\text{dif}}$). We do not cut on the hadronic activity of incoherent events.

contribution is reduced from 41% to 15% of the total trident signal. This reduction is, however, also subject to large uncertainties coming from nuclear effects. In summary, the set of results above are encouraging, suggesting that the signal of coherent-like trident production is sufficiently unique to allow for its search at near detectors despite naively large backgrounds.

Finally, we comment on some of the limitations of our analysis. The low rate of trident events calls for a more careful evaluation of other subdominant processes that could be easily be overlooked. For channels involving electrons, it is possible that de-excitation photons and internal bremsstrahlung become a source of background, as these also produce very soft EM showers, none of which are implemented in GENIE. The question of reconstruction of these soft EM showers, accompanied either by a high energy muon or by another soft EM shower also would have to be addressed, especially in the latter case where a trigger for these soft events would have to be in place. A more complete analysis is also needed for treating the decay products of charged pions and muons produced in neutrino interactions, as well as rare meson decay channels (like the Dalitz decay of neutral pions $\pi^0 \rightarrow \gamma e^+ e^-$). Cosmic ray events are not expected to be a problem due to the requirement of a vertex and a correlation with the beam for trident events. Perhaps even more exotic processes, such as the production of three final-state charged leptons ($\nu_\alpha(\bar{\nu}_\alpha) + \mathcal{H} \rightarrow \ell_\alpha^-(\ell_\alpha^+) + \ell_\beta^+ + \ell_\gamma^- + \mathcal{H}'$), can also become relevant. For instance, radiative trimuon production [109] can potentially serve as a background to dimuon tridents if one of the muons is undetected. Similarly,

¹¹Despite the fact that many incoherent events will likely deposit hadronic energy in the detector, we quote the efficiency of our cuts on incoherent events with no assumptions on their hadronic signature.

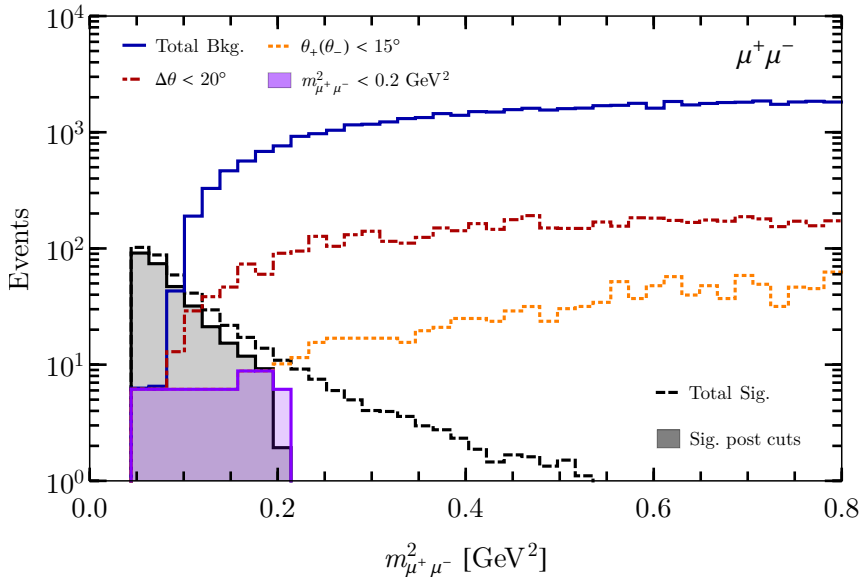


Fig. 3.7. Signal and background distributions in invariant mass. The total background events (blue) include the misID rates in table Table 3.3. We apply consecutive cuts on the background, starting with cuts on the separation angle $\Delta\theta$ (red), both charged lepton angles to the beamline (θ_+ and θ_-) (orange) and the invariant mass $m_{\mu^+\mu^-}^2$. We show the signal samples before and after all the cuts in dashed black and filled black, respectively.

production would fake a dielectron (mixed) trident signature if the muon (an electron) is missed. We are not aware of any estimates for the rate of these processes at the DUNE ND, but we note that their rate can be comparable to trident production at energies above 30 GeV [110]. Improvements on our analysis should come from the collaboration’s sophisticated simulations, allowing for a better quantification of hadronic activity, more realistic misID rates and more accurate detector responses.

3.5 Conclusions

Neutrino trident events are predicted by the SM, however, only $\bar{\nu}_\mu$ initiated dimuon tridents have been observed in small numbers, typically fewer than 100 events. This will change in the near future thanks to the current and future generations of precision neutrino scattering and oscillation experiments, which incorporate state-of-the-art detectors located at short distances from intense neutrino sources. In this work we discuss the calculation of the neutrino trident cross section for all flavours and hadronic targets, and provide estimates for the number and distributions of events at 9 current or future neutrino detectors: five detectors based on the new LAr technology (SBND, μ BooNE, ICARUS, DUNE ND and ν STORM ND) as well as four more conventional detectors (INGRID, MINOS ND, NO ν A

ND and MINER ν A). The search for tridents, however, need not be exclusive to near detectors of accelerator neutrino experiments. As pointed out by the authors of Ref. [78], atmospheric neutrino experiments can also look for these processes, benefiting from the increase of the cross section at large energies.

We have stressed the need for a full four-body phase space calculation of the trident cross sections without using the EPA. This approximation has been employed in recent calculations and can lead to overestimations of the cross section by 200% or more at the peak neutrino energies relevant for many accelerator neutrino experiments. Moreover, we show why the EPA is not applicable for computing trident cross sections, and provide the first quantitative assessment of this breakdown for coherent and incoherent hadronic regimes. We find that the breakdown of the approximation is most severe for processes with electrons in the final-state and for incoherent scattering of all final state flavours. For coherent dimuon production, the approximation can give a reasonable result at large neutrino energies. This is due to the nuclear form factors that serendipitously suppress those regions of phase space where the EPA is least applicable. We also demonstrated that the best results in this channel are achieved when applying artificial cuts to the phase space. However, even in this case, at energies relevant for the above experiments, the EPA can artificially suppress the coherent scattering contribution and increase the incoherent one giving rise to an incorrect rate and distributions of observable quantities. For instance, the invariant mass of the charged lepton pair $m_{\ell\ell}^2$ and their angular separation $\Delta\theta$ are more uniformly distributed for incoherent than for coherent trident scattering. Using the correct distributions is crucial to correctly disentangle the signal from the background by cutting on these powerful discriminators.

Our calculations show that DUNE ND is the future detector with the highest neutrino trident statistics, more than 6000 mixed events, 11% produced by incoherent scattering, more than 1900 dielectron events, 5% produced by incoherent scattering and about 750 dimuon events, almost 34% of those produced by a incoherent process. Making use of our efficiencies (see Table 3.4), assuming an ideal background suppression and neglecting systematic uncertainties, we quote the statistical uncertainty on the coherent-like flux averaged cross section for the DUNE ND. We do this for coherent only events and, in

brackets, for coherent plus incoherent events, yielding

$$\frac{\delta\langle\sigma^{e^\pm\mu^\mp}\rangle}{\langle\sigma^{e^\pm\mu^\mp}\rangle} = 1.8\% \text{ (1.6\%)}, \quad \frac{\delta\langle\sigma^{e^+e^-}\rangle}{\langle\sigma^{e^+e^-}\rangle} = 3.4\% \text{ (3.3\%)} \quad \text{and} \quad \frac{\delta\langle\sigma^{\mu^+\mu^-}\rangle}{\langle\sigma^{\mu^+\mu^-}\rangle} = 5.5\% \text{ (5.1\%).}$$

In this optimistic framework we expect the true statistical uncertainty on coherent-like tridents to lie between the two numbers quoted, depending on how many incoherent events contribute to the coherent-like event sample. This impressive precision would provide unprecedented knowledge of the trident process and the nuclear effects governing the interplay between coherent and incoherent regimes. We emphasize, however, that given these small values for the relative uncertainties, the trident cross section will likely be dominated by systematic uncertainties from detector response and backgrounds which are not modelled here.

For DUNE ND, we have studied the distribution of observables which could help distinguish trident events from the background. We have estimated the background for each trident channel via a Monte Carlo simulation using GENIE, and identified the dominant contributions arising primarily from particle misidentification. We conclude that reaching background rates of the order $\mathcal{O}(10^{-6} - 10^{-5})$ times the CC rate is necessary to observe trident events at DUNE ND, and given the distinctive kinematic behaviour of the trident signal a simple cut-based GENIE-level analysis suggests that this is an attainable goal in a LAr TPC.

Existing facilities may also be able to make a neutrino trident measurement at their near detectors. Despite not including reconstruction efficiencies nor an indication of the impact of backgrounds, we find that the largest trident statistics is available at INGRID, the T2K on-axis near detector. We predict about 660 (1700) events for the mixed flavour, 300 (770) events for the dielectron and 50 (130) events for the dimuon channel for T2K-I (T2K-II). The more fine-grained near detector of MINOS and MINOS+ is also expected to have collected a significant numbers of events during its run. As such, the very first measurement of neutrino trident production of mixed and dielectron channels may be at hand.

3.6 Individual Backgrounds

Here we discuss backgrounds to trident final-states in more detail. We start by motivating our misID rates shown in Table 3.3, and then discuss the dominant background processes individually.

In LAr photons can be distinguished from a single electron if their showers start displaced from the vertex (if present). Photons have a conversion length in LAr of around 18 cm, meaning 5–10% could be expected to convert quickly enough to hinder electron-photon discrimination by this means if the resolution on the gap is from 1–2 cm [111]. Once pair conversion happens, photons can be distinguished from a single electron purely by dE/dx measurements in the first 1–2 cm of their showers. Motivated by the success of this method as shown at ArgoNeuT [111] and based on projections for DUNE [85], we assume that 5% of photons would be taken as e^\pm with perfect efficiency, without the need for an event vertex. Needless to say that a dedicated study for trident topologies would be necessary for a more complete study. It is worth noting that our remarks concern only the misID of a single photon for a single electron, whilst the distinction between a photon and an overlapping e^+e^- pair without a vertex can be much more challenging. For this reason we take the misID rate between an overlapping e^+e^- pair and a photon to be 1 in the absence of a vertex.

Charged pions are notorious for faking long muon tracks. We estimate this misID rate as arising from through-going pions, which do not exhibit the decay kink used in their identification. We assume an interaction length of around 1 m, meaning that about 5% of particles travel ~ 3 meters and escape the fiducial volume. Assuming that this is the most likely way a pion can spoof a muon, we estimate a naive suppression rate of 10^{-2} . In a more complete study, it is desirable to explore the length of the muon and pion tracks inside the detector as a function of energy. The length of the contained tracks can also be an important tool for background suppression which we leave to future studies.

3.6.1 Pion Production

Coherent pion production in its charged ($\nu + A \rightarrow \ell^\mp + \pi^\pm + A$) and neutral ($\nu + A \rightarrow \nu + \pi^0 + A$) current version is very abundant at GeV energies. The cross section for these

processes is modelled in GENIE using a modern version of the Rein-Sehgal model [112, 113]. The charged current version serves mainly as a background to $\mu^+\mu^-$ tridents, but can also appear as a background for $e^\pm\mu^\mp$ tridents for incoming electron neutrinos or antineutrinos. It has been studied before at MiniBooNE [114], MINER ν A [115, 116], T2K [92, 117], and for the first time in LAr at ArgoNeuT [118]. This process has a very distinct low 4-momentum transfer to the nucleus $|t|$ [115], but a much flatter distribution in invariant mass if compared to trident. The neutral current version of coherent pion production serves as a background to e^+e^- tridents. This process has been studied before by the MiniBooNE [119], SciBooNE [120] and in LAr by the ArgoNeuT collaboration [121]. There are two possibilities for these events to fake an e^+e^- trident: when one of the gammas produced in the π^0 decay is missed and the other is misIDed for an overlapping e^+e^- pair, and when both photons are each misIDed for a single electron. This signature also comes with low hadronic activity, but for separated visible photons the invariant mass is a natural discriminator, as in the detector $m_{\gamma\gamma} \approx m_{\pi^0}$.

Resonant pion production can also contribute to trident backgrounds in the absence of any reconstructed protons. Resonant pion production can be larger than its coherent counterpart and is modelled in GENIE by the Rein-Sehgal model [122]. Its CC version was measured by MiniBooNE [114], K2K [123], MINOS [96], and MINER ν A [94]. In the latter measurement one can clearly see the large number of events with undetected protons. The misIDed photon and the charged lepton invariant mass are once more flatter than the trident ones, allowing for a kinematical discrimination whenever a single photon is undetected. It is worth noting that these are some of the dominant underlying processes for pion production in GENIE, but all events leading to topologies relevant for trident are included in our analysis.

3.6.2 Charm Production

Since the first observation of dimuon pairs from charm production in neutrino interaction by the HPWF experiment in 1974 [124], a lot has been learned about these processes (see [125] for a review) in neutrino experiments. Particularly, the production of charm quarks and their subsequent weak decays into muons or electrons have been identified as a major source of background for early trident searches. At the lower neutrino energies at

DUNE, however, this is expected to be a smaller yet non-negligible contribution. From our GENIE samples, we estimate that a charmed state is produced at a rate of around $10^{-4}(N_{CC} + N_{NC})$. Most of these produce either D mesons, Λ_c or Σ_c baryons. These particles decay in chains, emitting a muon with a branching ratio of around 0.1, and are always accompanied by pions or other hadronic particles. We therefore expect these rates to be negligible with a hadronic veto, and do not consider them further. We hope, however, that future studies will address these channels in more detail.

3.6.3 CC γ and NC γ

The emission of a single photon alongside a CC process could be a background for μe tridents if the photon is misIDed as a single electron. When the photon is produced in a NC event, it can be a background to overlapping e^+e^- tridents. In GENIE, these topologies arise mainly due to resonance radiative decays and from the intra-nuclear processes. For this reason, it usually comes accompanied with extra hadronic activity. For hadronic resonances, we have simulated CC processes in GENIE and estimated the multiplicities: 0.5% single photon and 1% double photon emission from CC rates. Radiative photon production from the charged lepton, on the other hand, does not need to come accompanied by hadrons. It is phase space and $\alpha \approx 1/137$ suppressed with respect to CCQE rates, and therefore could occur at appreciable rates compared to our signal. This contribution, however, is not included in GENIE and is absent from our samples. The rates of internal photon bremsstrahlung have been estimated before, particularly for T2K where a low-energy photon is an important background for electron appearance searches [126], and as a background to the low energy events at MiniBooNE [127]. De-excitation gammas from the struck nuclei can also generate CC γ or NC γ topologies [128]. These contributions for Ar are not included in GENIE, but are expected to come with a distinct energy profile, which can be tagged on.

Chapter 4

New fundamental forces at DUNE

4.1 Introduction

The discovery of neutrino oscillation is the first laboratory-based proof of physics Beyond the Standard Model (BSM) establishing that, in contrast to the predictions of the Standard Model (SM), the neutrino sector has at least three mass eigenstates distinct from the flavour states defined by the charged-leptons. However, the mechanism which generates neutrino masses remains unknown and many competing candidate theories exist, ranging from the simplicity of a Dirac mass term protected by a symmetry (see *e.g.* [129–131]) or the popular see-saw mechanisms [132–140] to proposals with a more elaborate spectrum of particles. In general, more elaborate scenarios have additional motivations, including the explanation of lepton mass and flavour hierarchies (see *e.g.* [141]), the matter-antimatter asymmetry of the universe [142–144], the existence of dark matter [145, 146], the scale of neutrino masses [147–149] or anomalous experimental results [150]. Uncovering the nature of new physics in the neutrino sector, and its connection to other BSM concerns, will be a central aim of the experimental and theoretical programs over the next few decades.

Although significant progress has already been made, the neutrino sector remains relatively poorly explored. There are still large uncertainties on the masses and on some of the mixing parameters of the light neutrinos [151], but even beyond the effects of neutrino mass, many SM cross sections are poorly known theoretically and infrequently measured. This is in part due to the typical energy scales of neutrino experiments which necessitate the modelling of the neutrino-nucleus interactions, but also because of the rareness of neutrino scattering

(see Ref. [152]). Much effort has gone into measuring crucial cross sections at oscillation experiments [91, 153, 154] and at the Main Injector Experiment for ν -A (MINER ν A) [155], a dedicated cross section experiment. However, given the necessity and potential richness of BSM physics in the neutrino sector, and the wide array of measurements yet to be made, it is conceivable that new physics will also manifest itself as detectable signatures in neutrino scattering. It is crucial to keep an open mind about what future experimental work might find, for instance, in the auxiliary physics program of the Near Detector (ND) of the next-generation Deep Underground Neutrino Experiment (DUNE) [156].

Novel interactions in the neutrino sector have been proposed for a variety of reasons, including as a potentially observable effect in the neutrino oscillation probabilities (see *e.g.* [157]), as a way of ameliorating tension introduced by sterile neutrinos in the early universe [158–165], and as a possible explanation of anomalous results at short baseline [166–168]. Models which introduce new interactions between neutrinos and matter have been discussed in simplified settings [169–171], via Effective Field Theory [80, 172] and specific UV complete models [173] (see also [174] for a neutrophilic Z' study at the DUNE ND). One class of models restricts the new interactions to leptons. This arises most naturally in settings with a gauged subgroup of lepton number, with most attention given to the anomaly free subgroups $L_\alpha - L_\beta$ for $\alpha, \beta \in \{e, \mu, \tau\}$ [175, 176]. Such leptophilic interactions must satisfy strong constraints from processes involving charged-leptons [177], but in the case of a gauged $L_\mu - L_\tau$ symmetry, neutrino processes have been found to be particularly competitive [178].

In this work, we study potential constraints which can be placed on a general set of leptophilic Z' models in the two most likely scattering channels for this type of BSM at the near detector of DUNE: $\nu - e$ scattering and $\nu \ell \ell$ trident scattering. During ten years of running, a 75-t near detector subjected to the intense neutrino beam at the Long-Baseline Neutrino Facility (LBNF) will provide tens of thousands of $\nu - e$ scattering events. The cross section for this process is theoretically well understood and can therefore be a sensitive probe of BSM physics. Additionally, this process has received special interest due to its potential in reducing systematic uncertainties in the neutrino flux [179, 180], an undertaking which can be affected by new physics. Despite not being a purely leptonic process, neutrino trident production can also be measured with reasonable precision at

DUNE, where hundreds of coherent and diffractive trident events are expected at the ND [181]. We study the neutral current channels with dielectron or dimuon final states, pointing out how the new physics contribution impacts the non-trivial kinematics of these processes. The main advantage in such measurements lies on the flavour structure of dimuon tridents, which can be used to constrain otherwise difficult to test models, such as the one where a new force is associated to the $L_\mu - L_\tau$ gauge symmetry [178].

Although these processes can place stringent bounds on many classes of mediators, many scenarios are already heavily constrained through other experimental work. A recent study of several different $U(1)_X$ models using $\nu - e$ scattering was presented in Ref. [62], where data from past $\nu - e$ experiments CHARM-II, GEMMA and TEXONO has been used to put bounds on the couplings and masses of general Z' 's. Novel charged particles are typically constrained to be very massive, leading to little enhancement of the charged current neutrino scattering rates. In particular, charged scalars have been considered in $\nu \ell \ell$ trident scattering in Ref. [79], where it is found that trident measurements can provide competitive bounds on charged scalars, albeit only in simplified theoretical settings. The requirement of doubly charged scalars or the connection to neutrino masses introduced by the typical UV completions of such models dilutes the relevance of the trident bounds. Neutral scalars are viable, but also present challenging UV completions. Novel Z' interactions in $\nu \ell \ell$ trident scattering with dimuon final states have been studied in Ref. [178], where it was shown to be a promising channel to probe a $L_\mu - L_\tau$ gauge symmetry. This model was revisited in Refs. [77] and [182], where the effects of kinetic mixing and the possibility of a measurement by T2K was alluded to. Finally, neutrino trident scattering with atmospheric neutrinos was shown to be sensitive to this model as well as to simplified scalar models in [183]. It should be noted, however, that as it was shown in Ref. [181] the Equivalent Photon Approximation (EPA) discussed in several recent studies [77, 79] for the calculation of the trident cross section leads to intolerably large errors in the predictions for the $\nu \ell \ell$ scattering channels in the SM. For this reason, we calculate this process without making this approximation.

The structure of the paper is as follows. In Section 4.2, we describe the basic properties of the leptophilic scenarios that we will consider in this work. In Section 4.3, we discuss the calculation of the trident and $\nu - e$ scattering cross sections in a general model of leptophilic

Z' . In Section 4.4, we show how DUNE can place bounds on a few popular leptophilic Z' models, discussing our assumptions for experimental configurations and backgrounds. We make our concluding remarks in Section 4.5.

4.2 Leptophilic Z' models

Since we are interested in models where the novel neutral currents are present only in the lepton sector, let us consider explicitly a $U(1)_{Z'}$ extension of the SM whose Lagrangian is given by

$$\mathcal{L} \supset -g' Z'_\mu \left[Q_\alpha^L \bar{L}_L^\alpha \gamma^\mu L_L^\alpha + Q_\alpha^R \bar{\ell}_R^\alpha \gamma^\mu \ell_R^\alpha + \sum_N Q_N \bar{N}_R \gamma^\mu N_R \right], \quad (4.2.1)$$

where L_α (ℓ_α) represents the leptonic $SU(2)$ doublet (singlet) of flavour $\alpha \in \{e, \mu, \tau\}$, and we included N right-handed neutrinos with charges Q_N under the new symmetry for completeness. Thus, we have $7 + N$ new parameters to characterize the couplings between the new boson and the lepton sector, one gauge coupling g' and $6 + N$ charges $\{Q_\alpha^L, Q_\alpha^R, Q_N\}$. Below the scale of the Electroweak Symmetry Breaking (EWSB), the relevant interaction terms in the Lagrangian are given by

$$\begin{aligned} \mathcal{L} \supset & -g' Z'_\mu [Q_\alpha^L \bar{\nu}_\alpha \gamma^\mu P_L \nu_\alpha + \frac{1}{2} \bar{\ell}_\alpha \gamma^\mu (Q_\alpha^V - Q_\alpha^A \gamma^5) \ell_\alpha \\ & + \sum_N Q_N \bar{N}_R \gamma^\mu N_R], \end{aligned} \quad (4.2.2)$$

where $Q_\alpha^V \equiv Q_\alpha^L + Q_\alpha^R$ and $Q_\alpha^A \equiv Q_\alpha^L - Q_\alpha^R$. We note that the right-handed singlets could modify the form of the neutrino interaction in Eq. (4.2.2) by introducing a right-chiral current. The details of this would depend on the relationship between these chiral states and the flavour-basis neutrino ν_α . However, in practice our Lagrangian is fully general, as the polarization effects in the neutrino beam ensure that only the left-handed charge is relevant for light-neutrino scattering experiments.

The Lagrangian in Eq. (5.4.1) contains all of the terms necessary for this analysis. However, when it comes to assigning specific charges to the particles, a few wider model-building considerations are worthy of discussion. In the SM, any non-vectorial symmetry would forbid the Yukawas responsible for the charged-lepton mass terms post-EWSB; similarly, possible negative implications for neutrino mass generation are expected. The precise implementation of the neutrino mass mechanism is highly model dependent, but neutrino

gauge charges are not compatible with many usual realizations¹. Furthermore, the novel gauge boson Z' will also require a mass generation mechanism, and indeed this could be achieved via the means of symmetry breaking. Although each of these is an important aspect of model building, their resolution can be expected to have little impact on the phenomenology of neutrino scattering, and we will not pursue them here. Anomaly freedom of our new symmetry, however, is a more pertinent concern. It has been shown that an anomalous group can always be made anomaly free via the introduction of exotically charged sets of fermions which can be given arbitrarily large masses [184]. Yet these novel fermionic states necessarily introduce effects at low-scales, which in some cases can strongly affect the phenomenology of the model [185]. Therefore, while it seems likely that mass generation can be addressed with the addition of new particles which do not interfere with neutrino scattering phenomenology, anomaly freedom is more pernicious. For this reason we will briefly discuss how anomaly freedom will dictate the types of leptonic symmetries that we consider in the remainder of this work.

Anomaly freedom. The most general anomaly-free symmetries compatible with the SM were first deduced in the context of Grand Unification Theories (GUT) [186, 187]. More recently, an atlas of all anomaly-free $U(1)$ extensions of the SM with flavour-dependent charges has been provided by Ref. [188]. Interestingly, the only anomaly-free subgroups of the SM with renormalisable Yukawa sector are leptophilic: the lepton-family number differences $L_\alpha - L_\beta$ ($\alpha, \beta = e, \mu, \tau$) [175, 176]. The popular $B - L$ symmetry is in fact anomalous unless right-handed SM singlets are added with the appropriate charges. This is well motivated by the necessity of neutrino mass generation but remains a hypothesis, as not all models of neutrino mass require novel fermionic content. For the sake of discussion, we follow a similar logic and consider the most general anomaly free subgroups of the SM accidental leptonic symmetries allowing for an arbitrary number of right-handed fermionic singlets. These would presumably be associated with the neutrino mass generation mechanism, but we impose no specific relations in this regard due to the significant model-building freedom. The anomaly conditions for a leptophilic model with right-handed

¹If neutrino masses are thought of as coming from a Weinberg operator, it is clear that the leptonic doublet must be uncharged under any unbroken $U(1)'$ group.

neutrinos are given below [189]²

$$\text{SU}(2)_W^2 \times \text{U}(1)_{Z'} \quad \sum_{\alpha} Q_{\alpha}^L = 0, \quad (4.2.3a)$$

$$\text{U}(1)_Y^2 \times \text{U}(1)_{Z'} \quad \sum_{\alpha} \left[\frac{1}{2} Q_{\alpha}^L - Q_{\alpha}^R \right] = 0, \quad (4.2.3b)$$

$$\text{U}(1)_Y \times \text{U}(1)_{Z'}^2 \quad \sum_{\alpha} \left[(Q_{\alpha}^L)^2 - (Q_{\alpha}^R)^2 \right] = 0, \quad (4.2.3c)$$

$$\text{U}(1)_{Z'}^3 \quad \sum_{\alpha} \left[2(Q_{\alpha}^L)^3 - (Q_{\alpha}^R)^3 \right] - \sum_N Q_N^3 = 0, \quad (4.2.3d)$$

$$\text{Gauge-Gravity} \quad \sum_{\alpha} \left[2Q_{\alpha}^L - Q_{\alpha}^R \right] - \sum_N Q_N = 0. \quad (4.2.3e)$$

In the absence of new N_R particles ($Q_N = 0$) and assuming that $Q_{\alpha}^L = Q_{\alpha}^R$, that is considering vector couplings, we find the three well-known discrete solutions for the Eqs. (4.2.3): the antisymmetric pairs $L_{\alpha} - L_{\beta}$, $\alpha, \beta = \{e, \mu, \tau\}$, $\alpha \neq \beta$. As far as anomalies are concerned, all three pairs are equal, but frequently focus falls on $L_{\mu} - L_{\tau}$, which has no coupling to electrons and correspondingly weaker constraints. If we reconsider these conditions with charged right-handed neutrinos, we find a one dimensional continuous family of potential symmetries which can be consistently gauged. We can parametrise this as

$$\varrho(L_{\alpha} - L_{\beta}) + \vartheta(L_{\beta} - L_{\lambda}), \quad (4.2.4)$$

with

$$3\varrho\vartheta(\vartheta - \varrho) = \sum_N Q_N^3. \quad (4.2.5)$$

What we have shown is that linear combinations of the $(L_{\alpha} - L_{\beta})$ choice of charges yield an anomaly free scenario provided N right-handed neutrinos respecting Eq. (4.2.5) are added to the theory. We have checked that the “anomaly-free atlas” in [190] contains a subset of these solutions, which are more general.

The above conclusions are based on the assumption of vectorial charge assignments. In the SM, this requirement is a consequence of the origin of mass assuming a chargeless Higgs. However, in non-minimal models this requirement could be relaxed. Even with this extra freedom, not all charge assignments are allowed: for example, a purely chiral $U(1)'$ cannot satisfy Eq. (4.2.3c) without additional matter charged under the SM gauge

²Notice that $\text{U}(1)_{Z'}^3$, together with gauge-gravity conditions imply that the number of right-handed states must be at least $N = 3$.

group. The axial-vector case, however, does have further solutions: we find that the same one-dimensional family of charges is allowed as for the vectorial gauge boson — in this case, the charges apply to the left-handed fields and the right-handed ones have the opposite charges. In such a model the leptonic mass generation mechanism would necessarily be more complicated than in the SM, but such a possibility is not excluded. UV completions of an axial-vector Z' have been presented in [191, 192], however, these generally introduce extra bounds that are expected to be stronger than neutrino scattering bounds (see *e.g.* [185, 193]). For this reason, we only comment on the consequences of an axial-vector case in our calculations, but do not develop any particular model or constraint.

Kinetic mixing. The symmetries of our SM extensions allow for kinetic mixing between the Z' and the SM gauge bosons [194–196]

$$\mathcal{L}_{\text{mix}} = -\frac{\varepsilon}{2} F_{\kappa\rho} F'^{\kappa\rho}, \quad (4.2.6)$$

where $F_{\kappa\rho}$ and $F'^{\kappa\rho}$ are the field strength tensors of the hypercharge and the Z' boson, respectively. The presence of such coupling introduces a very rich phenomenology and has been explored in great detail in the literature [197]. In this work, we choose to focus on the less constrained possibility of vanishing tree-level kinetic mixing. In this case, kinetic mixing is still radiatively generated due to the presence of particles charged under both the SM and the new $U(1)$ group. As well as the SM particle content, additional particles present in the UV theory may also contribute to kinetic mixing, but we will neglect these contributions in this study as they are highly model dependent³. We compute ε between the Z' and the SM *photon*, and find the one-loop result to be finite for any $\varrho(L_\alpha - L_\beta) + \vartheta(L_\beta - L_\lambda)$ gauge group, with divergences cancelling between families. In particular, for the $L_\mu - L_\tau$ model our result is in agreement with Refs. [182, 198]

$$\begin{aligned} \varepsilon(q^2) &= \frac{eg'}{2\pi^2} \int_0^1 dx x(1-x) \ln \frac{m_\mu^2 - x(1-x)q^2}{m_\tau^2 - x(1-x)q^2} \\ &\xrightarrow{q^2 \rightarrow 0} \frac{eg'}{12\pi^2} \ln \frac{m_\mu^2}{m_\tau^2}. \end{aligned} \quad (4.2.7)$$

³The authors of Ref. [198] have calculated the contribution to kinetic mixing in the $L_\mu - L_\tau$ model from a pair of scalars with opposite charges. These are typically subdominant, provided the mass hierarchy between the two scalars is not much larger than that of the charged leptons.

Note that the finiteness of the one-loop result has important consequences for the leptophilic theories we consider. As pointed out in Ref. [177], the finiteness of ε implies that one is able to forbid tree-level kinetic mixing, albeit in a model dependent manner. This happens, for instance, when embedding the new leptophilic $U(1)$ group in a larger non-abelian group G , which is completely independent from the SM sector. This choice of one-loop generated kinetic mixing should be seen as a conservative choice; in the absence of cancellation between tree and loop-level kinetic mixing, this yields the least constrained scenario for an $L_\mu - L_\tau$ model. Additional constraints from first-family leptons are now relevant [195, 199], especially $\nu - e$ scattering measurements, where the strength of the constraint makes up for the loop suppression in the coupling. For neutrino trident scattering, one can safely ignore loop-induced kinetic mixing contributions in the calculation since these are either smaller than the tree-level new physics contribution or yield very weak bounds compared to other processes.

We emphasize that if accompanied by a consistent mechanism for the generation of the Z' mass terms and leptonic Yukawa terms, the models we consider constitute a UV complete extension of the SM. The treatment of such scenarios lies beyond the scope of this work, but we note that if their scalar sectors are light enough they can also yield rich phenomenology at low scales [200].

4.3 Signatures of leptonic neutral currents

When a neutrino impinges on a detector it has only two options for BSM scattering via a leptophilic mediator. In the simplest scenario, the neutrino interacts via the new mediator with the electrons of the detection medium. In this case, there is a tree-level $\nu - e$ scattering process which would be expected to show the clearest signs of new physics. For scattering off a hadron, however, the leptophilic nature of the mediator means that the first tree-level contribution will necessarily come from a diagram which also includes at least one additional SM mediator. Any neutrino-hadron scattering process can be embellished with the new boson to create a BSM signature. In general, the final states of these processes will be either identical to the original un-embellished process (perhaps with missing energy) or it will have an extra pair of leptons in the final state. These neutrino trilepton production processes, which we will refer to as tridents for simplicity, can be subdivided into four

types:

- $\ell\ell\ell$ trident: $\mathcal{H} + \nu_\alpha \rightarrow \mathcal{H}' + \ell_\alpha^- + \ell_\beta^+ + \ell_\beta^-$
- $\nu\ell\ell$ trident: $\mathcal{H} + \nu_\alpha \rightarrow \mathcal{H} + \nu_\beta + \ell_\gamma^+ + \ell_\delta^-$
- $\nu\nu\ell$ trident: $\mathcal{H} + \nu_\alpha \rightarrow \mathcal{H}' + \ell_\alpha^- + \nu_\beta + \bar{\nu}_\beta$
- $\nu\nu\nu$ trident: $\mathcal{H} + \nu_\alpha \rightarrow \mathcal{H} + \nu_\alpha + \nu_\beta + \bar{\nu}_\beta$

We note that these processes all occur in the SM, and so the hunt for new physics will necessarily be competing against a background of genuine SM events. Moreover, for final states with missing energy in the form of neutrinos, isolating a BSM signal would necessarily rely on spectral measurements and other backgrounds have the potential to be large. In particular, the trident production of $\nu\nu\nu$ and $\nu\nu\ell$ will be seen as contributions to the neutral-current (NC) elastic and charged-current quasi-elastic (CCQE) processes, and we expect backgrounds to be insurmountable (see *e.g.* Ref. [201] for new physics contributions to CCQE processes). The $\ell\ell\ell$ channels, on the other hand, are expected to have a much more manageable SM background. Trumuon production, for instance, has been measured in the past and provides a multitude of kinematical observables in the final state [202, 203]. The SM rate for this channel contains radiative photon diagrams as well as hadronic contributions [204–206], whilst for leptophilic neutral bosons, the dominant contributions comes from a weak process with initial and final state radiation of a Z' , making it a less sensitive probe of light new physics. Finally, the $\nu\ell\ell$ production, the most discussed trident signature in the literature, has already been observed in the dimuon channel [71, 72, 207]. This channel is by far the most important trident process for our study, as the leptonic subdiagrams contain only weak vertices in the SM.

4.3.1 Neutrino trident scattering

In the $\nu\ell\ell$ neutrino trident scattering, an initial neutrino scatters off a hadronic target producing a pair of charged leptons in the process. Since we focus solely on neutral current processes and on flavour conserving new physics, no mixed flavour tridents are relevant and we can write

$$\mathcal{H}(P) + \nu_\alpha(k_1) \rightarrow \mathcal{H}(P') + \nu_\alpha(k_2) + \ell_\beta^-(p_-) + \ell_\beta^+(p_+).$$

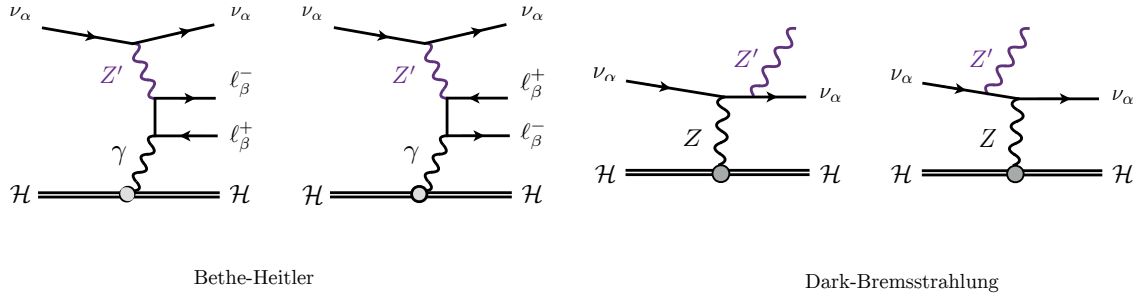


Fig. 4.1. The BSM contributions to neutrino trident production considered in our calculation. The diagrams on the left are referred to as Bethe-Heitler contributions due to their resemblance to pair-production. On the right, we show diagrams with a radiative-like Z' emission, which allows for the production of on-shell Z' particles, which subsequently decays into a charged-lepton pair.

In the SM this process receives CC and NC contributions when $\alpha = \beta$, and is a purely NC process if $\alpha \neq \beta$. The BSM contributions to trident production we consider are shown in Fig. 4.1. Beyond computing the Bethe-Heitler (BH) contributions considered previously, we show that radiative contributions to these processes are generally small. Using the Narrow-Width-Approximation (NWA), we compute the cross section for the radiation of a Z' particle from a neutrino-nucleus interaction, which can then promptly decay to an $\ell^+\ell^-$ pair. We call these contributions Dark-Bremsstrahlung (DB) processes for their similarity with electron bremsstrahlung in QED. We now discuss the two amplitudes individually.

Bethe-Heitler. The BH amplitude is identical to the calculation performed in the previous chapter when we take the substitution

$$V \rightarrow V + \frac{Q_\alpha^L Q_\beta^V}{2\sqrt{2}G_F} \frac{(g')^2}{K^2 + M_{Z'}^2}, \quad A \rightarrow A + \frac{Q_\alpha^L Q_\beta^A}{2\sqrt{2}G_F} \frac{(g')^2}{K^2 + M_{Z'}^2}, \quad (4.3.1)$$

where $K^2 = -(p_1 - p_2)^2$ and V (A) is the SM vector (axial) couplings defined in the previous chapter. Note the dependence on the positive kinematic variable K^2 in the BSM contribution, which can lead to a significant peaked behaviour in the cross section. To avoid numerical difficulties, we have modified the phase space treatment proposed in [208, 209], as shown in Appendix A.

Dark-Bremsstrahlung. Due to the small decay width of the Z' ($\Gamma \propto g'^2 M_{Z'}$), one can obtain an estimate for its resonant production using the NWA. In the true narrow-width

limit, this process reduces to a 3-body phase space calculation and does not interfere with the BH amplitude ⁴. Our DB amplitude for $\nu_\alpha(k_a) + A(k_b) \rightarrow \nu_\alpha(k_1) + Z'(k_2) + A(k_3)$ reads

$$\mathcal{M}_{\text{DB}} = g' Q_\alpha^L \frac{G_F}{\sqrt{2}} J_\mu H_W^\mu, \quad (4.3.2)$$

where H_W^μ is the weak hadronic current (see Appendix ??) and

$$J_\mu = \bar{u}(k_1) \left[\gamma^\alpha \frac{k'_1 + k'_2}{(k_1 + k_2)^2} \gamma_\mu \right. \\ \left. + \gamma_\mu \frac{k'_a - k'_2}{(k_a - k_2)^2} \gamma^\alpha \right] (1 - \gamma^5) u(k_2) \epsilon_\alpha^*(k_2), \quad (4.3.3)$$

where $\epsilon_\alpha^*(k_2)$ is the polarization vector of the Z' . The previous amplitude can then be squared and integrated over phase-space for the total DB cross section. The different charged lepton final states can then be imposed with their respective branching ratios (BR). As a final remark, we note that the typical decay lengths of the new boson are typically below 1 cm for the parameter space of interest, such that their decay is indeed prompt.

From the previous discussions it is clear that the contributions to the total cross section at the lowest order in g' come from the interference between the BSM and the SM BH diagrams, and from the DB. The latter, however, contains an extra power of G_F and is expected to be subdominant with respect to the BH interference. Our results for the individual flux integrated cross sections are shown in Fig. 4.2 for the $\mu^+ \mu^-$ and in Fig. 4.3 for the $e^+ e^-$ trident channels. We show the BH contributions as well as the DB one normalized by the SM trident cross section. All cross sections are flux integrated using the 62.4 GeV p^+ DUNE flux described in Section 4.4.1. For generality, we do not include the BR factors in the DB contributions, and so the green lines only apply for $\mu^+ \mu^-$ tridents if $M_{Z'} > 2m_\mu$ and would suffer additional suppression due to the BR. In each figure we show two panels, one for vector couplings and one for axial-vector couplings. This is interesting from a purely computational point of view, as it shows explicitly the BH cross section scaling with the $M_{Z'}$ in the two cases. Whilst the scaling is similar for dielectron tridents, it differs significantly between the vector and axial-vector cases of the dimuon

⁴We note that despite the fact that interference terms between resonant and non-resonant contributions vanish in the narrow-width limit, the errors induced by the NWA can no longer be shown to be of the order of $\Gamma_{Z'}/M_{Z'}$ [210]. Nevertheless, we do not expect a more careful evaluation of the resonant contribution to change our conclusions.

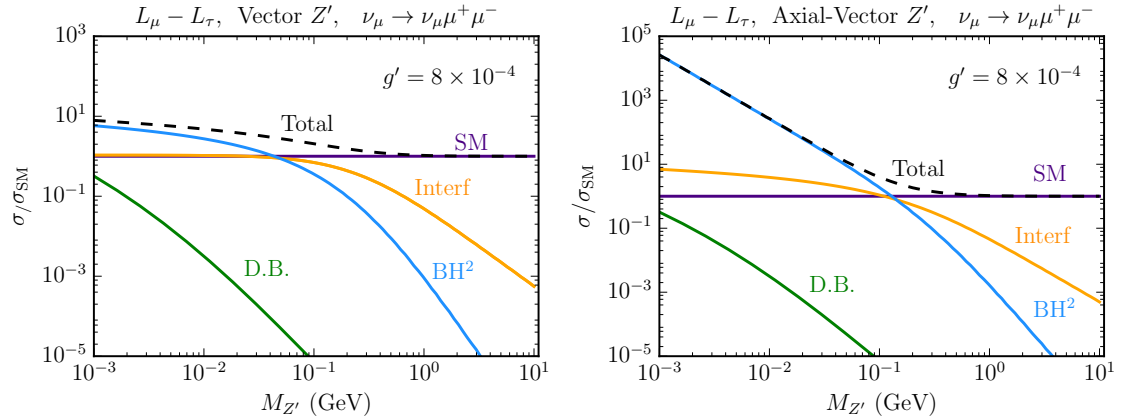


Fig. 4.2. Flux integrated cross sections normalized to the flux integrated SM trident cross section for dimuon production. On the left (right) panel we show the vector (axial-vector) Z' case. We separate the different contributions: SM only, interference between SM and BSM Bethe-Heitler contributions (interf) and BSM Bethe-Heitler only (BH^2). The Dark-Bremsstrahlung (DB) cross section is also shown, but does not take the branching ratio into final state charged leptons into account.

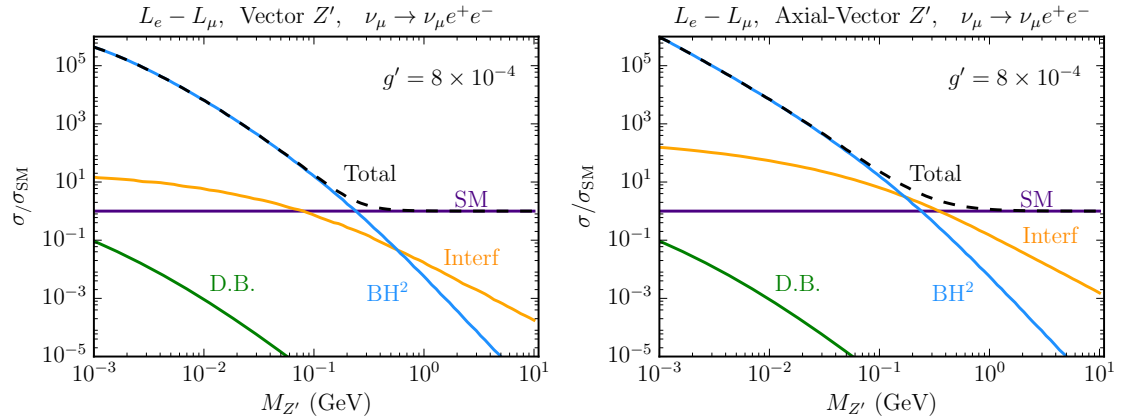


Fig. 4.3. Same as Fig. 4.2 but for the $e^+ e^-$ trident channel.

cross section. This suggests the presence of mass suppression effects in the BH process. We do not investigate this further, but note that there are large cancellations between the two BH diagrams in Fig. 4.1 which are only present for vector-like couplings.

The Equivalent Photon Approximation

We now comment on the EPA for neutrino trident production. This approximation is known to perform quite badly for the SM neutrino trident production cross section [181]. One may wonder, however, if the EPA gets better or worse when computing our BSM cross sections. Naturally, it would be most inadequate for the resonant-like cross sections, since the photon propagator and the strong $1/Q^4$ behaviour is absent. However, if one focuses

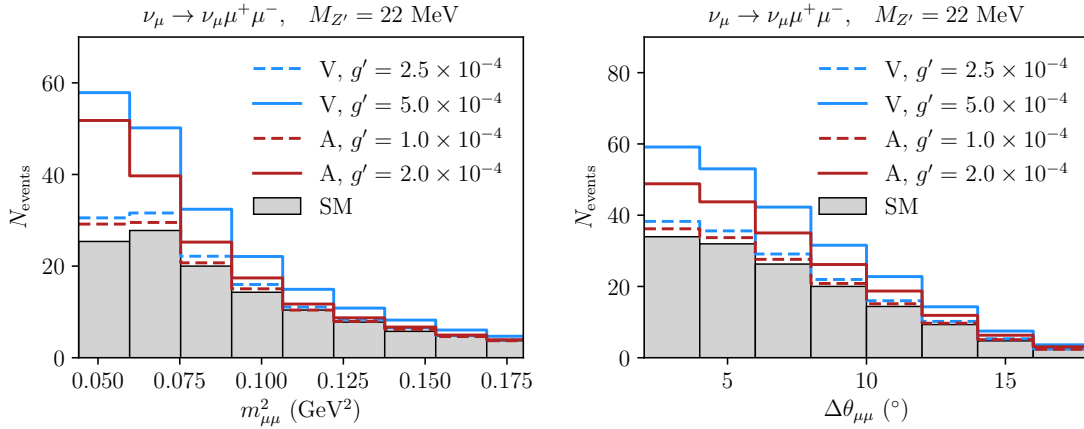


Fig. 4.4. Distribution of the number of neutrino trident events as a function of the invariant mass of the dimuon pair (left) and their separation angle (right) at the DUNE ND. The distributions were produced using the DUNE 120 GeV p^+ neutrino beam and have been smeared as described in Section 4.4.1. For the new physics, we plot the case of a vector (V), $Q^L = Q^R$, and axial-vector (A), $Q^L = -Q^R$, Z' assuming Q_α^L to be given by $L_\mu - L_\tau$.

on the BH contributions, a marginal improvement of the accuracy of the approximation is seen as one lowers the mass of the Z' mediator. In the SM, the $\nu - \gamma$ cross sections scale as a typical weak cross section, $\sigma_{\nu\gamma} \propto G_F^2 \hat{s}$, where \hat{s} is the square of the center of mass energy of the $\nu - \gamma$ system. On the other hand, if the cross section is dominated by the BSM BH contributions, then as we take the limit of small Z' masses, it scales more similarly to a QED cross section, $\sigma_{\nu\gamma} \propto 1/\hat{s}$. This behaviour, however, is only present at low masses and only for the BSM contribution. Since we are interested in regions of the parameter space where BSM and SM cross sections are of similar size, then we expect the total cross section to have a behaviour which is a combination of the two. As a sanity check, we numerically verified that for parameter space points where the BSM contributions are of the same order as the SM cross section, the improvement in the accuracy of the EPA is still not satisfactory. For instance, the ratio between the EPA prediction and the full calculation for the dimuon channel assuming a $Q_{\max} = (140 \text{ MeV})/A^{1/3}$ goes from $\approx 30\%$ in the SM to $\approx 60\%$ for $g' = 8 \times 10^{-4}$ and $M_{Z'} = 5 \text{ MeV}$. For this reason, we only use the full $2 \rightarrow 4$ calculation in what follows.

Trident kinematical distributions

The impact of new physics on the total cross section for trident production has been explored in the previous section. It is then natural to ask what the impact of new physics

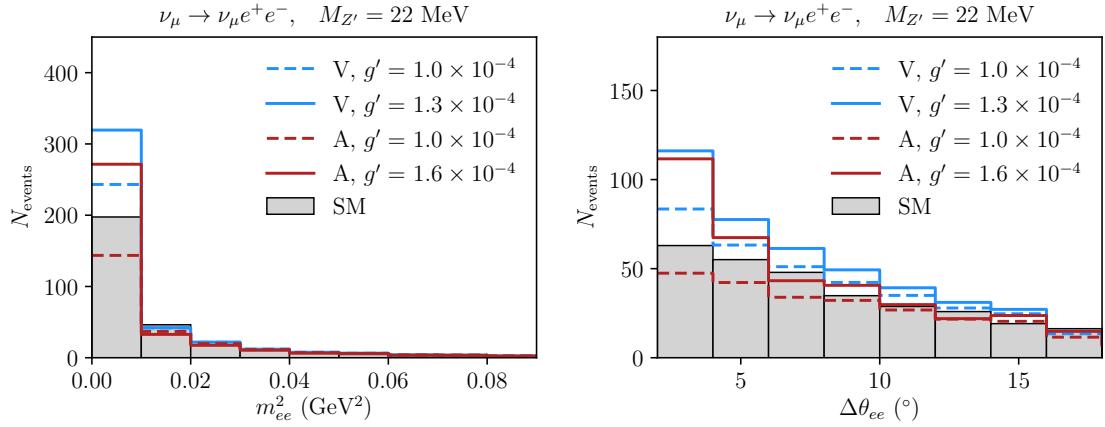


Fig. 4.5. Same as Fig. 4.4 but for e^+e^- trident events. In all cases we assume Q_α^L to be given by $L_e - L_\mu$.

is on the kinematics of trident production which are, especially in the case of the invariant mass and angular variables, of utmost importance for background reduction. In this section we show how the new physics can alter the distributions of these important variables. All results that follow have been obtained using trident events produced by our dedicated Monte Carlo (MC). Smearing and selection cuts have been applied as detailed in Sec. 4.4.

The variables of interest in background reduction are the charged lepton invariant mass $m_{\ell\ell}^2$ and their separation angle $\Delta\theta_{\ell\ell}$. In Fig. 4.4 we show the dimuon invariant mass spectrum between $4m_\mu^2$ and 0.2 GeV^2 , and the dimuon separation angle between 2° and 18° for a light vector boson with $M_{Z'} = 22 \text{ MeV}$. We show the results for the dielectron channel in Fig. 4.5. The light new physics here enhances these distributions at low values of these parameters. We show our results for two types of mediators, vector and axial-vector leptophilic bosons. Comparing the couplings necessary to produce similar BSM enhancements of the number of events, we see that axial-vector bosons lead to larger enhancements with smaller couplings. In particular, it leads to greater spectral distortions for the Z' mass shown.

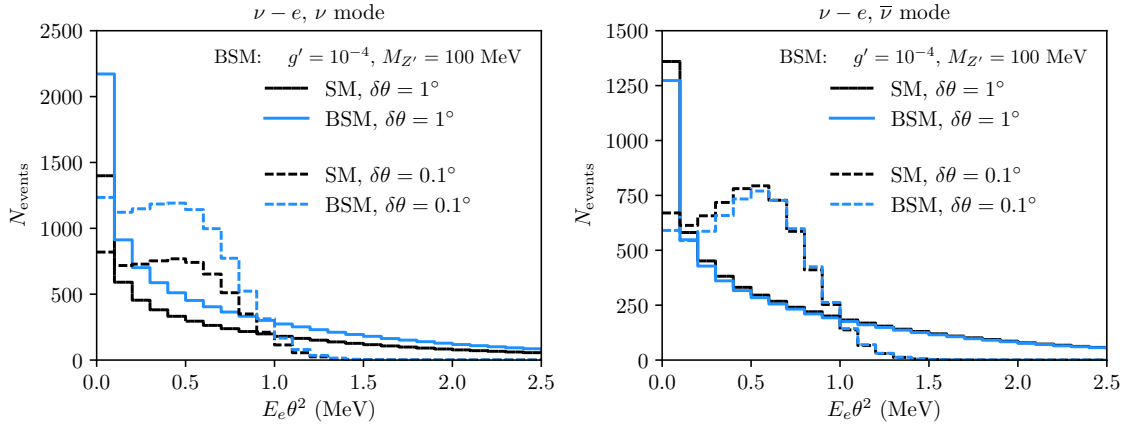


Fig. 4.6. Number of $\nu - e$ scattering events in the DUNE ND as a function of $E_e\theta^2$ for the neutrino (left) and antineutrino (right) beams from the 120 GeV p^+ configuration. We show the prediction in the SM and in a vector $L_e - L_\mu Z'$ model for two angular resolutions $\delta\theta$. The electron kinetic energy threshold is taken to be 600 MeV and the energy resolution is fixed at $\sigma/E = 15\%/\sqrt{E}$.

4.3.2 Neutrino-electron scattering

$\nu - e$ kinematical distributions

The angle between the scattered electron and the outgoing neutrino θ is related to their energies as

$$1 - \cos \theta = m_e \frac{1 - y}{E_e},$$

where $y \equiv T_e/E_\nu$ is the inelasticity ($T_{\text{th}}/E_\nu < y < 1$) and $E_e = T_e + m_e$ is the outgoing electron energy. This implies that at $\mathcal{O}(\text{GeV})$ neutrino energies, the electron recoil is very forward and obey $E_e\theta^2 < 2m_e$, up to detector resolution. For this reason, we choose to analyse our results in terms of $E_e\theta^2$. In this case, the differential cross section becomes

$$\frac{d\sigma_{\nu_\alpha - e}}{d(E_e\theta^2)} = \frac{E_\nu}{2m_e} \frac{d\sigma_{\nu_\alpha - e}}{dT_e} \Bigg|_{T_e=E_\nu(1-\frac{E_e\theta^2}{2m_e})}. \quad (4.3.4)$$

This distribution is particularly important for suppressing the background. Given the kinematics explained above, $E_e\theta^2$ must be smaller than $2m_e$ for $\nu - e$ scattering, while it is often much larger for neutrino-nucleon scattering, the dominant background (See Section 4.4.1). We show in Fig. 4.6 the expected $\nu - e$ event distribution as a function of $E_e\theta^2$ for the SM and a light Z' case, in the neutrino and anti-neutrino modes at the DUNE ND. As expected, the signal is extremely forward and the final distribution is highly sensitive to the angular resolution $\delta\theta$ of the detector. At a conservative value of $\delta\theta = 1^\circ$,

little information about the true distribution is left, and a significant portion of the signal lies in a region where $E_e\theta^2 > 2m_e$. Therefore, shape information may improve the search for a light new physics only when the angular and energy resolutions of the detector are well understood.

4.3.3 Interference effects

Since for $\nu - e$ scattering and neutrino trident production there exists a SM contribution, we expect the experimental sensitivity to new physics to be dominated by the interference between SM and BSM contributions. We now argue what kind of interference one can expect in each one of these processes.

For neutrino trident production we follow Ref. [211] and separate the differential cross section as

$$d\sigma = \hat{V}^2 d\sigma_V + \hat{V}\hat{A} d\sigma_{V-A} + \hat{A}^2 d\sigma_A, \quad (4.3.5)$$

where we dropped the flavour indices in \hat{V} and \hat{A} from (4.3.1) for simplicity. This allows us to write the interference between the SM and the vector new physics as

$$d\sigma_{\text{INT}} = \frac{Q_\alpha^L Q_\beta^V}{2\sqrt{2}G_F} \frac{(g')^2}{K^2 + M_{Z'}^2} \left(2C_V^{\text{SM}} d\sigma_V + C_A^{\text{SM}} d\sigma_{V-A} \right). \quad (4.3.6)$$

Depending on the region of phase space considered, the term proportional to $d\sigma_{V-A}$ can be of similar size to $d\sigma_V$. However, $d\sigma_{V-A}$ changes sign as a function of the angular variables or energies, leading to small integrated cross sections (typically two orders of magnitude smaller than the integral of the $d\sigma_V$ term). Ignoring this term, one can then completely predict the type of interference in trident production. For $\nu_\mu \rightarrow \nu_\mu \mu^+ \mu^-$ trident production, for instance, $C_V^{\text{SM}} > 0$ and the second generation charge appears squared, leading to constructive interference in all cases. For $\nu_\mu \rightarrow \nu_\mu e^+ e^-$ trident events, on the other hand, $C_V^{\text{SM}} < 0$. If the first and second generation charges come in with opposite signs, then the interference is still constructive, otherwise destructive interference happens. The same considerations also apply to antineutrino scattering if one ignores the $d\sigma_{V-A}$ term. Finally, the axial-vector case is completely analogous taking $V \leftrightarrow A$ in Eq. (4.3.6).

For $\nu - e$ scattering analytical expressions can easily be used [62]. Taking $C_L^{\text{SM}} = -1/2 +$

$s_W^2 \sim -1/4$ and $C_L^{\text{SM}} = s_W^2 \sim 1/4$ we have

$$\frac{d\sigma_{\text{INT}\nu_\mu-e}}{dT_e} \sim -\frac{\sqrt{2}m_eG_F}{4\pi} \frac{g'^2}{m_{Z'}^2 + 2m_eT_e} (-1 + (1-y)^2) \quad (4.3.7a)$$

$$\frac{d\sigma_{\text{INT}\bar{\nu}_\mu-e}}{dT_e} \sim -\frac{\sqrt{2}m_eG_F}{4\pi} \frac{g'^2}{m_{Z'}^2 + 2m_eT_e} (1 - (1-y)^2). \quad (4.3.7b)$$

Since $y < 1$, the interference term for $\nu_\mu - e$ is always positive (constructive), and for $\bar{\nu}_\mu - e$ it is always negative (destructive).

4.4 DUNE sensitivities

Having studied the behaviour of neutrino trident production and neutrino-electron scattering cross sections in the presence of light new bosons, we now apply our results in sensitivity studies for the DUNE ND. As discussed in Section 4.2, we limit our studies to $L_e - L_\mu$ and $L_\mu - L_\tau$ models with vector gauge bosons. We start with a discussion on the experimental details, highlighting the challenges of backgrounds and laying out our statistical methods in Section 4.4.1. Then we show our main results in Sections 4.4.2 and 4.4.3, comparing our sensitivity curves to the leading bounds in the parameter space of the leptophilic models from other experiments.

4.4.1 Analysis techniques

The LBNF is expected to produce an intense beam of neutrinos and antineutrinos from a 1.2 MW proton beam colliding against a fixed target [156]. The DUNE ND, where the number of neutrino interactions is the largest, is expected to be located at a distance of 574 m from the target. Despite its design not being final yet [212, 213], we focus on the possibility of a 75-t fiducial mass Liquid Argon (LAr) detector. Regarding the neutrino fluxes, we now concentrate on the option of a beam from 120 GeV protons with 1.1×10^{21} POT per year. The LBNF could also provide higher or lower energy neutrinos depending on the proton energy, target and focusing system used. We explore other possibilities shown in Table 4.1 and we take the flux files provided in Ref. [214, 215]. We assume that the experiment will run 5 years in neutrino and another 5 years in antineutrino mode. The final exposure, therefore, will vary with beam designs, and is equal to a total of 11×10^{22} POT in the case of 120 GeV protons. To generate neutrino scattering events,

Design	Mode	$\mu^+\mu^-$ trident	e^+e^- trident	$\nu - e$ scattering	POTs/year
62.4 GeV p^+	ν	36.5	92.7	7670	1.83×10^{21}
	$\bar{\nu}$	27.3	73.4	4620	1.83×10^{21}
80 GeV p^+	ν	42.0	102	8380	1.4×10^{21}
	$\bar{\nu}$	33.0	84.3	5320	1.4×10^{21}
120 GeV p^+	ν	47.6	110	8930	1.1×10^{21}
	$\bar{\nu}$	40.7	97.6	6450	1.1×10^{21}
ν_τ app optm	ν	210	321	24900	1.1×10^{21}
	$\bar{\nu}$	156	243	14700	1.1×10^{21}

Tab. 4.1. The SM rates for neutrino trident production and neutrino-electron scattering per year at the 75-t DUNE ND after kinematical cuts.

we use our own dedicated MC, Gaussian smearing the true MC energies and angles as a proxy for the detector effects during reconstruction. We assume an energy resolution of $\sigma/E = 15\%/\sqrt{E}$ ($\sigma/E = 6\%/\sqrt{E}$) for e/γ showers (muons) and angular resolutions of $\delta\theta = 1^\circ$ for all particles [86].

An interesting addition to the design of the DUNE ND would be a magnetized high-pressure Gaseous Argon (GAr) tracker placed directly behind the LAr module [216]. The lower thresholds for particle reconstruction and the presence of a magnetic field is expected to improve event reconstruction and reduce backgrounds to neutrino-electron scattering and neutrino trident production. We note that despite the relatively small fiducial mass of such a GAr module, $\lesssim 1$ tonne, it would still provide a sizeable number of these rare leptonic neutrino scattering processes.

With the intense flux at DUNE and the large number of POT, the $\nu - e$ scattering measurement will not be statistically limited, with order 10^4 events in the DUNE ND after a few years. Systematics from the beam and detector are then the limiting factor for the sensitivity to new physics in this measurement. Current work on neutrino flux uncertainties shows that normalization uncertainties can be reduced to the order of 5% [217–219], with similar projections for DUNE [156]. The electron energy threshold also plays a role in the new physics search. In particular, for new light bosons the enhancement at very low momentum transfer $2T_e m_e$ has a cut-off at the minimum electron recoil energy (see Eq. (3.1.6)). This implies that the experiment is no longer sensitive to the Z' mass below $\sqrt{2T_{\text{th}} m_e}$. In our analysis, we assume a realistic overall normalization systematic

uncertainty of 5% and a $\nu - e$ scattering electron kinetic energy threshold of 600 MeV.

Lowering systematic uncertainties on the flux is challenging given the large hadroproduction and focusing uncertainties at the LBNF beam. Here, improvements on the experimental side in determining the neutrino flux will be extremely valuable (see *e.g.* Ref. [220]). If one is searching for novel leptophilic neutral currents, hadronic processes and inverse muon decay measurements are available, but these are limited either by theoretical uncertainties or by statistics, and might not be applicable in the whole energy region of interest. As to the electron energy, assuming a threshold as low as 30 MeV would be safe for electron detection, but at these low energies backgrounds can be incredibly challenging due to the overwhelming π^0 backgrounds. Increasing this threshold to 600 MeV, however, has little impact in our sensitivities and is only 200 MeV below the threshold used in the most recent MINER ν A analysis [179], where good reconstruction is important for measuring the flux. For e^+e^- and $\mu^+\mu^-$ tridents, we refrain from increasing the analysis thresholds from a naive 30 MeV. This is certainly an aggressive assumption but it is necessary if e^+e^- tridents are to be measured, since these events are quite soft [181]. Thresholds for $\mu^+\mu^-$ tridents are much less important since the events are generally more energetic than their dielectron analogue.

Backgrounds ($\nu_\mu \rightarrow \nu_\mu \ell^+ \ell^-$) We now discuss the individual sources of backgrounds to neutrino trident production. A pair of charged leptons is very rarely produced in neutrino interactions, usually coming from heavy resonance decays [152, 207, 221–223]. Since our signal is mostly coming from coherent interactions with nuclei, cuts in the hadronic energy deposition in the detector E_{had} , often large in heavy meson production processes, can help reduce backgrounds. Coherent and diffractive production of mesons is an exception to this, in particular pion production [115, 116, 118, 121], which is the main background to trident due to particle mis-identification (misID). Muons are known to be easily spoofed by charged pions, making CC ν_μ interactions with π^\pm in the final state (CC1 π) one of the largest contributions to the backgrounds of $\mu^+\mu^-$ tridents. Similarly, NC π^0 production stands as the leading background to e^+e^- tridents when the photons are misIDed as two electrons, or if one of the photons pair converts and the other escapes detection. In Ref. [181], we have shown that the $\mu^+\mu^-$ and e^+e^- pairs produced in trident have small separation angles ($\Delta\theta$), possess small invariant masses ($m_{\ell\ell}^2$) and that both charged leptons

are produced with small angles with respect to the neutrino beam (θ_{\pm}). With simplified misID rates, we used the GENIE [89] event generator to show that simple kinematical cuts can reduce backgrounds significantly, achieving a significance of $S_{\mu\mu}/\sqrt{B_{\mu\mu}} \sim 44$ and $S_{ee}/\sqrt{B_{ee}} \sim 17.3$ for the DUNE ND in neutrino mode, where S and B stand for signal and background, respectively. In our current analysis we implement the same kinematical cuts, which are as follows: $m_{\mu\mu}^2 < 0.2 \text{ GeV}^2$, $\theta_{\pm} < 15^\circ$ and $\Delta\theta < 20^\circ$ for the $\mu^+\mu^-$ channel, and $m_{ee}^2 < 0.1 \text{ GeV}^2$, $\theta_{\pm} < 20^\circ$ and $\Delta\theta < 40^\circ$ for the e^+e^- one. We impose these cuts again in our signal analysis, and point out that the new physics enhancement happens precisely in this favourable kinematical region, (see Section 4.3.1). Given the background rejection we find with our naive misID rates, we do not include backgrounds in our results, unless indicated otherwise.

Backgrounds ($\nu - e$) For neutrino-electron scattering, backgrounds will arise from either the genuine production of an electron or via the misID of particle showers in the detector, both in the absence of observable hadronic energy deposition. The former scenario happens mostly by the CC interactions of the flux suppressed ν_e states present in the beam. The main contribution will be from CCQE interactions where the struck nucleon is invisible either for being below threshold or due to nuclear re-absorption. The misID of a photon initiated EM shower for an electron one is expected to be rare in LAr, where the first few cm of the showers can be used to separate electrons and photons by their characteristic dE/dx . However, the large NC rates for the production of single photons and π^0 can become a non-negligible background. For instance, coherent NC π^0 production leaves no observable hadronic signature and may look like a single electron if one of the photons is mis-identified and the other escapes detection. Finally, after misID happens, the signal can still look unique in its kinematical properties. In particular, $E_e\theta^2$ cuts can dramatically reduce backgrounds due to the forwardness of our signal (see e.g. [179, 224]).

Statistics. In order to assess the potential of DUNE to discover new physics, we perform a sensitivity analysis using a χ^2 test with a pull method for systematic uncertainties. Our goal is to assess when DUNE would be able to rule out the SM, and so we generate BSM

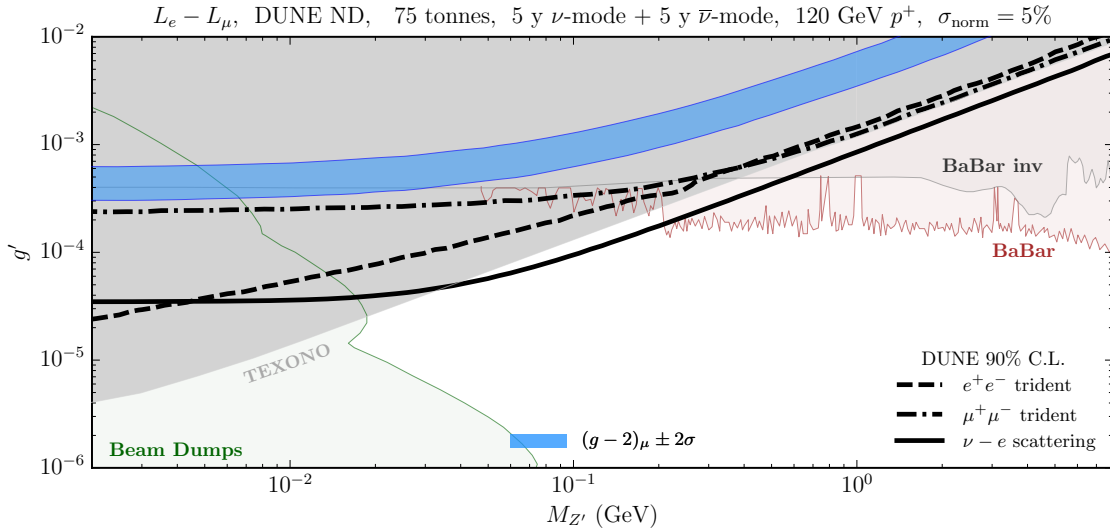


Fig. 4.7. The DUNE ND neutrino scattering sensitivities to the $L_e - L_\mu Z'$ at 90% C.L. The solid line shows the $\nu - e$ scattering sensitivity, followed by the dielectron trident in dashed line, and the dimuon trident in dot-dashed line. The coloured regions are excluded by other experiments, where we highlight the neutrino-electron scattering measurements at reactor experiments [225–227], searches at the BaBar e^+e^- collider [228, 229] and beam dump experiments [177].

events and fit the SM prediction to it. Our χ^2 function is defined as

$$\begin{aligned} \chi^2 = \min_{\alpha} & \left[\frac{(N_{\text{BSM}} - (1 + \alpha)N_{\text{SM}} - (\alpha + \beta)N_{\text{BKG}})^2}{N_{\text{BSM}}} \right. \\ & \left. + \left(\frac{\alpha}{\sigma_{\text{norm}}} \right)^2 + \left(\frac{\beta}{\sigma_{\text{BKG}}} \right)^2 \right], \end{aligned} \quad (4.4.1)$$

where the number of events for the BSM case is given by N_{BSM} , the SM number of events is N_{SM} and the number of background events is N_{BKG} . The nuisance parameters α and β , with their uncertainties σ_{norm} and σ_{BKG} , take into account normalization uncertainties from the flux and detector, and uncertainties on the background prediction, respectively. For the DUNE ND, we assume $\sigma_{\text{norm}} = 5\%$ and $\sigma_{\text{BKG}} = 10\%$. These systematics will likely be dominated by flux normalization uncertainties, and can only be measured with interactions that do not depend on the leptophilic BSM physics.

4.4.2 $L_e - L_\mu$

New vector bosons with couplings to the first and second generation leptons can be probed very effectively in neutrino experiments by measuring the $\nu - e$ scattering rate. This has been recognized in the literature [62, 177, 230], where bounds from various experiments, including CHARM-II [231], TEXONO [225–227] and Borexino [232] have been derived

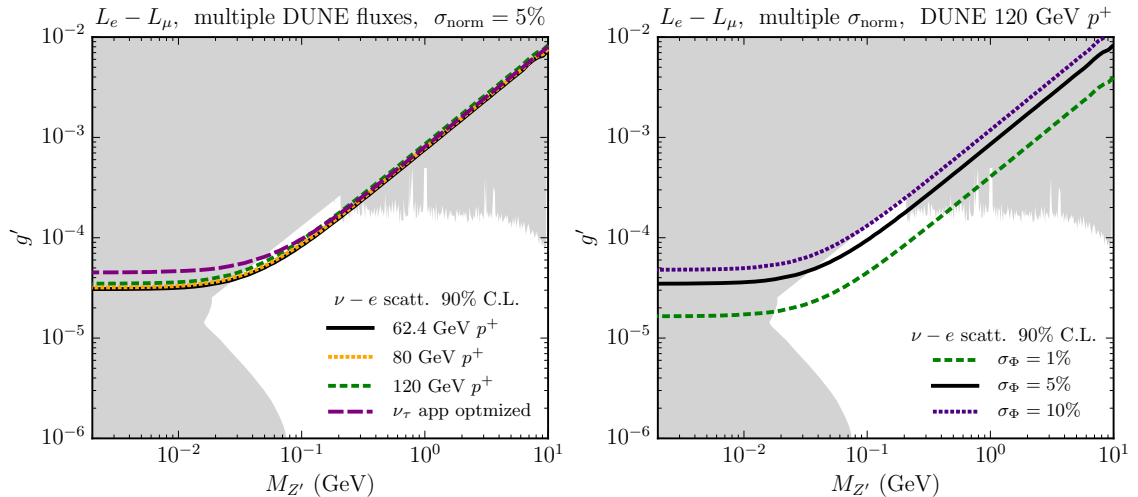


Fig. 4.8. The $\nu - e$ scattering sensitivity to the $L_e - L_\mu$ model at 90% C.L. On the left panel we show the sensitivity using different choices for the neutrino flux, and on the right we use the neutrino beam from 120 GeV protons and vary the normalization systematic uncertainty from an aggressive 1% to a conservative 10%.

on these bosons. Curiously, the bound calculated from the CHARM-II data has been pointed out by Ref. [177] to be too optimistic. The uncertainty on the neutrino flux is a real hindrance for these measurements which has not been taken into account when these bounds were computed. This is particularly important for measurements with large statistics, and for this reason we do not show the CHARM-II bound here. The measurement of $\bar{\nu}_e - e$ scattering at TEXONO, on the other hand, is statistically limited, and the bound it places on this class of models can safely ignore the flux systematics. This turns out to provide the strongest limit in a large region of the $L_e - L_\mu$ parameter space. Trident bounds can be obtained for this model, but due to their lower statistics and more involved kinematics, are subdominant.

We show our results for the DUNE ND in Fig. 4.7. Our results are for the combined $\nu + \bar{\nu}$ modes and do not include backgrounds. The opposite charges between the first and second families implies constructive interference between the SM and BSM contributions for neutrino scattering, contrary to what happens in a $B - L$ model, for instance. Therefore, the strongest bounds on this model can be obtained at DUNE in neutrino mode. It is clear, however, that the degree with which DUNE can probe unexplored parameter space is a question of how much the uncertainties on the flux can be lowered. To illustrate this effect, we vary the normalization systematics on the right panel of Fig. 4.8, going from a conservative 10% to an aggressive 1% uncertainty. The effect of changing the thresholds

is very small, being most important in a region already probed by other experiments. Different beam designs seem to have only a small impact on the sensitivity, as shown on the left panel of Fig. 4.8.

Since we show the bounds obtained from the neutrino and antineutrino runs combined, it is not possible to see the effects of destructive interference. If only channels with destructive interference were available, however, it would have been possible to allow for cancellations between the total interference and the square of the BSM contributions in certain regions of parameter space at the level of the total rate. The region where this cancellation happens depends strongly on the neutrino energies involved and on the integrated phase space of the recoiled electron. In that case, one expects that the sensitivity to the lowest new physics couplings comes, in fact, from the search for a deficit of $\nu - e$ scattering events, as opposed to the constructive interference case where an excess of events is always produced. We note that this has no significant impact on the sensitivity of a leptophilic Z' , but might provide crucial information about the nature of the Z' charges in case of detection.

The trident bounds we obtain are not competitive for this model despite the fact that the trident cross sections receive similar enhancements to that of $\nu - e$ scattering. This is due to two reasons: the low number of events and the non-trivial kinematics of trident processes. Since the neutrino is essentially scattering off virtual charged leptons produced in the Coulomb field of the nucleus, it has to typically transfer more energy to the system than it would in a scattering off real particles in order to produce visible signatures. This remark also helps us to explain the behaviour of the sensitivity curves at the lowest masses. Whilst $\nu - e$ scattering cross sections become insensitive to the boson mass at $\sqrt{2m_e T_{\text{th}}}$, the trident cross sections do not. This behaviour is most dramatic in the e^+e^- tridents, but is also present in the $\mu^+\mu^-$ one. This is a consequence of the 4-body phase space kinematics, where now the momentum transfer through the Z' propagator is no longer trivially related to the final state particle energies, as in $2 \rightarrow 2$ processes. It should be noted, however, that both the dimuon and the dielectron trident rates become nearly independent of $M_{Z'}$ below the muon and the electron mass, respectively, where only a logarithmic dependence is expected [178].

DUNE can also probe this class of models in a different way. In the context of long range forces in neutrino oscillation experiments and with the same choice of charges,

Ref. [233] places competitive bounds in this model with Super-Kamiokande data and makes projections for DUNE. The matter potential created by the local matter density modifies the dispersion relation of the neutrinos with lepton non-universal charges, leading to very competitive bounds in our region of interest. Similar considerations have also been explored in the context of high-energy astrophysical neutrinos [234]. Other experimental searches have been conducted at electron beam dumps. This technique consists of producing the Z' boson at the target via radiative processes such as $e + A \rightarrow e + A + Z'$, and look for the visible decays of the boson in the detector. In this model, the decay products are mostly e^+e^- states and the bounds are only applicable at appreciably small values of g' and $M_{Z'}$, where the lifetime of the Z' is sufficiently large. Probing the large mass region, on the other hand, requires high-energy experiments. In that regime, the strongest bounds come from searches at the e^+e^- collider BaBar. These come about in two ways: looking for the visible decay products of a Z' produced radiatively or in heavy meson decays [228], or exploring the BR into invisible final states [229].

4.4.3 $L_\mu - L_\tau$

In this section we evaluate the DUNE ND sensitivity to the presence of a light vector Z' charged under $L_\mu - L_\tau$. Beyond being anomaly free, this choice of charges allows for positive contributions to the anomalous magnetic moment of the muon, $a_\mu = (g - 2)_\mu$, as discussed in Refs. [195, 199, 237–239]. This quantity is well known for a $\sim 3.7\sigma$ discrepancy between the experimental measurement [240] and the theory predictions [241, 242]. If future efforts to measure it [243] confirm this disagreement and if theoretical uncertainties are better controlled in the next few years, then constraining new physics scenarios that could contribute to a_μ is of utmost importance.

This model can significantly impact neutrino trident production of a muon pair. In fact, the leading bound in this parameter space for masses $M_{Z'} \lesssim 200$ MeV comes from the CCFR measurement of the same neutrino trident channel [72]. CCFR observed 37.0 ± 12.4 events, extracting a measurement of the trident cross section of $\sigma_{CCFR}/\sigma_{SM} = 0.82 \pm 0.28$. Curiously, the measurement by CHARM-II [71] provides weaker constraints on this model despite seeing a larger number of trident events, namely 55 ± 16 events in total, most likely due to the 1σ upward fluctuation of the measurement: $\sigma_{CHARM-II}/\sigma_{SM} = 1.58 \pm 0.57$. Other

important bounds from $\nu - e$ scattering have also been obtained using the kinetic mixing parameter generated at one-loop. The strongest of which uses data from Borexino [77], and are only relevant for the low mass region $M_{Z'} \lesssim 20$ MeV.

At DUNE, both of these measurements are possible, allowing to constrain this model in different ways. We show our results in Fig. 4.9, without including backgrounds. In this scenario, DUNE would be able to cover all the 2σ region compatible with the $(g - 2)_\mu$ measurement only with the $\mu^+ \mu^-$ trident events. For the low mass region, measuring the $\nu - e$ scattering rate can provide a complementary probe of this region, depending most strongly on the systematic uncertainties DUNE can achieve. We note that analysis thresholds used for $\nu - e$ scattering have little impact on the sensitivity in the region of interest. Our conclusion that DUNE can cover all of the $(g - 2)_\mu$ region holds provided backgrounds are kept below the SM signal rate. This can be seen when we include backgrounds with different assumption on the right panel of Fig. 4.10. Finally, different assumption for the beam design have little impact on the sensitivity, as show on the left panel of Fig. 4.10.

Apart from neutrino scattering, dedicated searches for resonances decaying into $\mu^+ \mu^-$ in four muon final states have been performed at BaBar [235], looking for $e^+ e^- \rightarrow \mu^+ \mu^- Z' (\rightarrow \mu^+ \mu^-)$. At the LHC, the searches for $Z \rightarrow 4\mu$ [236] performed by the ATLAS collaboration can be recast into a bound on Z' . Here, we show the bounds derived in [178]. Big Bang Nucleosynthesis bounds were studied in [195, 239], and shown to constrain the mass of the boson to be $M_{Z'} \gtrsim 5$ MeV. Recently, additional constraints from Cosmology were derived given that the presence of very light Z' bosons changes the evolution of the early Universe [198]. In particular, the decays and inverse decays induced by the new leptophilic interactions can modify the neutrino relativistic degrees of freedom, requiring $M_{Z'} \gtrsim 10$ MeV in order for $\Delta N_{\text{eff}} < 0.5$ for the case with no kinetic mixing. The authors of Ref. [198] also found that an additional Z' boson can alleviate the tension in the different measurements of the Hubble parameter. Let us stress here that all these bounds will be complementary to possible future constraints that can be obtained by the DUNE program, as shown in Fig. 4.9.

4.5 Conclusions

Although the next generation neutrino oscillation experiments are primarily designed for making precision measurements of the neutrino mixing parameters, the unprecedented fluxes and large detectors will allow for many non-minimal new physics searches. In this work, we have considered the physics potential of the DUNE ND for constraining the existence of an additional anomaly-free $U(1)$ gauge group giving rise to a Z' boson which only couples to leptons — a form of a purely leptophilic neutral current. Specifically, we have considered the anomaly free scenarios with charges associated to the lepton number difference $L_\alpha - L_\beta$. Focusing on the two most promising neutrino scattering processes, $\nu - e$ and $\nu \ell \ell$ trident scattering, we have computed expected sensitivity curves for the DUNE ND for a variety of charge assignments.

In performing our sensitivity studies as a function of the coupling and mass of the Z' boson, we have remained as faithful as possible to the real experimental conditions of a LAr detector. Our main results rely on the realistic assumptions of flux uncertainties of 5% and feasible exposures. To avoid large backgrounds, we have also implemented kinematical cuts on the neutrino trident sample, and a kinetic energy threshold of 600 MeV for $\nu - e$ scattering events. The parameter space which can be probed by $\nu - e$ scattering in the $L_e - L_\mu$ scenario is at least two times better than the e^+e^- and almost twenty times better than the $\mu^+\mu^-$ trident channels, specially for the lower mass region. In this case, the DUNE ND would improve only slightly on previous $\nu - e$ scattering bounds, especially at around $M_{Z'} \sim 100$ MeV. We do not expect e^+e^- trident measurements at DUNE to improve our coverage of the $L_e - L_\mu$ Z' parameter space, but note this process has a distinct dependence on $M_{Z'}$ if compared to $\nu - e$ scattering.

If the light vector Z' is charged under $L_\mu - L_\tau$, we have found that the dimuon trident measurement could provide the leading bound in this parameter space. This is particularly interesting as these models can also explain the discrepancy between the measurement of the anomalous magnetic moment of the muon and its SM prediction. We expect that DUNE will be able to fully explore the $(g - 2)_\mu$ motivated parameter space provided backgrounds are kept under control. The robustness of our results is tested against different choices of neutrino fluxes, where we find that despite the larger rates at higher neutrino energies and the larger BSM enhancement at lower energies, the sensitivities are very similar.

Improvements to the experimental sensitivities we have displayed in Figs. 4.7 and 4.9 can be achieved by reducing uncertainties on the neutrino flux and detection. From the experimental side, novel detection techniques suitable to rare neutrino events are currently under discussion, such as the magnetized HPgTPC [216] and the Straw Tube Tracker [244, 245]. Together with improved analysis techniques, these will help to improve upon our projections for the sensitivity of DUNE to new physics that might be hiding at light masses and small couplings.

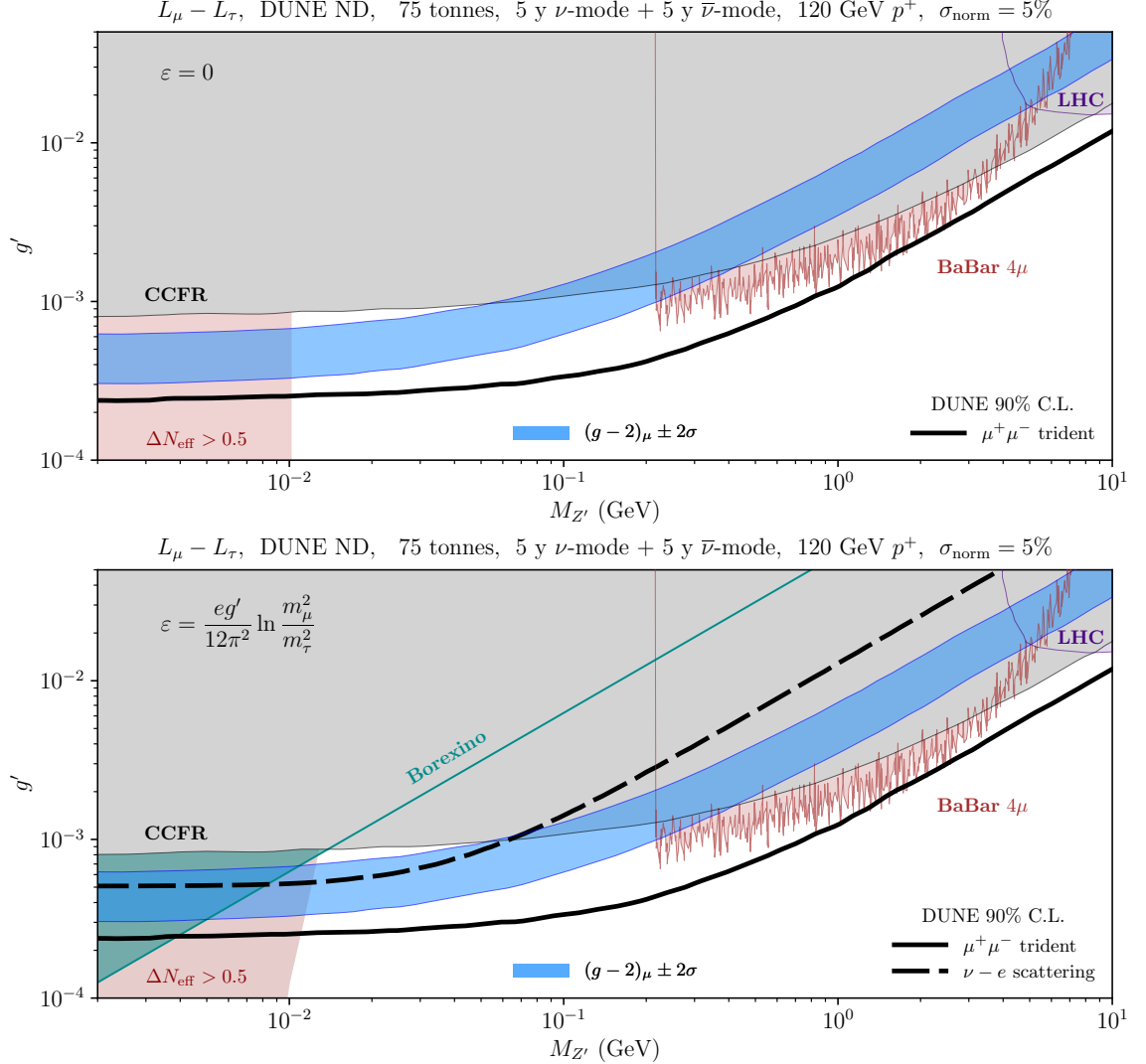


Fig. 4.9. The DUNE ND neutrino scattering sensitivities for $L_\mu - L_\tau$ at 90% C.L. The upper panel shows the case with no kinetic mixing, and the lower panel the case with the loop-induced mixing. Bounds from neutrino-electron scattering apply only to the latter. We also show bounds from BaBar [235], LHC [236], Borexino [77] and from the neutrino trident production measurement at CCFR [72,178]. Recent cosmological bounds for the two kinetic mixing cases derived in Ref. [198] are also shown.

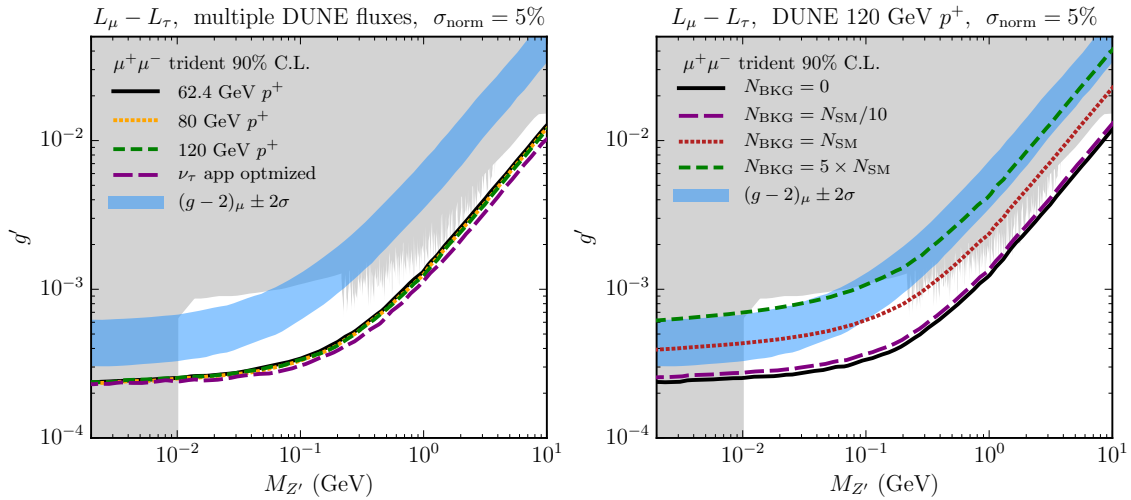


Fig. 4.10. The dimuon neutrino trident sensitivity to the $L_\mu - L_\tau$ model with no kinetic mixing at 90% C.L. On the left panel we show the sensitivity using different choices for the neutrino flux, and on the right we use the neutrino beam from 120 GeV protons and scale the background with respect to the total number of SM trident events after cuts.

Chapter 5

A light dark neutrino sector

The most important evidences that the Standard Model (SM) of particle physics is incomplete are neutrino masses and mixing, and the presence of dark matter (DM) in the Universe. Both call for extensions of the SM and the possible existence of dark sectors which do not partake in SM interactions, or do so with extremely weak couplings while displaying strong “dark” interactions [?, 197, 246]. Such sectors might exist at relatively light scales below the electroweak one, being within reach of present and future non-collider experiments. Generically, a neutral dark sector can communicate with the SM via three renormalizable portals. New neutral fermions mix with light neutrinos unless a symmetry differentiates the two, a possibility usually denoted as the neutrino portal. New vector particles can kinetically mix with the SM hypercharge, and new scalars mix with the Higgs boson through the so-called vector and scalar portals, respectively. The latter terms are generically allowed in the Lagrangian and an explanation of their smallness requires specific UV completions.

In this article, we propose a new neutrino model with a hidden $U(1)'$ gauge symmetry under which no SM fields are charged. We introduce new SM-neutral fermions, ν_D and an additional sterile neutrino N . The symmetry is subsequently broken by the vacuum expectation value (vev) of a complex dark scalar Φ , which gives mass to the new gauge boson. For concreteness, we restrict the scale of the breaking to be below the electroweak one.

Models with heavy neutrinos which are not completely sterile and might participate in new gauge interactions have been studied in several contexts, including $B - L$, $L_\mu - L_\tau$ and

left-right symmetric models [247–255], but here we focus on the possibility of a symmetry under which no SM fields are charged [256–258]. New heavy neutral fermions that feel such hidden forces, such as ν_D , are referred to as *dark neutrinos*, since they define a dark sector separate from the SM. Nevertheless, the dark interactions “leak” into the SM sector via neutrino mixing, where they may dominate [259, 260]. Models of this type have been invoked to generate large neutrino non-standard interactions [173, 261], generate new signals in DM experiments [?, 259, 262–264], weaken cosmological and terrestrial bounds on eV scale sterile neutrinos [?, ?, ?, ?, ?, ?, 158, 163], and as a potential explanation of anomalous short-baseline results at the MiniBooNE [?, 265] and/or LSND [?, 266] experiments with new degrees of freedom at the MeV/GeV scale [166–168, 267–270].

Our model presents all the three renormalizable portals to the SM. The Yukawa interactions between the leptonic doublet and N , and between N and ν_D induce neutrino mixing. The gauge symmetry allows a cross-coupling term in the potential between the Higgs and the real part of the scalar, inducing mixing between the two after symmetry breaking. The broken gauge symmetry implies the existence of a light hidden gauge boson X_μ , which mediates the dark neutrino interactions and generically kinetically mixes with the SM hypercharge. The set-up is self-consistent and combines the three portals into a unified picture that exhibits significantly different phenomenology with respect to each portal taken separately, as we discuss. The interplay of the different portal degrees of freedom leads to novel signatures which would have escaped searches performed to date, and that can explain long-standing anomalies. For the latter, we focus on the MiniBooNE anomaly as discussed in Ref. [167] (see also [166]) and on new neutrino scattering signatures at neutrino experiments [168]. We also reconsider the possibility to explain the discrepancy between the prediction and measurement of the anomalous magnetic moment of the muon (Δa_μ) [240] via kinetic mixing [?, 271].

An interesting feature of the model is the generation of neutrino masses at loop-level. This requires only two key features of our setup, namely a light Z' and neutrino mixing, but not the vector and scalar portals. For this reason, we discuss it elsewhere [272].

In its minimal form, the model is not anomaly-free. We discuss how this can be cured and propose a minor extension that introduces additional dark sector neutral fermions charged under the new symmetry [?, 246]. Neutrinos, we argue, may be a window into such dark

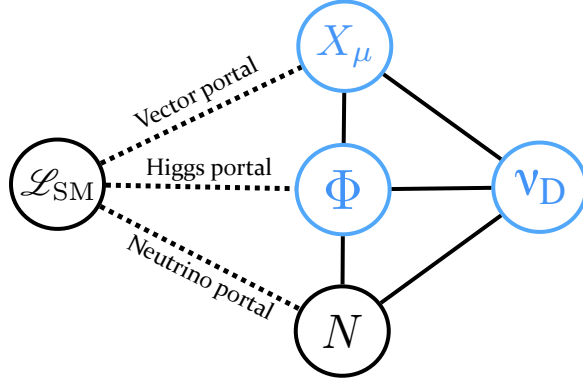


Fig. 5.1. Schematic representation of our dark neutrino model. The dark neutrino, ν_D and the complex scalar Φ are the only fields charged under the new $U(1)'$ gauge symmetry. The new vector boson X_μ acquires a mass after spontaneous symmetry breaking, and N remains a complete singlet.

sectors, bridging the puzzles of neutrino masses and DM [146, 162, 273–281]. We briefly outline the key features of a DM extension and leave a more detailed analysis to future work.

5.1 The Model

We extend the SM gauge group with a new abelian gauge symmetry $U(1)'$ with associated mediator X_μ and introduce three new singlets of the SM gauge group: a complex scalar Φ , and two left-handed fermions $\nu_{D,L} \equiv \nu_D$ and $N_L \equiv N$. The scalar Φ and the fermion ν_D are equally charged under the new symmetry, and N is neutral with respect to all gauge symmetries of the model. For simplicity, we restrict our discussion to a single generation of hidden fermions. The relevant terms in the gauge-invariant Lagrangian are

$$\begin{aligned} \mathcal{L} \supset & (D_\mu \Phi)^\dagger (D^\mu \Phi) - V(\Phi, H) \\ & - \frac{1}{4} X^{\mu\nu} X_{\mu\nu} + \bar{N} i \not{\partial} N + \bar{\nu}_D i \not{\partial} \nu_D \\ & - \left[y_\nu^\alpha (\bar{L}_\alpha \cdot \tilde{H}) N^c + \frac{\mu'}{2} \bar{N} N^c + y_N \bar{N} \nu_D^c \Phi + \text{h.c.} \right], \end{aligned} \quad (5.1.1)$$

where $X^{\mu\nu}$ is the field strength tensor for X_μ , $D_\mu \equiv (\partial_\mu - ig' X_\mu)$ the covariant derivative, $L_\alpha \equiv (\nu_\alpha^T, \ell_\alpha^T)^T$ the SM leptonic doublet of flavour $\alpha = e, \mu, \tau$ and $\tilde{H} \equiv i\sigma_2 H^*$ is the charge conjugate of the SM Higgs doublet. We write y_ν^α for the L_α - N Yukawa coupling, y_N for the ν_D - N one, and μ' for the Majorana mass of N , which is allowed by the SM and the new gauge interaction, although it breaks lepton number by 2 units.

The minimisation of the scalar potential $V(\Phi, H)$ leads the neutral component of the fields H and Φ to acquire vevs v_H and v_φ , respectively. The latter also generates a mass for both the new gauge boson X_μ and the real component of the scalar field φ . Although v_φ is arbitrary, we choose it to be below the electroweak scale, $v_\varphi < v_H$, as we are interested in building a model testable at low scales.

Neutrino portal In the neutral fermion sector and after symmetry breaking, two Dirac mass terms are induced with $m_D \equiv y_\nu^\alpha v_H / \sqrt{2}$ and $\Lambda \equiv y_N v_\varphi / \sqrt{2}$. It is useful to consider the form of the neutrino mass matrix in the single generation case to clarify its main features. For one active neutrino ν_α ($\alpha = e, \mu, \tau$), it reads

$$\mathcal{L}_{\text{mass}} \supset \frac{1}{2} \begin{pmatrix} \bar{\nu}_\alpha & \bar{N} & \bar{\nu}_D \end{pmatrix} \begin{pmatrix} 0 & m_D & 0 \\ m_D & \mu' & \Lambda \\ 0 & \Lambda & 0 \end{pmatrix} \begin{pmatrix} \nu_\alpha^c \\ N^c \\ \nu_D^c \end{pmatrix} + \text{h.c.} \quad (5.1.2)$$

The form of this matrix appears in Inverse Seesaw (ISS) [?, 282] and in Extended Seesaw (ESS) [?, 283] models. In fact, it is the same matrix discussed in the so-called Minimal ISS [284], with the difference that in our case its structure is a consequence of the hidden symmetry. After diagonalisation of the mass matrix, the two heavy neutrinos, ν_h with $h = 4, 5$, acquire masses. Assuming that $m_D \ll \Lambda$, we focus on two interesting limiting cases.

In the *ISS-like* limit, where $\Lambda \gg \mu'$ and the two heavy neutrinos are nearly degenerate, we have

$$\begin{aligned} m_5 &\simeq -m_4 \simeq \Lambda, \quad m_5 - |m_4| = \mu', \quad U_{\alpha 5} \simeq U_{\alpha 4} \simeq \frac{m_D}{\sqrt{2}\Lambda}, \\ U_{Di} &\simeq \frac{m_D}{\Lambda}, \quad U_{D5} \simeq U_{D4} \simeq \frac{1}{\sqrt{2}}, \quad U_{N5} \simeq U_{N4} \simeq \frac{1}{\sqrt{2}}. \end{aligned}$$

In the *ESS-like* case, $\Lambda \ll \mu'$, one neutral lepton remains very heavy and mainly in the completely neutral direction N , and the other acquires a small mass via the seesaw mechanism in the hidden sector. We find

$$\begin{aligned} m_4 &\simeq -\frac{\Lambda^2}{\mu'}, \quad m_5 \simeq \mu', \quad U_{\alpha 4} \simeq U_{\alpha 5} \sqrt{\frac{m_5}{|m_4|}} \simeq \frac{m_D}{\Lambda}, \\ U_{Di} &\simeq \frac{m_D}{\Lambda}, \quad U_{N5} \simeq U_{D4} \simeq 1, \quad U_{D5} \simeq U_{N4} \simeq \frac{\Lambda}{\mu'}. \end{aligned}$$

From the discussion above, it is clear that the masses of Z' and φ' are typically above the heavy neutrino ones, unless we are in the ESS-like regime.

The Yukawa terms in Eq. (5.4.1) induce *neutrino mixing* between the active (light) and heavy (sterile, dark) neutrinos. In this model, similarly to the ISS and the ESS cases, this mixing can be much larger than the typical values required in type-I seesaw extensions to explain neutrino masses, making its phenomenology more interesting. The determinant of the mass matrix in Eq. (5.5.1) is zero, and so light neutrino masses vanish at tree-level and do not constrain the values of the active-heavy mixing angles. This, however, is no longer the case at one-loop level, as light neutrino masses emerge through radiative corrections from diagrams involving the φ' and Z' degrees of freedom [272].

Scalar portal In the scalar potential, the symmetries of the model allow us to write down the following term

$$V(\Phi, H) \supset \lambda_{\Phi H} H^\dagger H |\Phi|^2, \quad (5.1.3)$$

where we identify $\lambda_{\Phi H}$ as the scalar portal coupling [285], responsible for mixing in the neutral scalar sector. If such a term exists, the scalar mass eigenstates (h', φ') mix with the gauge eigenstates (h, φ) with a mixing angle α defined by

$$\tan(2\alpha) \equiv \frac{\lambda_{\Phi H} v_H v_\varphi}{\lambda_h v_H^2 - \lambda_\varphi v_\varphi^2}, \quad (5.1.4)$$

where λ_h and λ_φ are the quartic couplings of the Higgs and Φ scalars, respectively.

Vector portal Similarly, mixing also arises in the neutral vector boson sector from the allowed kinetic mixing term [194]

$$\mathcal{L} \supset -\frac{\sin \chi}{2} F^{\mu\nu} X_{\mu\nu}, \quad (5.1.5)$$

where $F_{\mu\nu}$ is the SM hypercharge field strength. This term may be removed with a field redefinition, resulting in three mass eigenstates (A, Z^0, Z') , corresponding to the photon, Z^0 -boson and the hypothetical Z' -boson. For a light Z' , the Z' coupling to SM fermions f to first order in the small parameter χ is given by

$$\mathcal{L} \supset -(e q_f c_W) \chi \bar{f} \gamma^\mu f Z'_\mu, \quad (5.1.6)$$

with q_f the fermion electric charge.

The values of χ and $\lambda_{\Phi H}$ are arbitrary and could be expected to be rather large. As such, we treat them as free parameters within their allowed ranges. Here, we merely note that with our current minimal matter content, χ and $\lambda_{\Phi H}$ receive contributions at loop level from the $(\bar{L}_\alpha \cdot \tilde{H})N^c$ and $\bar{N}\nu_D^c\Phi$ terms, which are necessarily suppressed by neutrino mixing ($\chi \propto g'e|U_{\alpha h}|^2$ and $\lambda_{\Phi H} \propto |U_{\alpha h}|^2$). These values constitute a lower bound and larger values should be expected in a complete model.

5.1.1 Portal phenomenology

The interplay between portal couplings and the heavy neutrinos ν_h ($h = 4, 5$) leads to a distinct, and possibly richer, phenomenology to what is commonly discussed in the presence of a single portal. We present here some of the most relevant signatures, devolving a longer study to future work.

Heavy neutrino searches The strongest bounds on heavy neutrinos in the MeV–GeV mass range come from peak searches in meson decays [286–288] and beam dump experiments [289–294] looking for visible ν_h decays. These, however, can be weakened if the ν_h decays are sufficiently different from the case of “standard” sterile neutrinos with SM interactions suppressed by neutrino mixing. We now discuss how this may happen, depending on the mass hierarchy of the two heavy neutrinos and the values of neutrino and kinetic mixing. For concreteness, we focus on specific benchmark points (BP) that illustrate the key features. In the ISS-like regime, we take $m_4/m_5 = 99\%$ and choose $m_4 \simeq m_5 = 100$ MeV. If χ is negligible, we have that ν_h decays as in the standard sterile case via SM interactions. This is because the $\nu_5 \rightarrow \nu_4 \bar{\nu}_\alpha \nu_\alpha$ decay is phase-space suppressed ($\Gamma_{\nu_5 \rightarrow \nu_4 \nu \nu} \propto \mu'^5$), and because Z' mediated decays into three light neutrinos are negligible for small mixing, as $\Gamma_{\nu_h \rightarrow \nu \nu \nu} \propto |U_{\alpha h}|^6 m_h^5 / m_{Z'}^4$. If χ is sizeable, on the other hand, new visible decay channels dominate, specifically $\nu_4 \rightarrow \nu_\alpha e^+ e^-$ for this BP. The corresponding decay rate is given by

$$\Gamma(\nu_4 \rightarrow \nu_\alpha e^+ e^-) \approx \frac{1}{2} \frac{e^2 \chi^2 g'^2 |U_{\alpha 4}|^2}{192\pi^3} \frac{m_4^5}{m_{Z'}^4}. \quad (5.1.7)$$

Depending on the value of χ and $m_{Z'}$ this decay can be much faster than in the SM, implying stronger constraints on the neutrino mixing parameters as discussed in Ref. [295]. For heavier masses, additional decay channels, e.g. $\nu_4 \rightarrow \nu_\alpha \mu^+ \mu^-$, would open. A feature

of the model is that such channel would have the same BR as the electron one, albeit phase space suppressed. No two-body decays into neutral pseudoscalars arise due to the vector nature of the gauge coupling, unless mass mixing is introduced (see [296] for a thorough discussion of the decay products of a dark photon). We consider also a BP in the ESS-like regime. We take $m_4 = m_5/10$. In this case, ν_5 decays into 3 ν_4 states very rapidly. The subsequent decays of ν_4 would proceed as discussed above and would be much slower than the ν_5 one, given the hierarchy of masses and the further suppression due to neutrino and/or kinetic mixing.

For large χ , peak searches and bounds on lepton number violation (LNV) from meson and tau decays may be affected [297, 298]. Despite simply relying on kinematics, we note that in peak searches the strict requirement of a single charged track in the detector [287] would, in fact, veto a large fraction of new physics events if ν_h decays promptly into $\nu_\alpha e^+ e^-$, for instance. In addition, LNV meson and tau decays would need to be reconsidered as the intermediate on-shell ν_h could decay dominantly via the novel NC interactions and the $\ell\pi$ and ℓK final states would be absent.

Dark photon searches Bounds on the vector portal come from several different sources [177, 299]. Electroweak precision data and measurements of the $g - 2$ of the muon and electron constrain our model [300]. Major efforts at collider and beam dump experiments led to strong constraints on dark photons by searching for the production and decay of these particles. Such bounds, however, depend on the lifetime of the Z' and on its branching ratio (BR) into charged particles. In our model, the Z' decays invisibly into heavy fermions if $m_{Z'} > 2m_4$ and into light neutrinos otherwise. In the latter case, constraints would be much weaker than usually quoted with only mono-photon searches [229] applying. In the former case, however, new signatures arise, where the subsequent decay of ν_h leads to multi-lepton/multi-meson events, potentially with displaced vertices and providing a very clean experimental signature. Notably, if the Z' decays into ν_h states that subsequently decay sufficiently fast within the detector, even the “invisible decay” bounds will be weakened.

Revisiting Δa_μ The above possibility opens the option to explain the discrepancy between the theoretical prediction [?, 241] and the experimental value [240] of the $(g - 2)$

of the muon via kinetic mixing. For instance, a 1 GeV Z' with $\chi = 2.2 \times 10^{-2}$ can explain a_μ . Taking ν_4 around 400 MeV (800 MeV) and $m_5 > m_{Z'}$, then the Z' would decay into $2\nu_4$ ($\nu_4\nu_\alpha$) immediately. For the quoted value of the kinetic mixing and the largest neutrino mixing allowed, these heavy fermions would further decay into e^+e^- and $\mu^+\mu^-$ pairs plus missing energy with sub-meter decay lengths. This region of the χ parameter space is constrained only by the BaBar e^+e^- collider searches for visible [228] and invisible decays [229] of a standard dark photon. Both of these searches would veto the three-body decays of ν_4 , opening up a large region of parameter space (see Ref. [301] for a similar discussion in an inelastic DM model). Resonance searches still constrain the Z' BR into e^+e^- and $\mu^+\mu^-$ which are proportional to χ^2 , providing a weak upper bound. In order to shorten the lifetime of ν_4 , we can increase mixing with the tau neutrino in order to avoid constraints from neutrino scattering. A detailed analysis to identify the viable parameter space is required and will be done elsewhere.

Fake rare meson decays The ν_h states can fake leptonic decays of charged mesons M^\pm and charged leptons ℓ^\pm through the decay chains $M^\pm \rightarrow \ell_\alpha^\pm (\nu_h \rightarrow \nu \ell_\beta^\pm \ell_\beta^-)$ and $\ell_\alpha^\pm \rightarrow \ell_\beta^\pm \nu (\nu_h \rightarrow \nu \ell^+ \ell^-)$. If the decays of ν_h are prompt, these could mimic rare SM 5-body decays, setting stringent constraints on $\Gamma_{M^\pm \rightarrow \ell_\alpha^\pm \nu_h} \propto |U_{\alpha h}|^2$. Measurements compatible with the SM prediction exist for pions [?, 302] and kaons [?, ?, 303], where the BR are of the order of 10^{-8} , and for muons [304] and taus [305], where the BR are around 10^{-5} . This type of signature can also lead to displaced vertices and are complementary to peak searches.

Neutrino scattering The presence of a light vector mediator and kinetic mixing can also enhance neutrino scattering cross sections. For a hadronic target Z , the active neutrinos may upscatter electromagnetically into ν_h , which subsequently decays into observable particles ($\nu_\alpha Z \rightarrow (\nu_h \rightarrow \nu \ell_\beta^+ \ell_\beta^-) Z$). Beyond explaining MiniBooNE, see below, such upscattering signatures can also produce exotic final states in neutrino detectors such as $\mu^+\mu^-$, $\tau^+\tau^-$ and multi-meson final states.

MiniBooNE low energy excess The above signatures with $\ell^\pm = e^\pm$ have been invoked as an explanation of the excess of electron-like low energy events at MiniBooNE in Ref. [167],

where a good fit to energy and angular data is achieved with a similar model containing a single heavy neutrino with $m_4 = 140$ MeV, $m_{Z'} = 1$ GeV and $\chi^2 = 5 \times 10^{-6}$. There, the prompt decays of ν_4 were achieved by requiring large mixing with the tau flavour. In a ESS-like limit of our current model, ν_4 would be dominantly produced via upscattering, decaying into $\nu_\alpha e^+ e^-$ inside the detector. A dedicated analysis to understand the resulting energy and angular distribution is underway.

Dark scalar searches For the scalar portal, the coupling $\lambda_{\Phi H}$ is rather weakly bound by electroweak precision data and the measurement of the Higgs invisible decay at the level of $\lambda_{\Phi H} \lesssim 0.1$ [306]. For processes involving $\lambda_{\Phi H}$, the physical observables are suppressed by mass insertions due to the nature of the Higgs interaction. Nevertheless, if φ' decays to ν_h states, this scalar may also lead to multi-lepton signatures inherited from ν_h decays, potentially also in the form of displaced vertices.

In the limiting case of a neutrinoophilic model ($\chi = \lambda_{\Phi H} = 0$), the vector and scalar particles present a challenge for detection. Nonetheless, if light, they can be searched for in meson decays [307, 308] and at neutrino experiments [174].

Finally, the faster decays of ν_h and its self-interactions can help ameliorate tensions with cosmological observations. We do not comment further on this, but note that great effort has been put into accommodating eV scale sterile neutrinos charged under new forces with cosmological observables [158–161, 164, 309, 310] (see also Ref. [198] for an interesting discussion where the Z' decay to neutrinos leads to an altered expansion history of the Universe). We note that an eV sterile neutrino with relatively large mixing could be easily accommodated in our ESS framework. The eV neutrino would be mainly in the ν_D direction and would have strong hidden gauge interactions.

5.2 Dark Matter

Given the presence of a dark sector, we can ask if the model can accommodate a DM candidate. This can be achieved introducing new fermions that do not mix with the neutrinos, in order to preserve their stability. A minimal solution would be to introduce a fermionic field ψ_L which has $U(1)'$ charge 1/2. The different charges of ψ , ν_D and

N would forbid neutrino mixing. A Majorana mass term $\psi_L^T C^\dagger \psi_L$ would emerge after hidden-symmetry breaking leading to a Majorana DM candidate.

Another minimal realisation has the advantage of being anomaly free. Following Ref. [281], we introduce a pair of chiral fermion fields ψ_L and ψ_R , and charge only the latter under the $U(1)'$ symmetry with the same charge as ν_D . This choice ensures anomaly cancellation, and allows us to write $y_\psi \overline{\psi_L} \psi_R \Phi^\dagger$, which after hidden-symmetry breaking yields a Dirac mass m_ψ . In order to avoid $\psi_R - \nu_D$ and $\psi_L - N$ mixing, an additional \mathbb{Z}_2 symmetry may be imposed, under which all particles have charge +1, except for ψ_L and ψ_R , which have charge -1.

If the scalar and vector portal couplings are small in such scenarios, DM interacts mainly with neutrinos. Direct detection bounds are then evaded, since interactions with matter are loop-suppressed. Indirect detection, on the other hand, is more promising as DM annihilation into neutrinos would dominate. For instance, take the mass of ψ to be smaller than the masses of the Z' , φ' and of both heavy neutrinos. In this case, the DM annihilation is directly into light neutrinos via $\psi\bar{\psi} \rightarrow \nu_i\nu_i$. This yields a mono-energetic neutrino line that can be looked for in large volume neutrino [311, 312] or direct detection experiments [264]. Alternatively, if m_ψ is larger than the mass of any of our new particles, then the annihilation may be predominantly into such states via $\psi\bar{\psi} \rightarrow XX$, where $X = \varphi', Z'$ or ν_h , which subsequently decay to light neutrinos. In this secluded realisation [313], the search strategy for DM can be very different since the neutrino spectrum from such annihilation is continuous [278]. Nevertheless, neutrino-DM interactions are expected to be large and can be searched for in a variety of ways [280, 314–317].

5.3 Radiative generation of neutrino masses

Neutrino oscillations have been established by several experiments [?, ?, 318], implying small but non-vanishing neutrino masses. In the Standard Model (SM), neutrinos are strictly massless due to the absence of right-handed neutrino fields, urging for extensions of the theory. The Type-I seesaw mechanism [?, ?, ?, ?, ?, ?, ?, ?, ?, 132], arguably the most popular mechanism to explain the lightness of neutrino masses, relies on the addition of at least 2 heavy right-handed neutrinos N_R . The large scales of N_R and/or the smallness of the Yukawa couplings makes the minimal realisation of this model difficult to test. Therefore,

searching for variations of the Type-I seesaw where novel and testable phenomena are present is an essential part of solving the neutrino mass puzzle [52]. A few notable examples of such alternatives are the Inverse Seesaw (ISS) [?, 282] and the Linear Seesaw (LSS) [?, ?, 319], where the lightness of neutrino masses is explained by an approximate conservation of lepton number, and the Extended Seesaw (ESS) [?, 283], where new heavy neutral fermions generally appear at small scales. This class of models assumes additional SM gauge neutral fermions that mix with light neutrinos, usually referred to as sterile neutrinos. These, however, need not be completely sterile and might have new gauge interactions shared with the SM fermions [247–255] or not [149, 256–258, 320]. In the latter case, we refer to these new heavy fermions as *dark neutrinos*. The interest in such particles arises from their novel interactions which may “leak” into the SM sector via neutrino mixing, where they offer a variety of phenomenological and cosmological consequences.

In this article, we consider the new minimal model introduced in Ref. [321]. It introduces two type of new neutral fermions, namely dark neutrinos ν_D and additional sterile neutrinos N . We impose a hidden $U(1)'$ gauge symmetry with the associated hidden gauge boson X_μ , which mediates the dark neutrino interactions. The symmetry is subsequently broken by the vacuum expectation value (vev) of a complex dark scalar Φ . As discussed in Ref. [321], the model can exhibit a significantly different phenomenology than the case of neutrino mixing only. Beyond evading many current bounds, such dark neutrinos could explain the MiniBooNE anomaly as discussed in [167] (see also [166]) and lead to novel neutrino scattering signatures [168]. Bounds on dark photons might also be severely weakened. If kinematically allowed, they would mainly decay into heavy neutrinos, which may be invisible or lead to multi-lepton plus missing energy signatures.

In this article, we discuss the generation of neutrino masses in our dark neutrino model. Crucially, the new gauge symmetry forbids Majorana mass terms for the ν_D states and, after symmetry breaking, leads to a mass matrix similar to the one in the so-called Minimal ISS [284]. As such, this symmetry-enhanced seesaw predicts vanishing light neutrino masses at tree-level. Here, we show that it induces their radiative generation via one-loop diagrams involving the new scalar and vector particles [257, 284, 322]. After identifying the range of heavy neutrino parameters required to explain the observed light neutrino masses, we point out interesting phenomenological consequences.

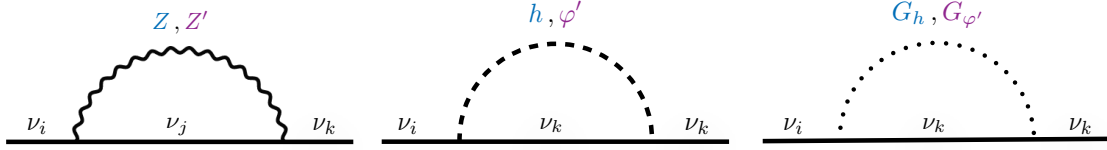


Fig. 5.2. The three contributions to the neutrino self-energy arising from novel bosons in the theory.

5.4 Model set-up

Following [321], we add two types of heavy neutral fermions to the SM, namely a dark neutrino $\nu_{D,L} \equiv \nu_D$ and a sterile state $N_L \equiv N$. For simplicity, we restrict the discussion to one generation in order to focus on the main features of the model.

We impose a new abelian gauge symmetry $U(1)'$ with associated mediator X_μ and introduce a neutral complex scalar Φ . No SM fields are charged under $U(1)'$. The scalar Φ and the fermion ν_D carry the same $U(1)'$ charge, while N remains completely neutral. The gauge-invariant Lagrangian is given by

$$\begin{aligned} \mathcal{L} = & \mathcal{L}_{\text{SM}} + (D_\mu \Phi)^\dagger (D^\mu \Phi) - V(\Phi, H) \\ & - \frac{1}{4} X^{\mu\nu} X_{\mu\nu} + \bar{N} i \not{\partial} N + \bar{\nu}_D i \not{\partial} \nu_D \\ & - \left[y_\nu^\alpha (\bar{L}_\alpha \cdot \tilde{H}) N^c + \frac{\mu'}{2} \bar{N} N^c + y_N \bar{N} \nu_D^c \Phi + \text{h.c.} \right], \end{aligned} \quad (5.4.1)$$

where $X^{\mu\nu} \equiv \partial^\mu X^\nu - \partial^\nu X^\mu$, $D_\mu \equiv (\partial_\mu - ig' X_\mu)$, $L_\alpha \equiv (\nu_\alpha^T, \ell_\alpha^T)^T$ is the SM leptonic doublet of flavour $\alpha = e, \mu, \tau$ and $\tilde{H} \equiv i\sigma_2 H^*$ is the charge conjugate of the SM Higgs doublet. In the neutral fermion sector, we have Yukawa couplings y_ν^α and y_N responsible for L_α - N and ν_D - N interactions, respectively, and a Majorana mass μ' for N . The latter term violates by two units any lepton number assignment which leaves the Yukawa term L_α - N invariant. As such, it plays a crucial role in the generation of light neutrino masses, as we discuss.

We are interested in the case in which both the neutral component of the fields H and Φ acquire non-vanishing vevs, v_H and v_φ . They induce mixing between active and heavy fermions, and give a mass to the gauge boson X_μ and to the real component of the scalar field φ . We are interested in proposing a model for neutrino masses which is testable in current and future non-collider experiments, and as such we focus on a new physics scale

which is below the electroweak one, $v_\varphi < v_H$. In addition to the neutrino portal, this model can accommodate a vector portal arising from vector kinetic mixing term and a scalar portal coming from the cross-coupling term $H^\dagger H \Phi^\dagger \Phi$ in the potential [321]. Kinetic mixing can be reabsorbed in a redefinition of vector fields, leading to a new gauge boson which has vector couplings to the SM fermions proportional to their electric charge. For our neutrino mass generation mechanism, the vector and scalar mixing do not play a relevant role and we set them to zero from here onward, unless otherwise specified. Regarding the vector boson, we refer to it as a Z' , independently of kinetic mixing.

5.5 Neutrino masses

After symmetry breaking, two Dirac mass terms are induced with $m_D \equiv y_\nu^\alpha v_H / \sqrt{2}$ and $\Lambda \equiv y_N v_\varphi / \sqrt{2}$. For one active neutrino ν_α , $\alpha = e, \mu, \tau$, the mass matrix is given by

$$\mathcal{L}_{\text{mass}} \supset \frac{1}{2} \begin{pmatrix} \bar{\nu}_\alpha & \bar{N} & \bar{\nu}_D \end{pmatrix} \begin{pmatrix} 0 & m_D & 0 \\ m_D & \mu' & \Lambda \\ 0 & \Lambda & 0 \end{pmatrix} \begin{pmatrix} \nu_\alpha^c \\ N^c \\ \nu_D^c \end{pmatrix} + \text{h.c.} \quad (5.5.1)$$

Let us emphasize the fact that in our model the zeros in the ν_D - ν_D and ν_α - ν_D entries are enforced by the $U(1)'$ symmetry, differently from LSS and ISS models, in which these are generically assumed to be nonzero and small due to the quasi-preservation of lepton number. Here, lepton number violation (LNV) may be large, as the μ' term breaks it by 2 units. Alternatively, it can be small and technically natural, leading to quasi-degenerate heavy neutrinos, see below.

After diagonalisation of the mass matrix, the two heavy neutrinos, ν_h ($h = 4, 5$), acquire masses

$$m_{4,5} = \frac{\mu' \mp \sqrt{\mu'^2 + 4(\Lambda^2 + m_D^2)}}{2}.$$

Assuming that $m_D \ll \Lambda$, we focus on two interesting limiting cases.

The ISS-like scenario is defined by $\Lambda \gg \mu'$: the two heavy neutrinos are nearly degenerate with a mass Λ and mass splitting μ' . The relevant mixing parameters are $U_{\alpha 4,5} \sim m_D / \sqrt{2}\Lambda$ and $U_{D4,5} \sim 1/\sqrt{2}$. The ESS-like case has $\Lambda \ll \mu'$: one neutral lepton remains very heavy, $m_5 \sim \mu'$, and mainly in the completely neutral direction N , and the other acquires a small

mass via the seesaw mechanism in the hidden sector with $m_4 \sim -\Lambda^2/\mu'$ and $U_{D5} \sim \Lambda/\mu'$. The mixing with active neutrinos is given by $U_{\alpha 5} \sim m_D/\mu' \ll U_{\alpha 4} \sim m_D/\Lambda$.

The specific form of the mass matrix in Eq. 5.5.1 implies vanishing light neutrino masses at tree level, as its determinant is zero [284, 323]. This feature holds to all orders in the seesaw expansion [323–325]. The light neutrino masses, however, are not protected by any symmetry and arise from radiative corrections (for a review of radiative neutrino mass models see, *e.g.*, Ref. [326]).

5.5.1 Radiative corrections

We now show that our model generically leads to the generation of light neutrino masses at one loop. The calculation of the radiative mass term follows Refs. [327, 328] with the addition of the loops with the new boson and scalar particles shown in Fig. 5.2. The self-energy of the Majorana neutrino fields is given by

$$\Sigma_{ij}(\not{q}) = \not{q} P_L \Sigma_{ij}^L(\not{q}) + \not{q} P_R \Sigma_{ij}^{L*}(\not{q}) + P_L \Sigma_{ij}^M(q^2) + P_R \Sigma_{ij}^{M*}(q^2).$$

Using the on-shell renormalization scheme, the renormalized mass matrix for the light neutrinos, massless at tree level, emerges at one-loop and is given by [328]

$$m_{ij}^{\text{one-loop}} = \text{Re} \left[\Sigma_{ij}^M(0) \right], \quad i, j < 4.$$

The self energy can be decomposed as

$$\begin{aligned} \Sigma_{ij}^M(0) = & \Sigma_{ij}^Z(0) + \Sigma_{ij}^h(0) + \Sigma_{ij}^{G_h}(0) + \\ & \Sigma_{ij}^{Z'}(0) + \Sigma_{ij}^{\varphi'}(0) + \Sigma_{ij}^{G_\varphi}(0), \end{aligned} \quad (5.5.2)$$

where Σ^{Z,h,G_h} come from the SM particles, Z^0 , the Higgs and the associated Goldstone boson, respectively, and $\Sigma^{Z',\varphi',G_\varphi}$ are the new terms present in our model, mediated by the new gauge boson and new scalar components. From it, we write the 3×3 light neutrino mass matrix

$$\begin{aligned} m_{ij} = & \frac{1}{4\pi^2} \sum_{k=4}^5 \left[C_{ik} C_{jk} \frac{m_k^3}{m_Z^2} F(m_k^2, m_Z^2, m_h^2) + \right. \\ & \left. D_{ik} D_{jk} \frac{m_k^3}{m_{Z'}^2} F(m_k^2, m_{Z'}^2, m_{\varphi'}^2) \right], \end{aligned} \quad (5.5.3)$$

where we defined coupling matrices corresponding to the SM and new physics interaction terms assuming $\chi = \lambda_{\Phi H} = 0$:

$$C_{ik} \equiv \frac{g}{4c_W} \sum_{\alpha=e}^{\tau} U_{\alpha i}^* U_{\alpha k} \quad \text{and} \quad D_{ik} \equiv \frac{g'}{2} U_{Di}^* U_{Dk}. \quad (5.5.4)$$

Equivalent expressions can be found for non-vanishing portal couplings, but considering experimental constraints we find that these do not play a role in the neutrino mass generation. It is possible to show that in general $\sum_k m_k C_{ik} C_{jk} = 0$ and $\sum_k m_k D_{ik} D_{jk} = 0$ for any i, j . By virtue of the latter property, the loop function can be written as

$$F(a, b, c) \equiv \frac{3 \ln(a/b)}{a/b - 1} + \frac{\ln(a/c)}{a/c - 1}. \quad (5.5.5)$$

Turning off the g' gauge coupling, we recover the expression for the Type-I seesaw case [327]:

$$m_{ij} = \frac{\alpha_W}{16\pi} \sum_{\alpha, \beta=e}^{\tau} U_{\alpha i}^* U_{\beta j}^* U_{\alpha 5} U_{\beta 5} \frac{m_5}{m_W^2} \times \\ (m_5^2 F(m_5^2, m_Z^2, m_h^2) - m_4^2 F(m_4^2, m_Z^2, m_h^2)). \quad (5.5.6)$$

These SM corrections to neutrino masses also arise in the Minimal ISS model [284, 323]. In the latter, however, no explanation is provided as to why they dominate neutrino masses. Moreover, if we restrict the discussion to scales well below the electroweak one, $m_5 \ll 10$ GeV, bounds on the mixing angles severely constrain the parameter space viable to generate the observed values of the masses.

For a light Z' , the second term in Eq. E.0.8 dominates

$$m_{ij} \simeq \frac{g'^2}{16\pi^2} U_{Di}^* U_{Dj}^* U_{D5}^2 \frac{m_5}{m_{Z'}^2} \times \\ (m_5^2 F(m_5^2, m_{Z'}^2, m_{\varphi'}^2) - m_4^2 F(m_4^2, m_{Z'}^2, m_{\varphi'}^2)). \quad (5.5.7)$$

We notice that the resulting mass matrix has only one nonzero eigenvalue. This suggests that a typical prediction of our model is a normal ordering mass spectrum, in which m_3 is given by this radiative mechanism and m_2 has another origin, for example the loops mediated by the SM gauge bosons or by additional particle content. Our simplifying assumption of one generation of hidden fermions is by no means necessary and more generations of new fermions are possible, leading to a much richer structure for the light neutrino mass matrix. The additional μ' terms would not be constrained and could be at different scales, while the Λ terms arise from the $U(1)'$ breaking and are therefore

constrained to be at/below v_φ . Therefore, the full model could present a combination of relatively light Majorana ν_h , mainly in dark direction, some very heavy nearly-neutral neutrinos and pseudo-Dirac pairs at intermediate scales. A discussion of this extension is beyond our scope, but we note that it has interesting consequences for both the heavy and light neutrino mass spectra and mixing structure.

Working in a single family case, we derive expressions for Eq. 5.5.7 in the seesaw limit for both the ISS and ESS-like scenarios. In the ISS-like regime and assuming $m_{Z'}, m_{\varphi'} \ll \Lambda$, Eq. (5.5.7) simplifies to

$$m_3 \simeq \frac{g'^2}{8\pi^2} \frac{m_D^2}{m_{Z'}^2} \mu' \left(3 \ln \frac{m_{Z'}^2}{\Lambda^2} + \ln \frac{m_{\varphi'}^2}{\Lambda^2} - 4 \right), \quad (5.5.8)$$

while for $m_{Z'}, m_{\varphi'} \gg \Lambda$ it reduces to

$$m_3 \simeq \frac{g'^2}{16\pi^2} \frac{m_D^2}{\Lambda^2} \mu' \left(3 + \frac{m_{\varphi'}^2}{m_{Z'}^2} \right). \quad (5.5.9)$$

As it can be expected, neutrino masses are controlled by the LNV parameter μ' and are enhanced with respect to the SM contribution by a factor of $(m_Z/m_{Z'})^2$ in the former, or $(m_Z/\Lambda)^2$ in the latter case.

For the ESS-like regime, taking $m_{Z'}, m_{\varphi'} \ll \mu'$, the light neutrino mass is approximately

$$m_3 \simeq \frac{g'^2}{16\pi^2} \frac{m_D^2}{\Lambda^2 + m_D^2} \frac{\Lambda^2}{m_{Z'}^2} \mu' \left(3 \ln \frac{m_{Z'}^2}{\mu'^2} + \ln \frac{m_{\varphi'}^2}{\mu'^2} \right), \quad (5.5.10)$$

while for $m_{Z'}, m_{\varphi'} \gg \mu'$, it is

$$m_3 \simeq \frac{g'^2}{8\pi^2} \frac{m_D^2}{\Lambda^2 + m_D^2} \frac{\Lambda^2}{\mu'} \left(3 \ln \frac{m_{Z'}^2}{\Lambda^2} + \ln \frac{m_{\varphi'}^2}{\Lambda^2} - 4 \right). \quad (5.5.11)$$

In this case, the light neutrino masses are controlled mainly by ν_5 , and the intermediate state ν_4 can be much lighter.

5.6 Searching for the origin of neutrino masses

In what follows, we discuss the experimental reach to the heavy neutrinos responsible for neutrino mass generation in our model. Since the vector and scalar portals do not contribute significantly to neutrino masses, we first restrict the study to the case $\chi = \lambda_{\Phi H} = 0$. For the sake of simplicity and concreteness, we work with a single generation of light neutrinos

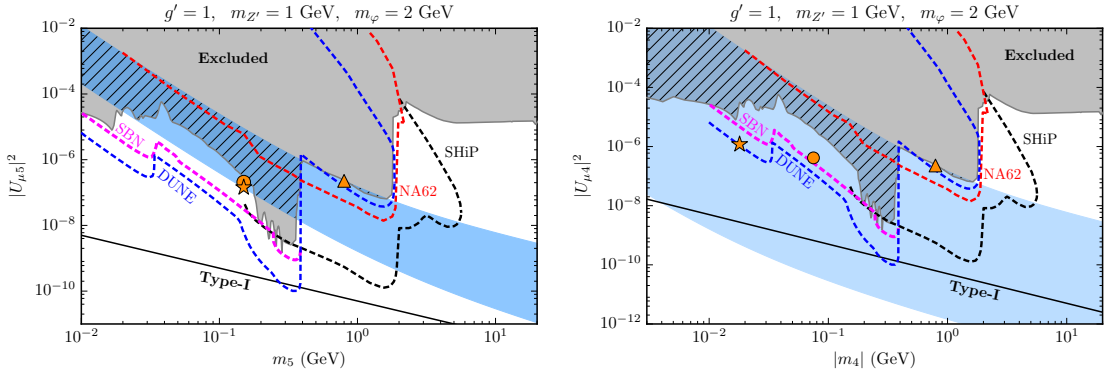


Fig. 5.3. The region of interest for neutrino mass generation in our model in the parameter space of the ν_5 (left) and ν_4 (right) mass states. We require $m_3 = \sqrt{\Delta m_{\text{atm}}^2}$ and vary $1\% < m_4/m_5 < 99\%$. Our BPs are \triangle) $m_5 = 800$ MeV, $m_4/m_5 = 99\%$, \circ) $m_5 = 150$ MeV, $m_4/m_5 = 50\%$ and \star) $m_5 = 150$ MeV, $m_4/m_5 = 12\%$. All bounds and projections displayed assume $\chi = \lambda_{\Phi H} = 0$. The dashed black line shows the equivalent Type-I seesaw contribution to the light neutrino mass.

and focus on the mixing with the muon neutrino. We emphasise that our model predicts

$$\frac{m_4}{m_5} = -\frac{U_{\alpha 5}^2}{U_{\alpha 4}^2}, \quad (5.6.1)$$

implying that both heavy neutrinos should be searched for. For a real mixing matrix one can write $\sum_i^3 U_{Di}^2 \sim U_{\mu 4}^2$ and $U_{D5}^2 \sim 1$ for small $U_{\mu 4}$. Using these relations and Eq. (E.0.8), we plot the region of interest for neutrino mass generation in Fig. 5.3. We require $m_3 = \sqrt{\Delta m_{\text{atm}}^2} \sim 0.05$ eV and vary m_4/m_5 from 1% (ESS-like) to 99% (ISS-like). For the hidden sector parameters, we fix $m_{Z'} = 1$ GeV, $m_{\varphi'} = 2$ GeV and $g' = 1$. By decreasing (increasing) the mass of the Z' , it is possible to shift the band to smaller (larger) values of the mixing angles, although for values smaller than a few hundred MeV, the neutrino masses have a very mild dependence on $m_{Z'}$ (Eqs. 5.5.9 and 5.5.11). Increasing m_4/m_5 to values closer to 100% (*i.e.*, decreasing μ' below $m_5/100$) shifts the top of the band to larger values of mixing angle and asymptotically recovers lepton number as a symmetry. Although this possibility appears excluded for $m_{Z'} = 1$ GeV, it can be achieved by lowering the mass of the mediator particles. For instance, for $m_{Z'} = m_{\varphi'}/2 = 100$ MeV and $m_5 < 100$ MeV, we find that values as small as $\mu' \gtrsim 10^{-3}m_5$ are not covered by the grey region in Fig. 5.3. Values of $m_4/m_5 < 1\%$ have no effect in the parameter space of ν_5 , since in that limit the ν_5 state (mostly in the N direction) dominates the loop contribution.

The region labelled as excluded in Fig. 5.3 is composed of bounds from peak searches [286–

288], beam dump [289–294] and collider experiments [329–331]. Current and future neutrino experiments can also cover a large region of parameter space with $m_h \lesssim 2$ GeV. For instance, we show the sensitivity of the Short-Baseline Neutrino program (SBN) [295] and of the Deep Underground Neutrino Experiment (DUNE) near detector [332, 333] to heavy neutrinos in decay-in-flight searches. We also show the reach of the NA62 Kaon factory operating in beam dump mode [334], and the dedicated beam dump experiment Search for Hidden Particles (SHiP) [335, 336], which will cover a much larger region of parameter space from 400 MeV to $\lesssim 6$ GeV. All bounds and sensitivities shown do not take into account the new invisible decays of the heavy neutrinos. Searches that rely on the visible decay products of the heavy neutrinos need to be revisited if the ν_h can decay invisibly or if new channels mediated by the vector (and/or scalar) portal dominate. In particular, faster decays of ν_h can shift decay-in-flight bounds to lower values of mixing angles, as discussed in detail in Ref. [295]. Peak searches apply as shown provided ν_h does not decay immediately via neutral-current channels with visible charged particles.

Let us first consider the case of subdominant vector and scalar portals. Compared to the “standard” sterile neutrino case, in which ν_h have only SM interactions suppressed by neutrino mixing, the new neutral-current interaction can enhance the ν_h decays into light and heavy neutrinos. A comprehensive analysis is beyond the scope of this article and we focus on three benchmark points (BP) shown in Fig. 5.3 to exemplify the most characteristic properties. The BP represented as a triangle (\triangle) corresponds to $m_5 = 800$ MeV and $m_4/m_5 = 99\%$. In this case, the two heavy states are very degenerate in mass and decay like a “standard” sterile neutrino via $|U_{\mu 4}|^2$ -suppressed SM charge- and neutral-current interactions. The channel $\nu_5 \rightarrow \nu_4 \nu_\alpha \bar{\nu}_\alpha$ via the Z' is phase space suppressed and becomes relevant only for larger mass splittings. The invisible ν_4 decay mediated by the Z' is subdominant as it scales as $|U_{\mu 4}|^6$ and becomes important only for larger values of the mixing angles.

For the next BPs we fix $m_5 = 150$ MeV. If we take $m_4/m_5 = 50\%$, as we do for the BP represented by the circle (\circ), ν_5 will predominantly decay to $\nu_4 \nu_\alpha \bar{\nu}_\alpha$ due to the Z' contribution (provided $|U_{\mu 5}|^2 \gtrsim (m_{Z'}/m_Z)^4$). Consequently, the best candidate for detection is the ν_4 via the SM weak decays $\nu_4 \rightarrow \nu_\alpha e^+ e^-$. The values of the mixing angles for this BP, $|U_{\mu 4}|^2 \sim 3 \times 10^{-7}$ and $|U_{\mu 5}|^2 \sim 10^{-7}$, are within reach of the SBN and DUNE

experiments. For a larger mass hierarchy, e.g. $m_4/m_5 = 12\%$, see star BP (\star), the Z' mediated decay $\nu_5 \rightarrow \nu_4 \bar{\nu}_4 \nu_4$ dominates, inducing a large ν_4 population in addition to the states already produced in the beam. The intermediate state ν_4 can further decay as in the previous case into $\nu_4 \rightarrow \nu_\alpha e^+ e^-$. For the mixing angles we are considering, $|U_{\mu 4}|^2 \sim 10^{-6}$ and $|U_{\mu 5}|^2 \sim 10^{-7}$, DUNE will be able to test this BP. Similar considerations apply to the case where $m_5 > m_4 + m_{Z'}$, where now the Z' can be produced on-shell in the ν_5 decay. The behaviour of ν_4 is as discussed above. If $m_{Z'} < m_4$, then both heavy neutrinos predominantly decay into neutrinos and the Z' , which presents a challenge for detection as it produces mainly light neutrinos.

Experimental detection of the Z' and φ' particles in the absence of kinetic and scalar mixing is also daunting. Nevertheless, they can be searched for in the kinematics of charged particles from meson decays [307, 308]. Another strategy is to search for the neutrino byproducts of the decay of a Z' produced at accelerator neutrino facilities [174].

If the vector (and scalar) portals are non-negligible, the phenomenology could be significantly richer, as discussed in [321]. In particular, Z' -mediated decays into $\nu_\alpha e^+ e^-$, and $\nu_\alpha \mu^+ \mu^-$ if kinematically allowed, could dominate even for tiny values of χ^2 . For instance, for the circle BP, χ^2 as low as 10^{-8} would make the above decays the main channels. Pseudo-scalar final states are suppressed due to the vector nature of the Z' . The scalar portal is expected to give subdominant contributions due to the small Higgs-electron Yukawa coupling, although decay chains with intermediate ν_4 states may become relevant. Finally, cosmological bounds on heavy neutrino in the 10 MeV – GeV scale may be weakened as they would decay well before Big Bang Nucleosynthesis [337] (see also the discussion in Ref. [?, ?, ?, ?, ?, ?, ?, 158])

We have focused on the mixing with muon neutrinos as these provide one of the most sensitive avenue to test the model. In the electron sector, direct bounds on the active-heavy mixing are similar, with peak searches from π^\pm decay being most relevant below ≈ 100 MeV. For cases with large LNV, heavy neutrinos can dominate neutrinoless double beta decay [323], and this sets the strongest constraints in the parameter space. The tau sector is relatively poorly constrained, so greater freedom exists if such entries are relevant for neutrino mass generation.

Chapter 6

Tests of the MiniBooNE anomaly

The MiniBooNE excess is currently in tension with the standard three-neutrino prediction at a level of 4.7σ [338]. While it is possible that the excess is fully or partially due to systematic uncertainties or SM backgrounds (see, *e.g.*, [339–341]), many Beyond the Standard Model (BSM) explanations have been put forth. These new physics (NP) scenarios typically require the existence of new particles, which can: participate in short-baseline oscillations [342–364], change the neutrino propagation in matter [361,365–367], be produced in the beam or in the detector and its surroundings [267–269,368–372]. These models either increase the conversion of muon- to electron-neutrinos or produce electron-neutrino-like signatures in the detector, where in the latter category one typically exploits the fact that the LSND and MiniBooNE are Cherenkov detectors that cannot distinguish between electrons and photons. Although it is possible to consider MiniBooNE explanations that have little to no theoretical motivation, recent models [166,167,320] are motivated by neutrino-mass generation via hidden interactions in the heavy neutrino sector. In particular, the common feature of these models is the upscattering into a heavy neutrino, usually with tens to hundreds of MeV in mass, which subsequently decays into a pair of electrons. If collimated, this pair of electrons can fake a single-electron signature.

In this article, we introduce new techniques to probe these testable neutrino mass generation models in past, present, and future neutrino experiments. In addition, our analysis showcases a generic way to look for models that rely on the ambiguity between photons and electrons to explain the MiniBooNE observation. Due to the electron-like nature of the excess, we consider neutrino-electron scattering measurements [179,226,231,232,373].

Although these experiments have been shown to provide powerful constraints on light NP [62, 374, 375], the unique topology of the signatures we consider requires us to go beyond the final processed sample quoted by the experiments and develop new ways to search for them. Since the typical heavy neutrino mass is in the hundreds-of-MeV regime, we focus on two high-energy neutrino experiments: MINER ν A [179, 224, 376] and CHARM-II [231, 377, 378]. These experiments are complementary in neutrino energy and background composition. In both cases we make use of sideband measurements, taking advantage of the excellent particle reconstruction capabilities of MINER ν A and the precise measurements at CHARM-II to constrain NP.

6.1 Dark neutrinos at MiniBooNE

Non-zero neutrino masses have been established in the last twenty years by measurements of neutrino flavor conversion in natural and human-made sources, including long- and short-baseline experiments. The overwhelming majority of data points towards a three-neutrino framework. Within this framework, we have measured the mixing angles that parametrize the relationship between mass and flavor eigenstates to percent-level precision [151]. The remaining unknowns are the absolute scale of neutrino masses and their origin, the CP-violating phase, and the mass ordering of the neutrinos. In addition, anomalies in short-baseline accelerator and reactor experiments [265, 338, 379, 380] are yet to have satisfying explanations. The most significant anomalies are beyond statistical doubt. Minimal extensions of the three-neutrino framework to explain the anomalies introduce the so-called sterile neutrino states, which do not participate in Standard Model (SM) interactions in order to agree with measurements of the Z-boson invisible decay width [381]. Unfortunately, these minimal scenarios are disfavoured as they fail to explain all data [382–384]. This has led the community to explore nonminimal scenarios. Along this direction, it is interesting to study well-motivated neutrino-mass models that can also explain the short-baseline anomalies and are testable in the laboratory. In this work, we will examine the class of neutrino-mass-related models that have been proposed as an explanation of the anomalous observation of electron-neutrino-like events in MiniBooNE [338].

We limit our discussion to the minimal version of the model that could explain the MiniBooNE excess. This contains at least one heavy neutrino, ν_D , charged under a new $U(1)'$

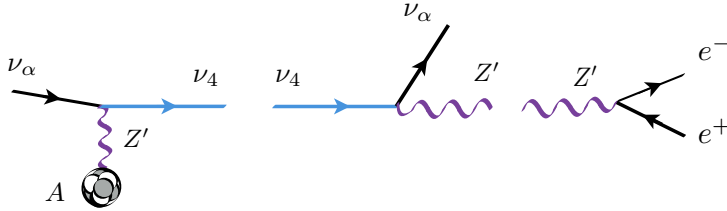


Fig. 6.1. Illustration of heavy neutrino production. Left: production of the heavy mass state via upscattering. Center: Decay of the heavy neutrino into a light neutrino and a gauge boson. Right: Decay of a gauge boson into a pair of electrons that produce the experimental signature.

gauge group, which is part of the particle content and gauge structure needed for mass generation. The ν_D can be either of a Dirac or Majorana [320] nature. In this paper, we show our results for a Dirac particle since the Majorana case is more severely in tension with the angular distribution [385, 386]. The dark sector is connected to the SM in two ways: through kinetic mixing between the new gauge boson and hypercharge, and through neutrino mass mixing. We start by specifying the kinetic part of the NP Lagrangian

$$\mathcal{L}_{\text{kin}} \supset \frac{1}{4} \hat{Z}'_{\mu\nu} \hat{Z}'^{\mu\nu} + \frac{\sin \chi}{2} \hat{Z}'_{\mu\nu} \hat{B}^{\mu\nu} + \frac{m_{Z'}^2}{2} \hat{Z}'^\mu \hat{Z}'_\mu, \quad (6.1.1)$$

where \hat{Z}'^μ stands for the new gauge boson field, $\hat{Z}'^{\mu\nu}$ its field strength, and $\hat{B}^{\mu\nu}$ the hypercharge field strength. After usual field redefinitions [387], we arrive at the physical states of the theory. Working at leading order in χ and assuming $m_{Z'}^2/m_Z^2$ to be small, we can specify the relevant interaction Lagrangian as

$$\mathcal{L}_{\text{int}} \supset g_D \bar{\nu}_D \gamma_\mu \nu_D Z'^\mu + e \varepsilon Z'^\mu J_\mu^{\text{EM}}, \quad (6.1.2)$$

where J_μ^{EM} is the SM electromagnetic current, g_D is the $U(1)'$ gauge coupling assumed to be $\mathcal{O}(1)$, and $\varepsilon \equiv c_w \chi$, with c_w being the cosine of the weak angle. Additional terms would be present at higher orders in χ and mass mixing with the SM Z is also possible, though severely constrained. After electroweak symmetry breaking, the dark neutrino ν_D is a superposition of neutrino mass states. The flavor and mass eigenstates are related via

$$\nu_\alpha = \sum_{i=1}^4 U_{\alpha i} \nu_i, \quad (\alpha = e, \mu, \tau, D), \quad (6.1.3)$$

where U is a 4×4 unitary matrix. It is expected that $|U_{\alpha 4}|$ is small for $\alpha = e, \mu, \tau$, but $|U_{D 4}|$ can be of $\mathcal{O}(1)$ [382, 388]. The choice of m_4 and $m_{Z'}$ has important consequences for the allowed decays of the new particle content. We focus on the case in which $m_4 > m_{Z'}$,

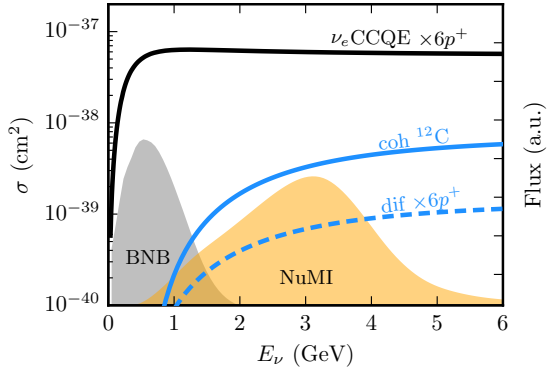


Fig. 6.2. Upscattering cross section compared to the quasi-elastic. The quasi-elastic cross section for $6p^+$ is shown as a function of the neutrino energy (solid black line). Similarly the coherent, out of a carbon atom, and the diffractive NP contributions for the benchmark point of [166] are shown as solid and dashed blue lines, respectively. In the background, the light gray shaded region is the Booster Neutrino Beam (BNB) flux shape, while the light golden region is the Neutrinos at the Main Injector (NuMI) low-energy neutrino-mode flux.

where the two body $\nu_4 \rightarrow \nu_\alpha Z'$ decay is allowed. In addition, the mass of the new gauge boson is kept below ~ 100 MeV, making the decay into e^+e^- pairs the dominant channel. Decay into a pair of neutrinos is possible, but is subdominant provided the mixing is small.

6.2 Dark neutrinos in neutrino-electron scattering measurements

As illustrated in Fig. 6.1, the heavy neutrino is produced by upscattering from an active neutrino flavour state. The production cross section is proportional to $\alpha_D \alpha_{\text{QED}} \varepsilon^2 |U_{\alpha 4}|^2$, usually dominated by the muon-neutrino contribution due to the flavor composition of the beam. This production can happen off the whole nucleus in a coherent way or off individual nucleons. For $m_{Z'} \lesssim 100$ MeV, the production will be mainly coherent, but for heavier masses, such as the ones considered in [167], the upscattering happens predominantly in a diffractive regime. In Fig. 6.2, we show the cross section at the benchmark point of [320] and compare it with the quasi-elastic cross section. By superimposing the cross section on the neutrino fluxes of MINERνA and MiniBooNE, we make it explicit that the larger energies at MINERνA and CHARM-II are ideal to probe these models. Once produced, ν_4 is then expected to decay promptly inside of the detector, setting a requirement on

its lifetime. The mass of the heavy neutrino also controls the angular distribution of the signal with respect to the beam. The lighter ν_4 is, the more forward the signal will be. The produced Z' is required to decay into an overlapping e^+e^- pair, setting a lower bound on its mass of a few MeV. To summarize, increasing $m_{Z'}$ has two effects. On one hand, it increases the ratio of diffractive to coherent upscattering, and on the other hand, it makes the electron pair less collimated. Even though we focus on overlapping e^+e^- pairs, we note that a significant fraction of events would appear as well-separated electrons or as a pair of electrons with large energy asymmetry, similarly to the neutral current π^0 events. The asymmetric events also contribute to the MiniBooNE excess and can also be looked for in $\nu - e$ scattering analyses.

6.3 MINER ν A and CHARM-II analyses

Neutrino-electron scattering measurements at MINER ν A and CHARM-II predicate their cuts in the following core ideas: no hadronic activity near the interaction vertex, small opening angle from the beam, $E_e\theta^2 < 2m_e$, and the requirement that the measured energy deposition dE/dx be consistent with that of a single electron. When the coherent process dominates and the mass of the Z' is small, the first two conditions are satisfied. However, the requirement of a single-electron-like energy deposition removes a significant fraction of the new-physics induced events. This presents a challenge, as the signal events are mostly overlapping electron pairs and will potentially be removed by the dE/dx cut. In order to circumvent this problem, we do our analysis not at the final-cut level, but at an intermediate one. The CHARM-II experiment provides data as a function of $E_e\theta^2$ without the dE/dx cut, and in the case of MINER ν A we have access to the data as a function of the measured dE/dx after analysis cuts on $E_e\theta^2$.

We briefly describe the main features of the MINER ν A event selection here (for more details see [224]). The minimum electron energy required is 0.8 GeV in order to remove the π^0 background and have reliable angular and energy reconstruction. Events are kept only when they meet the following angular separation criterion: $E_e\theta^2 < 3.2 \times 10^{-3}$ GeV rad 2 . A final cut is applied, ensuring $dE/dx < 4.5$ MeV/1.7 cm. The MINER ν A analysis uses the data outside the previous dE/dx cut to constrain backgrounds. This sideband is defined as all events with $E_e\theta^2 > 5 \times 10^{-3}$ GeV rad 2 and $dE/dx < 20$ MeV/1.7 cm. Using this

sideband measurement, the collaboration tunes their backgrounds by (0.76, 0.64, 1.0) for (ν_e CCQE, ν_μ NC, ν_μ CCQE) processes. We perform our analysis with the data shown in Fig. 3 of [224] where all the cuts are applied except for the final dE/dx cut. We have developed our own Monte Carlo (MC) to simulate candidate electron pair events; in our MC simulation, detector-resolution effects are assumed to be Gaussian with appropriate widths taken from [218]. We only consider the coherent part of the cross section to avoid hadronic-activity cuts, which is conservative. We also select only events with small energy asymmetries and small opening electron angles. We calculate the mean dE/dx in plastic scintillators [389] according to [390, 391]. In our final event selection, we require that the sum of the energy deposited by each electron be more than 4.5 MeV/1.7 cm, which yields an efficiency of 90%. We obtain the expected size of neutrino-electron scattering and background events in this range from Fig. 3 of [224]. To place our limits, we perform a rate-only analysis by means of a χ^2 test statistic. We incorporate uncertainties in background size and flux normalization as nuisance parameters with Gaussian constraint terms. For the neutrino electron scattering and BSM signal, we allow the normalization to scale proportionally to the same flux uncertainty parameter. The background term also scales with the flux-uncertainty parameter but has an additional nuisance parameter to account for its unknown size. We obtain our constraint as a function of heavy neutrino mass m_4 , and mixing $|U_{\mu 4}|$ assuming with two degrees of freedom [391]. In our nominal MINER ν A analysis, we allow for 30% uncertainty on the background motivated by the amount of tuning performed on the original backgrounds. Note that the nominal background predictions in the MINER ν A analysis overpredicts the data before tuning, and that tuning parameters are measured at the 3% level [179]. We also perform a background-ignorant analysis in which we assume 100% uncertainty for the background normalization, which changes our conclusions by only less than a factor of two. This emphasizes the robustness of our MINER ν A bound, since the NP typically overshoots the low number of events in the sideband.

Our CHARM-II analysis is mostly based on Fig. 1 of [231]. This sample is shown as a function of $E\theta^2$ and does not have any cuts on dE/dx . The NP signal lies mostly in a region with small $E\theta^2$. Thus, we constrain backgrounds using the data from $30 < E\theta^2 < 60$ MeV rad 2 . This sideband measurement constrains the normalization of the backgrounds in the signal region at the level of 3%. The extrapolation of the shape of the background

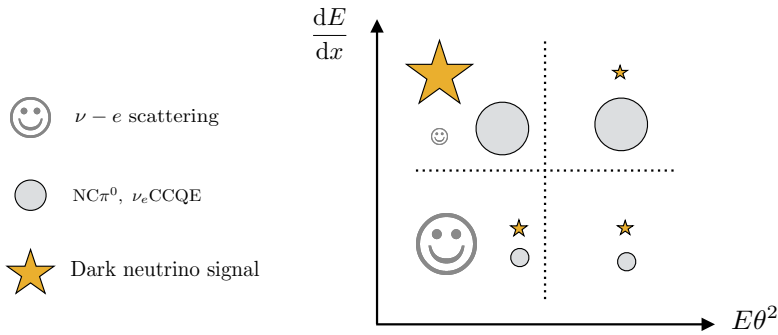


Fig. 6.3. A schematic representation of the relative number of events in sideband regions of neutrino-electron scattering analyses.

to the signal region introduces the largest uncertainty in our analysis. For this reason, we raise the uncertainty of the background normalization from 3% to a conservative 10% when setting the limits. Flux uncertainties are assumed to be 4% [392] and are applicable to the new-physics signal, $\nu - e$ scattering prediction, and backgrounds. Our χ^2 test is similar to the one used in the MINER ν A analysis and carries normalization nuisance parameters for the background and flux predictions. Uncertainties in the $\nu - e$ scattering cross sections are expected to be sub-dominant and are neglected in the analysis [60].

We have performed our own fit to the MiniBooNE energy spectrum using the data release from [338], and our results agree with [166]. The data release, however, only contains information about the neutrino energy and baseline distance. Thus, the re-weighting procedure for the model of interest can only be performed approximately. A proper analysis can be performed only if true and reconstructed electron angles and energies per simulated event are given.

6.4 Results and prospects

The resulting limits at 90% confidence level (CL) in the $|U_{\mu 4}|$ vs m_4 plane are shown in Fig. 6.4, together with the MiniBooNE fit from [166]. For comparison, we have chosen the same values of ε , α_D , and $m_{Z'}$ as used in [166]. We note that the MiniBooNE event rate scales identically to our signal rate in all the couplings, and the dependence of our bounds on $m_{Z'}$ is subleading due to the large Q^2 involved. This implies that changing the values of these parameters does not modify the overall conclusions of our work. In

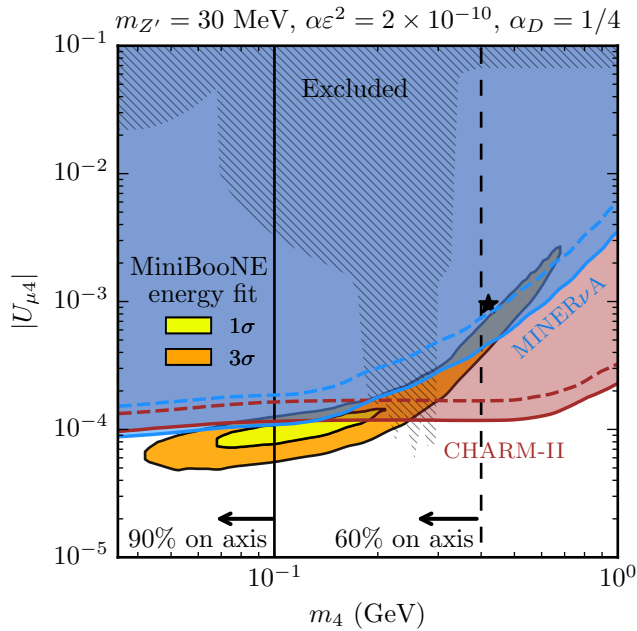


Fig. 6.4. *New constraints on mass generation model as a MiniBooNE explanation.* The MiniBooNE region of interest from [166], only fitted to the energy distribution, is shown as closed yellow (orange) regions for one (three) sigma C.L. The benchmark point, chosen to provide a good angular distribution fit, is shown as a black star. Exclusion from heavy neutrino searches is shown as a hatched background. Our new constraints at 90% C.L. using MINER ν A are shown in blue for our nominal 30% background normalization uncertainty (solid) and conservative case of 100% background uncertainty (dashed). Our CHARM-II bound is shown in cherry red, where the 3% background normalization from the sideband is shown as a solid curve and the conservative 10% case as a dashed curve. The solid vertical black line at 100 MeV signals the point where 90% of NP events lie in the most forward bin in the MiniBooNE angular distribution, and the dashed one where 60% of events do so. Other relevant assumed parameters are shown above the plot; changing them does not change our conclusion.

addition, one can lower the value of $m_{Z'}$ to only around 10 MeV before hitting beam dump constraints [177]. On the other hand, for this realization of the model, larger $m_{Z'}$ implies larger values of m_4 , increasing the tension between the MiniBooNE fit and our bounds. Our results from MINER ν A and CHARM-II are compatible given that they impose similar constraints for $m_4 \lesssim 200$ MeV. For larger masses, the kinematics of the signal becomes less forward and the production thresholds start being important. This explains the upturns visible in our bounds, where we observe it first in MINER ν A and later in CHARM-II as we increase m_4 , since CHARM-II has higher beam energy and the neutrino flux peaks at approximately 20 GeV.

The preferred region of [166] results from doing an energy-spectrum only fit to the MiniBooNE data. This neglects the angular distribution of the MiniBooNE excess. The

preferred region of this energy-only fit is excluded by our analysis for masses of m_4 greater than ≈ 250 MeV. As was recently pointed out in [393], reasonable angular distribution of NP explanations of the MiniBooNE excess requires hundreds of MeV NP particles. Since the released MiniBooNE data do not provide the correlation between angle and energy and their associated systematics, a rigorous assessment of the tension is hard to quantify. The angular distribution of observed excess contains $\approx 50\%$ of the events in the most forward bin, with a statistical uncorrelated uncertainty of 5% on this quantity. We use this information and our calculation of the angular distribution of the NP events from our dedicated MC to give an assessment of the tension in this observable. We draw a vertical line at $m_4 = 100$ MeV, where 90% of the NP events would lie in the most forward bin and a dashed line at 60%. This 60% line, as expected, is close to the benchmark point of [320]. This consideration suggests that our analysis targets precisely the region where the model can lead to agreement in the angular data.

In the near future, the MINER ν A medium-energy results on neutrino-electron scattering will be available. With the increase in energy, we estimate that it can improve the probe significantly if backgrounds, which are also rising, are well understood. This class of analyses will thus greatly benefit from improved calculations and measurements of coherent π^0 production and single-photon emitting processes. This is particularly important if an excess is observed in these channels. A complementary result can also be obtained by measuring this process in NO ν A, which will sample a different kinematic regime as its off-axis beam peaks at lower energies and expects fewer NC π^0 events per ton. Interestingly, we note that this class of BSM signatures could be lurking in current measurements of π^0 production, *e.g.*, at MINOS [394] and MINER ν A [395]. The latter measurement observes a significant excess of diffractive events, which are abundant in similar realizations of this NP model [167]. To summarize, a variety of measurements are underway to further lay siege to this explanation of the MiniBooNE observation and, simultaneously, start probing testable neutrino mass generation models, as well as other similar NP signatures. It is clear that understanding neutrino cross sections will be crucial as we move forward.

Chapter 7

The future of neutrino precision physics

Chapter 8

Conclusions

Particle physics is at a very important moment of its history. The Standard Model has surprised us with its unprecedent accuracy in describing particle data, but a few mysteries remain. Perhaps neutrino masses and dark matter are to the Standard Model what blackbody radiation was to classical physics in the beginning of the 20th century, a scientific revolution on the wait.

Appendix A

Phase space

In this appendix we derive some key results for the phase space treatment we use in calculating cross sections and decay rates. We begin with the factorization of N -final state phase-space factors into $N - 2$ two-body ones. In general, the N -body phase space can be written as

$$d\Phi_N(P, \{p_i\}) = (2\pi)^4 \delta^4(P - \sum_i^N p_i) \prod_i^N \frac{d^3 p_i}{(2\pi)^3 2E_i}, \quad (\text{A.0.1})$$

where $\{p_i\} = p_1, \dots, p_N$. Focusing on the 1-2 subsystem with total momentum $p_{12} = p_1 + p_2$, we can write

$$\begin{aligned} d\Phi_N(P, \{p_i\}) &= \int d^4 p_{12} \delta^4(p_{12} - p_1 - p_2) (2\pi)^4 \delta^4(P - \sum_i^N p_i) \prod_i^N \frac{d^3 p_i}{(2\pi)^3 2E_i} \\ &= \int d^4 p_{12} d\Phi_2(p_{12}, p_1, p_2) (2\pi)^4 \delta^4(P - p_{12} - \sum_{i=3}^N p_i) \prod_{i=3}^N \frac{d^3 p_i}{(2\pi)^3 2E_i} \\ &= \int d^4 p_{12} dm_{12}^2 \delta(p_{12}^2 - m_{12}^2) d\Phi_2(p_{12}, p_1, p_2) \\ &\quad \times (2\pi)^4 \delta^4(P - p_{12} - \sum_{i=3}^N p_i) \prod_{i=3}^N \frac{d^3 p_i}{(2\pi)^3 2E_i}, \quad (\text{A.0.2}) \end{aligned}$$

which from

$$\int d^4 p_{12} \delta(p_{12}^2 - m_{12}^2) = \int d^4 p_{12} \frac{\delta(E_{12} - \sqrt{m_{12}^2 + |\vec{p}_{12}|^2})}{2\sqrt{m_{12}^2 + |\vec{p}_{12}|^2}} = \int \frac{d^3 p_{12}}{2E_{12}},$$

yields the final results

$$d\Phi_N(P, p_1, \dots, p_N) = \frac{dm_{12}^2}{2\pi} d\Phi_2(p_{12}, p_1, p_2) d\Phi_N(P, p_{12}, p_3, \dots, p_N). \quad (\text{A.0.3})$$

This result not only lets us factorize any resonant features in phase space, but also provides a recipe to tackle the kinematics of any process in terms of a series of 2-body problems, which are much simpler. The 2-body phase-space factors and associated four-momenta in the respective center-of-mass (CM) frame can always be written as

$$\begin{aligned} d\Phi_2(p_{12}, p_1, p_2) &= \frac{\lambda^{1/2} \left(1, m_1^2/E_{12}^{\text{CM}\,2}, m_2^2/E_{12}^{\text{CM}\,2}\right)}{32\pi^2} d\Omega^{\text{CM}}, \\ p_{12} &= \left(E_{12}^{\text{CM}}, \vec{0}\right), \\ p_1 &= \left(\frac{E_{12}^{\text{CM}\,2} + m_1^2 - m_2^2}{2E_{12}^{\text{CM}\,2}}, |\vec{p}_1| \sin \theta \cos \phi, |\vec{p}_1| \sin \theta \sin \phi, |\vec{p}_1| \cos \theta\right), \\ p_2 &= \left(\frac{E_{12}^{\text{CM}\,2} + m_2^2 - m_1^2}{2E_{12}^{\text{CM}\,2}}, -\vec{p}_1\right), \end{aligned} \quad (\text{A.0.4})$$

where $\lambda(a, b, c) = (a - b - c)^2 - 4bc$ is the Källén function. Now, the problem is reduced to finding the CM frame of every p_{ij} subsystem, and the transformation between all such frames, if necessary. Of course, the dependence of the matrix element on the kinematics makes certain phase space parametrization better than others, making each problem unique. Lab variables, for instance, are the standard parametrization for DIS scattering as they preserve crucial physical intuition of the process at hand.

Dark-bremsstrahlung Here we take the Dark-Bremsstrahlung (DB) process discussed in Section ?? as an example of a 3-body phase space. In this process, the neutrino scatters off the nuclear target with momentum exchange $Q^2 = ()$.

Neutrino trident production Now we derive a phase space parametrization for neutrino trident production in terms of the momentum transfer $K^2 = 2p_1 \cdot p_2$. This is important if one wants to change variables to smooth out the integrand at low $M_{Z'}$ masses. We follow the calculation in [208] and [181], and proceed to define K^2 as one of the integration variables. The relevant Lorentz invariant phase space for the $2 \rightarrow 3$ leptonic part of the

cross section is given by

$$\int d^3\Pi_{\text{LIPS}} = \int \frac{d\vec{p}_2}{(2\pi)^3 2E_2} \frac{d\vec{p}_3}{(2\pi)^3 2E_3} \frac{d\vec{p}_4}{(2\pi)^3 2E_4} (2\pi)^4 \delta^{(4)}(p_1 + q - p_2 - p_3 - p_4). \quad (\text{A.0.5})$$

Following [208] we start by working in the frame $\vec{p}_1 + \vec{q} - \vec{p}_3 = 0$, putting \vec{p}_1 along the \hat{z} direction instead. The delta function can be integrated with the \vec{p}_4 and $|\vec{p}_2|$ integrals, such that

$$\int \frac{d\vec{p}_2}{2E_2} \frac{d\vec{p}_4}{2E_4} \delta^{(4)}(p_1 + q - p_2 - p_3 - p_4) = \int \frac{|\vec{p}_2|}{4W_c} \frac{1}{E_1 E_2} dK^2 d\phi_2, \quad (\text{A.0.6})$$

where we defined

$$\begin{aligned} |\vec{p}_2| &= (W_c^2 - m_1^2)/2W_c, \\ W_c &= q^0 + E_1 - E_3, \\ K^2 &= 2E_1 E_2 (1 - \cos \theta_2). \end{aligned} \quad (\text{A.0.7})$$

Since we conserve energy and momentum in this frame, we can take $-1 \leq \cos \theta_2 \leq 1$ and $0 \leq \phi_2 \leq 2\pi$. The remaining \vec{p}_3 integral can be performed with the variables defined in [208] to yield

$$\int \frac{d\vec{p}_3}{2E_3} = \int \frac{2\pi}{\hat{s}} dx_5 dx_3, \quad (\text{A.0.8})$$

where a trivial azimuthal angle was integrated over. Their limits are more easily found in the frame $\vec{p}_1 + \vec{q} = 0$, with \vec{q} along the \hat{z} direction. Finally, our main result is given by

$$\int d^3\Pi_{\text{LIPS}} = \frac{1}{(2\pi)^4} \int \frac{|\vec{p}_2|}{4W_c} \frac{1}{\hat{s}} \frac{1}{E_1 E_2} dx_5 dx_3 dK^2 d\phi_2. \quad (\text{A.0.9})$$

There remains two non-trivial integrations to be performed to obtain the full 4-body phase space cross section, namely the ones over q^2 and \hat{s} . The substitutions suggested in [209] for these two invariants are still convenient, and we make use of them in our numerical

integrations.

Appendix B

Form factors

Electromagnetic form factors In the coherent regime, we use a Woods-Saxon (WS) form factor due to its success in reproducing the experimental data [396, 397]. The WS form factor is the Fourier transform of the nuclear charge distribution, defined as

$$\rho(r) = \frac{\rho_0}{1 + \exp\left(\frac{r - r_0}{a}\right)}, \quad (\text{B.0.1})$$

where we take $r_0 = 1.126 A^{1/3}$ fm and $a = 0.523$ fm. One can then calculate the WS form factor as

$$F(Q^2) = \frac{1}{\int \rho(r) d^3r} \int \rho(r) \exp(-i\vec{q} \cdot \vec{r}) d^3r. \quad (\text{B.0.2})$$

Here we use an analytic expression for the symmetrized Fermi function [398, 399] instead of calculating the WS form factor numerically. This symmetrized form is found to agree very well with the full calculation and reads

$$F(Q^2) = \frac{3\pi a}{r_0^2 + \pi^2 a^2} \frac{\pi a \coth(\pi Q a) \sin(Qr_0) - r_0 \cos(Qr_0)}{Qr_0 \sinh(\pi Q a)}. \quad (\text{B.0.3})$$

In the incoherent regime, we work with the functions $H_1^N(Q^2)$ and $H_2^N(Q^2)$, which depend on the Dirac and Pauli form factors of the nucleon N as follows

$$H_1^N(Q^2) = |F_1^N(Q^2)|^2 - \tau |F_2^N(Q^2)|^2, \quad \text{and} \quad H_2^N(Q^2) = \left| F_1^N(Q^2) + F_2^N(Q^2) \right|^2, \quad (\text{B.0.4})$$

where $\tau = -Q^2/4M^2$. The form factors $F_1^N(Q^2)$ and $F_2^N(Q^2)$ can be related to the usual Sachs electric G_E and magnetic G_M form factors. These have a simple dipole

parametrization

$$G_E^N(Q^2) = F_1^N(Q^2) + \tau F_2^N(Q^2) = \begin{cases} 0, & \text{if } N = n, \\ G_D(Q^2), & \text{if } N = p, \end{cases} \quad (\text{B.0.5})$$

$$G_M^N(Q^2) = F_1^N(Q^2) + F_2^N(Q^2) = \begin{cases} \mu_n G_D(Q^2), & \text{if } N = n, \\ \mu_p G_D(Q^2), & \text{if } N = p, \end{cases} \quad (\text{B.0.6})$$

where $\mu_{p,n}$ is the nucleon magnetic moment in units of the nuclear magneton and $G_D(Q^2) = (1 + Q^2/M_V^2)^{-2}$ is a simple dipole form factor with $M_V = 0.84$ GeV.

Neutral current form factor Here we show our weak hadronic current used in the dark-bremsstrahlung calculation. Similarly to the electromagnetic case, we write the weak hadronic current for a spin-0 nucleus with Z protons and N neutrons as

$$\begin{aligned} H_W^\mu &= \langle \mathcal{H}(k_3) | J_W^\mu(Q^2) | \mathcal{H}(k_b) \rangle \\ &= Q_W(k_b + k_3)^\mu F_W(Q^2), \end{aligned} \quad (\text{B.0.7})$$

% where $Q_W = (1 - 4s_w^2)Z - N$ and $F_W(Q^2)$ stands for the weak form factor of the nucleus.

We implement the Helm form factor as in [400], defined as

$$|F(Q^2)|^2 = \left(\frac{3j_1(QR)}{QR} \right)^2 e^{-Q^2 s^2}, \quad (\text{B.0.8})$$

where $j_1(x)$ stands for the spherical Bessel function of the first kind, $s = 0.9$ fm and $R = 3.9$ fm for ${}^{40}\text{Ar}$.

Appendix C

Trident distributions

In this appendix we explore the trident signal in more detail, showing some relevant kinematical distributions for coherent and diffractive events. For concreteness, and due to its large number of events, we choose to focus on the DUNE ND, only commenting slightly on the signal at the lower energies of SBN and ν STORM. The observables we calculate are the invariant mass of the charged leptons $m_{\ell^+\ell^-}^2$, their separation angle $\Delta\theta$ and their individual energies E_\pm . The flux convolved distributions of these observables are shown for the DUNE ND in neutrino mode in Fig. C.1. In these plots, we sum all trident channels with a given undistinguishable final-state proportionally to their rates, although ν_μ initiated processes always dominate. The coherent and diffractive contributions are shown separately and on the same axes, but we do not worry about their relative normalization. Other potentially interesting quantities are the angle between the cone formed by the two charged leptons and the beam, α_C , and the angle of each charged lepton with respect to the beam direction, θ_\pm . These additional observables are explored in Appendix ???. We also report the distributions of the momentum transfer to the hadronic system, Q^2 . Although this is not a directly measurable quantity, it is a strong discriminant between the coherent and diffractive processes. We do not present the antineutrino distributions here, but they are qualitatively similar.

Perhaps one of the most valuable tools for background suppression in the measurement of the $\mu^+\mu^-$ trident signal at CHARM II, CCFR and NuTeV [71–73] was the smallness of the invariant mass $m_{\ell^+\ell^-}^2$. This feature, shown here on the top row of Fig. C.1, is also

present at lower energies, where the distributions become even more peaked at lower values; although, the diffractive events tend to have a more uniform distribution in this variable. This is also true for the angular separation $\Delta\theta$, where coherent dimuon tridents tends to be quite collimated, with 90% of events having $\Delta\theta < 20^\circ$, whilst diffractive ones are less so, with only 47% of events surviving the cut. This difference is much less pronounced for mixed and dielectron channels, where only half of our coherent events obey $\Delta\theta < 20^\circ$, when 37% of diffractive events do so.

An interesting feature of same flavour tridents induced by a neutrino (antineutrino) is that the negative (positive) charged lepton tends to be slightly more energetic than its counterpart, whilst for mixed tridents muons tend to carry away most of the energy. These considerations are also reflected in the angular distributions. The most energetic particle is also the more forward one. For instance, in mixed neutrino induced tridents, $\sim 80\%$ of the μ^- are expected to be within 10° of the beam direction, whilst only $\sim 35\%$ of their e^+ counterparts do so (see Appendix ?? for additional distributions).

Finally, we mention that detection thresholds can also be important for trident channels with electrons in the final-state. Assuming, for example, a detection threshold for muons and electromagnetic (EM) showers of 30 MeV in LAr, we end up with efficiencies of (99%, 71%, 77%, 86%) for $(\mu^+\mu^-, e^+e^-, e^+\mu^-, e^-\mu^+)$ coherent tridents. These efficiencies become (96%, 91%, 93%, 96%) for incoherent tridents, dropping for $\mu^+\mu^-$ and increasing for all others. For comparison, at the lower neutrino energies of SBND and assuming the same detection thresholds, the efficiencies for coherent and incoherent tridents are slightly lower, (97%, 57%, 67%, 77%) and (90%, 81%, 85%, 90%) respectively.

While trident events are generally quite forward going, their angular behaviour is quite interesting. We consider here the angle between the charged lepton cone and the neutrino beam, α_C , defined as

$$\cos \alpha_C = \frac{(\vec{p}_3 + \vec{p}_4) \cdot \vec{p}_1}{|\vec{p}_3 + \vec{p}_4| |\vec{p}_1|},$$

and in the individual angle of the charged lepton to the neutrino beam, θ . For same flavour tridents we define θ for each charge of the visible final-state, whilst for mixed tridents we use their flavour. We also show the distribution in $Q^2 = -q^2$, where $q = (P - P')$, which is of particular interest when considering coherency and the impact of form factors.

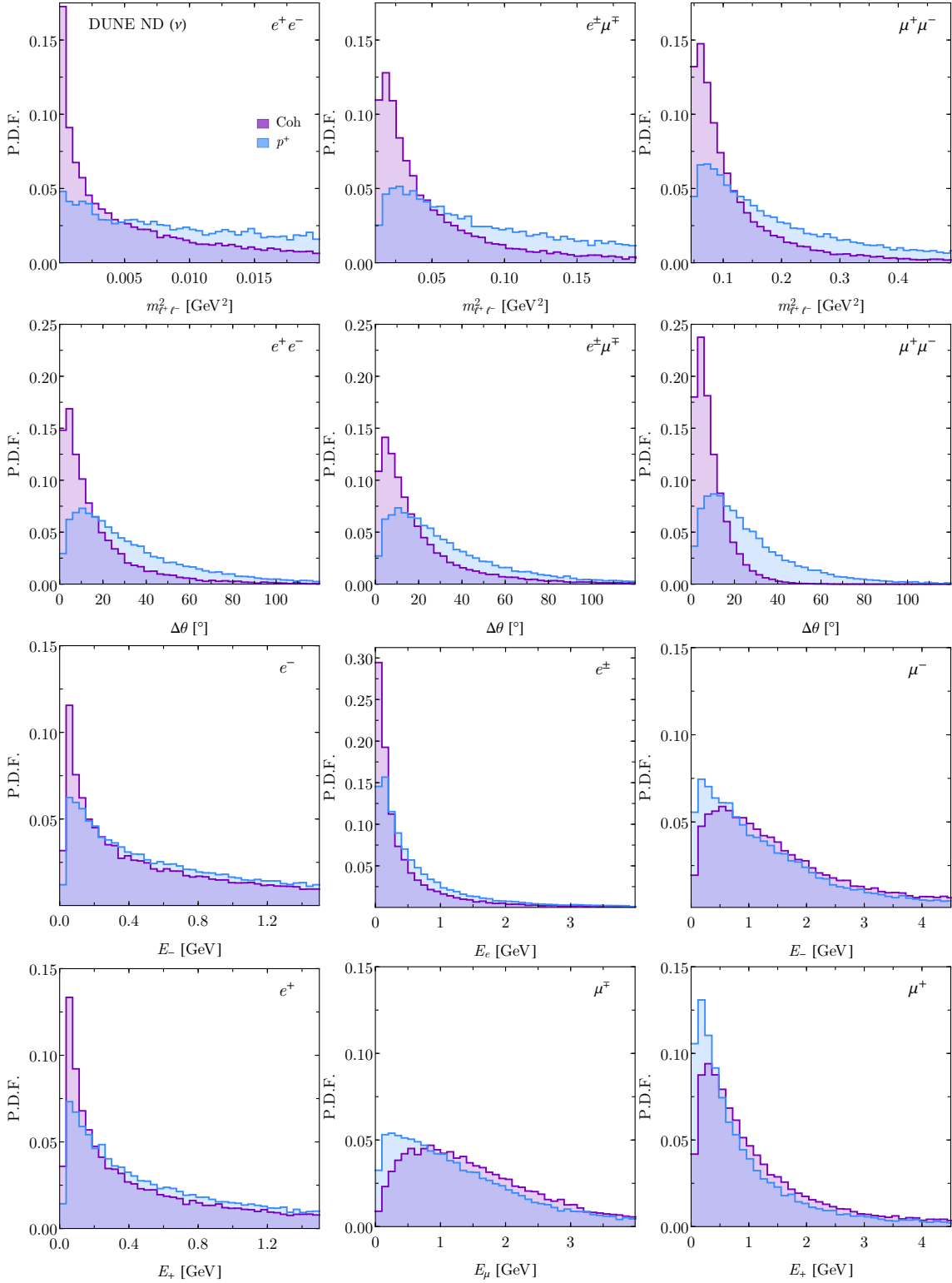


Fig. C.1. Flux convolved neutrino trident production distributions for DUNE ND in neutrino mode. In purple we show the coherent contribution in ^{40}Ar and in blue the incoherent contribution from protons as targets only (including Pauli blocking). The coherent and incoherent distributions are normalized independently. The relative importance of each contribution as a function of E_ν can be seen in Fig. 3.6.

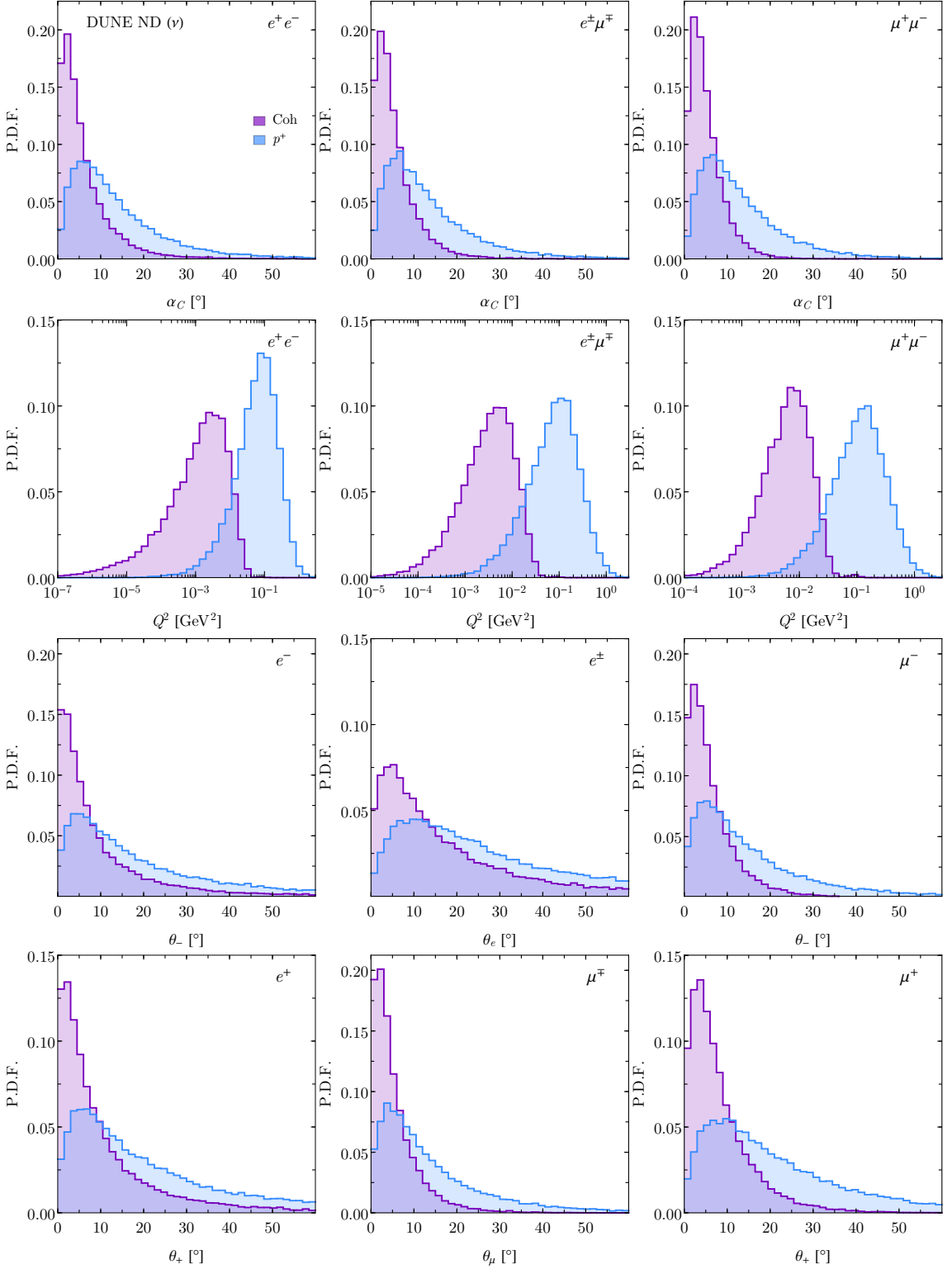


Fig. C.2. Flux convolved neutrino trident production distributions for DUNE ND in neutrino mode in additional variables. In purple we show the coherent contribution in ^{40}Ar and in blue the incoherent contribution from protons as targets only (including Pauli blocking). The coherent and incoherent distributions are normalized independently.

Appendix D

Trident rates at current facilities

D.1 Trident rates in current facilities

The search for neutrino trident production events certainly benefits from the capabilities of LAr technologies but need not be limited to it. In this section we study neutrino trident production rates at non-LAr experiments which have finished data taking or are still running: the on-axis near detector of T2K (INGRID), the near detectors of MINOS and NO ν A and the MINER ν A experiment. We calculate the total number of trident events as in Eq. (3.4.1), taking into account the fact that some detectors are made of composite material. We summarize in Tab. D.1 the details of all non-LAr detectors considered in this section. We limit ourselves to a discussion of the total rates in the fiducial volume, but remark that a careful consideration of each detector is needed in order to assess their true potential to detect a trident signal. For instance, requirements about low energy EM shower reconstruction, hadronic activity measurements and event containment would have to be met to a good degree in order for the detector to be competitive.

INGRID INGRID, the on-axis near detector of the T2K experiment, is located 280 m from the beam source. It consists of 14 identical iron modules, each with a mass of 7.1 t, resulting in a total fiducial mass of 99.4 t [90]. The modules are spread over a range of angles between 0° and 1.1° with respect to the beam axis. The currently approved T2K exposure is $(3.9 + 3.9) \times 10^{21}$ POT in neutrino + antineutrino modes (T2K-I), with the goal to increase it to a total exposure of $(1 + 1) \times 10^{22}$ POT in the second phase of the

Experiment	Material	Baseline (m)	Exposure (POT)	Mass (t)	E_ν (GeV)
T2K	Fe	280	$3.9 (3.9) \times 10^{21}$	99.4	0 – 4
T2K-II	Fe	280	$10 (10) \times 10^{21}$	99.4	0 – 4
MINOS	Fe and C	1040	$10.6 (3.36) \times 10^{20}$	28.6	0 – 20
MINOS+	Fe and C	1040	9.69×10^{20}	28.6	0 – 20
NO ν A	C ₂ H ₃ Cl and CH ₂	1000	$8.85 (6.9) \times 10^{20}$	231	0 – 20
NO ν A-II	C ₂ H ₃ Cl and CH ₂	1000	$36 (36) \times 10^{20}$	231	0 – 20
MINER ν A	CH, H ₂ O, Fe, Pb, C	1035	$12 (12) \times 10^{20}$	7.98	0 – 20

Tab. D.1. Summary of the non-LAr detector set-up and values used in our calculations. The POT numbers are given for a neutrino (antineutrino) beam.

experiment (T2K-II) [93]. Hence we expect approximately 2.6 times more trident events for T2K-II.

We use the on-axis neutrino mode flux spectra at the INGRID module-3 from Ref. [91]. The flux contribution for each neutrino flavour and energy range is listed in Table 1 of Ref. [91]. We assume here that the fluxes at the other 13 modules are the same as at module-3. Although this is not exactly correct it should provide a reasonable estimate of the total rate.

MINOS/MINOS+ Near Detector The MINOS near detector is a magnetized, coarse-grained tracking calorimeter, made primarily of steel and plastic scintillator. Placed 1.04 km away from the NuMI target at Fermilab [401], it weighs 980 t and is similar to the far detector in design. In our analysis, we assume a similar fiducial volume cut to the standard ν_μ CC analyses, namely a fiducial mass of 28.6 t made of 80% of iron and 20% of carbon [402].

The experiment ran from 2005 till 2012 in the low energy (LE) configuration of the NuMI beam ($E_\nu^{\text{peak}} \approx 3$ GeV) and collected 10.56×10^{20} (3.36×10^{20}) POT in the neutrino (antineutrino) beam [403]. The successor to MINOS, MINOS+, ran with the same detectors subjected to the medium energy (ME) configuration of the NuMI beam ($E_\nu^{\text{peak}} \approx 7$ GeV) from 2013 to 2016, and has collected 9.69×10^{20} POT in the neutrino mode. To calculate the trident event rates we use the fluxes taken from Ref. [404]. We assume that the MINOS+ neutrino flux is identical to the one at the MINER ν A experiment (see section ??). Although the cross section for iron is about two times larger than for argon and the neutrino fluxes similar, the number of trident events at MINOS ND is much smaller than

the expected one at DUNE ND due to a lower exposure and fiducial mass. The stringent cut on the fiducial volume assumed here implies a reduction from the 980 t near detector bulk mass to 28.6 t. This cut can be relaxed, depending on the signature considered, and may significantly enhance the rates we quote. A careful analysis of trident signatures outside the fiducial volume would be necessary, but we point out that our rates can increase by at most a factor of ≈ 30 .

NO ν A Near Detector The NO ν A near detector is a fine grained low-Z liquid-scintillator detector placed off-axis from the NuMI beam at a distance of 1 km. Its total mass is 330 t, with almost 70% of it active mass (231 t). In this estimate we assume all of this active mass to also be fiducial. The detector material is approximately 70% mineral oil (CH_2) and 30% of PVC ($\text{C}_2\text{H}_3\text{Cl}$) [98]. A total exposure of $8.85(6.9) \times 10^{20}$ POT has been collected in the neutrino (antineutrino) beam mode prior to 2018 [99].

The NO ν A ND neutrino fluxes (taken from Ref. [404]) peak at slightly lower energies than the MINOS or MINER ν A ones, $E_\nu^{\text{peak}} \approx 2$ GeV. The flavour composition is 91% (11%) ν_μ and 8% (88%) $\bar{\nu}_\mu$ in the neutrino (antineutrino) mode and about 1% $\nu_e + \bar{\nu}_e$ in each mode.

Comparing NO ν A and MINOS, we see that while NO ν A ND has a fiducial mass almost 8 times larger, the flux times total cross section at MINOS ND is at least two orders of magnitude larger than at NO ν A ND, especially above 4 GeV, making the rates at MINOS ND larger than the rates at NO ν A ND.

NO ν A is planning to collect a total exposure of $36(36) \times 10^{20}$ POT in the neutrino (antineutrino) mode (NO ν A-II) [99, 405], making the expected rates almost 4.1(5.2) times larger (shown in Tab. D.2). In this case the expected dimuons and mixed events at MINOS+ would be at least two times larger than NO ν A-II. On the other hand, for NO ν A-II there will be two times more dielectron events given the much higher exposure.

MINER ν A The multi-component MINER ν A detector was mainly designed to measure neutrino and antineutrino interaction cross sections with different nuclei in the 1-20 GeV range of energy [95]. The detector is located at 1.035 km from the NuMI target. We assume a fiducial mass of about 8 t, with a composition of 75% CH, 9% Pb, 8% Fe, 6% H₂O and 2% C. The experiment has collected 12×10^{20} POT in the neutrino mode and is planning

to reach the same exposure in the antineutrino mode by 2019, both using the medium energy flux of NuMI beam configuration. We do not include the low energy runs, as these have lower number of POT and lower neutrino energies. The neutrino (antineutrino) beam is composed of 95% (7%) ν_μ and 4% (92%) $\bar{\nu}_\mu$, both beams have about 1% of $\nu_e + \bar{\nu}_e$. As expected, the event rate is lower than at MINOS+, as the latter has a larger fiducial mass. MINER ν A, however, benefits from its fine grained technology and its dedicated design for cross section measurements.

Channel	T2K-I	T2K-II	MINOS	MINOS+	NO ν A-I	NO ν A-II	MINER ν A
$\nu_\mu \rightarrow \nu_e e^+ \mu^-$	538	1379	179 (25)	688	71 (14)	291 (73)	140 (13)
	49	126	21 (3)	82	21 (4)	86 (21)	30 (3)
$\bar{\nu}_\mu \rightarrow \bar{\nu}_e e^- \mu^+$	23	58	42 (31)	38	10 (57)	41 (296)	8 (89)
	2	5	5 (4)	5	3 (17)	12 (88)	2 (19)
$\nu_e \rightarrow \nu_\mu e^- \mu^+$	2	6	1 (0.2)	4	2 (0.5)	8 (3)	1 (0.09)
	0.3	1	0.3 (0.04)	0.8	0.9 (0.2)	4 (1)	0.3 (0.03)
$\bar{\nu}_e \rightarrow \bar{\nu}_\mu e^+ \mu^-$	0.2	0.6	0.4 (0.3)	0.4	0.5 (0.9)	2 (5)	0.06 (0.5)
	0.04	0.1	0.08 (0.06)	0.08	0.2 (0.4)	0.8 (2)	0.02 (0.2)
Total $e^\pm \mu^\mp$	563	1444	222 (56)	730	83 (72)	340 (374)	149 (102)
	52	132	27 (7)	88	25 (22)	102 (114)	32 (22)
$\nu_\mu \rightarrow \nu_\mu e^+ e^-$	257	659	48 (5)	44	22 (3)	90 (16)	35 (3)
	9	23	3 (0.4)	3	3 (0.6)	00	4 (0.4)
$\bar{\nu}_\mu \rightarrow \bar{\nu}_\mu e^- e^+$	10	26	9 (8)	9	2 (16)	8 (83)	2 (23)
	0.4	1	0.7 (0.5)	0.7	0.4 (3)	2 (15)	0.2 (3)
$\nu_e \rightarrow \nu_e e^- e^+$	9	24	3 (0.3)	8	3 (0.9)	12 (5)	2 (0.2)
	0.3	0.8	0.2 (0.03)	0.6	0.7 (0.2)	3 (1)	0.2 (0.02)
$\bar{\nu}_e \rightarrow \bar{\nu}_e e^+ e^-$	0.9	2	0.7 (0.6)	0.7	0.8 (2)	3 (10)	0.1 (0.9)
	0.03	0.08	0.06 (0.04)	0.05	0.2 (0.3)	0.8 (1)	0.01 (0.1)
Total $e^+ e^-$	277	711	61 (15)	62	29 (22)	119 (114)	39 (27)
	10	25	4 (1)	4	4 (4)	16 (21)	4 (3)
$\nu_\mu \rightarrow \nu_\mu \mu^+ \mu^-$	29	73	21 (3)	81	7 (2)	28 (11)	17 (2)
	15	38	8 (1)	33	7 (2)	29 (10)	12 (1)
$\bar{\nu}_\mu \rightarrow \bar{\nu}_\mu \mu^- \mu^+$	1	3	5 (3)	5	1 (7)	4 (35)	1 (11)
	0.7	2	2 (1)	2	1 (6)	4 (30)	0.7 (8)
$\nu_e \rightarrow \nu_e \mu^+ \mu^-$	0.09	0.2	0.09 (0.01)	0.3	0.1 (0.04)	0.4 (0.2)	0.06 (0.007)
	0.04	0.1	0.03 (0.004)	0.1	0.1 (0.03)	0.4 (0.1)	0.03 (0.004)
$\bar{\nu}_e \rightarrow \bar{\nu}_e \mu^+ \mu^-$	0.01	0.03	0.03 (0.02)	0.03	0.04 (0.06)	0.2 (0.3)	0.004 (0.03)
	0.004	0.01	0.01 (0.009)	0.01	0.03(0.05)	0.1 (0.3)	0.003 (0.02)
Total $\mu^+ \mu^-$	30	76	26 (6)	86	9 (9)	37 (47)	18 (13)
	16	40	10 (2)	35	8 (8)	34 (36)	13 (9)

Tab. D.2. Total number of **coherent** (top row) and **incoherent** (bottom row) trident events expected at different non-LAr detectors for each channel. The numbers in parentheses are for the antineutrino running mode, when present. These calculations consider a detection efficiency of 100%.

Appendix E

Dark neutrino self-energies

In this appendix, we compute the one-loop corrections to the light neutrino masses in our dark neutrino model, following Refs. [328, 406, 407].

We work with the on-shell (OS) renormalization scheme. This is ensured by requiring that the off-diagonal elements of the self-energy be diagonal when the external particles are on their mass shell, and that the residue of the renormalized propagator are equal to one. Note this is only applicable to the off-diagonal entries that involve at least one heavy neutrino, and that the light-light entries are all non-zero and finite at one-loop.

Assuming Majorana neutrino fields, one can write the self-energy tensor in its most general form:

$$\Sigma_{ij}(q) = q P_L \Sigma_{ij}^L(q^2) + q P_R \Sigma_{ij}^R(q^2) + P_L \Sigma_{ij}^M(q^2) + P_R \Sigma_{ij}^{M*}(q^2), \quad (\text{E.0.1})$$

where by virtue of the Majorana nature the previous terms obey

$$\Sigma_{ij}^L(q^2) = \Sigma_{ij}^{R*}(q^2), \quad \Sigma_{ij}^M(q^2) = \Sigma_{ji}^M(q^2).$$

E.0.1 Self-energy

For now, we will ignore kinetic and scalar mixing effects, as these can be shown to be small given current experimental bounds. The contribution from the scalar fields $s = h^0, \varphi^0$, the goldstones $G = G_h, G_\varphi$ and the vector bosons $V = Z, Z'$ are

$$-i \Sigma_{ij}^s(p^2) = (-i)^2 (\Delta_s P_R + \Delta_s^* P_L)_{ik} \times$$

$$\begin{aligned}
& \int \frac{d^d k}{(2\pi)^d} \frac{i(\not{p} + \not{k} + m_k)}{(p+k)^2 - m_k^2} \frac{i}{k^2 - m_s^2} (\Delta_s P_R + \Delta_s^* P_L)_{kj}, \\
-i \Sigma_{ij}^G(p^2) &= (-i)^2 (i \Delta_G P_R + i \Delta_G^* P_L)_{ik} \times \\
&\quad \int \frac{d^d k}{(2\pi)^d} \frac{i(\not{p} + \not{k} + m_k)}{(p+k)^2 - m_k^2} \frac{i}{k^2 - \xi_V m_V^2} (i \Delta_G P_R + i \Delta_G^* P_L)_{kj}, \\
-i \Sigma_{ij}^G(p^2) &= -(-i)^2 \gamma^\mu \left(C_V P_L - C_V^T P_R \right)_{ik} \times \\
&\quad \int \frac{d^d k}{(2\pi)^d} \frac{i(\not{p} + \not{k} + m_k)}{(p+k)^2 - m_k^2} \frac{i P_{\mu\nu}}{k^2 - m_V^2} \gamma^\nu \left(C_P L - C_P^T R \right)_{kj},
\end{aligned}$$

with no index summation notation. In the latter term, we defined the vector boson propagator numerator, which we rewrite as

$$\begin{aligned}
\gamma^\mu P_{\mu\nu} \gamma^\nu &= \gamma^\mu \left[g_{\mu\nu} - (1 - \xi_V) \frac{k_\mu k_\nu}{k^2 - \xi_V m_V^2} \right] \gamma^\nu \\
&= d - (1 - \xi_V) \frac{k^2 - m_k^2}{k^2 - \xi_V m_V^2} - \frac{m_k^2}{m_V^2} \frac{(k^2 - \xi_V m_V^2) - (k^2 - m_V^2)}{k^2 - \xi_V m_V^2}.
\end{aligned}$$

This allows us to write the relevant part of the self-energy as functions of the scalar two-point loop function

$$B_0(l, m_a^2, m_c^2) = \mu^{2\epsilon} \int \frac{d^d k}{(2\pi)^d} \frac{1}{(k^2 - m_a^2)((l+k)^2 - m_c^2)}, \quad (\text{E.0.2})$$

such that

$$\Sigma_{ij}^s(0) P_R = -\frac{\pi^2}{(2\pi)^4} \mu^{d-4} \left[(\Delta_s)_{ik} m_k B_0(0, m_k^2, m_s^2) (\Delta_s)_{kj} \right] P_R \quad (\text{E.0.3})$$

$$\Sigma_{ij}^G(0) P_R = \frac{\pi^2}{(2\pi)^4} \mu^{d-4} \left[(\Delta_G)_{ik} m_k B_0(0, m_k^2, \xi_V m_V^2) (\Delta_G)_{kj} \right] P_R \quad (\text{E.0.4})$$

$$\Sigma_{ij}^V(0) P_R = -\frac{\pi^2}{(2\pi)^4} \mu^{d-4} \left[(C_V)_{ik} m_k f(m_k^2, m_V^2, \xi m_V^2) (C_V^*)_{kj} \right] P_R, \quad (\text{E.0.5})$$

where the rearrangement of the boson propagator allowed us to write $f(m_k^2, m_V^2, \xi m_V^2)$ as

$$\begin{aligned}
f(m_k^2, m_V^2, \xi m_V^2) &= d B_0(0, m_k^2, m_V^2) - (1 - \xi_V) B_0(0, m_V^2, \xi m_V^2) + \\
&\quad \frac{m_k^2}{m_V^2} B_0(0, m_k^2, \xi m_V^2) - \frac{m_k^2}{m_V^2} B_0(0, m_k^2, m_V^2).
\end{aligned}$$

Finally, the scalar loop function is given by

$$\begin{aligned}
B_0(0, m_a^2, m_b^2) &= \frac{1}{\epsilon} - \gamma_E + \ln 4\pi - \int_0^1 dx \ln \frac{m_a^2 - x(m_a^2 - m_b^2)}{\mu^2} \\
&= \frac{1}{\epsilon} - \gamma_E + \ln 4\pi - \frac{m_a^2}{m_b^2 - m_a^2} \left[\ln \frac{m_a^2}{\mu^2} - 1 \right] + \frac{m_b^2}{m_b^2 - m_a^2} \left[\ln \frac{m_b^2}{\mu^2} - 1 \right].
\end{aligned}$$

The finiteness of our final result and its gauge invariance are a consequence of the two following identities

$$\Delta_G = \Delta_S = C \frac{\hat{m}}{m_V} + \frac{\hat{m}}{m_V} C^T, \quad C \hat{m} C^T = 0. \quad (\text{E.0.6})$$

For light neutrinos ($i, j = 1, 2, 3$), the final result reads

$$\Sigma_{ij} P_R = -\frac{\pi^2}{(2\pi)^4} C \hat{m} \left[d B_0(0, \hat{m}^2, m_V^2) + \frac{\hat{m}^2}{m_V^2} (B_0(0, \hat{m}^2, m_S^2) - B_0(0, \hat{m}^2, m_V^2)) \right] C^T P_R. \quad (\text{E.0.7})$$

After significant algebra, and checking the cancellation of divergencies, we arrive at

$$m_{ij} = \frac{1}{4\pi^2} \sum_{k=4}^5 \left[C_{ik} C_{jk} \frac{m_k^3}{m_Z^2} F(m_k^2, m_Z^2, m_h^2) + D_{ik} D_{jk} \frac{m_k^3}{m_{Z'}^2} F(m_k^2, m_{Z'}^2, m_{\varphi'}^2) \right], \quad (\text{E.0.8})$$

where

$$F(a, b, c) \equiv \frac{3 \ln(a/b)}{a/b - 1} + \frac{\ln(a/c)}{a/c - 1}. \quad (\text{E.0.9})$$

For the full expression, involving mixing, we find ($B_0(x^2) \equiv B_0(0, \hat{m}^2, x^2)$) needs some checking! This is only for light neutrinos

$$\begin{aligned} \Sigma^M(0) &= C \hat{m} \left\{ 4 B_0(m_Z^2) - \frac{\hat{m}^2}{m_Z^2} [B_0(m_Z^2) - c_{\omega'}^2 B_0(m_{h'}^2) - s_{\omega'}^2 B_0(m_{\varphi'}^2)] \right\} C^T \\ &\quad + D \hat{m} \left\{ 4 B_0(m_{Z'}^2) - \frac{\hat{m}^2}{m_{Z'}^2} [B_0(m_{Z'}^2) - c_{\omega'}^2 B_0(m_{\varphi'}^2) - s_{\omega'}^2 B_0(m_{h'}^2)] \right\} D^T \\ &\quad + s_{\omega'} c_{\omega'} \left\{ C \hat{m} [B_0(m_{h'}^2) - B_0(m_{\varphi'}^2)] D^T + D \hat{m} [B_0(m_{h'}^2) - B_0(m_{\varphi'}^2)] C^T \right\}. \end{aligned}$$

Bibliography

- [1] C.-N. Yang and R. L. Mills, *Conservation of Isotopic Spin and Isotopic Gauge Invariance*, *Phys. Rev.* **96** (1954) 191–195.
- [2] S. L. Glashow, *Partial Symmetries of Weak Interactions*, *Nucl. Phys.* **22** (1961) 579–588.
- [3] S. Weinberg, *A Model of Leptons*, *Phys. Rev. Lett.* **19** (1967) 1264–1266.
- [4] A. Salam, *Weak and Electromagnetic Interactions*, *Conf. Proc. C680519* (1968) 367–377.
- [5] P. W. Higgs, *Broken symmetries, massless particles and gauge fields*, *Phys. Lett.* **12** (1964) 132–133.
- [6] P. W. Higgs, *Broken Symmetries and the Masses of Gauge Bosons*, *Phys. Rev. Lett.* **13** (1964) 508–509.
- [7] CMS collaboration, S. Chatrchyan et al., *Observation of a new boson at a mass of 125 GeV with the CMS experiment at the LHC*, *Phys. Lett.* **B716** (2012) 30–61, [1207.7235].
- [8] ATLAS collaboration, G. Aad et al., *Observation of a new particle in the search for the Standard Model Higgs boson with the ATLAS detector at the LHC*, *Phys. Lett.* **B716** (2012) 1–29, [1207.7214].
- [9] G. Zweig, *An SU(3) model for strong interaction symmetry and its breaking. Version 1*, .
- [10] M. Gell-Mann, *A Schematic Model of Baryons and Mesons*, *Phys. Lett.* **8** (1964) 214–215.

- [11] D. J. Gross and F. Wilczek, *Ultraviolet Behavior of Nonabelian Gauge Theories*, *Phys. Rev. Lett.* **30** (1973) 1343–1346.
- [12] H. D. Politzer, *Reliable Perturbative Results for Strong Interactions?*, *Phys. Rev. Lett.* **30** (1973) 1346–1349.
- [13] T. Nakano and K. Nishijima, *Charge Independence for V-particles*, *Prog. Theor. Phys.* **10** (1953) 581–582.
- [14] M. Gell-Mann, *The interpretation of the new particles as displaced charge multiplets*, *Nuovo Cim.* **4** (1956) 848–866.
- [15] GARGAMELLE NEUTRINO collaboration, F. J. Hasert et al., *Observation of Neutrino Like Interactions Without Muon Or Electron in the Gargamelle Neutrino Experiment*, *Phys. Lett.* **B46** (1973) 138–140.
- [16] PARTICLE DATA GROUP collaboration, M. Tanabashi et al., *Review of Particle Physics*, *Phys. Rev.* **D98** (2018) 030001.
- [17] ALEPH, DELPHI, L3, OPAL, SLD, LEP ELECTROWEAK WORKING GROUP, SLD ELECTROWEAK GROUP, SLD HEAVY FLAVOUR GROUP collaboration, S. Schael et al., *Precision electroweak measurements on the Z resonance*, *Phys. Rept.* **427** (2006) 257–454, [[hep-ex/0509008](#)].
- [18] J. M. Cornwall, D. N. Levin and G. Tiktopoulos, *Derivation of Gauge Invariance from High-Energy Unitarity Bounds on the s Matrix*, *Phys. Rev.* **D10** (1974) 1145.
- [19] C. H. Llewellyn Smith, *High-Energy Behavior and Gauge Symmetry*, *Phys. Lett.* **46B** (1973) 233–236.
- [20] N. Cabibbo, *Unitary Symmetry and Leptonic Decays*, *Phys. Rev. Lett.* **10** (1963) 531–533.
- [21] M. Kobayashi and T. Maskawa, *CP Violation in the Renormalizable Theory of Weak Interaction*, *Prog. Theor. Phys.* **49** (1973) 652–657.
- [22] D. A. Kirzhnits and A. D. Linde, *Macroscopic Consequences of the Weinberg Model*, *Phys. Lett.* **42B** (1972) 471–474.

- [23] L. Dolan and R. Jackiw, *Symmetry Behavior at Finite Temperature*, *Phys. Rev.* **D9** (1974) 3320–3341.
- [24] S. Weinberg, *Gauge and Global Symmetries at High Temperature*, *Phys. Rev.* **D9** (1974) 3357–3378.
- [25] N. Cabibbo, L. Maiani, G. Parisi and R. Petronzio, *Bounds on the Fermions and Higgs Boson Masses in Grand Unified Theories*, *Nucl. Phys.* **B158** (1979) 295–305.
- [26] G. Degrassi, S. Di Vita, J. Elias-Miro, J. R. Espinosa, G. F. Giudice, G. Isidori et al., *Higgs mass and vacuum stability in the Standard Model at NNLO*, *JHEP* **08** (2012) 098, [1205.6497].
- [27] R. J. Crewther, P. Di Vecchia, G. Veneziano and E. Witten, *Chiral Estimate of the Electric Dipole Moment of the Neutron in Quantum Chromodynamics*, *Phys. Lett.* **88B** (1979) 123.
- [28] J. M. Pendlebury et al., *Revised experimental upper limit on the electric dipole moment of the neutron*, *Phys. Rev.* **D92** (2015) 092003, [1509.04411].
- [29] R. D. Peccei and H. R. Quinn, *Constraints Imposed by CP Conservation in the Presence of Instantons*, *Phys. Rev.* **D16** (1977) 1791–1797.
- [30] F. Zwicky, *Die Rotverschiebung von extragalaktischen Nebeln*, *Helv. Phys. Acta* **6** (1933) 110–127.
- [31] V. C. Rubin and W. K. Ford, Jr., *Rotation of the Andromeda Nebula from a Spectroscopic Survey of Emission Regions*, *Astrophys. J.* **159** (1970) 379–403.
- [32] PLANCK collaboration, Y. Akrami et al., *Planck 2018 results. I. Overview and the cosmological legacy of Planck*, 1807.06205.
- [33] D. Clowe, M. Bradac, A. H. Gonzalez, M. Markevitch, S. W. Randall, C. Jones et al., *A direct empirical proof of the existence of dark matter*, *Astrophys. J.* **648** (2006) L109–L113, [astro-ph/0608407].
- [34] G. R. Blumenthal, S. M. Faber, J. R. Primack and M. J. Rees, *Formation of Galaxies and Large Scale Structure with Cold Dark Matter*, *Nature* **311** (1984) 517–525.

- [35] R. Cooke, M. Pettini, R. A. Jorgenson, M. T. Murphy and C. C. Steidel, *Precision measures of the primordial abundance of deuterium*, *Astrophys. J.* **781** (2014) 31, [1308.3240].
- [36] B. Famaey and S. McGaugh, *Modified Newtonian Dynamics (MOND): Observational Phenomenology and Relativistic Extensions*, *Living Rev. Rel.* **15** (2012) 10, [1112.3960].
- [37] L. Barack et al., *Black holes, gravitational waves and fundamental physics: a roadmap*, *Class. Quant. Grav.* **36** (2019) 143001, [1806.05195].
- [38] A. Fradette, M. Pospelov, J. Pradler and A. Ritz, *Cosmological beam dump: constraints on dark scalars mixed with the Higgs boson*, *Phys. Rev.* **D99** (2019) 075004, [1812.07585].
- [39] V. Silveira and A. Zee, *SCALAR PHANTOMS*, *Phys. Lett.* **161B** (1985) 136–140.
- [40] N. Craig, C. Englert and M. McCullough, *New Probe of Naturalness*, *Phys. Rev. Lett.* **111** (2013) 121803, [1305.5251].
- [41] S. Weinberg, *A New Light Boson?*, *Phys. Rev. Lett.* **40** (1978) 223–226.
- [42] C. Y. Cardall, *Coherence of neutrino flavor mixing in quantum field theory*, *Phys. Rev.* **D61** (2000) 073006, [hep-ph/9909332].
- [43] M. Beuthe, *Oscillations of neutrinos and mesons in quantum field theory*, *Phys. Rept.* **375** (2003) 105–218, [hep-ph/0109119].
- [44] C. Giunti, *Neutrino wave packets in quantum field theory*, *JHEP* **11** (2002) 017, [hep-ph/0205014].
- [45] E. K. Akhmedov and J. Kopp, *Neutrino Oscillations: Quantum Mechanics vs. Quantum Field Theory*, *JHEP* **04** (2010) 008, [1001.4815].
- [46] A. Kobach, A. V. Manohar and J. McGreevy, *Neutrino Oscillation Measurements Computed in Quantum Field Theory*, *Phys. Lett.* **B783** (2018) 59–75, [1711.07491].
- [47] D. Notzold and G. Raffelt, *Neutrino Dispersion at Finite Temperature and Density*, *Nucl. Phys.* **B307** (1988) 924–936.

- [48] J. F. Nieves, *Neutrinos in a Medium*, *Phys. Rev.* **D40** (1989) 866.
- [49] H. A. Weldon, *Covariant Calculations at Finite Temperature: The Relativistic Plasma*, *Phys. Rev.* **D26** (1982) 1394.
- [50] J. C. D’Olivo, J. F. Nieves and M. Torres, *Finite temperature corrections to the effective potential of neutrinos in a medium*, *Phys. Rev.* **D46** (1992) 1172–1179.
- [51] F. J. Botella, C. S. Lim and W. J. Marciano, *Radiative Corrections to Neutrino Indices of Refraction*, *Phys. Rev.* **D35** (1987) 896.
- [52] S. M. Boucenna, S. Morisi and J. W. F. Valle, *The low-scale approach to neutrino masses*, *Adv. High Energy Phys.* **2014** (2014) 831598, [[1404.3751](#)].
- [53] MINIBoNE collaboration, A. A. Aguilar-Arevalo et al., *First Measurement of the Muon Neutrino Charged Current Quasielastic Double Differential Cross Section*, *Phys. Rev.* **D81** (2010) 092005, [[1002.2680](#)].
- [54] J. Nieves, I. Ruiz Simo and M. J. Vicente Vacas, *The nucleon axial mass and the MiniBooNE Quasielastic Neutrino-Nucleus Scattering problem*, *Phys. Lett.* **B707** (2012) 72–75, [[1106.5374](#)].
- [55] C. Andreopoulos et al., *The GENIE Neutrino Monte Carlo Generator*, *Nucl. Instrum. Meth.* **A614** (2010) 87–104, [[0905.2517](#)].
- [56] O. Buss, T. Gaitanos, K. Gallmeister, H. van Hees, M. Kaskulov, O. Lalakulich et al., *Transport-theoretical Description of Nuclear Reactions*, *Phys. Rept.* **512** (2012) 1–124, [[1106.1344](#)].
- [57] Y. Hayato, *NEUT*, *Nucl. Phys. Proc. Suppl.* **112** (2002) 171–176.
- [58] C. Juszczak, J. A. Nowak and J. T. Sobczyk, *Simulations from a new neutrino event generator*, *Nucl. Phys. Proc. Suppl.* **159** (2006) 211–216, [[hep-ph/0512365](#)].
- [59] W. J. Marciano and Z. Parsa, *Neutrino electron scattering theory*, *J. Phys.* **G29** (2003) 2629–2645, [[hep-ph/0403168](#)].
- [60] A. de Gouvea and J. Jenkins, *What can we learn from neutrino electron scattering?*, *Phys. Rev.* **D74** (2006) 033004, [[hep-ph/0603036](#)].

- [61] A. N. Khan, *Global analysis of the source and detector nonstandard interactions using the short baseline $\nu - e$ and $\bar{\nu} - e$ scattering data*, *Phys. Rev. D* **93** (May, 2016) 093019.
- [62] M. Lindner, F. S. Queiroz, W. Rodejohann and X.-J. Xu, *Neutrino-electron scattering: general constraints on Z' and dark photon models*, *JHEP* **05** (2018) 098, [1803.00060].
- [63] J. N. Bahcall, M. Kamionkowski and A. Sirlin, *Solar neutrinos: Radiative corrections in neutrino - electron scattering experiments*, *Phys. Rev.* **D51** (1995) 6146–6158, [astro-ph/9502003].
- [64] M. Passera, *QED corrections to neutrino electron scattering*, *Phys. Rev.* **D64** (2001) 113002, [hep-ph/0011190].
- [65] W. Czyz, G. C. Sheppley and J. D. Walecka, *Neutrino production of lepton pairs through the point four-fermion interaction*, *Nuovo Cim.* **34** (1964) 404–435.
- [66] J. Lovseth and M. Radomiski, *Kinematical distributions of neutrino-produced lepton triplets*, *Phys. Rev.* **D3** (1971) 2686–2706.
- [67] K. Fujikawa, *The self-coupling of weak lepton currents in high-energy neutrino and muon reactions*, *Annals Phys.* **68** (1971) 102–162.
- [68] R. W. Brown, *Intermediate boson. i. theoretical production cross-sections in high-energy neutrino and muon experiments*, *Phys. Rev.* **D3** (1971) 207–223.
- [69] K. Koike, M. Konuma, K. Kurata and K. Sugano, *Neutrino production of lepton pairs. 1. -, Prog. Theor. Phys.* **46** (1971) 1150–1169.
- [70] G. Magill and R. Plestid, *Neutrino Trident Production at the Intensity Frontier*, *Phys. Rev.* **D95** (2017) 073004, [1612.05642].
- [71] CHARM-II collaboration, D. Geiregat et al., *First observation of neutrino trident production*, *Phys. Lett.* **B245** (1990) 271–275.
- [72] CCFR collaboration, S. R. Mishra et al., *Neutrino tridents and WZ interference*, *Phys. Rev. Lett.* **66** (1991) 3117–3120.

- [73] NuTeV collaboration, T. Adams et al., *Neutrino trident production from NuTeV*, in *High-energy physics. Proceedings, 29th International Conference, ICHEP'98, Vancouver, Canada, July 23-29, 1998. Vol. 1, 2*, pp. 631–634, 1998, [hep-ex/9811012](#).
- [74] R. W. Brown, R. H. Hobbs, J. Smith and N. Stanko, *Intermediate boson. iii. virtual-boson effects in neutrino trident production*, *Phys. Rev.* **D6** (1972) 3273–3292.
- [75] I. V. Gaidenko, V. A. Novikov and M. I. Vysotsky, *On the production of a lepton pair in the collision of ultrarelativistic neutral particle with nonzero magnetic moment with nuclei*, *Phys. Lett.* **B497** (2001) 49–54, [[hep-ph/0007204](#)].
- [76] W. Altmannshofer, S. Gori, M. Pospelov and I. Yavin, *Neutrino Trident Production: A Powerful Probe of New Physics with Neutrino Beams*, *Phys. Rev. Lett.* **113** (2014) 091801, [[1406.2332](#)].
- [77] Y. Kaneta and T. Shimomura, *On the possibility of a search for the $L_\mu - L_\tau$ gauge boson at Belle-II and neutrino beam experiments*, *PTEP* **2017** (2017) 053B04, [[1701.00156](#)].
- [78] S.-F. Ge, M. Lindner and W. Rodejohann, *New Physics and Atmospheric Neutrino Trident Production with PINGU and ORCA*, [1702.02617](#).
- [79] G. Magill and R. Plestid, *Probing new charged scalars with neutrino trident production*, *Phys. Rev.* **D97** (2018) 055003, [[1710.08431](#)].
- [80] A. Falkowski, G. Grilli di Cortona and Z. Tabrizi, *Future DUNE constraints on EFT*, *JHEP* **04** (2018) 101, [[1802.08296](#)].
- [81] R. Belusevic and J. Smith, *W - Z Interference in Neutrino - Nucleus Scattering*, *Phys. Rev.* **D37** (1988) 2419.
- [82] M. A. Kozhushner and E. P. Shabalin, *Production of lepton particle pairs on a Coulomb center*, *Sov. Phys. JETP* **14** (1962) 676.
- [83] E. P. Shabalin, *The $\mu^+\mu^-$ and e^+e^- pair production cross sections for neutrinos scattered by nuclei*, *Sov. Phys. JETP* **16** (1963) 125.

- [84] R. Acciarri et al., *A Proposal for a Three Detector Short-Baseline Neutrino Oscillation Program in the Fermilab Booster Neutrino Beam*, 1503.01520.
- [85] DUNE collaboration, R. Acciarri et al., *Long-Baseline Neutrino Facility (LBNF) and Deep Underground Neutrino Experiment (DUNE)*, 1601.02984.
- [86] D. DUNE Collaboration, R. Acciarri et al., *Long-Baseline Neutrino Facility (LBNF) and Deep Underground Neutrino Experiment (DUNE) Conceptual Design Report Volume 2: The Physics Program for DUNE at LBNF*, 1512.06148.
- [87] F. J. P. Soler, *nuSTORM: Neutrinos from Stored Muons*, in *Proceedings, Topical Research Meeting on Prospects in Neutrino Physics (NuPhys2014): London, UK, December 15-17, 2014*, 2015, 1507.08836.
- [88] D. Adey, R. Appleby, R. Bayes, A. Bogacz, A. Bross, J.-B. Lagrange et al., *Overview of the neutrinos from stored muons facility - nustorm*, *Journal of Instrumentation* **12** (2017) P07020.
- [89] C. Andreopoulos et al., *The GENIE Neutrino Monte Carlo Generator*, *Nucl. Instrum. Meth.* **A614** (2010) 87–104, [0905.2517].
- [90] K. Abe et al., *Measurements of the T2K neutrino beam properties using the INGRID on-axis near detector*, *Nucl. Instrum. Meth.* **A694** (2012) 211–223, [1111.3119].
- [91] T2K collaboration, K. Abe et al., *Measurement of the muon neutrino inclusive charged-current cross section in the energy range of 1–3 GeV with the T2K INGRID detector*, *Phys. Rev.* **D93** (2016) 072002, [1509.06940].
- [92] T2K collaboration, K. Abe et al., *Measurement of Coherent π^+ Production in Low Energy Neutrino-Carbon Scattering*, *Phys. Rev. Lett.* **117** (2016) 192501, [1604.04406].
- [93] T2K collaboration, K. Abe et al., *Sensitivity of the T2K accelerator-based neutrino experiment with an Extended run to 20×10^{21} POT*, 1607.08004.
- [94] MINERvA collaboration, O. Altinok et al., *Measurement of ν_μ charged-current single π^0 production on hydrocarbon in the few-GeV region using MINERvA*, *Phys. Rev.* **D96** (2017) 072003, [1708.03723].

- [95] MINERvA collaboration, “MINERvA Status Report and Request for 12×10^{20} POT in Antineutrino Mode.” 2017.
- [96] MINOS collaboration, P. Adamson et al., *Study of quasielastic scattering using charged-current ν_μ -iron interactions in the MINOS near detector*, *Phys. Rev.* **D91** (2015) 012005, [[1410.8613](#)].
- [97] J. A. Alpern Boehm, *A Measurement of Electron Neutrino Appearance with the MINOS Experiment*, Ph.D. thesis, Harvard University, 2009.
- [98] B. Wang, *Muon-Neutrino Electron Elastic Scattering and a Search for the Muon-Neutrino Magnetic Moment in the NOvA Near Detector*, Ph.D. thesis, Southern Methodist University, 2017.
- [99] M. Sanchez, “NOvA Results and Prospects.” June, 2018.
- [100] L. N. Hand, *Experimental investigation of pion electroproduction*, *Phys. Rev.* **129** (1963) 1834–1846.
- [101] B. A. Kniehl, *Elastic e p scattering and the Weizsäcker-Williams approximation*, *Phys. Lett.* **B254** (1991) 267–273.
- [102] C. F. von Weizsäcker, *Radiation emitted in collisions of very fast electrons*, *Z. Phys.* **88** (1934) 612–625.
- [103] E. J. Williams, *Nature of the high-energy particles of penetrating radiation and status of ionization and radiation formulae*, *Phys. Rev.* **45** (1934) 729–730.
- [104] E. Fermi, *On the Theory of the impact between atoms and electrically charged particles*, *Z. Phys.* **29** (1924) 315–327.
- [105] S. Frixione, M. L. Mangano, P. Nason and G. Ridolfi, *Improving the Weizsäcker-Williams approximation in electron - proton collisions*, *Phys. Lett.* **B319** (1993) 339–345, [[hep-ph/9310350](#)].
- [106] A. Weber, “ND(s) for DUNE.” May, 2018.
- [107] DUNE collaboration, V. Papadimitriou, “Design of the LBNF Beamline.” 2016.

- [108] ν STORM collaboration, D. Adey et al., *Light sterile neutrino sensitivity at the nuSTORM facility*, *Phys. Rev.* **D89** (2014) 071301, [1402.5250].
- [109] J. Smith and J. A. M. Vermaseren, *Electromagnetic Backgrounds in Neutrino Produced Trimuon Events*, *Phys. Rev.* **D17** (1978) 2288.
- [110] C. H. Albright, J. Smith and J. A. M. Vermaseren, *A Comparison of Trimuon Production Mechanisms*, *Phys. Rev.* **D18** (1978) 108.
- [111] ARGONEUT collaboration, R. Acciarri et al., *First Observation of Low Energy Electron Neutrinos in a Liquid Argon Time Projection Chamber*, *Phys. Rev.* **D95** (2017) 072005, [1610.04102].
- [112] D. Rein and L. M. Sehgal, *Coherent π^0 production in neutrino reactions*, *Nuclear Physics B* **223** (1983) 29 – 44.
- [113] D. Rein and L. M. Sehgal, *PCAC and the Deficit of Forward Muons in π^+ Production by Neutrinos*, *Phys. Lett.* **B657** (2007) 207–209, [hep-ph/0606185].
- [114] MINIBOONE collaboration, A. A. Aguilar-Arevalo et al., *Measurement of ν_μ -induced charged-current neutral pion production cross sections on mineral oil at $E_\nu \in 0.5 - 2.0$ GeV*, *Phys. Rev.* **D83** (2011) 052009, [1010.3264].
- [115] MINERVA collaboration, A. Higuera et al., *Measurement of Coherent Production of π^\pm in Neutrino and Antineutrino Beams on Carbon from E_ν of 1.5 to 20 GeV*, *Phys. Rev. Lett.* **113** (2014) 261802, [1409.3835].
- [116] MINERVA collaboration, A. Mislevic et al., *Measurement of total and differential cross sections of neutrino and antineutrino coherent π^\pm production on carbon*, *Phys. Rev.* **D97** (2018) 032014, [1711.01178].
- [117] T2K collaboration, K. Abe et al., *First measurement of the muon neutrino charged current single pion production cross section on water with the T2K near detector*, *Phys. Rev.* **D95** (2017) 012010, [1605.07964].
- [118] ARGONEUT collaboration, R. Acciarri et al., *First Measurement of Neutrino and Antineutrino Coherent Charged Pion Production on Argon*, *Phys. Rev. Lett.* **113** (2014) 261801, [1408.0598].

- [119] MINIBooNE collaboration, A. A. Aguilar-Arevalo et al., *Measurement of ν_μ and $\bar{\nu}_\mu$ induced neutral current single π^0 production cross sections on mineral oil at $E_\nu \sim \mathcal{O}(1\text{GeV})$* , *Phys. Rev.* **D81** (2010) 013005, [0911.2063].
- [120] SciBooNE collaboration, Y. Kurimoto et al., *Improved measurement of neutral current coherent π^0 production on carbon in a few-GeV neutrino beam*, *Phys. Rev.* **D81** (2010) 111102, [1005.0059].
- [121] ARGONEUT collaboration, R. Acciarri et al., *Measurement of ν_μ and $\bar{\nu}_\mu$ neutral current $\pi^0 \rightarrow \gamma\gamma$ production in the ArgoNeuT detector*, *Phys. Rev.* **D96** (2017) 012006, [1511.00941].
- [122] D. Rein and L. M. Sehgal, *Neutrino Excitation of Baryon Resonances and Single Pion Production*, *Annals Phys.* **133** (1981) 79–153.
- [123] K2K collaboration, C. Mariani et al., *Measurement of inclusive π^0 production in the Charged-Current Interactions of Neutrinos in a 1.3-GeV wide band beam*, *Phys. Rev.* **D83** (2011) 054023, [1012.1794].
- [124] A. C. Benvenuti et al., *Observation of New Particle Production by High-Energy Neutrinos and anti-neutrinos*, *Phys. Rev. Lett.* **34** (1975) 419.
- [125] G. De Lellis, P. Migliozzi and P. Santorelli, *Charm physics with neutrinos*, *Phys. Rept.* **399** (2004) 227–320.
- [126] V. P. Efrosinin, Yu. G. Kudenko and A. N. Khotjantsev, *Single-photon production in neutrino-nucleon interactions*, *Phys. Atom. Nucl.* **72** (2009) 459–464.
- [127] A. Bodek, *Muon internal bremsstrahlung: A Conventional explanation for the excess νe events in MiniBoone*, 0709.4004.
- [128] A. M. Ankowski, O. Benhar, T. Mori, R. Yamaguchi and M. Sakuda, *Analysis of γ -ray production in neutral-current neutrino-oxygen interactions at energies above 200 mev*, *Phys. Rev. Lett.* **108** (Feb, 2012) 052505.
- [129] S. Centelles Chuliá, E. Ma, R. Srivastava and J. W. F. Valle, *Dirac Neutrinos and Dark Matter Stability from Lepton Quarticity*, *Phys. Lett.* **B767** (2017) 209–213, [1606.04543].

- [130] E. Ma and R. Srivastava, *Dirac or inverse seesaw neutrino masses with $B - L$ gauge symmetry and S_3 flavor symmetry*, *Phys. Lett.* **B741** (2015) 217–222, [1411.5042].
- [131] A. Aranda, C. Bonilla, S. Morisi, E. Peinado and J. W. F. Valle, *Dirac neutrinos from flavor symmetry*, *Phys. Rev.* **D89** (2014) 033001, [1307.3553].
- [132] P. Minkowski, $\mu \rightarrow e\gamma$ at a Rate of One Out of 10^9 Muon Decays?, *Phys. Lett.* **67B** (1977) 421–428.
- [133] R. N. Mohapatra and G. Senjanovic, *Neutrino Mass and Spontaneous Parity Violation*, *Phys. Rev. Lett.* **44** (1980) 912.
- [134] M. Gell-Mann, P. Ramond and R. Slansky, *Complex Spinors and Unified Theories*, *Conf. Proc.* **C790927** (1979) 315–321, [1306.4669].
- [135] T. Yanagida, *HORIZONTAL SYMMETRY AND MASSES OF NEUTRINOS*, *Conf. Proc.* **C7902131** (1979) 95–99.
- [136] G. Lazarides, Q. Shafi and C. Wetterich, *Proton Lifetime and Fermion Masses in an $SO(10)$ Model*, *Nucl. Phys.* **B181** (1981) 287–300.
- [137] R. N. Mohapatra and G. Senjanovic, *Neutrino Masses and Mixings in Gauge Models with Spontaneous Parity Violation*, *Phys. Rev.* **D23** (1981) 165.
- [138] J. Schechter and J. W. F. Valle, *Neutrino Masses in $SU(2) \times U(1)$ Theories*, *Phys. Rev.* **D22** (1980) 2227.
- [139] T. P. Cheng and L.-F. Li, *Neutrino Masses, Mixings and Oscillations in $SU(2) \times U(1)$ Models of Electroweak Interactions*, *Phys. Rev.* **D22** (1980) 2860.
- [140] R. Foot, H. Lew, X. G. He and G. C. Joshi, *Seesaw Neutrino Masses Induced by a Triplet of Leptons*, *Z. Phys.* **C44** (1989) 441.
- [141] S. F. King and C. Luhn, *Neutrino Mass and Mixing with Discrete Symmetry*, *Rept. Prog. Phys.* **76** (2013) 056201, [1301.1340].
- [142] M. Fukugita and T. Yanagida, *Baryogenesis Without Grand Unification*, *Phys. Lett.* **B174** (1986) 45–47.

- [143] T. Asaka and M. Shaposhnikov, *The nuMSM, dark matter and baryon asymmetry of the universe*, *Phys. Lett.* **B620** (2005) 17–26, [[hep-ph/0505013](#)].
- [144] T. Asaka, S. Blanchet and M. Shaposhnikov, *The nuMSM, dark matter and neutrino masses*, *Phys. Lett.* **B631** (2005) 151–156, [[hep-ph/0503065](#)].
- [145] C. Boehm, Y. Farzan, T. Hambye, S. Palomares-Ruiz and S. Pascoli, *Is it possible to explain neutrino masses with scalar dark matter?*, *Phys. Rev.* **D77** (2008) 043516, [[hep-ph/0612228](#)].
- [146] E. Ma, *Verifiable radiative seesaw mechanism of neutrino mass and dark matter*, *Phys. Rev.* **D73** (2006) 077301, [[hep-ph/0601225](#)].
- [147] S. Gabriel and S. Nandi, *A New two Higgs doublet model*, *Phys. Lett.* **B655** (2007) 141–147, [[hep-ph/0610253](#)].
- [148] S. M. Davidson and H. E. Logan, *Dirac neutrinos from a second Higgs doublet*, *Phys. Rev.* **D80** (2009) 095008, [[0906.3335](#)].
- [149] E. Bertuzzo, P. A. N. Machado, Z. Tabrizi and R. Zukanovich Funchal, *A Neutrinophilic 2HDM as a UV Completion for the Inverse Seesaw Mechanism*, *JHEP* **11** (2017) 004, [[1706.10000](#)].
- [150] N. Nath, M. Ghosh, S. Goswami and S. Gupta, *Phenomenological study of extended seesaw model for light sterile neutrino*, *JHEP* **03** (2017) 075, [[1610.09090](#)].
- [151] I. Esteban, M. C. Gonzalez-Garcia, A. Hernandez-Cabezudo, M. Maltoni and T. Schwetz, *Global analysis of three-flavour neutrino oscillations: synergies and tensions in the determination of θ_{23} , δ_{CP} , and the mass ordering*, [1811.05487](#).
- [152] J. M. Conrad, M. H. Shaevitz and T. Bolton, *Precision measurements with high-energy neutrino beams*, *Rev. Mod. Phys.* **70** (1998) 1341–1392, [[hep-ex/9707015](#)].
- [153] MINOS collaboration, P. Adamson et al., *Neutrino and Antineutrino Inclusive Charged-current Cross Section Measurements with the MINOS Near Detector*, *Phys. Rev.* **D81** (2010) 072002, [[0910.2201](#)].

- [154] MINIBOONE collaboration, A. A. Aguilar-Arevalo et al., *First measurement of the muon antineutrino double-differential charged-current quasielastic cross section*, *Phys. Rev.* **D88** (2013) 032001, [[1301.7067](#)].
- [155] MINERvA collaboration, L. Ren et al., *Measurement of the antineutrino to neutrino charged-current interaction cross section ratio in MINERvA*, *Phys. Rev.* **D95** (2017) 072009, [[1701.04857](#)].
- [156] DUNE collaboration, R. Acciarri et al., *Long-Baseline Neutrino Facility (LBNF) and Deep Underground Neutrino Experiment (DUNE)*, [1601.05471](#).
- [157] M. Blennow, P. Coloma, E. Fernandez-Martinez, J. Hernandez-Garcia and J. Lopez-Pavon, *Non-Unitarity, sterile neutrinos, and Non-Standard neutrino Interactions*, *JHEP* **04** (2017) 153, [[1609.08637](#)].
- [158] S. Hannestad, R. S. Hansen and T. Tram, *How Self-Interactions can Reconcile Sterile Neutrinos with Cosmology*, *Phys. Rev. Lett.* **112** (2014) 031802, [[1310.5926](#)].
- [159] B. Dasgupta and J. Kopp, *Cosmologically Safe eV-Scale Sterile Neutrinos and Improved Dark Matter Structure*, *Phys. Rev. Lett.* **112** (2014) 031803, [[1310.6337](#)].
- [160] A. Mirizzi, G. Mangano, O. Pisanti and N. Saviano, *Collisional production of sterile neutrinos via secret interactions and cosmological implications*, *Phys. Rev.* **D91** (2015) 025019, [[1410.1385](#)].
- [161] J. F. Cherry, A. Friedland and I. M. Shoemaker, *Short-baseline neutrino oscillations, Planck, and IceCube*, [1605.06506](#).
- [162] F. Capozzi, I. M. Shoemaker and L. Vecchi, *Solar Neutrinos as a Probe of Dark Matter-Neutrino Interactions*, *JCAP* **1707** (2017) 021, [[1702.08464](#)].
- [163] P. B. Denton, Y. Farzan and I. M. Shoemaker, *Activating the fourth neutrino of the 3+1 scheme*, *Phys. Rev.* **D99** (2019) 035003, [[1811.01310](#)].
- [164] X. Chu, B. Dasgupta, M. Dentler, J. Kopp and N. Saviano, *Sterile neutrinos with secret interactions—cosmological discord?*, *JCAP* **1811** (2018) 049, [[1806.10629](#)].

- [165] A. Esmaili and H. Nunokawa, *On the robustness of IceCube’s bound on sterile neutrinos in the presence of non-standard interactions*, *Eur. Phys. J.* **C79** (2019) 70, [[1810.11940](#)].
- [166] E. Bertuzzo, S. Jana, P. A. N. Machado and R. Zukanovich Funchal, *Dark Neutrino Portal to Explain MiniBooNE excess*, *Phys. Rev. Lett.* **121** (2018) 241801, [[1807.09877](#)].
- [167] P. Ballett, S. Pascoli and M. Ross-Lonergan, *$U(1)'$ mediated decays of heavy sterile neutrinos in MiniBooNE*, [1808.02915](#).
- [168] C. A. Argüelles, M. Hostert and Y.-D. Tsai, *Testing New Physics Explanations of MiniBooNE Anomaly at Neutrino Scattering Experiments*, [1812.08768](#).
- [169] C. Boehm, *Implications of a new light gauge boson for neutrino physics*, *Phys. Rev.* **D70** (2004) 055007, [[hep-ph/0405240](#)].
- [170] D. G. Cerdeño, M. Fairbairn, T. Jubb, P. A. N. Machado, A. C. Vincent and C. Bœhm, *Physics from solar neutrinos in dark matter direct detection experiments*, *JHEP* **05** (2016) 118, [[1604.01025](#)].
- [171] P. B. Denton, Y. Farzan and I. M. Shoemaker, *Testing large non-standard neutrino interactions with arbitrary mediator mass after COHERENT data*, *JHEP* **07** (2018) 037, [[1804.03660](#)].
- [172] A. Falkowski, M. González-Alonso and Z. Tabrizi, *Reactor neutrino oscillations as constraints on Effective Field Theory*, [1901.04553](#).
- [173] Y. Farzan, *A model for large non-standard interactions of neutrinos leading to the LMA-Dark solution*, *Phys. Lett.* **B748** (2015) 311–315, [[1505.06906](#)].
- [174] P. Bakhti, Y. Farzan and M. Rajaei, *Secret interactions of neutrinos with light gauge boson at the DUNE near detector*, *Phys. Rev.* **D99** (2019) 055019, [[1810.04441](#)].
- [175] X.-G. He, G. C. Joshi, H. Lew and R. R. Volkas, *Simplest Z-prime model*, *Phys. Rev.* **D44** (1991) 2118–2132.

- [176] X. G. He, G. C. Joshi, H. Lew and R. R. Volkas, *NEW Z-prime PHENOMENOLOGY*, *Phys. Rev.* **D43** (1991) 22–24.
- [177] M. Bauer, P. Foldenauer and J. Jaeckel, *Hunting All the Hidden Photons*, *JHEP* **07** (2018) 094, [1803.05466].
- [178] W. Altmannshofer, S. Gori, M. Pospelov and I. Yavin, *Neutrino Trident Production: A Powerful Probe of New Physics with Neutrino Beams*, *Phys. Rev. Lett.* **113** (2014) 091801, [1406.2332].
- [179] J. Park, *Neutrino-Electron Scattering in MINERvA for Constraining the NuMI Neutrino Flux*, Ph.D. thesis, U. Rochester, 2013. 10.2172/1248363.
- [180] J. Bian, *Measurement of Neutrino-Electron Elastic Scattering at NOvA Near Detector*, in *Proceedings, Meeting of the APS Division of Particles and Fields (DPF 2017): Fermilab, Batavia, Illinois, USA, July 31 - August 4, 2017*, 2017, 1710.03428.
- [181] P. Ballett, M. Hostert, S. Pascoli, Y. F. Perez-Gonzalez, Z. Tabrizi and R. Zukanovich Funchal, *Neutrino Trident Scattering at Near Detectors*, *JHEP* **01** (2019) 119, [1807.10973].
- [182] T. Araki, S. Hoshino, T. Ota, J. Sato and T. Shimomura, *Detecting the $L_\mu - L_\tau$ gauge boson at Belle II*, *Phys. Rev.* **D95** (2017) 055006, [1702.01497].
- [183] S.-F. Ge, M. Lindner and W. Rodejohann, *Atmospheric Trident Production for Probing New Physics*, *Phys. Lett.* **B772** (2017) 164–168, [1702.02617].
- [184] P. Batra, B. A. Dobrescu and D. Spivak, *Anomaly-free sets of fermions*, *J. Math. Phys.* **47** (2006) 082301, [hep-ph/0510181].
- [185] J. A. Dror, R. Lasenby and M. Pospelov, *New constraints on light vectors coupled to anomalous currents*, *Phys. Rev. Lett.* **119** (2017) 141803, [1705.06726].
- [186] V. D. Barger, E. Ma and K. Whisnant, *General Analysis of a Possible Second Weak Neutral Current in Gauge Models*, *Phys. Rev.* **D26** (1982) 2378.
- [187] S. M. Barr, B. Bednarz and C. Benesh, *Anomaly Constraints and New $U(1)$ Gauge Bosons*, *Phys. Rev.* **D34** (1986) 235.

- [188] B. C. Allanach, J. Davighi and S. Melville, *An Anomaly-free Atlas: charting the space of flavour-dependent gauged $U(1)$ extensions of the Standard Model*, 1812.04602.
- [189] J. Ellis, M. Fairbairn and P. Tunney, *Anomaly-Free Models for Flavour Anomalies*, *Eur. Phys. J.* **C78** (2018) 238, [1705.03447].
- [190] B. C. Allanach, J. Davighi and S. Melville, *Anomaly-free, flavour-dependent $U(1)$ charge assignments for Standard Model/Standard Model plus three right-handed neutrino fermionic content*, Dec., 2018. 10.5281/zenodo.1478085.
- [191] A. Ismail, W.-Y. Keung, K.-H. Tsao and J. Unwin, *Axial vector Z' and anomaly cancellation*, *Nucl. Phys.* **B918** (2017) 220–244, [1609.02188].
- [192] Y. Kahn, G. Krnjaic, S. Mishra-Sharma and T. M. P. Tait, *Light Weakly Coupled Axial Forces: Models, Constraints, and Projections*, *JHEP* **05** (2017) 002, [1609.09072].
- [193] J. A. Dror, R. Lasenby and M. Pospelov, *Dark forces coupled to nonconserved currents*, *Phys. Rev.* **D96** (2017) 075036, [1707.01503].
- [194] B. Holdom, *Two $U(1)$'s and Epsilon Charge Shifts*, *Phys. Lett.* **166B** (1986) 196–198.
- [195] A. Kamada and H.-B. Yu, *Coherent Propagation of PeV Neutrinos and the Dip in the Neutrino Spectrum at IceCube*, *Phys. Rev.* **D92** (2015) 113004, [1504.00711].
- [196] M. Ibe, W. Nakano and M. Suzuki, *Constraints on $L_\mu - L_\tau$ gauge interactions from rare kaon decay*, *Phys. Rev.* **D95** (2017) 055022, [1611.08460].
- [197] J. Alexander et al., *Dark Sectors 2016 Workshop: Community Report*, 2016, 1608.08632, <http://lss.fnal.gov/archive/2016/conf/fermilab-conf-16-421.pdf>.
- [198] M. Escudero, D. Hooper, G. Krnjaic and M. Pierre, *Cosmology With a Very Light $L_\mu - L_\tau$ Gauge Boson*, 1901.02010.
- [199] T. Araki, F. Kaneko, T. Ota, J. Sato and T. Shimomura, *MeV scale leptonic force for cosmic neutrino spectrum and muon anomalous magnetic moment*, *Phys. Rev.* **D93** (2016) 013014, [1508.07471].

- [200] J. Heeck and W. Rodejohann, *Gauged $L_\mu - L_\tau$ Symmetry at the Electroweak Scale*, *Phys. Rev.* **D84** (2011) 075007, [1107.5238].
- [201] K. J. Kelly and Y. Zhang, *Mono-Neutrino at DUNE: New Signals From Neutrinophilic Thermal Dark Matter*, 1901.01259.
- [202] M. Holder et al., *Observation of Trimuon Events Produced in Neutrino and anti-neutrino Interactions*, *Phys. Lett.* **70B** (1977) 393–395.
- [203] CHORUS collaboration, A. Kayis-Topaksu et al., *Experimental study of trimuon events in neutrino charged-current interactions*, *Phys. Lett.* **B596** (2004) 44–53.
- [204] A. Benvenuti et al., *Observation of a new process with trimuon production by high-energy neutrinos*, *Physical Review Letters* **38** (may, 1977) 1110–1113.
- [205] B. C. Barish, J. F. Bartlett, A. Bodek, K. W. Brown, D. Buchholz, Y. K. Chu et al., *Observation of Trimuon Production by Neutrinos*, *Physical Review Letters* **38** (mar, 1977) 577–580.
- [206] J. Smith and J. A. M. Vermaseren, *PHYSICAL REVIEW E% 0 Electromagnetic backgrounds in neutrino-produced trimuon events*, .
- [207] NuTeV collaboration, M. Goncharov et al., *Precise Measurement of Dimuon Production Cross-Sections in ν_μ Fe and $\bar{\nu}_\mu$ Fe Deep Inelastic Scattering at the Tevatron*, *Phys. Rev.* **D64** (2001) 112006, [hep-ex/0102049].
- [208] W. Czyz, G. C. Sheppley and J. D. Walecka, *Neutrino production of lepton pairs through the point four-fermion interaction*, *Il Nuovo Cimento* **34** (oct, 1964) 404–435.
- [209] J. Løvseth and M. Radomski, *Kinematical distributions of neutrino-produced lepton triplets*, *Physical Review D* **3** (1971) 2686–2706.
- [210] C. F. Uhlemann and N. Kauer, *Narrow-width approximation accuracy*, *Nucl. Phys.* **B814** (2009) 195–211, [0807.4112].
- [211] R. W. Brown, R. H. Hobbs, J. Smith and N. Stanko, *Intermediate boson. iii. virtual-boson effects in neutrino trident production*, *Phys. Rev.* **D6** (1972) 3273–3292.

- [212] D. R. Albert, “The DUNE Near Detector.” Aug., 2018.
- [213] M. Steven, “Status of DUNE Near Detector.” Oct., 2018.
- [214] DUNE collaboration, “2016 DUNE fluxes.” 2016.
- [215] DUNE collaboration, “2016 DUNE fluxes.” 2017.
- [216] DUNE collaboration, “High-Pressure Argon gas TPC Option for the DUNE Near Detector.” 2019.
- [217] MINOS collaboration, D. G. Michael et al., *The Magnetized steel and scintillator calorimeters of the MINOS experiment*, *Nucl. Instrum. Meth.* **A596** (2008) 190–228, [0805.3170].
- [218] MINERvA collaboration, L. Aliaga et al., *Design, Calibration, and Performance of the MINERvA Detector*, *Nucl. Instrum. Meth.* **A743** (2014) 130–159, [1305.5199].
- [219] A. G. Abramov, N. A. Galyaev, V. I. Garkusha, J. Hylen, F. N. Novoskoltsev, A. D. Ryabov et al., *Beam optics and target conceptual designs for the NuMI project*, *Nucl. Instrum. Meth.* **A485** (2002) 209–227.
- [220] A. Bodek, U. Sarica, D. Naples and L. Ren, *Methods to Determine Neutrino Flux at Low Energies:Investigation of the Low ν Method*, *Eur. Phys. J.* **C72** (2012) 1973, [1201.3025].
- [221] NOMAD collaboration, P. Astier et al., *Neutrino production of opposite sign dimuons in the NOMAD experiment*, *Phys. Lett.* **B486** (2000) 35–48.
- [222] NuTeV collaboration, T. Adams et al., *Evidence for diffractive charm production in muon-neutrino Fe and anti-muon-neutrino Fe scattering at the Tevatron*, *Phys. Rev.* **D61** (2000) 092001, [[hep-ex/9909041](#)].
- [223] N. J. Baker, S. A. Kahn, M. J. Murtagh, N. P. Samios, M. Tanaka, C. Baltay et al., μ^-e^+ dilepton production in charged-current ν_μ interactions, *Phys. Rev. D* **43** (May, 1991) 2765–2777.
- [224] MINERvA collaboration, J. Park et al., *Measurement of Neutrino Flux from Neutrino-Electron Elastic Scattering*, *Phys. Rev.* **D93** (2016) 112007, [1512.07699].

- [225] TEXONO collaboration, H. T. Wong et al., *A Search of Neutrino Magnetic Moments with a High-Purity Germanium Detector at the Kuo-Sheng Nuclear Power Station*, *Phys. Rev.* **D75** (2007) 012001, [[hep-ex/0605006](#)].
- [226] TEXONO collaboration, M. Deniz et al., *Measurement of Nu(e)-bar -Electron Scattering Cross-Section with a CsI(Tl) Scintillating Crystal Array at the Kuo-Sheng Nuclear Power Reactor*, *Phys. Rev.* **D81** (2010) 072001, [[0911.1597](#)].
- [227] J.-W. Chen, H.-C. Chi, H.-B. Li, C. P. Liu, L. Singh, H. T. Wong et al., *Constraints on millicharged neutrinos via analysis of data from atomic ionizations with germanium detectors at sub-keV sensitivities*, *Phys. Rev.* **D90** (2014) 011301, [[1405.7168](#)].
- [228] BABAR collaboration, J. P. Lees et al., *Search for a Dark Photon in e^+e^- Collisions at BaBar*, *Phys. Rev. Lett.* **113** (2014) 201801, [[1406.2980](#)].
- [229] BABAR collaboration, J. P. Lees et al., *Search for Invisible Decays of a Dark Photon Produced in e^+e^- Collisions at BaBar*, *Phys. Rev. Lett.* **119** (2017) 131804, [[1702.03327](#)].
- [230] S. Bilmis, I. Turan, T. M. Aliev, M. Deniz, L. Singh and H. T. Wong, *Constraints on Dark Photon from Neutrino-Electron Scattering Experiments*, *Phys. Rev.* **D92** (2015) 033009, [[1502.07763](#)].
- [231] CHARM-II collaboration, P. Vilain et al., *Precision measurement of electroweak parameters from the scattering of muon-neutrinos on electrons*, *Phys. Lett.* **B335** (1994) 246–252.
- [232] G. Bellini et al., *Precision measurement of the ${}^{7}\text{Be}$ solar neutrino interaction rate in Borexino*, *Phys. Rev. Lett.* **107** (2011) 141302, [[1104.1816](#)].
- [233] M. B. Wise and Y. Zhang, *Lepton Flavorful Fifth Force and Depth-dependent Neutrino Matter Interactions*, *JHEP* **06** (2018) 053, [[1803.00591](#)].
- [234] M. Bustamante and S. K. Agarwalla, *Universe's Worth of Electrons to Probe Long-Range Interactions of High-Energy Astrophysical Neutrinos*, *Phys. Rev. Lett.* **122** (2019) 061103, [[1808.02042](#)].

- [235] BABAR collaboration, J. P. Lees et al., *Search for a muonic dark force at BABAR*, *Phys. Rev.* **D94** (2016) 011102, [1606.03501].
- [236] ATLAS collaboration, G. Aad et al., *Measurements of Four-Lepton Production at the Z Resonance in pp Collisions at $\sqrt{s} = 7$ and 8 TeV with ATLAS*, *Phys. Rev. Lett.* **112** (2014) 231806, [1403.5657].
- [237] S. Baek, N. G. Deshpande, X. G. He and P. Ko, *Muon anomalous g-2 and gauged $L(\mu)$ - $L(\tau)$ models*, *Phys. Rev.* **D64** (2001) 055006, [hep-ph/0104141].
- [238] M. Pospelov, *Secluded U(1) below the weak scale*, *Phys. Rev.* **D80** (2009) 095002, [0811.1030].
- [239] A. Kamada, K. Kaneta, K. Yanagi and H.-B. Yu, *Self-interacting dark matter and muon $g - 2$ in a gauged $U(1)_{L_\mu - L_\tau}$ model*, *JHEP* **06** (2018) 117, [1805.00651].
- [240] MUON G-2 collaboration, G. W. Bennett et al., *Final Report of the Muon E821 Anomalous Magnetic Moment Measurement at BNL*, *Phys. Rev.* **D73** (2006) 072003, [hep-ex/0602035].
- [241] RBC, UKQCD collaboration, T. Blum, P. A. Boyle, V. Gülpers, T. Izubuchi, L. Jin, C. Jung et al., *Calculation of the hadronic vacuum polarization contribution to the muon anomalous magnetic moment*, *Phys. Rev. Lett.* **121** (2018) 022003, [1801.07224].
- [242] A. Keshavarzi, D. Nomura and T. Teubner, *Muon $g - 2$ and $\alpha(M_Z^2)$: a new data-based analysis*, *Phys. Rev.* **D97** (2018) 114025, [1802.02995].
- [243] MUON G-2 collaboration, J. Grange et al., *Muon ($g-2$) Technical Design Report*, 1501.06858.
- [244] R. Petti, ““Precision measurements of fundamental interactions in the ND(s).”” 2018.
- [245] H. Duyang, B. Guo, S. R. Mishra and R. Petti, *A Novel Approach to Neutrino-Hydrogen Measurements*, 1809.08752.
- [246] C. Boehm and P. Fayet, *Scalar dark matter candidates*, *Nucl. Phys.* **B683** (2004) 219–263, [hep-ph/0305261].

- [247] W. Buchmuller, C. Greub and P. Minkowski, *Neutrino masses, neutral vector bosons and the scale of B-L breaking*, *Phys. Lett.* **B267** (1991) 395–399.
- [248] S. Khalil, *Low scale B - L extension of the Standard Model at the LHC*, *J. Phys. G* **35** (2008) 055001, [[hep-ph/0611205](#)].
- [249] P. Fileviez Perez, T. Han and T. Li, *Testability of Type I Seesaw at the CERN LHC: Revealing the Existence of the B-L Symmetry*, *Phys. Rev.* **D80** (2009) 073015, [[0907.4186](#)].
- [250] S. Khalil, *TeV-scale gauged B-L symmetry with inverse seesaw mechanism*, *Phys. Rev.* **D82** (2010) 077702, [[1004.0013](#)].
- [251] C. O. Dib, G. R. Moreno and N. A. Neill, *Neutrinos with a linear seesaw mechanism in a scenario of gauged B-L symmetry*, *Phys. Rev.* **D90** (2014) 113003, [[1409.1868](#)].
- [252] S. Baek, H. Okada and K. Yagyu, *Flavour Dependent Gauged Radiative Neutrino Mass Model*, *JHEP* **04** (2015) 049, [[1501.01530](#)].
- [253] V. De Romeri, E. Fernandez-Martinez, J. Gehrlein, P. A. N. Machado and V. Niro, *Dark Matter and the elusive Z' in a dynamical Inverse Seesaw scenario*, *JHEP* **10** (2017) 169, [[1707.08606](#)].
- [254] T. Nomura and H. Okada, *An inverse seesaw model with $U(1)_R$ gauge symmetry*, *LHEP* **1** (2018) 10–13, [[1806.01714](#)].
- [255] V. Brdar and A. Y. Smirnov, *Low Scale Left-Right Symmetry and Naturally Small Neutrino Mass*, *JHEP* **02** (2019) 045, [[1809.09115](#)].
- [256] H. Okada and K. Yagyu, *Radiative generation of lepton masses with the $U(1)'$ gauge symmetry*, *Phys. Rev.* **D90** (2014) 035019, [[1405.2368](#)].
- [257] C. E. Diaz, S. F. Mantilla and R. Martinez, *Radiative neutrino masses with forbidden seesaw mechanism in an abelian extension of the Standard Model*, [1712.05433](#).
- [258] T. Nomura and H. Okada, *A Linear seesaw model with hidden gauge symmetry*, [1806.07182](#).

- [259] M. Pospelov, *Neutrino Physics with Dark Matter Experiments and the Signature of New Baryonic Neutral Currents*, *Phys. Rev.* **D84** (2011) 085008, [1103.3261].
- [260] B. Batell, M. Pospelov and B. Shuve, *Shedding Light on Neutrino Masses with Dark Forces*, *JHEP* **08** (2016) 052, [1604.06099].
- [261] Y. Farzan and J. Heeck, *Neutrinophilic nonstandard interactions*, *Phys. Rev.* **D94** (2016) 053010, [1607.07616].
- [262] M. Pospelov and J. Pradler, *Elastic scattering signals of solar neutrinos with enhanced baryonic currents*, *Phys. Rev.* **D85** (2012) 113016, [1203.0545].
- [263] R. Harnik, J. Kopp and P. A. N. Machado, *Exploring nu Signals in Dark Matter Detectors*, *JCAP* **1207** (2012) 026, [1202.6073].
- [264] D. McKeen and N. Raj, *Monochromatic dark neutrinos and boosted dark matter in noble liquid direct detection*, 1812.05102.
- [265] MINIBOONE collaboration, A. A. Aguilar-Arevalo et al., *A Search for electron neutrino appearance at the $\Delta m^2 \sim 1\text{eV}^2$ scale*, *Phys. Rev. Lett.* **98** (2007) 231801, [0704.1500].
- [266] LSND COLLABORATION collaboration, C. Athanassopoulos, L. B. Auerbach, R. L. Burman, I. Cohen, D. O. Caldwell, B. D. Dieterle et al., *Evidence for $\bar{\nu}_\mu \rightarrow \bar{\nu}_e$ oscillations from the lsnd experiment at the los alamos meson physics facility*, *Phys. Rev. Lett.* **77** (Oct, 1996) 3082–3085.
- [267] S. N. Gninenko, *The MiniBooNE anomaly and heavy neutrino decay*, *Phys. Rev. Lett.* **103** (2009) 241802, [0902.3802].
- [268] S. N. Gninenko, *A resolution of puzzles from the LSND, KARMEN, and MiniBooNE experiments*, *Phys. Rev.* **D83** (2011) 015015, [1009.5536].
- [269] M. Masip, P. Masjuan and D. Meloni, *Heavy neutrino decays at MiniBooNE*, *JHEP* **01** (2013) 106, [1210.1519].
- [270] A. Radionov, *Constraints on electromagnetic properties of sterile neutrinos from MiniBooNE results*, *Phys. Rev.* **D88** (2013) 015016, [1303.4587].

- [271] P. Fayet, *U-boson production in $e+e-$ annihilations, psi and Upsilon decays, and Light Dark Matter*, *Phys. Rev.* **D75** (2007) 115017, [[hep-ph/0702176](#)].
- [272] P. Ballett, M. Hostert and S. Pascoli, *Neutrino Masses from a Dark Neutrino Sector below the Electroweak Scale*, [1903.07590](#).
- [273] Y. Farzan, *A Minimal model linking two great mysteries: neutrino mass and dark matter*, *Phys. Rev.* **D80** (2009) 073009, [[0908.3729](#)].
- [274] Y. Farzan, S. Pascoli and M. A. Schmidt, *AMEND: A model explaining neutrino masses and dark matter testable at the LHC and MEG*, *JHEP* **10** (2010) 111, [[1005.5323](#)].
- [275] A. Arhrib, C. Boehm, E. Ma and T.-C. Yuan, *Radiative Model of Neutrino Mass with Neutrino Interacting MeV Dark Matter*, *JCAP* **1604** (2016) 049, [[1512.08796](#)].
- [276] J. F. Cherry, A. Friedland and I. M. Shoemaker, *Neutrino Portal Dark Matter: From Dwarf Galaxies to IceCube*, [1411.1071](#).
- [277] M. Escudero, N. Rius and V. Sanz, *Sterile neutrino portal to Dark Matter I: The $U(1)_{B-L}$ case*, *JHEP* **02** (2017) 045, [[1606.01258](#)].
- [278] M. Escudero, N. Rius and V. Sanz, *Sterile Neutrino portal to Dark Matter II: Exact Dark symmetry*, *Eur. Phys. J.* **C77** (2017) 397, [[1607.02373](#)].
- [279] B. Batell, T. Han, D. McKeen and B. Shams Es Haghi, *Thermal Dark Matter Through the Dirac Neutrino Portal*, *Phys. Rev.* **D97** (2018) 075016, [[1709.07001](#)].
- [280] A. Olivares-Del Campo, C. Boehm, S. Palomares-Ruiz and S. Pascoli, *Dark matter-neutrino interactions through the lens of their cosmological implications*, *Phys. Rev.* **D97** (2018) 075039, [[1711.05283](#)].
- [281] M. Blennow, E. Fernandez-Martinez, A. O.-D. Campo, S. Pascoli, S. Rosauro-Alcaraz and A. V. Titov, *Neutrino Portals to Dark Matter*, [1903.00006](#).
- [282] R. N. Mohapatra and J. W. F. Valle, *Neutrino Mass and Baryon Number Nonconservation in Superstring Models*, *Phys. Rev.* **D34** (1986) 1642.
- [283] J. Barry, W. Rodejohann and H. Zhang, *Light Sterile Neutrinos: Models and Phenomenology*, *JHEP* **07** (2011) 091, [[1105.3911](#)].

- [284] P. S. B. Dev and A. Pilaftsis, *Minimal Radiative Neutrino Mass Mechanism for Inverse Seesaw Models*, *Phys. Rev.* **D86** (2012) 113001, [1209.4051].
- [285] V. Barger, P. Langacker, M. McCaskey, M. Ramsey-Musolf and G. Shaughnessy, *Complex Singlet Extension of the Standard Model*, *Phys. Rev.* **D79** (2009) 015018, [0811.0393].
- [286] T. Yamazaki et al., *Search for Heavy Neutrinos in Kaon Decay*, .
- [287] E949 collaboration, A. V. Artamonov et al., *Search for heavy neutrinos in $K^+ \rightarrow \mu^+ \nu_H$ decays*, *Phys. Rev.* **D91** (2015) 052001, [1411.3963].
- [288] NA48/2 collaboration, J. R. Batley et al., *Searches for lepton number violation and resonances in $K^\pm \rightarrow \pi \mu \mu$ decays*, *Phys. Lett.* **B769** (2017) 67–76, [1612.04723].
- [289] G. Bernardi et al., *Search for Neutrino Decay*, *Phys. Lett.* **166B** (1986) 479–483.
- [290] CHARM collaboration, F. Bergsma et al., *A Search for Decays of Heavy Neutrinos*, *Phys. Lett.* **128B** (1983) 361.
- [291] NA3 collaboration, J. Badier et al., *Mass and Lifetime Limits on New Longlived Particles in 300-GeV/c π^- Interactions*, *Z. Phys.* **C31** (1986) 21.
- [292] NuTeV, E815 collaboration, A. Vaitaitis et al., *Search for neutral heavy leptons in a high-energy neutrino beam*, *Phys. Rev. Lett.* **83** (1999) 4943–4946, [hep-ex/9908011].
- [293] WA66 collaboration, A. M. Cooper-Sarkar et al., *Search for Heavy Neutrino Decays in the BEBC Beam Dump Experiment*, *Phys. Lett.* **160B** (1985) 207–211.
- [294] NOMAD collaboration, P. Astier et al., *Search for heavy neutrinos mixing with tau neutrinos*, *Phys. Lett.* **B506** (2001) 27–38, [hep-ex/0101041].
- [295] P. Ballett, S. Pascoli and M. Ross-Lonergan, *MeV-scale sterile neutrino decays at the Fermilab Short-Baseline Neutrino program*, *JHEP* **04** (2017) 102, [1610.08512].
- [296] P. Ilten, Y. Soreq, M. Williams and W. Xue, *Serendipity in dark photon searches*, *JHEP* **06** (2018) 004, [1801.04847].

- [297] A. Atre, T. Han, S. Pascoli and B. Zhang, *The Search for Heavy Majorana Neutrinos*, *JHEP* **05** (2009) 030, [0901.3589].
- [298] A. Abada, V. De Romeri, M. Lucente, A. M. Teixeira and T. Toma, *Effective Majorana mass matrix from tau and pseudoscalar meson lepton number violating decays*, *JHEP* **02** (2018) 169, [1712.03984].
- [299] D. Curtin, R. Essig, S. Gori and J. Shelton, *Illuminating Dark Photons with High-Energy Colliders*, *JHEP* **02** (2015) 157, [1412.0018].
- [300] A. Hook, E. Izaguirre and J. G. Wacker, *Model Independent Bounds on Kinetic Mixing*, *Adv. High Energy Phys.* **2011** (2011) 859762, [1006.0973].
- [301] G. Mohlabeng, *Revisiting the Dark Photon Explanation of the Muon g-2 Anomaly*, 1902.05075.
- [302] SINDRUM collaboration, S. Egli et al., *First Observation of the Decay $\pi^+ \rightarrow e^+ Neutrino e^+e^-$ and a Determination of the Form-factors $F(V)$, $F(a)$, R* , *Phys. Lett.* **B175** (1986) 97.
- [303] A. A. Pobladuev et al., *Experimental study of the radiative decays $K+ \rightarrow mu+ nu e+ e-$ and $K+ \rightarrow e+ nu e+ e-$* , *Phys. Rev. Lett.* **89** (2002) 061803, [hep-ex/0204006].
- [304] SINDRUM collaboration, W. H. Bertl et al., *Search for the Decay $\mu^+ \rightarrow e^+e^+e^-$* , *Nucl. Phys.* **B260** (1985) 1–31.
- [305] CLEO collaboration, M. S. Alam et al., *Tau decays into three charged leptons and two neutrinos*, *Phys. Rev. Lett.* **76** (1996) 2637–2641.
- [306] CMS collaboration, A. M. Sirunyan et al., *Search for invisible decays of a Higgs boson produced through vector boson fusion in proton-proton collisions at $\sqrt{s} = 13$ TeV*, 1809.05937.
- [307] R. Laha, B. Dasgupta and J. F. Beacom, *Constraints on New Neutrino Interactions via Light Abelian Vector Bosons*, *Phys. Rev.* **D89** (2014) 093025, [1304.3460].
- [308] P. Bakhti and Y. Farzan, *Constraining secret gauge interactions of neutrinos by meson decays*, *Phys. Rev.* **D95** (2017) 095008, [1702.04187].

- [309] X. Chu, B. Dasgupta and J. Kopp, *Sterile neutrinos with secret interactions—lasting friendship with cosmology*, *JCAP* **1510** (2015) 011, [1505.02795].
- [310] N. Song, M. C. Gonzalez-Garcia and J. Salvado, *Cosmological constraints with self-interacting sterile neutrinos*, *JCAP* **1810** (2018) 055, [1805.08218].
- [311] J. F. Beacom, N. F. Bell and G. D. Mack, *General Upper Bound on the Dark Matter Total Annihilation Cross Section*, *Phys. Rev. Lett.* **99** (2007) 231301, [astro-ph/0608090].
- [312] S. Palomares-Ruiz and S. Pascoli, *Testing MeV dark matter with neutrino detectors*, *Phys. Rev.* **D77** (2008) 025025, [0710.5420].
- [313] M. Pospelov, A. Ritz and M. B. Voloshin, *Secluded WIMP Dark Matter*, *Phys. Lett.* **B662** (2008) 53–61, [0711.4866].
- [314] G. Mangano, A. Melchiorri, P. Serra, A. Cooray and M. Kamionkowski, *Cosmological bounds on dark matter-neutrino interactions*, *Phys. Rev.* **D74** (2006) 043517, [astro-ph/0606190].
- [315] R. J. Wilkinson, C. Boehm and J. Lesgourgues, *Constraining Dark Matter-Neutrino Interactions using the CMB and Large-Scale Structure*, *JCAP* **1405** (2014) 011, [1401.7597].
- [316] Y. Farzan and S. Palomares-Ruiz, *Dips in the Diffuse Supernova Neutrino Background*, *JCAP* **1406** (2014) 014, [1401.7019].
- [317] C. A. Argüelles, A. Kheirandish and A. C. Vincent, *Imaging Galactic Dark Matter with High-Energy Cosmic Neutrinos*, *Phys. Rev. Lett.* **119** (2017) 201801, [1703.00451].
- [318] SUPER-KAMIOKANDE collaboration, Y. Fukuda et al., *Measurement of the flux and zenith angle distribution of upward through going muons by Super-Kamiokande*, *Phys. Rev. Lett.* **82** (1999) 2644–2648, [hep-ex/9812014].
- [319] D. Wyler and L. Wolfenstein, *Massless Neutrinos in Left-Right Symmetric Models*, *Nucl. Phys.* **B218** (1983) 205–214.

- [320] E. Bertuzzo, S. Jana, P. A. N. Machado and R. Zukanovich Funchal, *Neutrino Masses and Mixings Dynamically Generated by a Light Dark Sector*, *Phys. Lett. B* **791** (2019) 210–214, [[1808.02500](#)].
- [321] P. Ballett, M. Hostert and S. Pascoli, *Dark Neutrinos and a Three Portal Connection to the Standard Model*, [1903.07589](#).
- [322] Y. Zhang, X. Ji and R. N. Mohapatra, *A Naturally Light Sterile neutrino in an Asymmetric Dark Matter Model*, *JHEP* **10** (2013) 104, [[1307.6178](#)].
- [323] J. Lopez-Pavon, S. Pascoli and C.-f. Wong, *Can heavy neutrinos dominate neutrinoless double beta decay?*, *Phys. Rev. D* **87** (2013) 093007, [[1209.5342](#)].
- [324] W. Grimus and L. Lavoura, *The Seesaw mechanism at arbitrary order: Disentangling the small scale from the large scale*, *JHEP* **11** (2000) 042, [[hep-ph/0008179](#)].
- [325] R. Adhikari and A. Raychaudhuri, *Light neutrinos from massless texture and below TeV seesaw scale*, *Phys. Rev. D* **84** (2011) 033002, [[1004.5111](#)].
- [326] Y. Cai, J. Herrero-García, M. A. Schmidt, A. Vicente and R. R. Volkas, *From the trees to the forest: a review of radiative neutrino mass models*, *Front.in Phys.* **5** (2017) 63, [[1706.08524](#)].
- [327] A. Pilaftsis, *Radiatively induced neutrino masses and large Higgs neutrino couplings in the standard model with Majorana fields*, *Z. Phys. C* **55** (1992) 275–282, [[hep-ph/9901206](#)].
- [328] B. A. Kniehl and A. Pilaftsis, *Mixing renormalization in Majorana neutrino theories*, *Nucl. Phys. B* **474** (1996) 286–308, [[hep-ph/9601390](#)].
- [329] DELPHI collaboration, P. Abreu et al., *Search for neutral heavy leptons produced in Z decays*, *Z. Phys. C* **74** (1997) 57–71.
- [330] OPAL collaboration, M. Z. Akrawy et al., *Limits on neutral heavy lepton production from Z0 decay*, *Phys. Lett. B* **247** (1990) 448–457.

- [331] CMS collaboration, A. M. Sirunyan et al., *Search for heavy neutral leptons in events with three charged leptons in proton-proton collisions at $\sqrt{s} = 13$ TeV*, *Phys. Rev. Lett.* **120** (2018) 221801, [1802.02965].
- [332] P. Ballett, T. Boschi and S. Pascoli, *Searching for MeV-scale Neutrinos with the DUNE Near Detector*, in *Proceedings, Prospects in Neutrino Physics (NuPhys2017): London, UK, December 20-22, 2017*, pp. 124–128, 2018, 1803.10824.
- [333] P. Ballett, T. Boschi and S. Pascoli, *Heavy Neutral Leptons from low-scale seesaws at the DUNE Near Detector*, 1905.00284.
- [334] M. Drewes, J. Hager, J. Klaric and G. Lanfranchi, *Perspectives to find heavy neutrinos with NA62*, in *53rd Rencontres de Moriond on Electroweak Interactions and Unified Theories (Moriond EW 2018) La Thuile, Italy, March 10-17, 2018*, 2018, 1806.00100.
- [335] W. Bonivento et al., *Proposal to Search for Heavy Neutral Leptons at the SPS*, 1310.1762.
- [336] S. Alekhin et al., *A facility to Search for Hidden Particles at the CERN SPS: the SHiP physics case*, *Rept. Prog. Phys.* **79** (2016) 124201, [1504.04855].
- [337] A. D. Dolgov, S. H. Hansen, G. Raffelt and D. V. Semikoz, *Heavy sterile neutrinos: Bounds from big bang nucleosynthesis and SN1987A*, *Nucl. Phys.* **B590** (2000) 562–574, [hep-ph/0008138].
- [338] MINIBooNE collaboration, A. A. Aguilar-Arevalo et al., *Significant Excess of ElectronLike Events in the MiniBooNE Short-Baseline Neutrino Experiment*, *Phys. Rev. Lett.* **121** (2018) 221801, [1805.12028].
- [339] MINIBooNE collaboration, A. A. Aguilar-Arevalo et al., *Unexplained Excess of Electron-Like Events From a 1-GeV Neutrino Beam*, *Phys. Rev. Lett.* **102** (2009) 101802, [0812.2243].
- [340] MINIBooNE collaboration, A. A. Aguilar-Arevalo et al., *A Combined $\nu_\mu \rightarrow \nu_e$ and $\bar{\nu}_\mu \rightarrow \bar{\nu}_e$ Oscillation Analysis of the MiniBooNE Excesses*, 2012, 1207.4809, <http://lss.fnal.gov/archive/2012/pub/fermilab-pub-12-394-ad-ppd.pdf>.

- [341] R. J. Hill, *On the single photon background to ν_e appearance at MiniBooNE*, *Phys. Rev.* **D84** (2011) 017501, [1002.4215].
- [342] H. Murayama and T. Yanagida, *LSND, SN1987A, and CPT violation*, *Phys. Lett.* **B520** (2001) 263–268, [hep-ph/0010178].
- [343] A. Strumia, *Interpreting the LSND anomaly: Sterile neutrinos or CPT violation or...?*, *Phys. Lett.* **B539** (2002) 91–101, [hep-ph/0201134].
- [344] G. Barenboim, L. Borissov and J. D. Lykken, *CPT violating neutrinos in the light of KamLAND*, hep-ph/0212116.
- [345] M. C. Gonzalez-Garcia, M. Maltoni and T. Schwetz, *Status of the CPT violating interpretations of the LSND signal*, *Phys. Rev.* **D68** (2003) 053007, [hep-ph/0306226].
- [346] V. Barger, D. Marfatia and K. Whisnant, *LSND anomaly from CPT violation in four neutrino models*, *Phys. Lett.* **B576** (2003) 303–308, [hep-ph/0308299].
- [347] M. Sorel, J. M. Conrad and M. H. Shaevitz, *A Combined analysis of short baseline neutrino experiments in the (3+1) and (3+2) sterile neutrino oscillation hypotheses*, *Phys. Rev.* **D70** (2004) 073004, [hep-ph/0305255].
- [348] G. Barenboim and N. E. Mavromatos, *CPT violating decoherence and LSND: A Possible window to Planck scale physics*, *JHEP* **01** (2005) 034, [hep-ph/0404014].
- [349] K. M. Zurek, *New matter effects in neutrino oscillation experiments*, *JHEP* **10** (2004) 058, [hep-ph/0405141].
- [350] D. B. Kaplan, A. E. Nelson and N. Weiner, *Neutrino oscillations as a probe of dark energy*, *Phys. Rev. Lett.* **93** (2004) 091801, [hep-ph/0401099].
- [351] H. Pas, S. Pakvasa and T. J. Weiler, *Sterile-active neutrino oscillations and shortcuts in the extra dimension*, *Phys. Rev.* **D72** (2005) 095017, [hep-ph/0504096].
- [352] A. de Gouvêa and Y. Grossman, *A Three-flavor, Lorentz-violating solution to the LSND anomaly*, *Phys. Rev.* **D74** (2006) 093008, [hep-ph/0602237].
- [353] T. Schwetz, *LSND versus MiniBooNE: Sterile neutrinos with energy dependent masses and mixing?*, *JHEP* **02** (2008) 011, [0710.2985].

- [354] Y. Farzan, T. Schwetz and A. Y. Smirnov, *Reconciling results of LSND, MiniBooNE and other experiments with soft decoherence*, *JHEP* **07** (2008) 067, [0805.2098].
- [355] S. Hollenberg, O. Micu, H. Pas and T. J. Weiler, *Baseline-dependent neutrino oscillations with extra-dimensional shortcuts*, *Phys. Rev.* **D80** (2009) 093005, [0906.0150].
- [356] A. E. Nelson, *Effects of CP Violation from Neutral Heavy Fermions on Neutrino Oscillations, and the LSND/MiniBooNE Anomalies*, *Phys. Rev.* **D84** (2011) 053001, [1010.3970].
- [357] E. Akhmedov and T. Schwetz, *MiniBooNE and LSND data: Non-standard neutrino interactions in a (3+1) scheme versus (3+2) oscillations*, *JHEP* **10** (2010) 115, [1007.4171].
- [358] J. S. Diaz and V. A. Kostelecky, *Three-parameter Lorentz-violating texture for neutrino mixing*, *Phys. Lett.* **B700** (2011) 25–28, [1012.5985].
- [359] Y. Bai, R. Lu, S. Lu, J. Salvado and B. A. Stefanek, *Three Twin Neutrinos: Evidence from LSND and MiniBooNE*, *Phys. Rev.* **D93** (2016) 073004, [1512.05357].
- [360] C. Giunti and E. M. Zavanin, *Appearance-disappearance relation in $3 + N_s$ short-baseline neutrino oscillations*, *Mod. Phys. Lett.* **A31** (2015) 1650003, [1508.03172].
- [361] J. Liao and D. Marfatia, *Impact of nonstandard interactions on sterile neutrino searches at IceCube*, *Phys. Rev. Lett.* **117** (2016) 071802, [1602.08766].
- [362] D. K. Papoulias and T. S. Kosmas, *Impact of Nonstandard Interactions on Neutrino-Nucleon Scattering*, *Adv. High Energy Phys.* **2016** (2016) 1490860, [1611.05069].
- [363] Moss, Zander and Moulai, Marjon H. and Argüelles, Carlos A. and Conrad, Janet M., *Exploring a nonminimal sterile neutrino model involving decay at IceCube*, *Phys. Rev.* **D97** (2018) 055017, [1711.05921].

- [364] M. Carena, Y.-Y. Li, C. S. Machado, P. A. N. Machado and C. E. M. Wagner, *Neutrinos in Large Extra Dimensions and Short-Baseline ν_e Appearance*, 1708.09548.
- [365] J. Liao, D. Marfatia and K. Whisnant, *MiniBooNE, MINOS+ and IceCube data imply a baroque neutrino sector*, 1810.01000.
- [366] J. Asaadi, E. Church, R. Guenette, B. J. P. Jones and A. M. Szelc, *New light Higgs boson and short-baseline neutrino anomalies*, *Phys. Rev.* **D97** (2018) 075021, [1712.08019].
- [367] D. Döring, H. Päs, P. Sicking and T. J. Weiler, *Sterile Neutrinos with Altered Dispersion Relations as an Explanation for the MiniBooNE, LSND, Gallium and Reactor Anomalies*, 1808.07460.
- [368] C. Dib, J. C. Helo, S. Kovalenko and I. Schmidt, *Sterile neutrino decay explanation of LSND and MiniBooNE anomalies*, *Phys. Rev.* **D84** (2011) 071301, [1105.4664].
- [369] D. McKeen and M. Pospelov, *Muon Capture Constraints on Sterile Neutrino Properties*, *Phys. Rev.* **D82** (2010) 113018, [1011.3046].
- [370] M. Masip and P. Masjuan, *Heavy-neutrino decays at neutrino telescopes*, *Phys. Rev.* **D83** (2011) 091301, [1103.0689].
- [371] S. N. Gninenko, *New limits on radiative sterile neutrino decays from a search for single photons in neutrino interactions*, *Phys. Lett.* **B710** (2012) 86–90, [1201.5194].
- [372] G. Magill, R. Plestid, M. Pospelov and Y.-D. Tsai, *Dipole portal to heavy neutral leptons*, 1803.03262.
- [373] LSND collaboration, L. B. Auerbach et al., *Measurement of electron - neutrino - electron elastic scattering*, *Phys. Rev.* **D63** (2001) 112001, [hep-ex/0101039].
- [374] M. Pospelov and Y.-D. Tsai, *Light scalars and dark photons in Borexino and LSND experiments*, *Phys. Lett.* **B785** (2018) 288–295, [1706.00424].
- [375] G. Magill, R. Plestid, M. Pospelov and Y.-D. Tsai, *Millicharged particles in neutrino experiments*, 1806.03310.

- [376] E. Valencia-Rodriguez, *Neutrino - Electron Scattering in MINERνA for Constraint NuMI Flux at Medium*, Ph.D. thesis, Guanajuato U., 2016. 10.2172/1341804.
- [377] CHARM-II collaboration, K. De Winter et al., *A Detector for the Study of Neutrino - Electron Scattering*, *Nucl. Instrum. Meth.* **A278** (1989) 670.
- [378] CHARM-II collaboration, D. Geiregat et al., *Calibration and performance of the CHARM-II detector*, *Nucl. Instrum. Meth.* **A325** (1993) 92–108.
- [379] LSND collaboration, C. Athanassopoulos et al., *Evidence for anti-muon-neutrino → anti-electron-neutrino oscillations from the LSND experiment at LAMPF*, *Phys. Rev. Lett.* **77** (1996) 3082–3085, [[nucl-ex/9605003](#)].
- [380] LSND collaboration, A. Aguilar-Arevalo et al., *Evidence for neutrino oscillations from the observation of anti-neutrino(electron) appearance in a anti-neutrino(muon) beam*, *Phys. Rev.* **D64** (2001) 112007, [[hep-ex/0104049](#)].
- [381] ALEPH, CDF, D0, DELPHI, L3, OPAL, SLD, LEP ELECTROWEAK WORKING GROUP, TEVATRON ELECTROWEAK WORKING GROUP, SLD ELECTROWEAK AND HEAVY FLAVOUR GROUPS collaboration, L. E. W. Group, *Precision Electroweak Measurements and Constraints on the Standard Model*, 1012.2367.
- [382] Collin, G. H. and Argüelles, C. A. and Conrad, J. M. and Shaevitz, M. H., *First Constraints on the Complete Neutrino Mixing Matrix with a Sterile Neutrino*, 1607.00011.
- [383] F. Capozzi, C. Giunti, M. Laveder and A. Palazzo, *Joint short- and long-baseline constraints on light sterile neutrinos*, *Phys. Rev.* **D95** (2017) 033006, [[1612.07764](#)].
- [384] M. Dentler, Hernández-Cabezudo, J. Kopp, P. A. N. Machado, M. Maltoni, I. Martínez-Soler et al., *Updated Global Analysis of Neutrino Oscillations in the Presence of eV-Scale Sterile Neutrinos*, *JHEP* **08** (2018) 010, [[1803.10661](#)].
- [385] J. A. Formaggio, J. M. Conrad, M. Shaevitz, A. Vaitaitis and R. Drucker, *Helicity effects in neutral heavy lepton decays*, *Phys. Rev.* **D57** (1998) 7037–7040.

- [386] A. B. Balantekin, A. de Gouv  a and B. Kayser, *Addressing the Majorana vs. Dirac Question with Neutrino Decays*, 1808.10518.
- [387] E. J. Chun, J.-C. Park and S. Scopel, *Dark matter and a new gauge boson through kinetic mixing*, *JHEP* **02** (2011) 100, [1011.3300].
- [388] S. Parke and M. Ross-Lonergan, *Unitarity and the Three Flavour Neutrino Mixing Matrix*, 1508.05095.
- [389] Berger, M.J. and Coursey, J.S. and Zucker, M.A. and Chang, J., “<https://dx.doi.org/10.18434/T4NC7P>.”
- [390] W. R. Leo, *Techniques for Nuclear and Particle Physics Experiments: A How to Approach*. 1987.
- [391] PARTICLE DATA GROUP collaboration, M. Tanabashi et al., *Review of Particle Physics*, *Phys. Rev.* **D98** (2018) 030001.
- [392] CHARM collaboration, J. V. Allaby et al., *Total Cross-sections of Charged Current Neutrino and Anti-neutrino Interactions on Isoscalar Nuclei*, *Z. Phys.* **C38** (1988) 403–410.
- [393] J. R. Jordan, Y. Kahn, G. Krnjaic, M. Moschella and J. Spitz, *Severe Constraints on New Physics Explanations of the MiniBooNE Excess*, 1810.07185.
- [394] MINOS collaboration, P. Adamson et al., *Measurement of single π^0 production by coherent neutral-current ν Fe interactions in the MINOS Near Detector*, *Phys. Rev.* **D94** (2016) 072006, [1608.05702].
- [395] MINERvA collaboration, J. Wolcott et al., *Evidence for Neutral-Current Diffractive π^0 Production from Hydrogen in Neutrino Interactions on Hydrocarbon*, *Phys. Rev. Lett.* **117** (2016) 111801, [1604.01728].
- [396] G. Fricke, C. Bernhardt, K. Heilig, L. A. Schaller, L. Schellenberg, E. B. Shera et al., *Nuclear Ground State Charge Radii from Electromagnetic Interactions*, *Atom. Data Nucl. Data Tabl.* **60** (1995) 177–285.
- [397] U. D. Jentschura and V. G. Serbo, *Nuclear form factor, validity of the equivalent photon approximation and Coulomb corrections to muon pair production in*

- photon-nucleus and nucleus-nucleus collisions, European Physical Journal C* **64** (aug, 2009) 309–317, [0908.3853].
- [398] R. Anni, G. Co and P. Pellegrino, *Nuclear charge density distributions from elastic electron scattering data, Nucl. Phys.* **A584** (1995) 35–59, [nucl-th/9410023].
- [399] D. W. L. Sprung and J. Martorell, *The symmetrized fermi function and its transforms, Journal of Physics A: Mathematical and General* **30** (1997) 6525.
- [400] G. Duda, A. Kemper and P. Gondolo, *Model Independent Form Factors for Spin Independent Neutralino-Nucleon Scattering from Elastic Electron Scattering Data, JCAP* **0704** (2007) 012, [hep-ph/0608035].
- [401] MINERVA collaboration, L. Aliaga et al., *Neutrino Flux Predictions for the NuMI Beam, Phys. Rev.* **D94** (2016) 092005, [1607.00704].
- [402] J. A. A. Boehm, *Measurement of electron neutrino appearance with the MINOS experiment*, Ph.D. thesis, Harvard U., 2009. 10.2172/957077.
- [403] A. Aurisano, “Recent Results from MINOS and MINOS+.” June, 2018.
- [404] L. Loiacono, “Neutrino Flux Simulations with an Evacuated and Helium Gas Filled Decay Pipe .” 2007.
- [405] P. Vahle, “NOvA Status and Prospects, 2018 July PUBLIC PAC Meeting.” July, 2018.
- [406] W. Grimus and L. Lavoura, *One-loop corrections to the seesaw mechanism in the multi-Higgs-doublet standard model, Phys. Lett.* **B546** (2002) 86–95, [hep-ph/0207229].
- [407] D. Aristizabal Sierra and C. E. Yaguna, *On the importance of the 1-loop finite corrections to seesaw neutrino masses, JHEP* **08** (2011) 013, [1106.3587].